Modelling, Analysis and Forecasting of Deep Sea Oxygen Isotope Variations Response to Orbital Forcing

Eliza - Patricia Condrea

Department of Automatic Control and Systems Engineering

University of Sheffield

A thesis submitted for the degree of

Doctor of Philosophy

June, 2014

"Does the flap of a butterfly's wings in Brazil set off a tornado in Texas?"

Edward Lorentz

To my parents

Abstract

Over the Pleistocene Period, which covers the time interval [2.588, 0.0117] million years ago, the dominant period of glacial-interglacial cycles changed from 41 000 years to 100 000 years. According to Milankovitch's Theory the variations of Earth's orbital parameters eccentricity, obliquity and precession are driving the growth and melting of glaciers. Despite being generally accepted, Milankovitch's Theory is still being challenged by some scientists largely because of lack of models that are driven by the orbital parameters, which can adequately reproduce climate proxy variables.

In this context, the aim of this thesis was to study the link between Earth's orbital parameters and climate proxy data and more specifically the role of orbital forcing in the shift of dominant oscillation cycle during the Pleistocene and the origins of the 100 000 years cycle.

In this work, nonlinear system identification tools were used to model oxygen isotope ratios time-series extracted from the Western Pacific Drilling Site 806B. By analysing the resulting models in the time and frequency domain, using Generalized Frequency Response Functions and Output Frequency Responses, it was possible to determine which frequencies and combinations of frequencies from the spectrum of the orbital parameters contribute most significantly in the output spectrum, with focus on the frequency corresponding to the 100 000 years cycle.

More specifically, two new polynomial models, each dealing with one of the two Pleistocene time periods dominated by a different cycle, were developed, analysed and compared. The estimated models predict very well the oxygen isotope ratio time-series extracted from Site 806B.

The identified models not only predict well the oxygen isotope ratios, but also capture

the dynamics of the underlying processes before and after the Pleistocene dominant cycle shift. The models reproduce well the critical points in the data which correspond to climatic events, such as switching between a glacial and interglacial period. The models were used to compare the variability in the palaeoclimate data over the two time periods and analyse possible causes behind the observed change in period of oscillation.

By mapping the models into the frequency domain it was possible to characterize the linear and nonlinear coupling between the individual orbital parameters and the climate proxy variable of interest and to characterize the role of nonlinear interactions over different glacial and interglacial periods.

The results presented in this thesis arguably provide the most compelling quantitative evidence in support of Milankovitch's Theory.

Acknowledgment

I would like to sincerely thank Professor Daniel Coca for giving me the opportunity to pursue this PhD. I benefitted immensely from the discussions, guidance and constructive feedback during the time spent working with him.

I would also like to thank Professor Stephen Billings for providing me with the NSFRA Toolbox, that help me in understanding key concepts and developing my own software.

I would like to thank my colleagues from room 316, Dr. Veronica Biga, Dr. Andrew Hills, Dr. Geoff Holmes and many others, for the work related and casual discussions.

I would like to give special thanks to my parents for their constant support and to my boyfriend for always keeping the hope alive.

Contents

List of Figures

List of Tables

Chapter 1

Introduction

1.1 Background and Motivation

The Quaternary era is the most recent geological era of the Earth and spans over the past 2.6 million years. Part of the Quaternary is the Pleistocene epoch, which covers the time interval [2.6, 0.0117] million years. Over this time, the global climate was characterized by succeeding cold and warm periods, which caused the glaciers and ice-sheets to grow and retreat. The glacial and interglacial periods alternation varies periodically. The period of each cycle changed though around $0.9 - 0.8$ million years ago. This change is called the Mid-Pleistocene Transition (MPT), and brought a shift in the glacial-interglacial variation cycle from 41 000 years ***before MPT*** to 100 000 years ***after MPT***. Although the effects of the change occurred at the MPT are known, it is still not clear what triggered this modification. Many authors have investigated the shift during the MPT and the possible origins of the 100 kyr cycle, but a unified theory could not be widely accepted. Among the possible explanations, scientists referred to: the influence of orbital parameters (Rial and Anaclerio, 2000, Berger, 1988, Berger and Loutre, 1997a, Berger et al., 1999, Imbrie et al., 1993), internal feedbacks caused by: ice sheets (Berger, 1988), CO_2 concentration (Ganopolski and Calov, 2011), ice albedo (Maslin and Ridgwell, 2005) or dust (Ganopolski and Calov, 2011), or external forcing cause by orbital inclination (Muller and MacDonald, 2005).

Given the alternation of glacial and interglacial periods are quasi-periodical, scientists tried to explain this by referring to the periodic variations in Earth's orbit around the Sun

(Rapp, 2008, Crucifix et al., 2009). This is called the Milankovitch theory (McGuffie and Henderson-Sellers, 2005), after the serbian scientist that studied the Earth's movements, calculated the changes in Earth's orbit and the temperature values at different points on Earth's surface. This allowed him to propose the theory that the ice ages are sustained by cold summers which prevent the winter snow from melting. This dismissed James Croll's theory (1875), that proposed that very severe winters counteracted the effects of short and hot summers (Finnegan, 2011). The astronomical theory developed by Milankovitch predicts the climate variability at the geological time scale (100 000 years), which allows the study of the relationship between orbital variations and seasonal, decadal and long to very long climate changes (Berger, 1988). It is thought that the orbital forcing acts as trigger and is not the sole factor of the extreme climatic changes (Berger and Loutre, 2002, Imbrie and Imbrie, 1980, Macdougall, 2004).

The orbital parameters *eccentricity*, *obliquity* and *precession* influence Earth's existence and length of seasons, orbit orientation and the distance between the planet and the Sun. By this influence, the amount of sunlight received at each latitude (insolation) is affected, and so the orbital parameters affect the Earth's climate. Each of the orbital parameters varies periodically with cycles between tens and hundreds of thousands of years, with the main period in *eccentricity* being 100 000 years, in *obliquity* 41 000 years and in *precession* 26 000 years.

Berger (1978a) and Berger(1978b) was able to prove, through tables of calculated values for the insolation, the link between the periods of the orbital elements and the evolution of climate (Imbrie and Imbrie, 1980). This link between climate change and insolation is nonlinear (Crucifix et al., 2009).

The orbital parameters cycles have also been associated with periods found through spectral analysis in deep-sea proxy records for the Pleistocene epoch (Crucifix et al., 2009). The Ocean Drilling Program (ODP), between the years 1983-2003 while it was operating, conducted 110 expeditions with 2000 drilled holes covering vast areas from the Arctic Ocean to the Weddell Sea, and was an international effort of exploring the Earth's subsea floors and their composition and structure. Through the recovery and analysis of sediment fossils that accumulated slowly on the ocean's bottom over geologic time, it was possible to gain a

better understanding into Earth's past, but also it's future. The fossils chemistry represents proxies for the ocean conditions of the time when the microorganisms lived. Because the deep ocean sediments are insulated from seasonal or other short-term noise, they give the cleanest overview of long-term global temperature changes on Earth.

The modelling efforts that use palaeoclimatic data aim to explain a number of intriguing climate events and features of the palaeoclimate, such as the appearance of a 100 000 years cycle, or to predict the evolution of the global ice volume, the global sea-surface temperature or the positions of the ice sheets at different times. The models developed in the past could reproduce the appearance of the 100 000 years cycles to some extent. However, none of the previous models could predict reasonably well the response of the proxy variables to orbital parameters (Oerlemans, 1982, Ghil and Tavantzis, 1983, Saltzman and Sutera, 1987, Saltzman and Maasch, 1990). Some models could also reproduce the MPT period shift (Le Treut et al., 1988). The most successful palaeoclimate models, which were able to also provide an explanation for the appearance of the 100 000 years cycles, were developed by: Rial and Anaclerio (2000), Imbrie et al. (1992), Berger et al. (1999) and Pollard (1983). However, these models still have some faults, such as: Rial's model (2000) can only reproduce the main periodicities in the data and not its subtle variabilities, Imbrie's model (1992) does not distinguish between two intermediary states (initial and preglacial) out of the four defined ones. Berger et al. (199) only models the time ***after MPT***, and for one third of the data, which corresponds to the interval $\sim [600\,000\,,\,400\,000]$ years Before Present (BP), the model simulation goes out of phase. Milankovitch (1941) mathematically proved the connection between irradiation and temperature.

1.2 Aims and Objectives

The aim of this research was to use nonlinear system identification techniques to develop models that describe the relationship between the orbital parameters and the ODP proxy data throughout the Pleistocene, which allow to elucidate the orbital parameters influence on the global climate variability, to explain the origin of the 100 000 cycle and characterize rigorously the dynamical changes that took place during the MPT.

System identification is a method inferring a mathematical model of a dynamical system from experimental measurements of the inputs and outputs (Billings, 2013). Therefore, by using system identification, a mathematical model describing the relationship between the orbital parameters and proxy data can be developed. System identification has been successfully applied in many fields, such as engineering, biology, medicine, finance, social sciences etc (Billings, 2013). The great advantage of system identification is that it requires no knowledge of the system, and only uses experimental measurements. A well established identification framework for nonlinear dynamic systems is the NARMAX methodology (Leontaritis and Billings, 1985). The aim is to use the identified NARMAX polynomial model to understand the relationship between the orbital forcing and climate variations. Using the NARMAX methodology to model environmental time-series provides a novel and powerful approach to characterize quantitatively the relationship between the orbital forcing parameters and the proxy variables. Furthermore by computing Generalized and Output Frequency Response Functions, the identified nonlinear NARMAX model can be mapped into the frequency domain and analysed in order to establish the nonlinear mechanisms by which the orbital parameters generate the 100 000 years cycle.

More specifically the main objectives of this work can be summarized as follows:

- Apply nonlinear system identification based on the NARMAX methodology to identify models corresponding to the time periods ***before*** and ***after MPT***. These models can help to understand the influence of the orbital parameters by comparison of their contribution to each model. Furthermore, given the orbital parameters values (Berger, 1978a), the models can be used to predict how the climate will change in the future and understand the underlying causes of the variations.

- Derive the Generalized Frequency Response Functions (GFRFs) and the Output Frequency Responses (OFRs) for the identified models. These frequency domain functions are very useful because, although many different time domain NARMAX model structures can describe the same system, their frequency domain functions will provide unique results. Frequency domain analysis can provide great insight into a system's characteristics, especially in the case where the time-domain model cannot yields any

straightforward relation to the underlying physical processes. By analysing the GFRFs it is possible to investigate the effect of different model terms to the output spectrum. This can be related back, through the model terms, to the contribution of the orbital parameters to the output spectrum. Also, the GFRFs are a powerful tool for investigating the energy transfer phenomena. The OFRs offer the advantage that, compared to the GFRFs, are one-dimensional functions of frequency, so they are easier to analyse and interpret. They can help in establishing the contribution of each input to the output spectrum. The OFRs are also used in analysing specific frequencies of interest and how the magnitude peaks at these frequencies are composed.

- Use the models to analyse the change that occurred during the MPT. The intriguing aspect of the MPT is the shift from a dominant period of 41 000 years (***before MPT***) to one of 100 000 years (***after MPT***), so it is important to obtain two NARMAX models that can also reproduce this shift.

- Use the frequency domain analysis tools described above to analyse individual output frequencies and which of the input frequencies contribute to their magnitude peaks. These methods can be used to investigate the "100 000 years Problem", which refers to the appearance of the dominant 100 000 years cycles ***after MPT***, the origin of which is still debated.

- Use the OFR to decompose the time domain response of the model into contributions associated to individual kernels of the Volterra series expansion. This allows quantifying the contribution of each order of nonlinearity to the model output.

- Compare the performance of the identified NARMAX models with existing models.

- Determine, compare and characterize the equilibrium points of the system ***before*** and ***after MPT***.

- Model, analyse and compare the oxygen isotope time-series from two different ODP Sites. This can help understand why data-sets from adjacent drilling holes are slightly different and identify a model structure that can explain the observed differences.

1.3 Overview of the Thesis

The work presented in this thesis is structured into 9 chapters. The remaining chapters are organized as follows.

- *Chapter 2* provides an overview of the paleoclimate data. This includes a description of the changes that happened during the *Mid-Pleistocene Transition*, equations and description of the three orbital parameters *eccentricity*, *obliquity* and *longitude of perihelion* and their influence on the Earth, details on the proxy data and how this is recovered and dated. The chapter also reviews the previously developed models that attempt to model the MPT and/or to reproduce the 100 kyr cycle.

- *Chapter 3* introduces the NARMAX methodology. This chapter provides a detailed description of all the major steps of the system identification methodology, namely: model structure detection, parameter estimation and model validation techniques, with particular emphasis on the polynomial NARMAX representation. The methodology presented in this chapter provides the basis for the subsequent development of the mathematical models based on palaeoclimatic records.

- *Chapter 4* introduces the theoretical concepts of Generalized Frequency Response Functions and Output Frequency Responses. Firstly the multi-tone inputs and the contribution given by each type of model term are defined in order to compute the GFRFs. This chapter presents the derivations of the expressions of both the GFRFs and OFRs. In order to help with the implementation of the higher-order frequency response functions simple examples are provided.

- *Chapter 5* describes for the first time the identification directly from temperature proxy measurements of two NARMAX models that can describe the relationship between the three orbital parameters (*eccentricity*, *obliquity* and *longitude of perihelion*) and the oxygen isotope ratios time-series. This chapter starts by presenting the palaeoclimatic proxy data used and the orbital parameters time-series. The modelling procedure involves rigorous selection of the best model structure and parameter estimation. The resulting models are validated using correlation tests and coherence analysis. This

methodology is applied separately for the data corresponding to each of the two time periods: ***before*** and ***after MPT***, and two models describing each period are obtained. The results demonstrate that the identified models can describe the dynamic response of the climate proxy variable to orbital forcing with unprecedented accuracy.

- *Chapter 6* presents the results of mapping the NARMAX models developed in Chapter 5 in the frequency domain through the GFRFs and OFRs. The computation of GFRFs involves two preliminary model transformation procedures. This chapter provides the analytical expressions of the GFRFs and OFRs associated with the identified models. The chapter also presents a comparative analysis of the simulation results for ***before*** and ***after MPT*** of the GFRF and OFR expressions. This analysis is targeted at finding differences and similarities between the results that can explain why the observed MPT change occurred. Moreover, the OFR results are used to quantify the contribution of each function and the observed changes at the frequency corresponding to the 100 kyr period.

- *Chapter 7* investigates the time domain properties of the models developed in Chapter 5. This involves comparing the model predicted output, calculating the predicted equilibrium points of the system and assessing their stability. An additional analysis is carried out to determine the contribution to the output of the first, second and third order terms in the Volterra series expansion by mapping the OFRs back into the time domain. This chapter also presents a comparison of the identified model results and the simulated results of Rial's model (2000), which clearly proves the improved accuracy that NARMAX modelling offers.

- *Chapter 8* presents a model which relates the variations of the proxy variables obtained from ocean sediments extracted at two adjacent ODP Sites of Leg 130: Site 806B and 805C. In the first instance, the two sites are compared with regards to their location and physical properties and the chemical gradients in the interstitial waters. An important contribution of this chapter is the identification of the casual link between the measurements recorded at the two sites, i.e. measurements at Site 806B provide the input and the measurements at Site 805C provide the output of the system.

- *Chapter 9* provides general conclusions on the thesis and offers suggestions for further developing this work.

Chapter 2

Orbital Parameters and Their Impact on Palaeoclimate Proxies

2.1 Introduction

A key point in understanding Earth's climate and being able to predict what it will be like in the future is to analyze the past climate and the periodic changes that it has gone through. Earth's climate has gone through a series of changes, over different time scales: long term (hundreds of millions of years), medium term (one million years), short term (approximately 160,000 years) and modern period (hundreds of years, which includes the human influence) (Pomerol, 1982). Intensive studies have been aimed towards understanding the origins and mechanisms behind these changes, and scientists have pointed towards modifications in palaeogeography, greenhouses gas concentrations, astronomically forced insolation and inter-regional heat transfer as the main causes of alteration (Loutre and Berger, 2000).

When studying the medium to long time periods, the planet has gone through a series of periods of glaciations, when the scene was dominated by ice sheets, and periods of warmer temperature, characterized by risen ocean levels. The Pleistocene time period presents great interest because of a change that happened around 900-800 kyr (1kyr = 1000 years) BP. After this time the interglacial periods have occurred approximately every 100 kyr, whereas before this time the dominant period in the ice volume variations was that of 41 kyr (Imbrie et al., 1993, Ruddiman, 2006, Mudelsee and Schulz, 1997). The observed shift in periods

around 900-800 kyr BP is known as the Mid-Pleistocene Transition (MPT).

Palaeoclimatology is the study of the geological past of Earth using climate proxies such as sea (lake, ocean) sediments, ice sheets and ice cores, tree rings, corals, shells and microfossils (Bridgman, 2006). By analysing climate proxies it is possible to extract proxy variables (stable isotope ratios, sedimentation rates, growth indicators etc) for water and air temperature, atmospheric gasses (methane, CO_2). Proxy data is commonly used when actual measurements of the processes are not available due to the extremely long span of the measured climate period. By studying the long climate evolution and major revolution events scientists can identify past climatic trends, better understand the current climate and predict easier the future one and its implications.

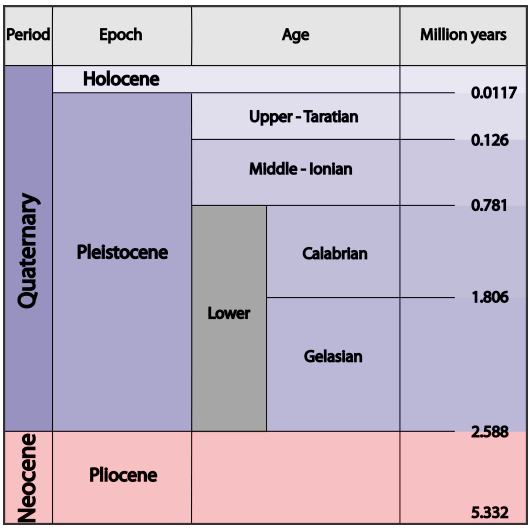

Figure 2.1: Earth's Geological Eras covering [2.588 , 0] Ma. Image made using materials from Trenberth (2006) and Ericson and Wollin (1964).

The palaeoclimate changes do not happen instantaneous, but over a long period of time. For this reason the scientists (Berger and Loutre, 2002, Imbrie and Imbrie, 1980, Macdougall, 2004), in order to characterize the changes in Earth's palaeoclimate, have investigated the link between insolation and orbital parameters (Crucifix et al., 2007, Rapp, 2008). Three orbital parameters (*eccentricity*, *obliquity* and *precession*) have been identified to have periodicities

greater than a few thousand years. This is why the variations of Earth's orbit are associated with climatic changes. The Earth's orbital parameters can be calculated using the equations by Berger (1978) over a period of 3 Myr (million years). This period is suitable for finding a model to describe The Quaternary era, which includes the Pleistocene period.

The quantity of solar radiation received on a given surface area at a given location on Earth is called insolation. Insolation is a function of the Sun-Earth distance thus it will depend on the Earth-orbit and the angle between solar rays and the normal to the Earth's surface. In turn, these parameters depend of the Earth's orbit and thus insolation will be a function of the orbital parameters. The greater the angle of the solar rays is, the larger the surface temperatures are. However, because insolation or temperature measurements are rare earlier than 1850 AD (Bridgman, 2006), it is necessary to assess past climates indirectly, through the means of proxies. The proxies do not give direct values of temperature, but indicators of how they changed (Bridgman, 2006).

This chapter is organized as follows. Section 2.2 provides an overview of the general climate features of the Quaternary era and, in more depth, of the Pleistocene time period. The Mid-Pleistocene Transition and the changes it brought to the climate scene are reviewed. Section 2.2 also gives a description of the "100 kyr Problem" and the different theories proposed by various authors to resolve it. Section 2.3 introduces the Earth's orbital parameters and details on how they influence the insolation. Section 2.4 describes the proxy data represented by foraminifera and explains how the data is obtained, what are the oxygen isotope ratios and what information it can provide for climate modelling. Also, the oxygen isotope ratios data-set extracted from the Western Pacific Ocean Drilling Programme Site 806B is described in this section. Section 2.5 gives an overview on the previously developed palaeoclimate models, with emphasis on the ones that use orbital forcing, can reproduce the orbital frequencies, and have been used to explain the appearance of the $\sim$ 100 kyr cycle.

2.2 The Mid - Pleistocene Transition

The Quaternary is the most recent geological era that spanned over the last 2.588 Myr and it includes the epochs Holocene and Pleistocene (Gradstein et al., 2005, Trenberth, 2006). It is

commonly known as an era of extremes due to its glacial (glacial advances) and interglacial (glacial retreats) intervals. The Earth is currently in an interglacial, and the last glacial period ended about 10,000 years ago (Jouzel et al., 1993, Crucifix et al., 2007). The sequence of glacial – interglacial cycles has received much attention from researchers. Although they do not offer a theory that can cover all angles of the problem, it does seem that this phenomenon was favoured by a series of simultaneous events, such as: the astronomical cycles and the incoming solar irradiation (insolation), atmospheric composition (trends in atmospheric CO_2), plate tectonics and ocean currents (movement and position of the continents), and other global and local phenomenon episodes (ice albedo, loess accumulation, deposits of ice debris, uplift of the Himalayas) (Gradstein et al., 2005). Scientists are still working on determining if some of the above mentioned incidents are causes or effects of the ice ages.

From the study of proxy data it has been shown that the first part of the Quaternary, known as the early Pleistocene, was dominated by an approximately 41 kyr signal, whereas the last part of it, also known as the late Pleistocene, was dominated by an approximately 100 kyr signal. Milankovitch (1941) was the first scientist to link the glacial cycles to the variations in Earth's orbital parameters, represented by *eccentricity*, *obliquity* and *precession*. His hypothesis has long been discussed and is widely accepted due to the long periods of the orbital elements, roughly 100, 41 and 26 kyr, and the similarity of the results with those from the more recent Deep-Sea Drilling Programmes ones (Berger et al., 1991a, Rial and Anaclerio, 2000, Berger et al., 2005, Paillard, 2001). Milankovitch's idea was that the orbital parameters influence the amount and seasonal distribution of sunlight that reached the Earth's surface and this in turn favours the forming of the glacial – interglacial cycles and the change from the 41 kyr to 100 kyr dominant signal. At the same time the theory is thought to be insufficient to explain the glacial – interglacial cycles, due to a mismatch in the timing of the glacial terminations from the terrestrial records (Maslin and Ridgwell, 2005). An explanation for this could be additional feedbacks (Berger, 1988, Ganopolski and Calov, 2011), but the cause and nature for these has not yet been satisfactory explained.

From a first investigation over the oxygen isotope record time series for the Quaternary Period extracted from Site 806B, it can be seen that the data can be split into three parts (marked on Figure 2.13 with dotted red line) that differ from each other both in amplitude

of the signal but also in the frequency of oscillation. The times of these modifications are approximately 0.85-0.9 Myr BP and 1.3-1.4 Myr BP. Hence, because the orbital parameters don't change their nature during this era, it is obvious now that the way in which the climate system responds to them changes at the given intervals.

2.2.1 The Mid-Pleistocene Features

The Pleistocene Epoch follows the Pliocene Epoch and is followed by the Holocene Epoch in the Quaternary Era sequence (Gradstein et al., 2005) (Figure 2.1).

The climate modification at the 0.85 - 0.9 Myr BP is widely known as the Mid-Pleistocene Transition or Revolution (Berger et al., 1994, Berger and Loutre, 1994). What happened at this point in Earth history is very interesting to unveil especially because there are many theories but not one unanimously accepted by palaeoclimate scientists. What it is known are the effects: a shift from a time with warmer temperature, less intensive glaciations and oscillations with a frequency of 41 kyr (found in the *obliquity* bands) to one with colder climate and oscillations characterized by a frequency of 100 kyr (Maasch, 1988, Berger et al., 1994, Paillard, 1998, Raymo and Nisancioglu, 2003).

There are two types of transitions identified throughout the geological past of Earth: *aberrations* and *quasiperiodical* oscillations (Zachos et al., 2001). Aberrations are characterized as abrupt changes due to exceeding of climatic thresholds. These happen fast (less than a few thousands of years) and can have extreme effects. The quasi-period variations are thought to be driven and paced by Earth's orbit which through their effect on daily insolation can inflict the periods of tens and hundreds of years found in the proxy data.

Spectral analysis for the oxygen isotope records have shown frequencies correspondent to the period of 41 kyr, associated with *obliquity*'s period, and 21 kyr, associated with *precession*'s period. Peaks were also found at the frequencies correspondent to the period of 413 kyr and the lower period of 100 kyr. It is known (Pisias and Moore Jr., 1981) that *eccentricity* varies with periods of 95, 125 and 413 kyr, so this factor seems to influence the oxygen isotope variations. The forcing or internal parameter behind the 100 kyr frequency

though could not be explained so far.

2.2.2 The "100 kyr Problem"

Through power spectra analysis on the oxygen isotope data scientists were able to confirm that orbital frequencies are present in the data, and that the dominant peak in the past 900 - 800 kyr is that corresponding to the 100 kyr one. *Obliquity* and *precession* frequency peaks were also found to be important climatic proxy data peaks. Even with these advances there are many still unanswered questions with regards to *eccentricity*'s connection to the $\sim$ 100 kyr period and the Mid-Pleistocene Transition, such as:

1. Why did the 100 kyr power increase so dramatically around 0.8 Ma, despite no apparent change in the orbital forcing (Lisiecki, 2010).

2. The nonlinear mechanisms behind the 100 kyr periods are yet to be explained. It has been recognized in literature that the 100 kyr cannot be explained as a linear (direct) response to *eccentricity* (Berger et al., 2005, Raymo and Nisancioglu, 2003, Lisiecki, 2010), and it has been suggested that this can be the result of bundling of either 4 or 5 precession cycles (Raymo, 1997) or 2 or 3 obliquity cycles (Huybers and Wunsch, 2005) that resulted in an average 100 kyr periodicity.

3. The oxygen isotope curves have revealed a nearly 300 kyr long stage of transition from a predominant 41 kyr to 100 kyr periodicity. Therefore, the "Mid-Pleistocene Revolution" should be considered as a process of transition rather than an abrupt change (Wang et al., 2001).

2.2.3 Potential Origins and Explanations for the "100 kyr Problem"

Extensive analysis has been conducted by many authors in order to obtain an explanation to the "100 kyr Problem". Most agree that because the nature of the orbital forcing does not

change in different times, it must be the way the climate system evolves and responses to external forcing, especially a nonlinear response to *precession*, that sets the amplitude and phase for the 100 kyr oscillation.

The main explanations from literature for what drives the 100 kyr oscillation cycles are:

- ***External forcing*** in the form of *orbital inclination*, which can be thought of as a possible forth orbital parameter. It has the desired period of 100 kyr, which matches the one in palaeoclimatic records. This orbital element represents the variation in the angle of the Earth's plane of orbit compared to the average orbit of the solar system (Farley and Patterson, 1995, Muller and MacDonald, 1997). However, due to the fact that inclination changes are too small compared to seasonal extremum, it is not plausible that this parameter can have such a big impact as to induce the 100 kyr periodicity in ice ages (Mudelsee and Schulz, 1997, Kortenkamp and Dermott, 1998, Berger et al., 1999). A second approach to external forcing is the argument that the total amount of radiation received on Earth's surface is influenced by the fact that Earth's orbit passes through an outer space cloud of dust (*Interplanetary Dust Particles*). Some researchers have hypothesized that this could induce glacial-interglacial alternations with the 100 kyr period.

- ***Internal feedbacks*** due to a number of factors:

  - *Ice sheets* have played, according to Berger (1988), an important role in modulating the 100 kyr cycle. DeBlonde and Peltier (1991) on the other hand talk about a feedback effect between the lithosphere and ice sheets.
  - CO_2 *concentration*, which accounts for the radiative forcing of three major *greenhouse gases*: carbon dioxide, methane and nitrous oxide (Ganopolski and Calov, 2011). The global climate state is dependent on the atmospheric concentration of many atmospheric components, like CO_2, CH_4 or water, and changes in these can drive the global climate towards cooling or warming. A very important role is played by the greenhouse gases, that absorb outgoing infrared radiations (e.g. Berger, 1988, Maasch, 1988, Maasch and Saltzman, 1990, Saltzman and Maasch, 1991, Saltzman and Verbitsky, 1993, Berger and Loutre, 1992, Li et al., 1998).

The scientists are torn between the hypothesis that climate sensitivity to the CO_2 concentrations variations is high enough to favour the presence of the 100 kyr cycle or that the changes in the CO_2 are merely an effect of the glacial-interglacial transitions.

- *Ice albedo* feedback (Maslin and Ridgwell, 2005) - as snow and ice accumulate due to initial changes in insolation regime, the ambient environment is modified and a repetitive climatic effect is produced. Firstly, an increase in albedo, will trigger more reflection of the solar radiation. Because this means a reduction in solar radiation absorbtions, the local climate will change with regards to temperature. This will in turn support the accumulation of more snow and ice and another modification of the local environment. Although ice albedo effects can be considerable, they are not global but latitudinal dependent.
- *Dust* feedback is thought by Ganopolski and Calov (2011) to be the required strong nonlinear feedback mechanisms that can explain glacial terminations. This feedback is activated after the ice sheets spread well into the area covered by thick terrestrial sediments. Large dust deposits over the ice sheets can reduce their albedo and in turn favour the ablation and the ice sheet's response to insolation. This mechanism is thought to give a possible explanation to the changes from the 41 kyr to the 100 kyr world.
- Saltzman and Verbitsky (1994) suggest an *internal* instability, which is generated by feedbacks among temperature, CO_2 and ice volume, that generates an internal oscillation with a 100 kyr period.

- ***Frequency modulation*** theories:

  - Rial and Anaclerio (2000) say that frequency modulation is a nonlinear phase- and frequency-locking process that transfers energy from one frequency band into another, and can create new frequencies (called sidebands) as combination tones of the *carrier* and the *modulating* frequencies. In this case the modulator and the sidebands will present strong phase coherence. Rial's theory suggests that:

  - The 75 and 123 kyr peaks coincide with the predicted sidebands of a 95 kyr carrier frequency modulated by a 413 kyr signal, as in $\frac{1}{75} = \frac{1}{95} + \frac{1}{413}$ and $\frac{1}{123} = \frac{1}{95} - \frac{1}{413}$.
  - The 85, 107 and 143 kyr peaks coincide with the predicted sidebands of a 95 kyr carrier frequency modulated by an 826 kyr subharmonic of the 413 kyr signal, as in $\frac{1}{85} = \frac{1}{95} + \frac{1}{826}$, $\frac{1}{107} = \frac{1}{95} - \frac{1}{826}$, and $\frac{1}{143} = \frac{1}{95} - \frac{3}{826}$.
  - Frequency modulation is a nonlinear process described by the equation (Chowning, 1977):

$$e = A\sin(2\pi f_c t + I\sin(2\pi f_m t))$$

where e is the instantaneous amplitude of the modulated carrier, f_c is the carrier frequency in Hz, f_m is the modulating frequency in Hz and I is the modulation index. Hence, if the role of the 413 kyr *eccentricity* component is indeed to frequency-modulate the higher frequency components, we can expect to find signal power at 413 kyr in all the $\delta^{18}O$ records, though not in the form of a spectral peak, but rather as the interval between sidebands (Rial, 2004a). So the fact that in the proxy data there is no substantial power at 413 kyr is entirely consistent with FM theory.

- Clemens and Tiedemann (1997) put forward the theory that eccentricity modulates the amplitude of precession. The eccentricity peaks in the oxygen isotope ratios ($\delta^{18}O$) spectrum suggests that the pre 1.2 Myr climate system transfers variance from the upper envelope of precession-dominated insolation into the 404, 124 and 95 kyr eccentricity bands. This suggestion is supported by the observation that the amplitudes of the 404, 124 and 95 kyr $\delta^{18}O$ cycles are approximately equal to the amplitude of the 23 kyr $\delta^{18}O$ cycle, each accounting for 0.1% of the total 0.6% amplitude. The remaining 0.2% is accounted for by the amplitude of the 41 kyr cycle.
- Berger and Loutre (1997a) also suggest that the 100 kyr power can be generated by transmission of 19 kyr and 23 kyr periods through a nonlinear system producing

substantial power in both harmonics and subharmonics.

- Berger et al. (1999) claim that a general problem for most of the simulations is that they can hardly reproduce a $\sim$ 100 kyr period without the $\sim$ 400 kyr one (e.g. Imbrie and Imbrie, 1980, Kukla et al., 1981) due to the nonlinear origin of the 100 kyr period which comes from the combination tone between the frequencies of the first and third terms in the precession trigonometrical expansion, whereas the 400 kyr period comes from the combination tone between the first and second precessional frequencies Berger (1988).

- ***Coupled response*** between the orbital forcing and an internal nonlinear amplification:

  - Berger's investigations (1988) show that the 100 kyr cycle seems in phase with the eccentricity cycle, although the exceptional strength of this cycle needs a nonlinear amplification.

  - Imbrie et al. (1993) suggest that larger Northern Hemisphere ice sheets are an essential condition for the development of feedbacks to drive the 100 kyr ice volume cycle. In low latitudes however, large 100 kyr cycles can be developed independently of large ice sheets. In this view, the 100 kyr cycle is a response to the Milankovitch forcing in which the coupled air - sea - ice system acts as a nonlinear amplifier.

Other unexplained features of this era are:

1. The notable absence in the $\delta^{18}O$ data of significant spectral amplitude at the 413 kyr in the last 1.2 million years, in spite of being the largest component of eccentricity forcing (Crucifix et al., 2007, Loutre et al., 1992, Berger and Loutre, 1992).

2. By which nonlinear mechanism can the spectral peaks at frequencies other than those in the insolation forcing be explained? Most researchers agree that these extra peaks are either harmonics or combination tones of the orbital forcing (Rial and Anaclerio, 2000).

2.3 Earth's Insolation and Orbital Parameters

Earth's orbit is influenced by the gravitational attraction of all the other planets in the Solar system, the Moon, the Sun and our planet's distance to them. She solution to the orbital system is very complex, and many scientists have worked on theories regarding this, such as: Johannes Kepler (1571-1630), Sir Isaac Newton (1643-1727), Lagrance, Pontecoulant and Louis Agassiz.

Due to their long periods (tens and even hundreds of thousands of years) the orbital parameters are the perfect candidates to explain the long-term variability observed in the climatic proxies. The three orbital parameters that are considered the most important (Berger, 1978a, Berger, 1978b, Saltzman and Sutera, 1987, Imbrie and Imbrie, 1980) for palaeoclimate study are: *eccentricity* (e), *obliquity* (ε) and *precession* (p). These influence: the appearance, shifts and effects of the seasons, the changes in Earth's orbit orientation, the closest and farthest points in the Earth's orbit with regards to the Sun (Figure 2.2).

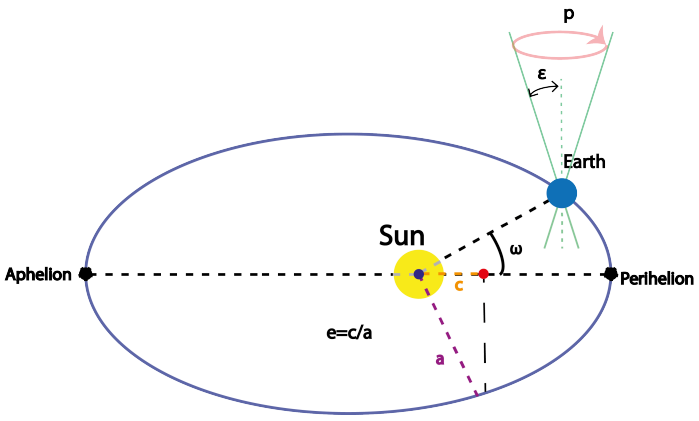

Figure 2.2: Earth's orbital parameters: e (*eccentricity*), ε (*obliquity*), ω (*longitude of perihelion*) and p (*precession*). Figure adapted from Jansen et al. (2007).

2.3.1 Eccentricity

Earth's orbit is described by an ellipse shape, which can be seen in Figure 2.3. The value of an orbit's *eccentricity* is given by the equation (Berger and Loutre, 1994):

$$e = \frac{\sqrt{a^2 - b^2}}{a}$$

where e is the *eccentricity*, and a and b are the semi-major and semi-minor axes of the elliptical orbit.

An *eccentricity* value of 0 corresponds to a circle (Figure 2.3). The meaning of the orbital *eccentricity* is the amount by which the orbit of a planet deviates from a perfect circle. This happens mostly due to the gravitational fields of the planets Jupiter and Saturn (Beer et al., 2006). The *eccentricity*, given is a ratio, is unitless. Figure 2.3 shows examples of various orbit shapes and their eccentricities.

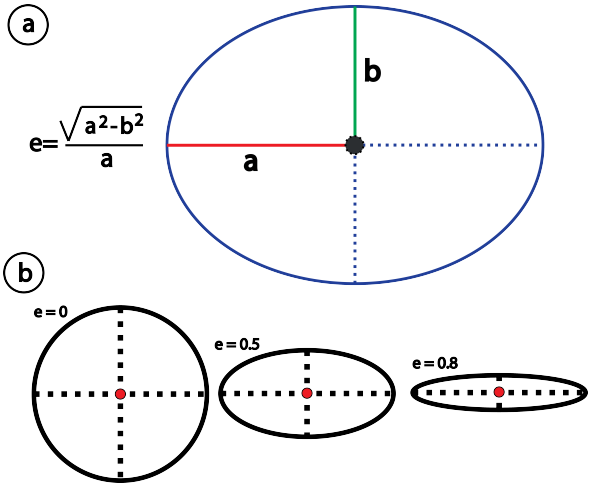

Figure 2.3: a. Defining elements in *eccentricity*'s definition and b. examples of different orbit's eccentricities and their values. Images adapted from "http://earth-www.larc.nasa.gov/ceresweb/IWG/glossary/e.html".

Earth's *eccentricity* values are very small, varying periodically over hundreds of millions of years between 0.000567 (near circular) and 0.053511. The current value of Earth's *eccentricity* is 0.0167 and this might have trigger an observed increase in July to January insolation of approximately 6.4% (Berger and Loutre, 2002). The mean value of *eccentricity* for the period [1400 , 0] kyr is 0.028. For the past 15 Myr, the three most important periods in the series expansion for *eccentricity* are about 413, 125 and 95 kyr.

Eccentricity has influence on the planet's seasons. Provided that the semi-major axes remain constant, when the *eccentricity* is bigger the seasons on the far side of the orbit can

get longer. Contrary, when the *eccentricity* takes smaller values, the Earth is closer to the Sun, thus summers will be warmer and winters less severe (Thomas, 2002).

For the considered time period 1400 - 0 kyr BP, the *eccentricity* values are presented in Figure 2.4.

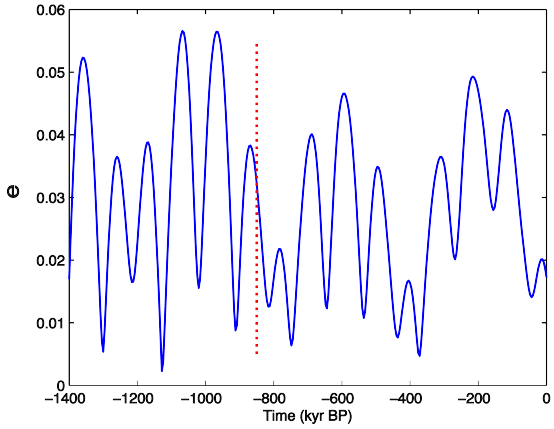

Figure 2.4: *Eccentricity* for the time period [1400 , 0] kyr BP.

2.3.2 Obliquity

Obliquity, or the Earth's tilt, represents the angle between the perpendicular to Earth's elliptical orbit plane and its axis of rotation (Figures 2.2 and 2.8). Because of this for half an orbit one pole will be directed towards the Sun and the second half away from it. This is what causes the planet's seasons and is known to be an important factor in climate change (McGuffie and Henderson-Sellers, 2005).

In the past million years, *obliquity* has varied with a period of 41 kyr between 22°02′ and 24°30′. The current value of this parameter is 23°30′ (McGuffie and Henderson-Sellers, 2005). *Obliquity* not only is responsible for the seasons, but also has a small influence in the annual mean insolation.

When *obliquity* is small the winters are milder and summers are cooler. This is a phenomena that can favour the appearance of ice ages, due to the fact that the summers are not warm enough to melt the ice sheets and can help in the expansion of continental ice (Berger et al., 1999, Raymo and Nisancioglu, 2003).

When *obliquity* gets larger values, the planet receives an increase in insolation, so the

winters are colder and summers warmer. Due to the fact that this phenomena is not equal in both hemispheres the mid-summer insolation in the Northern Hemisphere is considered to be critical to favouring ice ages (during periods of low *obliquity*) and melting the ice sheets (when high *obliquity* occurs) (Raymo et al., 2006).

The *obliquity* series for the time period 1400 - 0 kyr BP is presented in Figure 2.5.

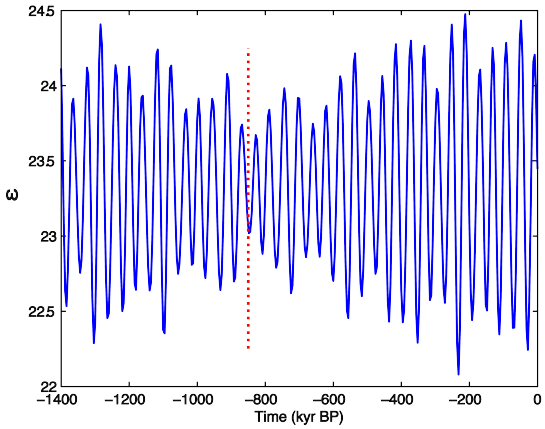

Figure 2.5: *Obliquity* for the time period [1400 , 0] kyr BP.

2.3.3 Climatic Precession (Precessional Index)

The climatic precession represents changes in the orientation of Earth's axis of rotation. This can be due to two possible causes: a wobble in the Earth's axis (Figure 2.2) and a turning around of the elliptical orbit itself (Thomas, 2002). The cause that makes more sense in terms of palaeoclimate studies and insolation changes is the first one, because it relates the location of the perihelion and aphelion to seasons in each hemisphere. As shown in Figure 2.2, the perihelion represents the point on the orbit closest to the Sun, and the aphelion is the farthest point on the orbit related to the Sun.

Precession varies between -0.05 and 0.05 and can induce changes in insolation greater than $20W/m^2$ at all the latitudes. This parameter usually varies with periods of 21 and 26 kyr (Berger and Loutre, 1994, McGuffie and Henderson-Sellers, 2005).

In palaeoclimate the usual variable used is called *climatic precession index*, which is proportional to eccentricity and can be determined by using the formula $p = e\sin\omega$, where ω is the approximation of the longitude of perihelion (Berger and Loutre, 1994).

2.3.4 Longitude of Perihelion

The *longitude of perihelion* ω is the angle between the point of Earth's perihelion (the point on Earth's orbit when the planet is the closest to the Sun) and its ascending node (Berger, 1978a) (Figure 2.2). This measurement is taken in the direction of motion. This parameter is also a measurement of the Earth-Sun distance. The timing of perihelion is usually measured as the angle of orbital displacement, and is measured in degrees and not in classical time measuring unit (days, hours).

The current value of this orbital parameter is 283.067° and it varies with periods between 19 and 23 kyr, but can go to the lower periods of 12 - 14 kyr as well.

For the time interval [1400, 0] kyr BP the *longitude of perihelion* time series are plotted in Figure 2.6.

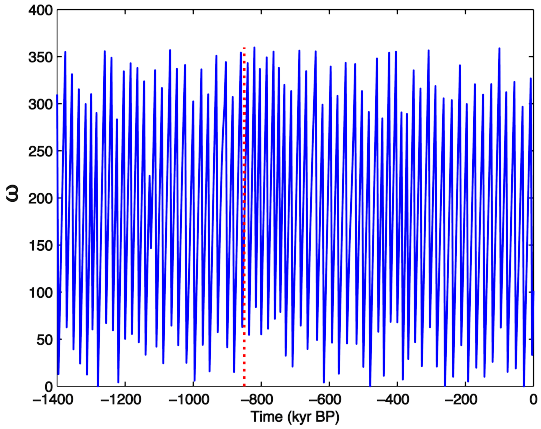

Figure 2.6: *Longitude of perihelion* for the time period [1400 , 0] kyr BP.

2.3.5 Insolation

Milankovitch (1941) was the first one to show how the insolation effects vary with regards to its distribution and angle. This is due to the fact that at higher latitudes the rays will cover larger areas but will be less concentrated, whereas at lower latitudes the angle of arrival is smaller, so the impact surface will be smaller and the rays more concentrated (Figure 2.7). There are two types of insolation: the *mean annual insolation* at the surface of the Earth and *the daily (or monthly) insolation* at any given point on the Earth.

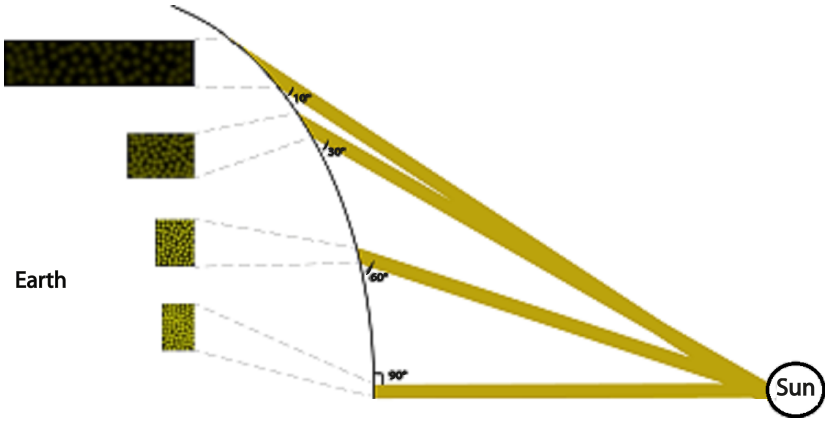

Figure 2.7: Insolation at different latitudes. Image adapted using the source at "*http://www.manogaublys.lt/home.26,p.0,e.5,l.lt*".

The mean annual insolation can be calculated by knowing the *eccentricity* value e and the solar constant S_0 using the formula:

$$W_{am} = \frac{S_0}{4\sqrt{(1-e^2)}} \tag{2.1}$$

Although the solar constant value varies with regards to the number of sunspots from $1.321 kW/m^2$ to $1.412 kW/m^2$, the approximate average value used in calculations is $1.361 kW/m^2$.

As it can be seen from formula (2.1), the mean annual insolation varies with the eccentricity square, so the maximum can be reaches with the largest eccentricity values. Given the changes induced in W_{am} are very small, they cannot solely account for the abrupt changes observed in the Pleistocene time-series.

The insolation for any time of the year can be calculated using the three orbital parameters (*eccentricity*, *obliquity* and *precession*) and is depended on the latitude for which it is calculated. According to Milankovitch's theory it is important to calculate the values for insolation at any given point on the Earth's surface, because summer insolation at high latitudes played an important role in expanding or melting of the ice sheets. If summer insolation at high latitudes was small than this could prevent the ice sheet from melting during the warm season and would favour ice accumulation.

Berger and Loutre (1997a) calculated that the insolation W received on a horizontal surface at latitude ϕ, at a given time H during the course of the year λ is given by:

$$W(\phi, \lambda, H) = s_0 \left(\frac{a}{r}\right)^2 \cos z \tag{2.2}$$

where r represents the distance to the Sun and z is the zenith distance (angle). This can be observed on Figure 2.8 as the angle between the zenith point and the position S of the Sun seen in the sky. The observer O is considered on a plane perpendicular to the zenith direction and right underneath the zenith point. The zenith distance varies from 0 to 180°.

The hour angle H can be calculated as the angle between the meridian through the points P_N and P_S and the meridian through the point S and the zenith and nadir (Figure 2.8). H varies from 0 at solar noon to 24h. Due to these definitions the following relationship can be extracted:

$$\cos z = \sin\phi \sin\delta + \cos\phi \cos\delta \cos H \tag{2.3}$$

where δ is called declination and represents the angle between the equator and the second great circle of latitude going through S. The declination δ is the angular distance of point S measured from the Equator on the secondary great circle (Figure 2.8). δ can be calculated using the obliquity ϵ and the true longitude of the Earth λ using $\sin\delta = \sin\lambda \sin\epsilon$. Over a one year period λ varies from 0 and 360° and δ between $-\epsilon$ and $+\epsilon$.

The Earth–Sun distance r used in equation equation (2.2) is given by the ellipse formula:

$$r = \frac{a(1 - e^2)}{1 + e \cos v} \tag{2.4}$$

where v represents the true anomaly and can be related to the true longitude λ and the longitude of perihelion $\overline{\omega}$ with

$$v = \lambda - \bar{\omega} \tag{2.5}$$

By substituting equations (2.3) - (2.5) into equation equation (2.2) the insolation can be written as:

$$W(\phi, \lambda, H) = S_0 \frac{(1 + e\cos(\lambda - \bar{\omega}))^2}{(1 - e^2)^2} \sin\phi\sin\lambda\sin\epsilon + \cos\phi\cos\delta\cos H \tag{2.6}$$

In the above equation (2.6) the orbital parameters values e, ϵ and $\overline{\omega}$ are assumed to be constant over one year, and the values for λ and δ are assumed constant over a given day period.

The long-term behaviour of each factor in equation (2.6) is thus governed by a different orbital parameter. The obliquity ε drives $\cos z$, the precession $p = e\sin\overline{\omega}$ drives $(1 + e\cos(\lambda - \bar{\omega}))^2$ and the eccentricity e drives $(1 - e^2)^{-2}$. It is important to observe that the eccentricity appears here as $(1 - e^2)^{-2}$ while in the mean annual insolation equation (2.1) it appears as $(1 - e^2)^{1/2}$.

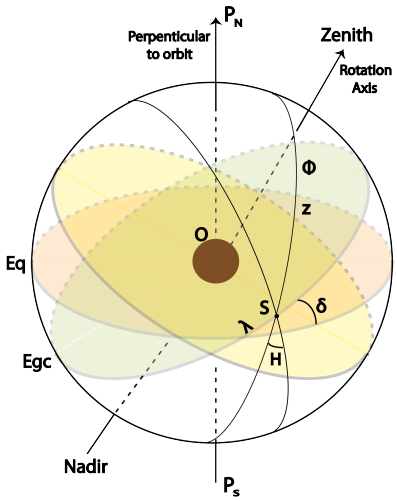

Figure 2.8: Planetary elements used in defining the insolation. Image adapted from Crucifix et al. (2007).

2.4 Paleoceanographic Proxies

One of the most important climate proxies used to study the MPT is the *oxygen isotope ratios* time-series. In order to reconstruct the ocean surface or ambient temperatures, proxy data is obtained from the shells of a number of microorganisms called ***foraminifera*** (Arnold et al., 2002). The proxy data can give indications of the climate scene of the particular area and at the time correspondent to the depth it was recovered from. Section 2.4.2 presents the proxy data recovered from the Western Pacific Site 806B.

2.4.1 Foraminifera

Figure 2.9: Marine sediment extraction point.
Image source: "http://www-odp.tamu.edu/public/life/index.html"

There are two types of forams (foraminifera): *benthic*, which is the most common one, and *planktic* (or planktonic) that incorporates about 40-50 morphospecies (Arnold et al., 2002). These two categories differ with regards to their living conditions and also their shell structures. Past water temperatures influence the chemistry composition of the shells of the forams. As their shells get buried on the bottom of the ocean the information is preserved for thousands of years. Once retrieved from the extraction point (Figure 2.9), due to their different living conditions and environments, the shells of forams can be used to reconstruct a broad time and area map of water temperature values variations.

Benthic foraminifera live on the ocean floor and abyssal plains or in the ocean sediments (Arnold et al., 2002). They are usually used to get information about the ocean depth and

the biostratigraphy of the ocean.

Planktic foraminifera live floating in the middle and upper zone of the ocean and have a calcium-carbonate shell (Arnold et al., 2002). Once dead, they settle on the bottom of the ocean and in time are buried in sediments. When recovered, they give indication of the ocean currents and upper ocean water temperatures and climates changes.

Foraminifera incorporate in their shells water temperature and stratification information through the oxygen isotope ratio values (Arnold et al., 2002). When the micro-organisms die and lay on the bottom of the ocean (and similarly in ice cores) they preserve the environmental records that can help reconstruct the climate changes of a particular past era (Arnold et al., 2002). This is possible by using the stable oxygen isotope composition to measure the ratio between the lighter ^{16}O and the heavier ^{18}O, which is a function of the environment (water temperature, salinity) where the foraminifera lived (Shackleton and Opdyke, 1973).

The formula (Shackleton and Opdyke, 1973) for the oxygen isotope ratio is:

$$\delta^{18}O(‰) = \left[\frac{(^{18}O/^{16}O)_{sample}}{(^{18}O/^{16}O)_{standard}} - 1\right] * 1000$$

Low values of $\delta^{18}O$ stand for a decrease in heavier ^{18}O, whereas high values occur when waters are rich in ^{18}O (Shackleton and Opdyke, 1973), as can be seen in Figure 2.10.

The present day spatial isotope/surface temperature relationship is described (Dansgaard, 1964) by:

$$\delta^{18}O = aT_s + b$$

where the isotope/temperature slope $a = \frac{d\delta}{dT_s}$ depends on the region the isotope is extracted from.

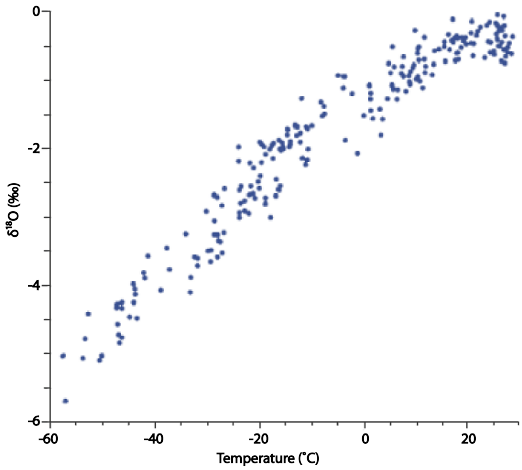

Figure 2.10: $\delta^{18}O$ dependence on temperature. Source: NASA Earth Observatory website http://earthobservatory.nasa.gov/Features/Paleoclimatology_OxygenBalance/, graph adapted from Jouzel et al. (1993).

The water molecules that contain the ^{16}O evaporate faster than the ones rich in ^{18}O. Cold ocean waters enable the ^{16}O to evaporate quicker and the waters become less depleted in ^{18}O and thus have low values. Higher values would be an indication of warmer ocean waters which are more depleted in ^{18}O.

Once the $\delta^{18}O$ time-series is reconstructed, it needs to have attached an age representing the period of time covered by the data. This is called dating of data, and can be relative or absolute (Shackleton et al., 1977). The absolute type gives a chronological age and is not usually extremely accurate especially for proxies going far back in time. The relative dating relates the given set to other fossils found in similar (and usually adjacent) sites. Dating accuracy depends on the time period that it covers and on the data type and it decays the further back in time the record goes (Jansen et al., 2007).

Many authors (Emiliani, 1955, Emiliani, 1966, Hays et al., 1976, Chappell and Shackleton, 1986), have studied and linked the changes in the oxygen isotope ratios in oceans and ice cores (and up to a certain level in terrestrial series) to the Milankovitch orbital forcing.

It is known that it is difficult for any Site to have constant sedimentation rates that are not influenced by the global and local climate and of course observational noise and dating accuracy (Shackleton et al., 1977). This is why most scientists turn to tuning of data, which can be of two types: *orbital tuning* or *depth tuning*.

Depth tuning refers to adjusting the time scale by using mean sedimentation rates (Shaw, 1964). This was mostly used in the past (Shackleton and Opdyke, 1973, Hays et al., 1976, Williams et al., 1988, Martinson et al., 1987, Raymo, 1997) and now most authors prefer using orbital tuning as a more accurate method.

Orbital tuning refers to the process of adjusting a proxy time scale to match Earth's orbital cycles in the Milankovitch theory. This method involves dating of paleoclimate records through correlation with insolation or the orbital parameters (Lisiecki, 2010, Cronin, 2013). Hays et al. (1976) were the first to confirm the presence of orbital periodicities in the $\delta^{18}O$ data. Although using orbital tuning increases dramatically the accuracy of the dating methods, care must be taken when performing this, because over tuning will introduce frequencies not native to the dataset (Muller and MacDonald, 1997, Rial, 1999). Because of this it is common practice to tune at frequencies other than those needed for analysis or to use data-sets which do not require orbital tuning (Muller and MacDonald, 1997).

2.4.2 Dataset from Hole 806B

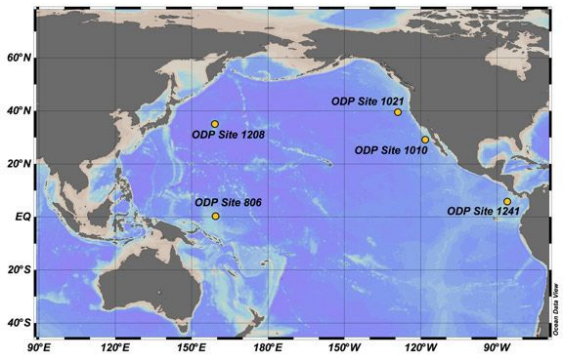

Figure 2.11: Ocean Drilling Programme Sites in the Pacific Ocean. Image source: Jonathan LaRiviere/Ocean Data View.

The dataset used in this thesis is from the Ocean Drilling Site 806B from the Western Pacific

$(0°19´N, 159°21´E)$, near the equator (Figure 2.11) . Site 806B shows remarkably constant sedimentation rate (Berger et al., 1991c), which allows the analysis without the need for orbital tuning, which can introduce the complications mentioned before. The time-series of

oxygen isotopes are from the fossil planktic foraminifera Globigerinoides Sacculifer (Berger et al., 1993) and is shown in Figure 2.12). The data, which is published on ODP sites and has been documented in Berger et al. (1993) is plotted in Figure 2.13. The vertical red dotted line at around $\sim$ 850 kyr BP emphasizes the time when the MPT occurred.

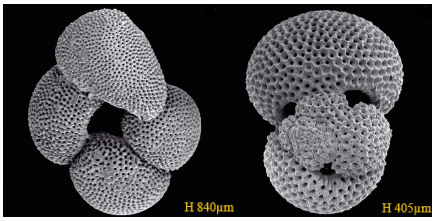

Figure 2.1: Planktic foraminifera Globigerinoides Sacculifer morphology. Images sources: Hesemann, M., 2013: Globigerinoides sacculifer (Brady, 1877), in: Foraminifera.eu Project Database. Accessed at
http://www.foraminifera.eu/single.php?no=1004618&aktion=suche and
http://www.foraminifera.eu/single.php?no=1004295&aktion=suche.

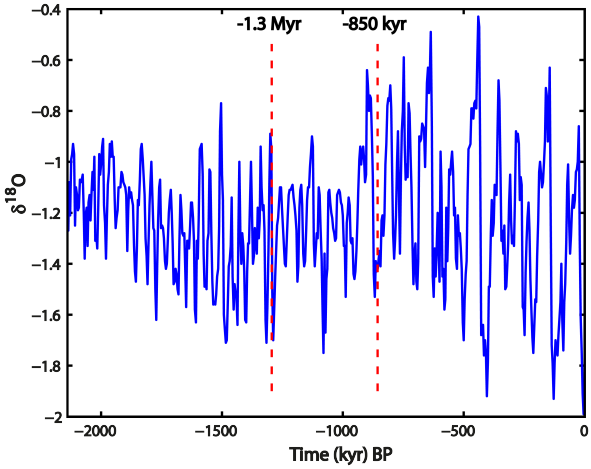

Figure 2.2: Oxygen isotope ratio data from Site 806B.

2.4.3 Spectral Peaks Discovered in the Oxygen Isotope Ratio Proxy Data from Hole 806B

Many authors (Berger et al. 2005, Rial and Anaclerio, 2000, Schmidt and Hertzberg, 2011, Mayer, 1993, Paillard, 2001) have performed spectral analysis on oxygen isotope time-series from deep-sea sediment extraction cores. Of course the results of these depend very much

on the method applied for obtaining the spectrum or spectral power, the window length used, the length of the available data (e.g. if the dataset is too short, a period of 413 kyr might not be emphasised in the results) and of course the location of the core. There are two types of periods considered: some authors (Berger et al. 2005, Schmidt and Hertzberg, 2011, Mayer, 1993) work using approximate periods ($\sim$ 100 kyr, $\sim$ 40 kyr), whereas others (Rial and Anaclerio, 2000, Paillard, 2001) use the actual frequencies found when performing spectrum analysis. The most important frequency components in the frequency spectrum of the $\delta^{18}O$ data set from Site 806B, which were analyzed by different authors, are summarized in Table 2.1.

Author	$\delta^{18}O$ **period**
Berger et al. (2005)	$\sim$ 100 kyr
Rial and Anaclerio (2000)	413 , 143, 123, 107, 95, 75 kyr
Schmidt and Hertzberg (2011)	$\sim$ 100, 31, 23 kyr
Mayer (1993)	$\sim$ 100, $\sim$ 40 kyr
Paillard (2001)	97.5, 41, 23,7, 19, 11.7 kyr

Table 2.1: The main frequency components in the spectrum of the $\delta^{18}O$ data from Site 806B.

The main frequencies in the frequency spectrum of the orbital parameters, which were studied by different authors in relation to the $\delta^{18}O$ data set from Site 806B are summarized in Table 2.2.

Author	**Eccentricity**	**Obliquity**	**Precession**
Rial (2004)	95 kyr	-	-
Loutre et al. (1992)	404.178,94.782, 123.818,98.715, 130.615,2379.077kyr	-	23.716, 22.428, 18.976, 19.155 kyr
Berger et al. (1991)	117.7 kyr	43.6 kyr	24.9, 19.3 kyr
Paillard (2001)	2Myr, 412, 131, 123, 99, 95 kyr	53.7, 41, 39.6 kyr	23.7, 22.4, 19 kyr
Maslin and Ridgwell (2005)	$\sim$ 100 kyr	$\sim$ 41 kyr	$\sim$ 21, $\sim$ 19 kyr
Muller and MacDonald (1997)	$\sim$ 125, $\sim$ 100 kyr	$\sim$ 41 kyr	$\sim$ 21, $\sim$ 19 kyr

Table 2.2: The main frequency components in the spectra of Earth's orbital parameters.

2.5 Previously Developed Models

This section summarizes the previous palaeoclimate models that have been developed to explain the impact of the orbital forcing in relation to the observed changes in sea surface temperature, ice volume and/or their proxies. Because each of them may be using different input parameters or may analyze different time periods, a classification of the models will be given. The climate models represent a simplification of the real life system and are used to capture and understand the dynamics and processes that sustain the climate system and produce climatic events. Understanding the underlying causes of change lies with analyzing both the climatic sensibility to external forcing and also the internal dynamics of the planet, such as coupled interactions of the Earth's subsystems (atmosphere, oceans, ice sheets and biosphere), as the climate shifts between glacial and interglacial states.

Most of the efforts in modelling the climate evolution of the geological record for the Pleistocene period have followed Milankovitch's theory about orbital forcing and its effect over the succession of glacial and interglacial periods. Because the 100 kyr frequency could not be definitely linked to the *eccentricity*, the inputs commonly used in the models are *obliquity* and *precession*. The response is seen as the global ice volume, this being influenced by the growth or decrease in ice-sheets. The climate system is represented by a nonlinear process.

Scientists have tried to develop several models in order to reconstruct parts of or even the whole climate system. These models have different complexities, varying from zero to three dimensional ones (Park and Maasch. 1993).

Climate models are usually classified (Berger et al., 1990, McGuffie and Henderson-Sellers, 2005, Petoukhov et al., 2005, Trenberth, 2006) in three categories: ***energy balance models*** (EBM), ***intermediate complexity models*** (EMIC) and ***global climate models*** (GCM, also known as global coupled circulation models).

The ***energy balance models*** are the simplest kind, usually zero- or one- dimensional models, but at the same time they are a very valuable tool that provide information on the surface temperature as a function of the energy balance of the Earth, changes in ice-sheet growth and decay or increase in greenhouse gases. They are based on the balance of

incoming and outgoing radiant energy and try to explain what happens when the balance is disturbed. The usual parameters for the zero-dimensional models are: the solar constant, the planetary albedo, the globally averaged surface temperature and a climate sensitivity factor λ. The one-dimensional model focuses on the processes on the vertical and also involves an atmospheric heat transfer parameter, vegetation and reflection of solar radiation. Next some main contributions to the energy balance models are given.

One attempt to explain the Pleistocene glacial cycles with a Northern Hemisphere ice sheets model was done by ***Oerlemans*** (1982). The model manages to successfully generate the 100 kyr cycles, but the reproducing of the ice-volume record is small.

Ghil and Tavantzis (1983) have developed a model of two coupled autonomous ordinary differential equations:

$$c_T \frac{dT}{dt} = R_i(T, L) = R_0(t) = R(T, L) \tag{2.7}$$

$$c_L \frac{dL}{dt} = F(T, L) \tag{2.8}$$

where T is the globally and annually averaged temperature, L is the latitudinal extent of the continental ice cover, with T and L positive, R_i denotes the short-wave radiation absorbed, R_0 is the long-wave radiation emitted by the system, F is a nonlinear function describing the continental ice-sheet dynamics, c_T represents the heat capacity of the atmosphere-hydrosphere system and c_L governs the dynamic relaxation time of the continental ice sheets.

The absorbed incoming short-wave radiations is dependent on the insolation Q and on the albedo α as follows:

$$R_i(T, L) = Q\{1 - (\gamma\alpha_{land}(L) + (1 - \gamma)\alpha_{ocean}(T))\}$$

where γ is the fraction of the Earth covered by continents.

The authors conclude that this fairly simple model has a periodic solution, and that the periods are those of the orbital parameters *obliquity* and *precession*. This shows that the system responds to orbital forcing and also to combination tones between them. The

frequency domain results match some of the peaks in the spectra of proxy records.

Variations of this one-dimension energy balance model have been developed in the works of Ghil (1976), Bhattacharya and Ghil (1978) and Ghil and Bhattacharya (1979).

Saltzman and Sutera's model (1987) is build around the theory that since orbital forcing had the same character for the entire Quaternary, the cause of change could be some modifications of internal dynamics that control the way the system responses to the forcing.

The model equations are:

$$\frac{dI^{'}}{dt} = -a_0 I^{'} - a_1 \mu^{'} \tag{2.9}$$

$$\frac{d\mu^{'}}{dt} = b_1 \mu^{'} + b_5 \theta^{'} - b_6 \theta'^2 \mu^{'} \tag{2.10}$$

$$\frac{d\theta^{'}}{dt} = c_0 I^{'} - c_2 \theta^{'} \tag{2.11}$$

where I represents the snow-derived ice mass, $-\mu$ represents the atmospheric carbon dioxide and θ is the bulk deep ocean temperature.

The facts that the model does not allow rapid deglaciations and it is sensitive to initial conditions count as the disadvantages of this model. Given that proportional changes in the ice mass should match those in the $\delta^{18}O$ records, when comparing with the data from the Caribbean Core 502B, the model predictions for ice mass follow the main trend, but the response is slower than the measurements and with lower amplitude ***before MPT*** and higher ***after***. Additional parameters representing the orbital forcing, parameters which account for the rapid deglaciations and the solar constant can be added to the model to make it more accurate.

Saltzman's later models (Saltzman and Maasch, 1990, Saltzman and Maasch, 1991) were able to reproduce, with some success, both the 100 kyr cycle and the transition from dominant 41 kyr ice volume fluctuations prior to $\sim$ 900 kyr BP to the dominant 100 kyr ice volume fluctuations after $\sim$ 900 kyr BP. The latter transition may also reflect the existence of "multiple equilibrium" states, whereby slowly changing boundary conditions can cause an abrupt transition in the climate state. Saltzman's explanation from a physical viewpoint is

that the decrease in carbon dioxide brings the climate system to a cooler state where positive feedbacks involving ice formation (Maasch, 1988) are activated, leading to the instability that can drive a long-term ($\sim$ 100 kyr period) oscillation.

The climate model developed by ***DeBlonde and Peltier*** (1991) tries to account for the "sea-level" temperature $T(\overrightarrow{r}, t)$ and its equation is:

$$C(\overrightarrow{r})\frac{\partial T(\overrightarrow{r}, t)}{\partial t} - \overrightarrow{\nabla}_h \cdot (D(x)\overrightarrow{\nabla}_h T(\overrightarrow{r}, t)) + A + BT(\overrightarrow{r}, t) = \frac{Q}{4}a(\overrightarrow{r})S(x, t) \tag{2.12}$$

where $\overrightarrow{r} = (\theta, \phi)$ is a position vector on the Earth's surface, with ϑ being the latitude (and $x = \sin\theta$) and ϕ being the longitude, the term $A + BT(\overrightarrow{r}, t)$ represents the infrared intensity emitted to space, the term $\frac{Q}{4}a(\overrightarrow{r})S(x, t)$ is the short-wave energy intensity absorbed by the earth-atmosphere system, Q is the solar constant, $D(x)\overrightarrow{\nabla}_h T(\overrightarrow{r}, t)$ represents the heat flux, with $D(x)$ a smooth diffusion coefficient, $C(\overrightarrow{r})$ is the effective heat capacity.

The above climate equation (14) is considered to be in equilibrium at all times with the ice sheets model described by:

$$\begin{aligned} \tfrac{\partial H}{\partial t} &= \nabla_h(D_i \nabla_h h) + G \\ \tfrac{\partial h'}{\partial t} &= \tfrac{(h' - h_0')}{\tau} + \left(\tfrac{\rho_i}{\rho_e \tau}\right) H \end{aligned} \tag{2.13}$$

where D_i represents a highly nonlinear diffusion coefficient, G is the net mass-balance function, $h_0^{'}$ represents the present topography, ρ_e is the density of the bedrock, and $h^{'} = H - h$.

The purpose of this coupled paleoclimate model is to simulate and study the position of the ice sheets at the last glacial maximum. The results show the temperature variations and the dominant influential orbital parameter, which appears as *obliquity*. Another interesting conclusion is that the European ice sheet, due to the higher continentality of Eurasia, is much more sensitive to solar forcing than the North American ice sheet. Compared to the real climate system the model has low sensitivity to the orbital forcing.

Tarasov and Peltier (1997) developed a coupled model of an energy-balance one and one of the ice-sheet. This accounts for changes in the surface temperature dependent on the

ablation, precipitation and rain/snow. This model also considers the atmospheric CO_2 concentration as a function of time. The results bring significant improvement to understanding the relationship between climate forcing and mass-balance response.

The model proposed by ***Rial and Anaclerio*** (2000) is based on the hypothesis that the frequencies present in the spectra of $\delta^{18}O$ time series arise through nonlinear interactions (frequency modulation in this case) of the orbital forcing frequencies.

$$\Phi_{FM}(t) = a\sin[\frac{2\pi t}{95}+\beta\sin(\frac{2\pi t}{413})+\beta'\sin(\frac{\pi t}{413})]+b\sin[\frac{2\pi t}{100}+\beta\sin(\frac{2\pi t}{413})]+c\sin[\frac{2\pi t}{125}+\beta\sin(\frac{2\pi t}{413})] \tag{2.14}$$

where Φ_{FM} represents the simulated frequency-modulated *eccentricity* signal, t is the time in kilo-years, a, b, c are constants and are adjustable, β' is the modulating index for the subharmonic. It was determined that $\beta \sim 1$ and $\beta' \sim 2$.

In equation (16) the carrier frequencies are assumed to have periods of 95, 100, and 125 kyr whilst the modulating signals are the subharmonics with periods of 413 and 826 kyr. Equation (16) is used by the authors to construct synthetic time series in order to simulate the $\delta^{18}O$ time series from the ODP Site 806.

A similar model, representing the simulated frequency-modulated *eccentricity* and *tilt* signal, is proposed in order to explain the power spectra of the deuterium (proxy of temperature), sodium (marine aerosol) and greenhouse gases (CO_2 and CH_4) time series obtained from the Vostok ice core (Petit et al., 1999):

$$I_{FM}(t) = \sin[\frac{2\pi t}{41} + a\sin(\frac{2\pi t}{413}) + b\sin(\frac{4\pi t}{413}) + c\sin(\frac{8\pi t}{413}) \tag{2.15}$$

The parameters a, b, c represent the intensity of modulation and by adjusting them the amplitude of the four mentioned time-series can be modeled. It is shown that the power spectra of the synthetic time series generated using equation (17), using the corresponding set of optimized parameters a, b, c, closely resemble the spectra of each experimental time series. In particular, the synthetic signal reproduces the structure of the carrier frequency at 41 kyr modulated by the 413 kyr frequency and its main harmonics, which suggest that the climate system responds nonlinearly to *obliquity* (with a spectral peak at 41 kyr) as well as

eccentricity (with a spectral peak at 413 kyr). The model catches well the periodicity of the data and its main dynamics, but cannot emphasize well the subtle changes that occur.

Rial's simple model shows the concept of frequency modulation of the 100 kyr *eccentricity* cycle by the 413 kyr one. Spectra of the model are consistent with the classic Milankovitch theory of insolation (making redundant the theories about orbital inclination and dust accretion). Rial reasons that the switch in the *eccentricity* period between 80 and 120 kyr every 413 kyr is an argument sustaining frequency-modulation. Also the spectrum does not contain the modulating signal as a peak, but as a separation interval between the sidebands. From the model, the 95 and 123 kyr are the predicted sidebands of the $\sim$ 100 kyr *eccentricity* component frequency modulated by the 413 kyr one. In the same manner, the 85 , 107, and 143 kyr peaks coincide with the predicted sidebands of a 95 kyr carrier frequency modulated by the 826 kyr sub-harmonic of the 413 kyr signal. Using the frequency modulation explanation, the absence of the 413 kyr peak from the $\delta^{18}O$ data is no longer a problem.

Another model developed by ***Rial*** (2004b) is the logistic-delayed differential equation (LODE) model

$$\frac{dL(t)}{dt} = \mu L(t-\tau)[1 - \frac{L(t-\tau)}{K(t)}] \tag{2.16}$$

$$C\frac{dT(t)}{dt} = Q[1-\alpha(L)] - [A + BT(t)] \tag{2.17}$$

where $L(t)$ represents the ice volume, μ is the ice sheet's time equilibration constant, $K(t)$ is the temperature-dependent carrying capacity of the system, defined by

$$K(t) = 1 + \varepsilon(t)T(t) \tag{2.18}$$

$T(t)$ is the global temperature and $\varepsilon(t)$ is the forcing function which amplitude-modulates $T(t)$, and is given by $\varepsilon(t) = \varepsilon_0\{1+\sum_{i=1}^{N} a_i\cos(w_i t+\phi_i)\}+\Phi(t)$. The sum involves the frequency components of any known or assumed astronomical forcing, ε_0 is a small quantity ($\varepsilon_0 < 0.1$), and the term $\Phi(t)$ accounts for any other internal or external forcing signals that might not have been considered.

An important feature of LODE is that it transforms amplitude modulation of the global

temperature $T(t)$ into frequency modulation of the ice volume $L(t)$, through the amplitude-modulating input $\varepsilon(t)$. Rial uses frequency modulation to explain the way the new peaks in the data appear. Although this model replicates the saw-tooth characteristic of the data, it has the disadvantage that it can only offer results for certain periods of time of the Pleistocene. Nonetheless LODE captures some essential physics and dynamics of the climate system, but is not able to fully explain the fast warming and slow cooling sequences.

The ***intermediate complexity models***, although involve some simplifications of the Earth's geography, are usually two- or three- dimensional models and can provide more than average information over the whole system or subsystems. Being more complex, the parameters of EMICs have more degrees of freedom. Some examples of EMICs are: CLIMBER-2 (Ganopolski et al., 2010), trying to model the last glacial maximum, ECBILT (Opsteegh et al., 1998), which takes into account the Holocene orbital variability in insolation, McGill Paleoclimate Model (developed at the McGill University by Stocker et al. (1992)), which tries to explain the nonlinearities of cold climates and the mechanisms of glaciations, and MoBidic (Crucifix et al., 2002), which takes into account the Milankovitch forcing, fresh water inputs to ocean, the Holocene volcanic and solar variability. Next some main contributions to the EMICs category are given.

A first noticeable model was the one developed by ***James Croll*** (1875), which still helps as a starting point for many current works. A very interesting hypothesis raised by Croll is the one that the initial point of glacial epochs is the Northern Hemisphere, due to insolation and *obliquity*. All three orbital parameters (*eccentricity*, *obliquity* and *precession*) are taken into account as inputs to the system.

Milankovitch's theory (1941) accounts for the Ice Ages by means of the astronomical forcing variables simultaneously affecting the Earth's insolation (Berger, 1988). Milankovitch's equations for the summer and winter insolation for caloric half-years (two equally long real half-years, one of each containing all those days of the year during which the irradiation at a specific latitude is stronger than on any day of the other half-year), ΔQ_s and ΔQ_w, respectively, which for a certain year are:

$$\Delta Q_s = \Delta W_s \Delta\varepsilon - m\Delta(e\sin\Pi_\gamma) \tag{2.19}$$

$$\Delta Q_w = \Delta W_w \Delta\varepsilon + m\Delta(e\sin\Pi_\gamma) \tag{2.20}$$

where $\Delta\varepsilon$ represents the change in orbital *obliquity* from the present value, e is the *eccentricity*, Π_γ represents the *perihelion* related to the vernal equinoctial point, ΔW_s and ΔW_w are the changes in irradiation at a certain latitude for summer and winter.

The given equations are for latitudes in the Northern Hemisphere. The equations for Southern Hemisphere are similar, but with opposite signs.

Milankovitch's comprehensive calculations and application of physical laws (227 equations) were able to mathematically prove the connection between the irradiation and temperature. Milankovitch's theory provides a prediction of the observed periodicity of the temperature variations, and does not focus on the actual temperature magnitude.

Le Treut (1988) modelled internally generated glacial-interglacial fluctuations which, when orbitally forced, produce characteristic Milankovitch periods, including their harmonics (e.g., 10 kyr) and subharmonics (e.g., 100 kyr).

Imbrie's model (1992) derives the conclusion that the ice-volume fluctuations are primarily driven by orbital forcing, and that the ice volume responds linearly to orbital forcing for the periods of 23 kyr and 41 kyr and nonlinearly to the 100 kyr period. The author agrees that the 100 kyr power can be generated by transmission of 19 kyr and 23 kyr periods through nonlinear mechanisms (Wigley, 1976) producing substantial power in both harmonics and subharmonics.

The Louvain-la-Neuve climate model, known as the LLN 2D, was developed by ***Berger and Gallee*** (1990), and it only considers the Northern Hemisphere (NH). This model takes into consideration the coupling between the atmosphere and the surface, and is an altitude-latitude one. Carbon dioxide cycles are not considered though and need to be accounted for externally. The model simulates well the general circulation and seasonal cycles of oceanic mixed layer, sea ice and snow cover. Most studies performed using these models try to simulate and explain the last glacial or interglacial period.

Another model proposed by ***Gallee et al.*** (1992) is the MoBidic model, and is an extension of the LLN 2D NH one. It represents a coupling between a quasi-geostrophic atmospheric one and three-basin ocean-sea ice subsystems. This model is designed for catching

the long term variations in climate and can simulate accurately the temperature, precipitation and ocean circulation. The parts where the model has slight failures are the atmospheric dynamics and the ocean salinity distributions.

Berger and Gallee (1992) used the LLN 2D model in order to reproduce the saw-toothed shape of the ice volume curve and confirm the hypothesis that the variations in the Earth's insolation are sufficient to induce feedbacks in the climate system which amplify the direct radiative impact and generate large climatic changes. On the same note, the second conclusion derived was that the CO_2 variations are not absolutely required to be taken into account to generate a rough 100 kyr cycle, which confirms the Hays et al. (1976)'s idea that the orbital forcing acts as a pacemaker of the ice ages.

Berger (1999) constructs his analysis using the LLN 2D model as well, but the model is forced by the astronomically-derived insolation and by different CO_2 concentration scenarios. The analysis reached the conclusion that before 1 Myr BP, under the influence of relatively high atmospheric CO_2 concentration, the insolation maxima could prevent the Northern Hemisphere ice-sheets from growing. After $\sim$ 1 Myr BP, because of lower CO_2 concentrations, larger ice sheets appeared and only at times of maximum insolation (occurring under high *eccentricity*, high *obliquity* and Northern Hemisphere summer at perihelion -minimum *climatic precession* - values) significant meltings of the ice sheets took place. This is how the interglacial period appeared making the $\sim$ 100 kyr periodicity the most remarkable feature of climate over the time interval from 1 Myr BP to present.

The CLIMBER-2 ice-sheet model was introduced by ***Ganopolski et al.*** (2010) and divides the Earth surface into horizontal grids containing fractions of both sea and land. The model also has vertical grids that account gradually for the atmospheric components: temperature, humidity, wind, transport of energy and water. CLIMBER-2 is developed for processes of large time scales, up to millennia, but has low spatial resolution and can only be used for continents. Validation of the model is done by comparing its features with empirical data. Tests were also done to verify CLIMBER's sensitivity to CO_2 concentrations, solar insolation and vegetation cover.

The ***global climate models*** are the most 'complete' models and are in fact a collection of models of the atmosphere, land, sea ice and ocean that look into the climate system as

a whole and that are connected by a separate coupler module. These types of models are three-dimensional ones and use discrete equations. Although some interactions are straight forward, others like the very important coupling between atmosphere and ocean models are not easy to achieve because of different parameter ranges in both space and time. So it is crucial to interface correctly all the subsystems.

Pollard (1983) modelled the nonlinear interactions between ice-sheet accumulation and ablation, ice-sheet flow, elastic lithosphere and viscoelastic mantle. The results show that the observed 100 kyr cycle is driven by external orbital forcing together with the internal forcing.

Out of all the theories proposed so far, the Milankovitch's orbital forcing theory seems to be the only one that is strongly supported by physical evidence.

Table 2.4 summarizes the conclusions of these studies with the focus on the explanations given for the appearance of the 100 kyr cycles and on relating it to the orbital forcing.

Study	**Achievements on answering the question regarding the origin of the 100 kyr cycle**
Pollard (1983)	100 kyr cycles driven by orbital forcing together with internal forcing
Le Treut et al. (1988)	the model produced Milankovitch periods, harmonics and subharmonics of them
Saltzman and Maasch (1990)	replicated the 100 kyr cycles, and the MPT transition from dominant 41 kyr to 100 kyr
Berger et al. (1998)	reproduced the saw tooth shape of ice volume curve
	the CO2 variations are not required to generate a rough 100 kyr cycle
	confirms the idea (Hays et al., 1976) that orbital forcing acts as a pacemaker of the ice ages
Imbrie et al. (1992)	concluded that ice-volume fluctuations are primarily driven by orbital forcing
	ice-volume responds linearly to forcing of the periods 23 and 41 kyr and nonlinearly to 100 kyr
	the 100 kyr power can be generated by transmission of 19 and 23 kyr periods through nonlinear mechanisms
Rial (1999), Rial and Anaclerio (2000)	shows through a simple model the frequency modulation of the 100 kyr cycle by the 413 kyr
	model spectra are consistent with classical Milankovitch theory ones
Rial (2004)	the model fits the saw tooth shape of ice volume data
	reproduces the switch from 41 to 100 kyr cycles
	explains the appearance of new peaks in the spectra using frequency modulation

Table 2.4: Summary of the results of the presented studies with the focus on the 100 kyr cycle.

2.6 Discussion

In order to analyse Earth's palaeoclimate, due to lack of long term (million years) insolation measurements, scientists (Maslin and Ridgwell, 2005) have looked at proxy data for ice volume or sea surface temperature (SST) (Lisiecki, 2010). A widely used proxy data for the SST is the high-resolution time series of planktonic foraminifera oxygen isotope ratios data from deep ocean cores. It has been proven firstly by Hays et al. (1976) that the frequencies

in the oxygen isotope ratios data match those in Milankovitch's astronomical theory (Rial and Anaclerio, 2000).This indicates that Earth's orbital parameters, *eccentricity*, *obliquity* and *precession* (*longitude of perihelion*), control the variations in insolation (Lisiecki, 2010, Imbrie et al., 1993). The peaks found in the Pleistocene $\delta^{18}O$ spectrum correspond to periods of *eccentricity* (95 - 122 kyr, 428 kyr), *obliquity* (41 kyr), *longitude of perihelion* (23 kyr, 19 kyr) but also there are frequencies not corresponding to periods of the orbital parameters (e.g. 71 kyr).

The Mid – Pleistocene Transition is a term used to describe a very unique and intensely studied climatic event that took place approximately 900 - 800 ka (kilo-years ago), when a switch from a time (Early Pleistocene) driven by the 41 kyr *obliquity* period characterized by low amplitude and high frequency to a time (later Pleistocene) dominated by a lower frequency corresponding to a period of 100 kyr (Maslin and Ridgwell, 2005, Berger and Loutre, 2010, Head et al., 2008) occurred. This brought also an amplitude increase in the SST proxy data. The spectrum shows a dramatic intensification in the power at the frequency corresponding to the $\sim$ 100 kyr cycle, but no noticeable change in the 41 kyr peak.

The MPT change happened without a corresponding change in the orbital parameters, which raised different theories that could explain this: a climate system internal change (Clark et al., 2006), nonlinear amplification and modulation of the orbital parameters or some nonlinear internal feedbacks in the climate system that could induce the change (Head et al., 2008). The nonlinear response of the climate system due to internal feedback can be supported by the non-orbital frequencies found in the insolation proxies (Rial and Anaclerio, 2000).

The numerous hypothesis that have been proposed to explain the MPT can be split into four categories: (i) ***external forcing*** – orbital inclination (Farley and Patterson, 1995, Muller and MacDonald, 2005), (ii) ***internal feedbacks*** – Northern Hemisphere ice sheets (Berger et al., 1999, DeBlonde and Peltier, 1991), CO_2 concentrations (Ganopolski and Calov, 2011, Berger and Loutre, 1997b, Saltzman and Sutera, 1987, Loutre and Berger, 2000, Li et al., 1998), dust feedback (Ganopolski and Calov, 2011), ice albedo, ocean circulation, uplift of mountains and an internal instability generated by all the previously mentioned feedbacks (Satzman and Verbitsky, 1992), (iii) ***frequency modulation*** of orbital parameters

carrier signals 23, 41 and 95 kyr (Berger et al., 2005, Clemens and Tiedemann, 1997, Rial and Anaclerio, 2000), (iv) a ***coupled response*** between the orbital forcing and an internal nonlinear amplification (Berger et al., 1990, Imbrie and Imbrie, 1980).

Several studies have linked the shift observed at the MPT to changes in insolation induced by the variability of Earth's orbital parameters (Hays et al., 1976, Imbrie et al., 1992, Raymo et al., 2006) but the underlying mechanisms behind this are still not fully understood. It is widely accepted that the climate system responds nonlinearly to orbital forcing. One explanation is that the climate sensitivity shifted from *obliquity* to *precession*/*eccentricity* (Liu et al., 2008), and that through frequency modulation the system can transfer energy from one frequency band into another (Li and Billings, 2005). Another theory says that *eccentricity* alone has very little influence on insolation, therefore a nonlinear amplification is needed to generate the observed periodicity in the Pleistocene time series (Clark et al., 2006).

The "100 kyr Problem" refers to the lack of a satisfactory explanation for the dramatic appearance of the 100 kyr cycle ***after MPT*** because it comes without a corresponding change in the orbital forcing. The 100 kyr cycle has been mainly linked to the *eccentricity* signal, but it cannot be a linear response because *eccentricity* has little influence on insolation, as shown in sub-section 2.3.5 of this chapter. A theory that will be explored in a following chapter is that *eccentricity* modulates the amplitude of *precession* and that the peak near 100 kyr could be generated by transmission of power from the *longitude of perihelion* (*precession*) frequency bands (Berger et al., 2005, Clemens and Tiedemann, 1997).

Chapter 3

Nonlinear System Identification using NARMAX Models

3.1 Introduction

Mathematical models are required in order to analyse, predict and control the behaviour of real-world dynamical systems. There are two main approaches used to derive a mathematical model for a dynamical system: physical modelling and system identification techniques. The physical modelling approach involves deriving a model based on the physical principles. This approach (also known as a white box modelling) assumes that all the information required to derive such a model, i.e. mathematical equations describing the behaviour of each component of the system, is available 'a priori'. Modelling very complex systems using this approach can be extremely challenging (Ljung, 1999, Billings, 2013).

An alternative approach is to use system identification methods to derive a mathematical model representing a system's behaviour (Billings, 2013). The advantage of the system identification approach is that a model can be obtained solely based on experimental input-output data without making any assumptions about the system's properties. However, a priori information can be incorporated if available. According to the available amount of a priori knowledge relating the system's inputs and outputs, the models obtained by system identification are classified as: *grey-box models*, which assume that certain underlying mechanisms of the system that do not fully describe the system under study, are known beforehand, and

black-box models which are derived solely based on experimental data. The black-box model provides a mathematical representation for the underlying dynamics but does not necessarily provide a straightforward physical interpretation (Billings, 2013).

Identifying an input-output mathematical relationship based only on input-output measurements depends on the choice of model class (e.g. linear, nonlinear, hybrid, parametric, non-parametric, discrete, continuous, time-variant, time-invariant, deterministic or stochastic etc (Ljung, 1999, Pearson, 1995, Billings, 2013). Linear models present the advantages of simplicity and of the large amount of literature available (Soderstrom and Stoica, 1989). Very often however the systems of interest are complex and nonlinear and thus cannot be described by simple linear relationships. In this case nonlinear models have to be used as linear models can only provide local approximations. Nonlinearity can lead the systems to complex and difficult to predict behaviour, such as that exhibited by the climate system.

According to the number of inputs and outputs, the systems can be classified into: Single-Input Single-Output (SISO), Multi-Input Multi-Output (MIMO), Single-Input Multi-Output (SIMO) and Multi-Input Single-Output (MISO) systems.

There are several methods to estimate dynamical models only from experimental measurements. The most comprehensive and powerful nonlinear system identification methodology available to date is based on a general discrete-time representation of a nonlinear dynamical system, known as the NARMAX model (Billings and Leontaritis, 1980, Leontaritis and Billings, 1985, Chen and Billings, 1989b, Billings, 2013).

The NARMAX methodology has been successfully applied to fields such as engineering, physics, finance, medicine, biology but it is quite a novel approach to modelling environmental time-series. A small selection of the real systems that have been modeled using NARMAX include: fly photoreceptor dynamics (Friederich, 2011), financial volatility (Zhao, 2010), eddy current braking process (Simeu and Georges, 1996), dynamic loudspeaker (Dobrucki and Pruchnicki, 1999), experimental human ankle dynamics (Kukreja et al., 2003), aircraft gas turbine (Chiras et al., 2001), plasma turbulence dynamics (Boynton et al., 2013). In this work, the NARMAX methodology will be used for the first time to model and analyse paleoclimatic data.

Current available climate models are usually simplified versions of the climate system

or sub-systems (used for general analysis purposes) or combinations of models that can reproduce global or local climate systems (atmosphere, hydrosphere, geosphere, cryosphere and biosphere). Modelling environmental time-series using the NARMAX methodology provides a powerful approach to characterize quantitatively the relationship between the orbital forcing parameters and the proxy variables representing various aspects of climate response. Although it can be more difficult to give physical meaning to the developed models, the analysis of the models in the time and frequency domain can provide great insight into the mechanisms behind abrupt climate changes and the system's dynamics.

This chapter provides a detailed overview of the NARMAX methodology which addresses the whole spectrum of system identification tasks including input design, model structure detection, parameter estimation and model validation. The chapter is organized as follows. Section 3.2 presents the general NARMAX model formulation and the polynomial NARMAX expansion. Section 3.3 presents the Orthogonal Least Squares and its extension the Orthogonal Forward Regression algorithms. Section 3.4 details on the common NARMAX model validation methods, namely prediction error results, coherence analysis results and correlation tests.

3.2 The NARMAX System Identification Methodology

The NARMAX model, originally proposed by Leontaritis and Billings (1985), has been intensely studied by many authors (Billings et al., 1989, Chen and Billings, 1989b, Aguirre and Billings, 1995, Hong and Harris, 2001, Guo and Billings, 2007, Chen et al., 1990a, Farina and Piroddi, 2010). The NARMAX model forms the basis for an entire nonlinear system identification and analysis methodology that has been developed over the past 30 years (Billings, 2013). The NARMAX methodology provides an unified solution to finding an input-output relationship when the underlying system is not known in advance and only the variable measurements are available. In particular, the NARMAX model can be used to analytically derive *Generalized Frequency Response Functions* associated with the system of interest, which provide a basis for studying the system's output frequency response and analysis of different frequency domain phenomena (Diaz and Desrochers, 1988, Peyton-Jones

and Billings, 1989, Billings and Tsang, 1989a, Zhao and Marmarelis, 1998, Peyton Jones, 2007).

The NARMAX representation can be used to describe a wide range of nonlinear dynamical systems. In this context, the Volterra, Wiener and Hammerstein models can be considered as special cases of the NARMAX model (Billings and Coca, 2001).

The NARMAX model (Leontaritis and Billings, 1985) can be written as:

$$y(t) = f(y(t-1), ..., y(t-n_y), u(t-1), ..., u(t-n_u), e(t-1), ..., e(t-n_e)) + e(t) \quad (3.1)$$

where $y(t) = \begin{bmatrix} y_1(t) \\ \vdots \\ y_m(t) \end{bmatrix}$, $u(t) = \begin{bmatrix} u_1(t) \\ \vdots \\ u_r(t) \end{bmatrix}$, $e(t) = \begin{bmatrix} e_1(t) \\ \vdots \\ e_m(t) \end{bmatrix}$ are the system's output, input and noise respectively; n_y, n_u and n_e are the maximum lags for the output, input and noise; $e(t)$ is assumed to be a white sequence; $f(\cdot)$ is some vector-valued nonlinear function.

3.2.1 The Polynomial NARMAX Model

The NARMAX model structure is rarely known a priori, so in practice the identification procedure assumes that the underlying system can be approximated using functions belonging to a certain class. The choice of functions used to implement the model is very important, because it will determine what type of nonlinear systems can be approximated with desired accuracy and the number of parameters needed to achieve this desired accuracy. Not all model representations are guaranteed to converge to an arbitrary function, and moreover the choice of representation will often determine what model selection and parameter estimation algorithms can be used. The NARMAX representations commonly used in practice include: *polynomial* (Chen and Billings, 1989a, Mendes, 1995), *rational* (Chen et al., 1990a, Billings and Zhu, 1994), *radial basis functions* (Chen et al., 1990b, Chen et al., 1990a) and *wavelets* (Coca and Billings, 2001). All these nonlinear representations provide general mathematical model structures that, although have far greater flexibility compared to the linear ones, involve an enormous number of terms.

The ***polynomial NARMAX model*** is widely used in practice because it leads to relatively simple linear-in-the-parameters models which can be estimated efficiently using the *Orthogonal Forward Regression (OFR)* for structure detection and parameter estimation (Billings and Coca, 2001). In addition, efficient algorithms have been developed to derive analytically the higher order (or Generalized) frequency response functions for polynomial NARMAX models, by using recursive harmonic probing (Zhang and Billings, 1993, Liu et al., 2006). The NARMAX polynomial expansion of a system with r inputs and one output is defined (Billings and Leontaritis, 1980) as:

$$\begin{aligned} y(t) &= f_{pol}(x(t)) = \theta_0 + \sum_{i_1=1}^{n} \theta_{i_1} x_{i_1}(t) + \sum_{i_1=1}^{n} \sum_{i_2=i_1}^{n} \theta_{i_1,i_2} x_{i_1}(t) x_{i_2}(t) \\ &\quad + \cdots + \sum_{i_L=1}^{n} \cdots \sum_{i_L=i_{L-1}}^{n} \theta_{i_1,\ldots,i_l} x_{i_1}(t) \ldots x_{i_l}(t) + e_i(t) \end{aligned} \tag{3.2}$$

where $x(t) = [x_1(t), \ldots, x_n(t)]$ denotes the vector of dimension $n = n_y + rn_u + n_e$ consisting of lagged variables in the outputs y, inputs u_j and noise terms e, $\theta_{i_{(\cdot)}}$ are the unknown scalar parameters to be estimated; L defines the model's nonlinear dimension.

According to the fundamental Weierstrass theorem (Soderstrom and Stoica, 1989), polynomials can uniformly approximate as closely as desired any continuous function defined over a closed interval. The polynomial NARMAX expansion could involve huge number of terms for large values of n. In practice however, only a small subset of polynomial terms are needed to approximate a given function. Finding the minimal set of relevant terms is known as the model structure selection problem. For linear-in-the-parameters models, such as the polynomial NARMAX models, Billings et al. (1989) proposed an efficient Forward Orthogonal Regression method which has been extensively used to successfully derive parsimonious models for a wide array of real-world systems from experimental input-output measurements (Chen et al., 1990b, Zhu and Billings, 1992, Billings and Coca, 2001, Boaghe et al., 2002).

The approximation capabilities of the polynomial NARMAX representation, the availability of fast and efficient algorithms for model structure selection, parameter estimation and for analysing the system's dynamics in the frequency domain motivate the use of this

representation for modelling and analysis of the paleoclimatic data.

The NARMAX methodology includes a number of steps (Billings and Coca, 2001, Billings, 2013), which are summarized below:

Step 1: Input design, data acquisition and pre-processing

This involves the design of an appropriate input for the NARMAX model used to persistently excite the dynamical system under study over the entire frequency and operating amplitude range. This ensures that the model captures the full dynamical behaviour of the underlying system. Methods for input design for nonlinear system identification using the NARMAX methodology are given in Leontaritis and Billings (1987), Aguirre and Billings (1995) and Billings and Zhu (1995).

For some real systems it is not possible to manipulate the input, so the modelling has to be performed on the available input measurements. This happens when the input data-set is obtained by simulations of physical equations, as is the case of the orbital parameters, or when the experiment that generated the data cannot be repeated in order to collect more measurements.

Data preparation refers to pre-processing procedures, such as normalization, interpolation, dimensionality reduction or discretization.

Step 2: Model structure detection and parameter estimation

Given the structure of the model is not known at the beginning, equation (3.1) presents the full model, with all the possible terms. In practice, the number of candidate terms that can be included in a model can be huge but only a small subset of these, usually 15-20 terms, is really needed to describe the systems's dynamics. It is easy to see that for a MISO system with few inputs, even a polynomial model of a relatively low order (three or four) can easily involve thousands of candidate model terms. Fitting a full-size model is impractical, leads to over-parametrization of the system and to numerical ill-conditioning and dynamical instability. The NARMAX system identification methodology includes very robust term selection and parameter estimation algorithms. The algorithm, which will be presented in Section 3.3, determines which are the relevant terms to include in the final model and which terms to

discard. Removing of terms must be done very carefully as not to lose significant ones and as an effect to change the behaviour of the system.

Step 3: Model validation

This step of the methodology involves testing that the model truly follows the behaviour of the system. Many types of validation tests have been studied and developed (Billings and Zhu, 1994, Aguirre and Billings, 1995, Billings and Zhu, 1994, Billings and Coca, 2001) and will be detailed in Section 3.4.

3.3 The Orthogonal Forward Regression for Model Structure Detection and Parameter Estimation

The estimation of NARMAX polynomial models can be formulated as a linear regression problem:

$$y(t) = \sum_{j=1}^{M} \theta_j p_j(t) + e(t) \tag{3.3}$$

where $p_j(t)$ denote the possible polynomial terms (monomials) that can be included in the model with degrees ranging from 0 (constant term) to L, each consisting of products of delayed outputs, inputs and/or noise terms, θ_j are unknown parameters to be estimated and $e(t)$ describes modelling error. The total number of terms is given by $M = \sum_{j=0}^{L} n_j$, with $n_0 = 1$ and $n_j = \frac{n_{j-1}\left[n_y + n_e + \sum_{k=1}^{r} n_{u_k} + j - 1\right]}{j}$, $j = 1, \ldots, L$, where n_y represents the maximum lag for the output, n_{u_k} represents the maximum lag for the k^{th} input and n_e is the maximum lag for the noise terms.

Given input and output time-series of lengths N, equation (3.3) can be written in matrix form as:

$$Y = P\Theta + \Xi \tag{3.4}$$

where $Y = \begin{bmatrix} y(1) \\ \vdots \\ y(N) \end{bmatrix}$, $P = \begin{bmatrix} p_1 & \dots & p_M \end{bmatrix}$, $\Theta = \begin{bmatrix} \theta_1 \\ \vdots \\ \theta_M \end{bmatrix}$, $\Xi = \begin{bmatrix} e(1) \\ \vdots \\ e(N) \end{bmatrix}$ and $p_i = \begin{bmatrix} p_i(x(1)) & \dots & p_i(x(N)) \end{bmatrix}^T$.

In equation (3.4), Y is commonly referred to as the dependent variable and P are the *regressors* or *predictors*.

In order to present the regressors associated with the process and noise models, equation (3.3) is re-written as:

$$y(t) = \sum_{j=1}^{M_p} \theta_{yu} x_{yu}(t) + \sum_{j=M_p+1}^{M} [\theta_{yue} x_{yue}(t) + \theta_e x_e(t)] + e(t) \tag{3.5}$$

where $x_{yu}(t)$ are functions of $y(t)$ and $u(t)$, $x_{yue}(t)$ are functions of cross-products between $e(t)$ and $y(t)$ and/or $u(t)$, $x_e(t)$ are functions of $e(t)$, θ_{yu}, θ_{yue} and θ_e are the unknown coefficients, M_p is the number of process terms, M is the total number of terms.

This can be written in matrix form, similarly to equation (3.4), as:

$$Y = P_{yu}\Theta_{yu} + P_{yue}\Theta_{yue} + P_e\Theta_e + \Xi \tag{3.6}$$

where $P_{yu} = [p_{yu_1} \dots p_{yu_{M_p}}]$, $[P_{yue}\ P_e] = [p_{yue_{M_p+1}} \dots p_{yue_{M_k}} p_{e_{M_{k+1}}} \dots p_{e_M}]$,

with $p_i = [p_i(x(1)) \dots p_i(x(N))]^T$, $\Theta_{yu} = \begin{bmatrix} \theta_{yu_1} \\ \vdots \\ \theta_{yu_{M_p}} \end{bmatrix}$, $\begin{bmatrix} \Theta_{yue} \\ \Theta_e \end{bmatrix} = \begin{bmatrix} \theta_{yue_{M_p+1}} \\ \vdots \\ \theta_{yue_{M_k}} \\ \theta_{e_{M_{k+1}}} \\ \vdots \\ \theta_{e_M} \end{bmatrix}$.

In equation (3.6), P_{yu} are the regressors associated with the process model and $[P_{yue}\ P_e]$ are the regressors associated with the noise model.

3.3.1 Orthogonal Least Squares

The orthogonal least squares (OLS) algorithm works by replacing the original set of regressors P in equation (3.4) with a set of orthogonal vectors (Liu, 1998, Chen and Billings, 1989b). The structure detection and coefficients estimation problem becomes one of selecting out of all the possible model terms M, a minimal set of $m \ll M$ terms that approximate the unknown system with a desired accuracy ρ. The coefficients $\hat{\Theta}_m$ can be calculated by solving the linear optimisation problem given by:

$$\hat{\Theta}_m = \underset{\Theta}{argmin} ||Y - P_m \Theta_m||_2^2 \tag{3.7}$$

such that $||Y - P\hat{\Theta}|| \leq \rho$, where $||\cdot||$ represents the commonly used Euclidean norm.

Assume that the regression matrix P is full rank in columns and can be orthogonally decomposed as:

$$P = WA \tag{3.8}$$

The derivation of equation (3.8) can be done by using the Classical Gram-Schmidt (CGS) or the Modified Gram-Schmidt (MGS) methods (Chen and Billings, 1989b).

In equation (3.8) A is an $M \times M$ unit upper triangular matrix with ones on the diagonal and zeros below the diagonal as:

$$A = \begin{bmatrix} 1 & \alpha_{12} & \alpha_{13} & \dots & \alpha_{1M} \\ 0 & 1 & \alpha_{23} & \dots & \alpha_{2M} \\ 0 & 0 & 1 & \dots & \vdots \\ \vdots & \vdots & \vdots & \vdots & \alpha_{M-1M} \\ 0 & \dots & \dots & \dots & 1 \end{bmatrix} \text{ and } W = \begin{bmatrix} w_1(1) & \dots & w_M(1) \\ \vdots & & \vdots \\ w_1(N) & \dots & w_M(N) \end{bmatrix} \text{ is an } N \times M \text{ orthogonal matrix such that:}$$

$W^T W = (PA^{-1})^T (PA^{-1}) = D = diag\left[\sum_{t=1}^{N} w_1^2(t), \dots, \sum_{t=1}^{N} w_M^2(t)\right]$.

This is true because $w_i(t)$, $i = 1, \dots, M$ are constructed to be orthogonal over the data record of length N such that $\sum_{t=1}^{N} w_j(t) w_{k+1}(t) = 0$ for $j = 1, \dots, k$ and $k = 1, \dots, M-1$.

The space spanned by the orthogonal set $w_1, \dots, w_M$ is the same as that spanned by the original set $p_1, \dots, p_m$ (Chen and Billings, 1989b).

By writing equation (3.8) as $Y = PA^{-1}A\Theta + \Xi$ and substituting $W = PA^{-1}$ and $G = A\Theta$, the regression model in equation (3.4) can be written as:

$$Y = WG + \Xi \tag{3.9}$$

where $G = \begin{bmatrix} g_1 \\ g_2 \\ \vdots \\ g_M \end{bmatrix}$ is a vector of auxiliary parameters.

In equation (3.9) the output is expressed as a sum of the explained variance given by WG and the unexplained variance represented by Ξ.

The auxiliary regressors $w_i,\ i = 1, \ldots, M$ are uncoupled and as a result the corresponding parameters g_i are uncoupled as well. This allows to evaluate independently the contribution from each w_i to minimising the cost function given in equation (3.7).

The solution of the OLS algorithm can be calculated as $\hat{G} = D^{-1}W^TY$ or $\hat{g} = \frac{w_i^T y}{w_i^T w_i}$, with $1 \leq i \leq M$.

The last step involved is the calculation of the original set of parameters $\hat{\Theta}$, which can be done by solving the triangular system $A\hat{\Theta} = \hat{G}$.

3.3.2 The Orthogonal Forward Regression

The model given in equation (3.3) is overparametrized and the powerful and efficient Forward Orthogonal Regression algorithm (Billings et al., 1989, Korenberg et al., 1988, Chen and Billings, 1989b) needs to be used for structure selection in order to only keep the relevant terms that describe the system's dynamics.

The OFR involves starting with no model terms in the model and then adding terms to the model in a stepwise manner until the desired accuracy or other stopping criterion is satisfied. At each step all the candidate model terms, not included already in the model, are evaluated and the model term which improves the most the model accuracy is selected. This technique simplifies significantly the estimation process and also provides an effective way of assessing the contribution of the most significant terms to the final model as it is

constructed step by step. The criterion that is used to compare and rank the relevance of each model term is called the *error reduction ratio* (err) and it represents the significance of each orthogonal regressor w_i with regards to the output signal variance. The err values provide a simple and effective way of making a quantitative judgment on each regressor's contribution. The err formula is:

$$[err]_i = \frac{g_i^2 w_i^T w_i}{y^T y} \tag{3.10}$$

An important feature of the *OFR* is that it allows for separate estimation of the process and noise model. The process model is estimated first, and then using the predicted residuals, $\varepsilon(k) = y(k) - \hat{y}(k)$, the noise model is obtained.

The estimation of the process model involves the following steps:

Step 1.

All the process terms $p_{yu_i},\ i = 1, \ldots, M_p$ in the regression model in equation (3.4) form the initial candidate model set. To select the first and most significant model term, for each process term compute:

$$w_1^{(i)} = p_{yu_i}$$

$$g_1^{(i)} = \frac{((w_1^{(i)})^T y)}{(w_1^{(i)})^T w_1^{(i)}}$$

$$[err]_1^{(i)} = \frac{(g_1^{(i)})^2 (w_1^{(i)})^T w_1^{(i)}}{y^T y}$$

The err due to w_i represents the proportion of the dependent variable y explained by w_i. The term selected as the first one in the model will be the one with the largest $[err]_1^{(i)}$ say $[err]_1^{(j)} = max\{[err]_1^{(i)}, 1 \leq i \leq M\}$. The term corresponding to the extracted index j becomes the first selected model term as $w_1 = w_1^{(j)} = p_{yu_j}$.

Step 2.

All the $p_{yu_i},\ i = 1, \ldots, M_p,\ i \neq j$ are considered as possible candidates for the second term in the model, and calculate:

$$w_2^{(i)} = p_{yu_i} - \alpha_{12}^{(i)} w_1$$

$$g_2^{(i)} = \frac{((w_2^{(i)})^T y)}{(w_2^{(i)})^T w_2^{(i)}}$$

$$[err]_2^{(i)} = \frac{(g_2^{(i)})^2 (w_2^{(i)})^T w_2^{(i)}}{y^T y}$$

where $\alpha_{12}^{(i)} = \frac{w_1^T p_{yu_i}}{w_1^T w_1}$.

Find the maximum $[err]_2^{(i)}$ say $[err]_2^{(k)} = max\{[err]_2^{(i)},\ 1 \leq i \leq M_p,\ i \neq j\}$. It follows that the second term in the model will be selected as $w_2 = w_2^{(k)} = p_{yu_k} - \alpha_{12}^{(k)} w_1$.

The procedures terminates when:

i. there are no more terms in the set of possible process terms.

ii. a predefined number of process terms has been selected.

iii. a desired tolerance ρ is obtained as $1 - \sum_{i=1}^{M_p} [err]_i < \rho,\ M_p < M$. The value of ρ indirectly determines the number of terms included in the final model and so its complexity as well.

The estimation of the ***noise model*** involves the following steps:

Step 1.

Set the number of selected noise terms as $M_n = 0$ and calculate the initial residuals as $\varepsilon = y - \sum_{l=1}^{M_p+M_n} g_l w_l$.

Step 2.

At each step $k > M_p$ in the noise estimation procedure calculate:

$$\alpha_{jk}^{(i)} = \frac{w_j^T p_{yue_i}}{w_j^T w_j},\ 1 \leq j < k$$

$$w_k^{(i)} = p_{yue_i} - \alpha_{jk}^{(i)} w_j$$

$$g_k^{(i)} = \frac{((w_k^{(i)})^T y)}{(w_k^{(i)})^T w_k^{(i)}}$$

$$[err]_k^{(i)} = \frac{(g_k^{(i)})^2 (w_k^{(i)})^T w_k^{(i)}}{y^T y}$$

As for process model term selection, the largest $[err]_k^{(i)}$ is selected as $[err]_k^{(h_k)} = max\{[err]_k^{(i)}, 1 \leq i \leq M_n,\ i \neq h_1, \ldots, i \neq h_{k-1}\}$. So, the selected noise term will be the one corresponding to the index h_k and given by $w_k = w_k^{(h_k)} = p_{yue_{ik}} - \alpha_{jk}^{(h_k)} w_j$.

Step 3.

Repeat the procedure iteratively until:

i. there are no more noise terms in the set of possible terms.

ii. a fixed number of pre-defined noise terms has been selected.

iii. when a chosen threshold for the noise is reached at the step M_p+M_n as $1-\sum_{j=1}^{M_p+M_n}[err]_j < \rho_\xi$.

The resultant model will contain a total of $M_p + M_n$ significant terms. Usually for noise model estimation only 3-5 iterations are necessary.

Once the orthogonalization and the estimation of parameters g_i in equation (3.9) is finished, the initial unknown parameters θ_i from equation (3.3) can be calculated as:

$$\theta_{M_s} = g_{M_s}$$
$$\theta_i = g_i - \sum_{j=i+1}^{M_s} \alpha_{ij}\theta_j$$

where $i = M_{s-1}, M_{s-2}, \ldots, 1$ and $M_s < M$.

3.4 Model Validation Methods

Model validation is the final step of system identification and is a very important one because it does checking that the model provides an accurate representation of the observed dynamical system of interest. There are two main classes of model validation methods. One class is the *statistical validation methods*, which includes methods that involve performing residual

analysis and goodness-of-fit tests (Ljung, 1999), as are the tests discussed in this section. The second class includes validation methods based on qualitative analysis techniques for nonlinear dynamical systems which compare the dynamical invariants, such as equilibrium points, Lyapunov exponents, bifurcation diagrams, Poincare sections (Mendes, 1995, Aguirre, 1996). The easiest way to evaluate the performance of a model is to compute the *one step ahead* model predicted output (*osa*) and the *model predicted output* (*mpo*).

The *osa* which is calculated at each step using the model and measured inputs and outputs is defined as:

$$\hat{y}_{osa}(t) = \hat{f}(y(t-1), \ldots, y(t-n_y), u(t-1), \ldots, u(t-n_u), \varepsilon(t-1, \hat{\theta}), \ldots, \varepsilon(t-n_e, \hat{\theta}) \quad (3.11)$$

where $\hat{f}$ is the estimated model and $\varepsilon(t, \hat{\theta})$ represent the residuals given by $\varepsilon(t, \hat{\theta}) = y(t) - \hat{y}(t)$.

The *mpo* is computed recursively using the model, the measured input and only the first few output measurements needed to initialize the model, and is defined as:

$$\hat{y}_{mpo}(t) = \hat{f}(\hat{y}(t-1), \ldots, \hat{y}(t-n_y), u(t-1), \ldots, u(t-n_u), 0, \ldots, 0) \quad (3.12)$$

As in practice we are interested in the behaviour of the deterministic part of the model, the noise model is usually discarded in simulation.

The *model predicted output* can be used to assess to what extent the model has captured the dynamics of the system. In contrast, the *one-step-ahead* prediction shows only how well the model approximated the output measurements. It is more accurate to use the *model predicted output* when assessing the model's prediction power rather than *one-step ahead* prediction, due to the fact that the *osa* does not take into consideration the accumulation of prediction error. Because of this, when considering the *osa* prediction, even a poor model can produce good results. If the tests fail then the model's structure and/or coefficients need to be re-estimated.

- **Model Prediction Error**

The model prediction error $\varepsilon(t)$ is given by

$$\varepsilon(t) = y(t) - \hat{y}(t)$$

where $y(t)$ represents the measured output data and $\hat{y}(t)$ represents the *model predicted output*.

A common measure of model performance is the *normalized root mean squared error*, defined as:

$$NRMSE = \frac{\sqrt{\frac{\sum_{i=1}^{N}(y(i)-\hat{y}(i))^2}{N}}}{\sigma_{y(t)}}$$

where $\sigma_{y(t)}$ denotes the standard deviation of the measured output signal $y(t)$.

- **Cross-Validation**

Cross-validation is a method of assessing how well a model can perform on "unseen" data. This is called *generalisation*. An overview on cross-validation methods and their application on regression modelling can be found in Browne (2000).

The cross-validation technique used in this work is known as *hold-out cross-validation* (Gutierrez-Osuna, 2005, Refaeilzadeh et al., 2008). This involves splitting the original data-set into two non-overlapping sets, one used for estimation (modelling) and the other for validation. Depending on the length of the available samples, the data-set can be split in two equal parts or, as in this work, 66.6% for estimation and 33.3% for validation. The first part of the data is used alone to perform model selection and parameter estimation, while the second one is used afterwards alone to test the selected model on new data points. A disadvantage of this method is the fact that because it does not use all of the available data, it is dependent on the choice for the modelling data.

Plotting the modelling error against the prediction error would show that the first one will decrease, while the latter will decrease and then increase again, marking the point of over-fitting for the model. Because the method works with unseen data, for certain combinations of values, the model might become unstable. The optimal value is given by the point on the graph where the prediction error for the validation data reaches the minimum point. The same method can be used to determine other hyper-parameters associated with the model

such as the number of process and noise to include in the model. Figure 3.1 shows the typical evolution of the prediction error with respect to the number of process terms over the estimation and validation data set. The number of process terms selected corresponds to a certain number of noise terms k.

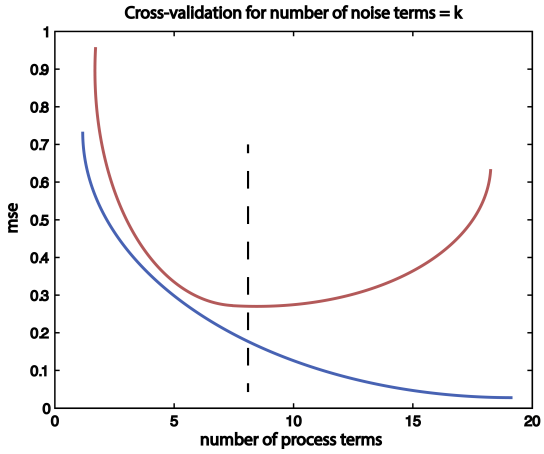

Figure 3.1: Example of using cross-validation for choosing the optimum number of process and noise terms in structure detection: blue is the modelling error, red is the prediction error, and the vertical dotted line is the optimum number of terms.

- **Correlation Tests**

A common approach to validate NARMAX models involves computing a set of five correlation tests (Billings and Voon, 1985, Chen and Billings, 1989b), which involve the residuals (estimation error) and the input-output data used in estimation. The identified model is considered to be adequate if the residuals are unpredictable from (uncorrelated with) all linear and nonlinear combinations of past inputs and outputs (Billings and Voon, 1985, Billings and Zhu, 1994). There are two types of correlation tests: auto-correlation function of the residuals and cross-correlation function between the residuals and the input. For the nonlinear SISO case these are:

$$\begin{cases} \phi_{\varepsilon\varepsilon}(\tau) = \delta(t), \tau \neq 0 \\ \phi_{u\varepsilon}(\tau) = 0, \forall\tau \\ \phi_{\varepsilon(\varepsilon u)}(\tau) = 0, \tau \geq 0 \\ \phi_{u^{2'}\varepsilon}(\tau) = 0, \forall\tau \\ \phi_{u^{2'}\varepsilon\hat{}2}(\tau) = 0, \forall\tau \end{cases} \tag{3.13}$$

where $u^{2'}(t) = u^2(t) - \overline{u^2(t)}$ and $\overline{u^2(t)}$ represents the mean value of $u^2(t)$. In order for a model to be considered adequate, the correlation tests must be within the confidence interval (95% of the points), defined by $\pm 1.96/\sqrt{N}$, where N is the number of data samples.

The correlation tests are usually inspected visually. The correlation tests for the SISO (equations (3.13)) case can be extended for a MIMO model, as will be shown in the modelling Chapter 5. Recently a new set of omni-directional (cross- and auto-) correlation tests were developed (Zhu et al., 2007) which represent concise and more effective testing methodologies for nonlinear higher order models.

- **Coherence Function Analysis**

Coherence function analysis is a statistical analysis used to investigate the correlation in frequency, at certain frequencies or frequency intervals of interest, between the measured data and the model predicted output.

The coherence function is defined by the formula:

$$C_{y\hat{y}} = \frac{|G_{y\hat{y}}|^2}{G_{yy}G_{\hat{y}\hat{y}}} \tag{3.14}$$

where $G_{y\hat{y}}$ is the cross-spectral density between y (measurement) and $\hat{y}$ (mpo), and G_{yy} and $G_{\hat{y}\hat{y}}$ are the auto-spectral density of y and $\hat{y}$ respectively.

The coherence takes values in the interval $[0, 1]$, so if two signals are perfectly correlated their coherence value is equal to 1, while two signals completely uncorrelated have the coherence value 0.

3.5 Discussion

This chapter introduced the NARMAX system identification methodology that will be used to subsequently derive two models that relate the orbital parameters to the oxygen isotope ratios proxy data for ***before*** and ***after MPT***. The procedure involves model structure detection, parameter estimation and model validation. It was shown that due to its versatility, the method is extremely useful and can provide great insight into system's dynamics and comes with meaningful analysis methods. NARMAX is a very powerful tool because it can overcome many difficulties arising from working with real data, such as: noisy data, random fluctuations in the data, short datasets, MIMO systems, higher nonlinearity orders, severe nonlinearities. The main advantages of the NARMAX methodology can be summarised as follows:

• The NARMAX representation can describe a wide range of nonlinear dynamical systems. In this context, many other representations such as the Volterra and Wiener series can be considered as special cases of the NARMAX model (Leontaritis and Billings, 1985, Billings et al., 1989).

• The NARMAX methodology ensures that only the relevant model terms are included in the model thus avoiding over-fitting.

• The methodology allows the separate approximation of the process and noise model.

• The NARMAX model can be easily mapped into the frequency domain by computing analytically the Generalized and Output Frequency Response Functions (Peyton-Jones and Billings, 1989, Peyton Jones, 2007), which will be defined in later chapters.

Chapter 4

Frequency Domain Analysis of Nonlinear Systems Using Generalized and Output Frequency Response Functions

4.1 Introduction

Nonlinear dynamical systems can be analysed in both the time and frequency domain. Frequency domain analysis has been widely applied for investigating systems behaviours in many fields of engineering, such as: control, electronics, communications, mechanical and civil engineering (Lang et al., 2007). These methods often provide a physical interpretation to NARMAX models derived using system identification (Lang et al., 2007). A discrete-time NARMAX model is not necessarily unique and several quite different time domain models can represent the same system dynamics. This can make it difficult to characterize and compare the underlying dynamics of two or more dynamical systems. In the frequency domain however, the dynamics of the system can be characterized uniquely using Generalized Frequency Response Functions (GFRFs). In other words, two alternative time-domain NARMAX representations of one system will have the same frequency domain representation.

Frequency domain analysis for linear systems has been very successful due to the simple analytical expression of the output frequency response, given by $Y(j\omega) = H(j\omega)U(j\omega)$, where $H(j\omega)$ represents the system's frequency function that relates the spectrum of the

input $U(j\omega)$ to the spectrum of the output $Y(j\omega)$ (Lang and Billings, 2005).

Nonlinear systems can exhibit certain types of phenomena, such as the generation of harmonics, inter-modulation, desensitisation and gain compression/expansion, which are not encountered when working with linear systems (Billings and Tsang, 1989b, Yue et al., 2005, Lang and Billings, 2005, Peng et al., 2007).

These phenomena are summarized as follows:

1. **Harmonics** are frequency components equal to multiples of the fundamental input frequency. So if the input frequency is ω, the harmonics will be: $2\omega, 3\omega, \ldots$.

2. **Desensitisation** represents, for nonlinear systems, the interference caused in the sinusoidal response at frequency ω_1 by the application of a second sinusoidal signal at the frequency ω_2. In this case, the gain at frequency ω_1 depends nonlinearly on the magnitude of the disturbing signal at the frequency ω_2.

3. **Gain compression/expansion** refers to the changes an increase in the input amplitude induces to the system's gain. For nonlinear systems, the system's gain is a function of the input magnitude. Gain compression refers to the effect where the system gain is reduced to a level that causes a nonlinear increase in the output power. Gain expansion represents the opposite phenomena of an increase in gain.

4. **Inter-modulation** is the process of nonlinear coupling between two or more input frequency components in order to produce new output components. Inter-modulation usually refers to the frequency mixes which cannot be included in the above categories (but are not restricted to this), for example: $(\omega_1 - \omega_2)$.

For the studied nonlinear system the phenomena of *harmonics* and *inter-modulation* are observed and analyzed in Chapter 6.

These nonlinear phenomena represent different mechanisms by which, in a nonlinear system, the output spectrum can be enriched compared to the input spectrum or that allow energy to be transferred from one frequency band to another (Lang and Billings, 2005). This is presented in Figure 4.1, where the input frequencies are considered to be ω_1 and ω_2. The

figure shows that for the output frequency domain there are frequencies that are passed unaltered to the output, (the green coloured lines) but also that new frequencies are formed through *harmonics* (the blue coloured lines) and *inter-modulation* (the red coloured lines).

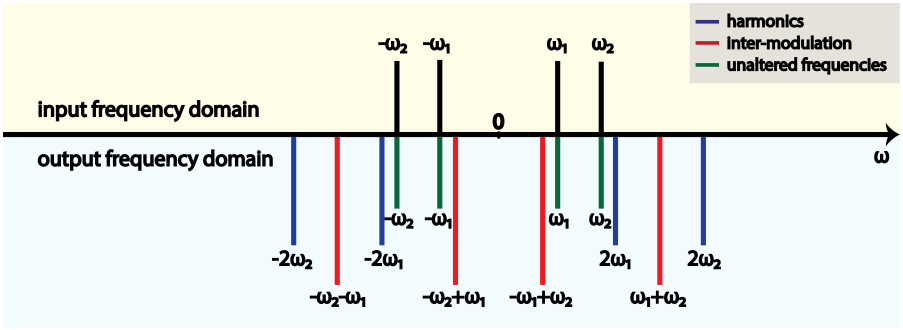

Figure 4.1: Input frequencies components for system with two fundamental frequencies ω_1 and ω_2 and the types of linear and nonlinear phenomena that generate the output frequency spectrum.

When studying nonlinear systems the output spectrum is often much richer than the input spectrum i.e. there are output frequency components that are not present in the input spectrum (Billings and Tsang, 1989b, Billings and Peyton Jones, 1990, Lang and Billings, 1997). Peyton-Jones and Billings (1989), Billings and Tsang (1989a), Billings and Tsang (1989b), Zhang and Billings (1993) studied and introduced the frequency response functions for nonlinear systems and developed algorithms for mapping the nonlinear NARMAX models into the frequency domain.

The study of nonlinear systems in the frequency domain is based on the extension of the concept of linear frequency response function (FRF) for nonlinear systems that have a Volterra series representation. The GFRFs are multi-dimensional functions of frequency (Lang et al., 2007, Peng et al., 2007) and can be determined from the system model (Billings and Tsang, 1989a, Peyton-Jones and Billings, 1989, Billings and Peyton Jones, 1990). The GFRFs are a powerful tool for representing a system in the frequency domain and explaining nonlinear energy transfer phenomena (Billings and Yusof, 1996, Boaghe, 2000, Boaghe et al., 2002). Although the multi-dimensional characteristic can make the GFRFs difficult to visualize and interpret, they are still a very useful way of relating the system behaviours and model terms to the time domain properties and give the analysis a physical interpretation

(Li and Billings, 2005, Peng et al., 2007).

More recently, GFRFs have been complemented by a new concept, the Output Frequency Response Functions, which characterize directly the relationship between the input and the output spectra of a nonlinear system. The OFRFs were introduced by Lang and Billings (2005) and are one-dimensional functions of frequency, which makes them easier to interpret and visualize. This is a great advantage, because a similar analysis to the linear case can be performed. At the same time, it can provide insight into how and which input frequencies contribute to the output frequency spectrum and in the end can offer an explanation to the system's nonlinear behaviour (Peng et al., 2007, Lang and Billings, 2005).

This chapter introduces the concepts of Generalized and Output Frequency Response Functions, which are nonlinear frequency analysis methods, and the method for computing them for polynomial NARMAX models. The chapter is organized as follows. In Section 4.2, the method of mapping the Volterra series in the frequency domain is introduced followed by theoretical derivations of the GFRFs and OFRFs. Section 4.3 starts with theoretical considerations on the harmonic probing technique for multi-tone split inputs. This section also presents types of terms and GFRF results that are encountered in practical examples and methods for data and model pre-processing, which are used in order to normalize the data and in order to prepare the model for the GFRF algorithm. Section 4.4 is concerned with the computation of the Output Frequency Responses (OFRs).

4.2 Generalized and Output Frequency Response Functions for Nonlinear MISO Systems

For a linear dynamical system, the time domain system response is given by:

$$y(t) = \int_{-\infty}^{\infty} h(\tau)u(t-\tau)d\tau \tag{4.1}$$

where $h(\tau)$ is the impulse response of the system and $u(t)$ is the system input.

In the frequency domain, the relationship between the input and the output spectrum is given by:

$$Y(j\omega) = H(j\omega)U(j\omega) \tag{4.2}$$

where $Y(j\omega)$ and $U(j\omega)$ are the spectrum of the output and input signals respectively and $H(j\omega)$ is the system frequency response function (FRF).

The output of a nonlinear system can be written as a Volterra series truncated to N number of terms as (Sandberg, 1983):

$$y(t) = \sum_{n=1}^{N} y^{(n)}(t) \tag{4.3}$$

where $y^{(n)}(t)$ is the n^{th} order component of the output $y(t)$ and each $y^{(n)}(t)$ is homogeneous of degree n. Written as in equation (4.3), the output of a nonlinear system is represented as the sum of the responses of all the orders of nonlinearity parallel systems that it is formed of (Swain and Billings, 2001).

For a MISO system with m inputs $u_1(t), \ldots, u_m(t)$, $y^{(n)}(t)$ is given by as:

$$\begin{aligned} y^{(n)}(t) &= \sum\nolimits_{n_1+\ldots+n_m=n} \int_{-\infty}^{\infty} \cdots \int_{-\infty}^{\infty} h^{(n)}_{(n_1,\ldots,n_m)}(\tau_1, \ldots, \tau_n) \\ &\quad \times u_{(n_1 \ldots n_m)}(\tau_1, \ldots, \tau_n) d\tau_1 \ldots d\tau_n, \end{aligned} \tag{4.4}$$

where

$$\begin{aligned} u_{(n_1 \ldots n_m)}(\tau_1, \ldots, \tau_n) &= u_1(t-\tau_1) \ldots u_1(t-\tau_{n_1}) \times u_2(t-\tau_{n_1+1}) \ldots u_2(t-\tau_{n_1+n_2}) \times \\ &\quad \cdots \times u_m(t-\tau_{n_1+\cdots+n_{m-1}+1}) \ldots u_m(t-\tau_n) \end{aligned}$$

and $h^{(n)}_{(n_1,\ldots,n_m)}$ represents the n^{th} order Volterra kernel or n^{th} order impulse response associated with the output and n_1^{th} input $u_1(t)$, n_2^{th} input $u_2(t)$, ..., n_m^{th} input $u_m(t)$.

The total number of kernels for a system with r inputs is given by $Tk^{(r)}_{(N)} = \sum_{i=1}^{N} Nk^{(r)}_{(i)}$, where the number of i^{th} order kernels is calculated recursively using the formula $Nk^{(r)}_{(i)} = Nk^{(r)}_{(i-1)} + Nk^{(r-1)}_{(i-1)} + \cdots + Nk^{(1)}_{(i-1)}$. $Nk^{(r)}_{(1)}$ represents the total number of first order kernels of

the system and is equal to the number of inputs to the model. For example, a system with $r = 2$ and $N = 3$ will have 9 unique kernels. These are:

- first order kernels: $h_1^1(\cdot)$, $h_2^1(\cdot)$
- second order kernels: $h_{11}^2(\cdot)$, $h_{12}^2(\cdot)$, $h_{22}^2(\cdot)$
- third order kernels: $h_{111}^3(\cdot)$, $h_{112}^3(\cdot)$, $h_{122}^3(\cdot)$, $h_{222}^3(\cdot)$

The kernels are called *self-kernels* if all the subscripts $(n_1, \ldots, n_m)$ are equal, as is the case of the kernels: $h_{11}^2(\cdot)$, $h_{22}^2(\cdot)$, $h_{111}^3(\cdot)$, ... If not all the subscripts are equal, the kernels are of the form $h_{12}^2(\cdot)$, $h_{112}^3(\cdot)$, $h_{122}^3(\cdot)$ and are referred to as *cross-kernels*. As it can be seen from equation (4.4), the self-kernels are convoluted with one input only, whereas the cross-kernels are convoluted with at least two different inputs.

Writing equation (4.3) in the frequency domain gives:

$$Y(j\omega) = \sum\nolimits_{n=1}^{N} Y^{(n)}(j\omega) \tag{4.5}$$

where $Y(j\omega)$ is the output spectrum and $Y^{(n)}(j\omega)$ represents the n^{th} order frequency response of the system.

This can be written as (Lang and Billings, 1997):

$$\begin{aligned} Y^{(n)}(j\omega) \;=\; & \frac{1}{2^{n-1}} \sum_{n_1+\cdots+n_m=n} \int_{\omega_1+\cdots+\omega_n=\omega} H^{(n)}_{(n_1,\ldots,n_m)}(j\omega_1 \ldots j\omega_n) \prod_{i=1}^{n_1} U_1(j\omega_i) \\ & \prod_{in_1+1}^{n_1+N_2} U_2(j\omega_i) \cdots \prod_{in_1+\cdots+n_{m-1}+1}^{m} U_m(j\omega_i) d\tau_{n\omega} \end{aligned} \tag{4.6}$$

and is a natural extension of equation (4.2).

$$H^{(n)}(j\omega_1, \ldots, j\omega_n) = \int_{-\infty}^{\infty} \ldots \int_{-\infty}^{\infty} h^{(n)}(\tau_1, \ldots, \tau_n) e^{-(\omega_1\tau_1+\cdots+\omega_n\tau_n)j} d\tau_1 \ldots \tau_n \tag{4.7}$$

represents the n^{th} order Generalized Frequency Response Function or n^{th} order transfer function and $\int_{\omega_1+\cdots+\omega_n=\omega} H^{(n)}_{(n_1,\ldots,n_m)}(j\omega_1 \ldots j\omega_n) \prod_{i=1}^{n} U(j\omega_i) d\tau_{n\omega}$ denotes the integration of $H^{(n)}_{(n_1,\ldots,n_m)}(j\omega_1 \ldots j\omega_n) \prod_{i=1}^{n} U(j\omega_i) d\tau_{n\omega}$ over the n-dimensional hyper-plane $\omega_1+\cdots+\omega_n = \omega$.

Compared to the linear case where only one transfer function describes a system in the frequency domain, for a nonlinear system the relationship between the input and output spectrum is described by an infinite number of frequency response functions. In practice however, the response can be approximated using a finite number of terms in the Volterra series, depending on the degree of nonlinearity. It follows that in practice only a finite number of GFRFs are significant and need to be considered (Zhang and Billings, 1993).

Define $n_0 = 0$, then

$$\begin{aligned} Y^{(n)}(j\omega) &= \frac{1}{2^{n-1}} \sum_{n_1+\cdots+n_m=n} \int_{\omega_1+\cdots+\omega_n=\omega} H^{(n)}_{(n_1,\ldots,n_m)}(j\omega_1 \ldots j\omega_n) \\ &\quad \prod_{j=1}^{m} \prod_{i=n_0+\cdots+n_{j-1}+1}^{n_0+\cdots+n_j}) U_j(j\omega_i) d\tau_{n\omega} \end{aligned} \tag{4.8}$$

Define

$$U^{(n)}_{(n_1,\ldots,n_m)}(j\omega) = \frac{1}{2^{n-1}} \int_{\omega_1+\cdots+\omega_n=\omega} \prod_{j=1}^{m} \prod_{i=n_0+\cdots+n_{j-1}+1}^{n_0+\cdots+n_j} U_j(j\omega_i) d\tau_{n\omega}$$

Then it follows that

$$\begin{aligned} Y^{(n)}_{(n_1,\ldots,n_m)}(j\omega) &= \frac{\int_{\omega_1+\cdots+\omega_n=\omega} (H^{(n)}_{(n_1,\ldots,n_m)}(j\omega_1,\ldots,j\omega_n) \times \prod_{j=1}^{m} \prod_{i=n_0+\ldots+n_{j-1}+1}^{n_0+\cdots+n_j} U_j(j\omega_i)) d\tau_{n\omega}}{\int_{\omega_1+\cdots+\omega_n=\omega} \prod_{j=1}^{m} \prod_{i=n_0+\ldots+n_{j-1}+1}^{n_0+\ldots+n_j} U_j(j\omega_i) d\tau_{n\omega})} \\ &\quad \times \frac{1}{2^{n-1}} \int_{\omega_1+\cdots+\omega_n=\omega} \prod_{j=1}^{m} \prod_{i=n_0+\ldots+n_{j-1}+1}^{n_0+\ldots+n_j} U_j(j\omega_i) d\tau_{n\omega} \end{aligned}$$

$$G^{(n)}_{(n_1,\ldots,n_m)}(j\omega) = \frac{\int_{\omega_1+\cdots+\omega_n=\omega} (H^{(n)}_{(n_1,\ldots,n_m)}(j\omega_1,\ldots,j\omega_n) \times \prod_{j=1}^{m} \prod_{i=n_0+\ldots+n_{j-1}+1}^{n_0+\cdots+n_j} U_j(j\omega_i)) d\tau_{n\omega}}{\int_{\omega_1+\cdots+\omega_n=\omega} \prod_{j=1}^{m} \prod_{i=n_0+\ldots+n_{j-1}+1}^{n_0+\ldots+n_j} U_j(j\omega_i)) d\tau_{n\omega}} \tag{4.9}$$

$$Y^{(n)}(j\omega) = \sum_{n_1+\cdots+n_m=n} G^{(n)}_{(n_1,\ldots,n_m)}(j\omega) U^{(n)}_{(n_1,\ldots,n_m)}(j\omega)$$

$G^{(n)}_{(n_1,\ldots,n_m)}(j\omega)$ will be referred to as the Nonlinear Output Frequency Response Function for multi-input nonlinear Volterra systems.

Using the equations derived above, equation (4.5) can be written in polynomial form as

$$\begin{aligned} Y(j\omega) &= \sum_{k_1=1}^{m} G_{k_1}^{(1)}(j\omega)[U_{k_1}(j\omega)] + \sum_{k_1=1}^{m}\sum_{k_2=k_1}^{m} G_{k_1k_2}^{(2)}(j\omega) \times [U_{k_1}(j\omega)U_{k_2}(j\omega)] + \ldots \\ &+ \sum_{k_1=1}^{m} \cdots \sum_{k_N=k_{N-1}}^{m} G_{k_1\ldots k_N}^{(N)}(j\omega)[U_{k_1}(j\omega)\ldots U_{k_N}(j\omega)], \end{aligned} \tag{4.10}$$

where

$$G_{(n_1,\ldots,n_m)}^{(n)}(j\omega) = G_{\underbrace{(1\ldots1)}_{n_1}\underbrace{(2\ldots2)}_{n_2}\ldots\underbrace{(m\ldots m)}_{n_m}}(j\omega)$$

with $n_1 + n_2 + \cdots + n_m = n$ and $n = 1, \ldots, N$ and

$$U_{(n_1,\ldots,n_m)}^{(n)}(j\omega) = \left[\underbrace{U_1(j\omega)\ldots U_1(j\omega)}_{n_1}\underbrace{U_2(j\omega)\ldots U_2(j\omega)}_{n_2}\ldots\underbrace{U_m(j\omega)\ldots U_m(j\omega)}_{n_m}\right]$$

$$Y(j\omega) = \sum\nolimits_{n=1}^{N} G_{(n_1,\ldots,n_m)}^{(n)}(j\omega)U_{(n_1,\ldots,n_m)}^{(n)}(j\omega) \tag{4.11}$$

In equation (4.11), $Y(j\omega)$ is defined in a similar manner to the description of the Output Frequency Response for linear systems given in equation (4.2).

The first, second and third order OFRs for nonlinear systems with three inputs and one output are as follows:

- First order ORFs: $Y_i^{(1)}(j\omega) = H_i^{(1)}(j\omega)U^{(1)}(j\omega)$, with $U^{(1)}(j\omega) = U_i(j\omega)$
- Second order ORFs: $Y_{ij}^{(2)}(j\omega) = \frac{1}{2}H_{ij}^{(2)}(j\omega_1, j\omega_2)U^{(2)}(j\omega)$, with $U^{(2)}(j\omega) = U_i(j\omega_1)U_j(j\omega_2)$
- Third order ORFs: $Y_{ijk}^{(3)}(j\omega) = \frac{1}{4}H_{ijk}^{(3)}(j\omega_1, j\omega_2, j\omega_3)U^{(3)}(j\omega)$, with

$U^{(3)}(j\omega) = U_i(j\omega_1)U_j(j\omega_2)U_k(j\omega_3)$.

In this example $i,\ j,\ k\ = 1, 2, 3$ and $H_i^1(j\omega)$ represent the first order GFRFs, $H_{ij}^2(j\omega_1, j\omega_2)$ are the second order GFRFs (*self-kernel* if $i = j$ and *cross-kernel* if $i \neq j$) and $H_{ijk}^3(j\omega_1, j\omega_2, j\omega_3)$ are the third order GFRFs (*self-kernel* if $i = j = k$ and *cross-kernel* otherwise).

The OFRs derivation rule and also the difference between the linear and nonlinear model cases is presented in Figure 4.2.

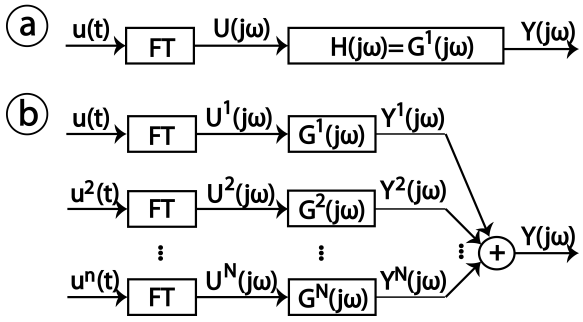

Figure 4.2: System output frequency representation using the OFRs, for: a. linear systems, b. nonlinear systems, where FT represents the frequency transform used.

4.3 Computation of the Generalized Frequency Response Functions using the Harmonic Probing Method

There are two methods for generating the GFRFs. The first refers to identifying the GFRFs from the input-output data (Kim and Powers, 1988, Tseng and Linebarger, 1991, Tseng and Powers, 1995). The disadvantage of this approach is that a considerable amount of data is required in order to accurately compute GFRFs of order higher than two even for a SISO system (Lang and Billings, 2000).

A better approach to obtaining the GFRFs, known as the ***harmonic probing*** method, allows deriving analytic expressions of GFRFs for parametric NARX models (Billings and Tsang, 1989a, Billings and Peyton Jones, 1990, Zhang and Billings, 1993, Swain et al., 2006).

4.3.1 Multi-tone inputs

In order to be able to apply the ***harmonic probing*** technique, the inputs of the system need to be re-written as n-tone inputs. It is assumed that all inputs have zero mean and that for $u = 0$ and $y = 0$ an asymptotically stable equilibrium for the system is reached.

For the multi-input Volterra series case with r inputs, the inputs are written as n-tone ones as (Liu et al., 2006) as:

$$\begin{cases} u_1(t) = e^{j\omega_1 t} + \ldots + e^{j\omega_{\gamma_1} t} \\ u_2(t) = e^{j\omega_{1+\gamma_1} t} + \ldots + e^{j\omega_{\gamma_1+\gamma_2} t} \\ \vdots \\ u_r(t) = e^{j\omega_{1+\gamma_1+\ldots+\gamma_{(r-1)}} t} + \ldots + e^{j\omega_n t} \end{cases} \tag{4.12}$$

For example, for a system with 2 inputs ($r = 2$), in order to calculate the 3^{rd} order GFRFs ($n = 3$), the inputs can be written in four ways, such as:

a. $u_1(t) = 0$ and $u_2(t) = e^{j(\omega_1+\omega_2+\omega_3)t}$, which will give $H^3_{222}(j\omega_1, j\omega_2, j\omega_3)$

b. $u_2(t) = e^{j\omega_1 t}$ and $u_2(t) = e^{j(\omega_1+\omega_2)t}$, which will give $H^3_{122}(j\omega_1, j\omega_2, j\omega_3)$

c. $u_1(t) = e^{j(\omega_1+\omega_2)t}$ and $u_2(t) = e^{j\omega_3 t}$, which will give $H^3_{112}(j\omega_1, j\omega_2, j\omega_3)$

d. $u_1(t) = e^{j(\omega_1+\omega_2+\omega_3)t}$ and $u_2(t) = 0$, which will give $H^3_{111}(j\omega_1, j\omega_2, j\omega_3)$

4.3.2 Symmetric and Averaged Generalized Transforms

In the case of SISO systems and MIMO systems *self-kernel* transforms, the GFRFs are computed by taking the average over all frequency arguments possible for each frequency combination of the *asymmetric* GFRFs.

For any given system, both $H^{(n)}(\cdot)$ and $h^n(\cdot)$ may not be unique since changing the order of

argument may give different function but will still yield the same output $y^{(n)}(t)$. These functions are called *symmetric* functions and they have the property that $H^{(n)}(-j\omega_1, \ldots, -j\omega_n) = H^{(n)*}(j\omega_1, \ldots, j\omega_n)$. $H^{(n)*}$ is called the *complex conjugate* transfer function (Zhang and Billings, 1993).

The common practice is to symmetrize the functions by summing all the asymmetric functions over all the permutations of the arguments and dividing by their number. That is

$$H^{(n)_{sym}}(j\omega_1, \ldots, j\omega_n) = \frac{1}{n!} \sum_{all\ permutation\ of\ \omega_1,\ldots,\omega_n} H^{(n)}(j\omega_1, \ldots, j\omega_n)$$

For example, the asymmetric GFRFs corresponding to the symmetric third order self-kernel transfer function $H^3_{111}(j\omega_1, j\omega_2, j\omega_3)$ are:

$$\begin{array}{lll} H^3_{111}(j\omega_1, j\omega_2, j\omega_3), & H^3_{111}(j\omega_2, j\omega_1, j\omega_3), & H^3_{111}(j\omega_3, j\omega_1, j\omega_2), \\ H^3_{111}(j\omega_1, j\omega_3, j\omega_2), & H^3_{111}(j\omega_2, j\omega_3, j\omega_1), & H^3_{111}(j\omega_3, j\omega_2, j\omega_1). \end{array}$$

For MIMO systems cross-kernel transformations however, the *averaged generalized kernel transform* needs to be computed (Billings and Swain, 2000), due to the fact that cross-kernels do not have the symmetry property. This can be obtained by taking $[\omega, \beta]$ permutations of the asymmetric kernel. For example for the second order cross-kernel, this means that $H^2_{\beta_1,\beta_2}(j\omega_1, j\omega_2)$ may not be equal to $H^2_{\beta_2,\beta_1}(j\omega_2, j\omega_1)$ (Swain and Billings, 2001). So, understanding the $[\omega, \beta]$ permutation is very important for deriving the *averaged generalized kernel transforms*. In the case of MIMO systems, the n-tone inputs are not applied at a single input point, but is split at various input points. In order to correctly obtain the GFRFs it is therefore fundamental to carefully identify in the n-tone defined input in equation (4.12), the frequencies $\{\omega_1, \ldots, \omega_{\gamma_1}\}$ as belonging to the input point β_1, $\omega_{1+\gamma_1}, \ldots, \omega_{\gamma_1+\gamma_2}$ as belonging to the input point β_2 and so on (Billings and Swain, 2000).

4.3.3 The $[\omega, \beta]$ permutation

The averaged GFRF is computed by permuting ω and β together so that if the frequency ω_i, belonging to the input point β_i, is permutated to say ω_k, β_i must change to β_k such that $e^{j\omega_k t}$ belongs to the input point β_k. This means that for $i = 1$ and $k = 2$, when ω_1 is permutated to

ω_2, the subscripts of the transfer function will also change from $H^2_{12}(j\omega_1, \omega_2)$ to $H^2_{21}(j\omega_2, \omega_1)$.

This shows that the arguments of the cross-kernel functions are not independent of the subscripts of the kernels and that they depend on the $[\omega, \beta]$ permutation. This allows the generalized transform to be defined as

$$H^{(n)_{avg}}_{\underbrace{(\beta_1,\dots)}_{\gamma_1 times},\underbrace{(\beta_2,\dots)}_{\gamma_2 times},\underbrace{(\beta_d,\dots)}_{\gamma_d times}}(j\omega_1,\dots,j\omega_n) = \frac{1}{n!}\sum_{all permutations [\omega,\beta]} H^{(n)}_{\underbrace{(\beta_1,\dots)}_{\gamma_1 times},\underbrace{(\beta_2,\dots)}_{\gamma_2 times},\underbrace{(\beta_d,\dots)}_{\gamma_d times}}(j\omega_1,\dots,j\omega_n)$$

where d = number of distinct inputs that take part in the n-dimensional convolution,

γ_1= number of times $u_{\beta_1}(t)$ takes part in the n-dimensional convolution, and γ_d= number of times $u_{\beta_d}(t)$ takes part in the n-dimensional convolution.

The procedure for the $[\omega, \beta]$ permutation, given the explanation above, involves the following steps (Billings and Swain, 2000):

1. Define β and ω as $\beta = [\delta_1, \delta_2, \dots, \delta_n]$, $\omega = [\omega_1, \omega_2, \dots, \omega_n]$ so that the frequencies $\omega_i,\ i = 1, \dots, n$ of the input $u(t)$ are associated with the corresponding input points $\delta_i,\ i = 1. \dots, n$.

2. Consider the pair (ω_i, δ_i) as a single entity so that the GFRF contains n such pairs $[(\omega_i, \delta_i), \dots, (\omega_n, \delta_n)]$.

3. Compute the permutations over $(\omega_i, \delta_i),\ i = 1, \dots, n$, and average to give the averaged GFRF as:

$$\begin{aligned} H^{(n)_{avg}}_{\beta}(j\omega) &= \frac{1}{n!}\sum_{all\ permutations\ of\ [\omega,\beta]} H^{(n)}_{\underbrace{\beta_1,\dots}_{\gamma_1 times},\underbrace{\beta_2,\dots}_{\gamma_2 times},\dots,\underbrace{\beta_d,\dots}_{\gamma_d times}} \\ &= \frac{1}{n!}\sum_{all\ permutations\ of\ (\omega_1,\delta_1),\dots,(\omega_n,\delta_n)} H^{(n)}_{\delta_1,\dots,\delta_n}(j\omega_1,\dots,j\omega_n) \end{aligned}$$

When $n = 2$ the averaged transfer function is:

$$2! H^{2_{avg}}_{12}(j\omega_1, j\omega_2) = [H^2_{12}(j\omega_1, j\omega_2) + H^2_{21}(j\omega_2, j\omega_1)]e^{j(\omega_1+\omega_2)t}$$

This procedure is illustrated with an example of a model with 3 inputs $u_i(t)$, $u_l(t)$ and $u_k(t)$ for which the GFRFs up to the order $n = 3$ are calculated. The GFRFs identified in this example are the ones derived for the palaeoclimate NARMAX models obtained in Chapter 5.

- for the ***first order*** GFRFs $H_i^1(j\omega_1)$, the inputs are $u_i(t) = e^{j\omega_1 t}$, $u_l(t) = 0$ and $u_k(t) = 0$ with $i, l, k = 1, \ldots, 3, i \neq l \neq k$ and the output is $y(t) = H_i^1(j\omega_1)e^{j\omega_1 t}$.

- for the ***second order self-kernels*** GFRFs $H_{ii}^2(j\omega_1, j\omega_2)$, the inputs are $u_i(t) = e^{j(\omega_1+\omega_2)t}$, $u_l(t) = 0$ and $u_k(t) = 0$ with $i, l, k = 1, \ldots, 3, i \neq l \neq k$ and the output is

$$y(t) = H_i^1(j\omega_1)e^{j\omega_1 t} + H_i^1(j\omega_2)e^{j\omega_2 t} + 2H_{ii}^2(j\omega_1, j\omega_2)e^{j(\omega_1+\omega_2)t}$$

- for the ***second order cross-kernels*** GFRFs $H_{il}^2(j\omega_1, j\omega_2)$, the inputs are $u_i(t) = e^{j\omega_1 t}$, $u_l(t) = e^{j\omega_2 t}$ and $u_k(t) = 0$, with $i, l, k = 1, \ldots, 3, i \neq l \neq k$ and the output is

$$y(t) = H_i^1(j\omega_1)e^{j\omega_1 t} + H_l^1(j\omega_2)e^{j\omega_2 t} + 2!H_{il}^{2_{avg}}(j\omega_1, j\omega_2)e^{j(\omega_1+\omega_2)t}$$

- for the ***third order self-kernels*** GFRFs $H_{iii}^3(j\omega_1, j\omega_2, j\omega_3)$, the inputs are $u_i(t) = e^{j(\omega_1+\omega_2+\omega_3)t}$, $u_l(t) = 0$ and $u_k(t) = 0$, with $i, l, k = 1, \ldots, 3, i \neq l \neq k$ and the output is

$$\begin{aligned} y(t) &= H_i^1(j\omega_1)e^{j\omega_1 t} + H_i^1(j\omega_2)e^{j\omega_2 t} + H_i^1(j\omega_3)e^{j\omega_3 t} \\ &+ 2!H_{ii}^2(j\omega_1, j\omega_2)e^{j(\omega_1+\omega_2)t} + 2!H_{ii}^2(j\omega_1, j\omega_3)e^{j(\omega_1+\omega_3)t} + 2!H_{ii}^2(j\omega_2, j\omega_3)e^{j(\omega_2+\omega_3)t} \\ &+ 3!H_{iii}^3(j\omega_1, j\omega_2, j\omega_3)e^{j(\omega_1+\omega_2+\omega_3)t}. \end{aligned}$$

- the ***third order cross-kernels*** are of two types, where the inputs are

  - $u_i(t) = e^{j(\omega_1+\omega_2)t}$, $u_l(t) = e^{j\omega_3 t}$, $u_k(t) = 0$, with $i, l, k = 1, \ldots, 3, i \neq l \neq k$. In this case the GFRFs to be estimated are $H_{iil}^{3_{avg}}(j\omega_1, j\omega_2, j\omega_3)$ and the output is

$$\begin{aligned} y(t) &= H_i^1(j\omega_1)e^{j\omega_1 t} + H_i^1(j\omega_2)e^{j\omega_2 t} + H_l^1(j\omega_3)e^{j\omega_3 t} \\ &+ 2!H_{ii}^2(j\omega_1, j\omega_2)e^{j(\omega_1+\omega_2)t} + 2!H_{il}^2(j\omega_1, j\omega_3)e^{j(\omega_1+\omega_3)t} + 2!H_{il}^2(j\omega_2, j\omega_3)e^{j(\omega_2+\omega_3)t} \\ &+ 3!H_{iil}^{3_{avg}}(j\omega_1, j\omega_2, j\omega_3)e^{j(\omega_1+\omega_2+\omega_3)t} \end{aligned}$$

– $u_i(t) = e^{j\omega_1 t}$, $u_l(t) = e^{j\omega_2 t}$, $u_k(t) = e^{j\omega_3 t}$, with $i, l, k = 1, \ldots, 3, i \neq l \neq k$. In this case the GFRFs to be estimated are $H^{3_{avg}}_{ilk}(j\omega_1, j\omega_2, j\omega_3)$ and output is

$$\begin{aligned} y(t) &= H^1_i(j\omega_1)e^{j\omega_1 t} + H^1_l(j\omega_2)e^{j\omega_2 t} + H^1_k(j\omega_3)e^{j\omega_3 t} \\ &+ 2!H^2_{il}(j\omega_1, j\omega_2)e^{j(\omega_1+\omega_2)t} + 2!H^2_{ik}(j\omega_1, j\omega_3)e^{j(\omega_1+\omega_3)t} + 2!H^2_{lk}(j\omega_2, j\omega_3)e^{j(\omega_2+\omega_3)t} \\ &+ 3!H^{3_{avg}}_{ilk}(j\omega_1, j\omega_2, j\omega_3)e^{j(\omega_1+\omega_2+\omega_3)t} \end{aligned}$$

The procedure for recursively computing the n^{th} order GFRFs starts by writing the n-tone inputs as in equation (4.12). Next, the inputs and output for each type of computed GFRFs are replaced into the NARMAX model equations given by $y(t)$, as explained in the example above. Finally, the coefficients of $e^{j(\omega_1+\cdots+\omega_n)t}$ are extracted.

Next an explanation of the contribution to the GFRF results of each type of terms in NARMAX polynomial models is given (Swain and Billings, 2001). For each category a description of the term, its contribution to the transfer functions and a brief clarifying example is given. The three possible terms that can appear in a polynomial model are: *pure input*, *pure output* and *input-output product* terms. Tables explaining the contribution of every kind of term in the third order NARMAX model are given in Appendix B.

4.3.4 Pure Input Terms

The pure input type terms for a MISO model are of the form

$$c_{0q_1\ldots q_r}(k_{l_1}, \ldots, k_{l_r}) \prod_{i=1}^{q_1} u_1(t - k_{l_i}) \cdots \prod_{i=r_{r-1}+1}^{q_r} u_r(t - k_{l_i})$$

The relevant contribution of this type of terms to the n^{th} order GFRFs results is given by the expression (Swain et al., 2006):

$$\sum_{all\ permutation\ of\ \omega_1,\ldots,\omega_n} e^{-j(\omega_1 k_{l_1}+\cdots+\omega_n k_{l_n})}$$

The condition for this to be true is that $q_1 + \cdots + q_r = n$. If this condition is not satisfied, the contribution of the term is 0.

For example if the term in the model is $c_{02}(k_1k_2)u(t-k_1)u(t-k_2)$, its contribution to the 2^{nd} order GFRF expression will be given by

$$c_{02}(12)[e^{-j(\omega_1 k_1+\omega_2 k_2)}+e^{-j(\omega_1 k_2+\omega_2 k_1)}]$$

4.3.5 Pure Output Terms

Pure output terms are written as

$$c_{p0\ldots0}(k_{l_1},\ldots,k_{l_p})\prod_{i=1}^{p}y(t-k_{l_i})$$

In this case the contribution to the GFRF results is estimated recursively as

$$\sum_{i=1}^{n-p+1}H^i_{n-p+1}(j\omega_1,\ldots,j\omega_i)H^{n-i}_{p-1}(j\omega_{i+1},\ldots,j\omega_n)e^{-j(\omega_1+\cdots+\omega_i)k_{l_p}}$$

with $p<n$.

The recursive procedure finishes with $p=1$ and $H^{(n,1)}(j\omega_1,\ldots,j\omega_n)$ has the property

$$H^{(n,1)}=H^{(n)}(j\omega_1,\ldots,j\omega_n)e^{-j(\omega_1+\cdots+\omega_n)k_{l_1}}$$

For example for a term having the form $c_{20\ldots0}(k_1k_2)y(t-k_1)y(t-k_2)$, assuming the system has a single input split as a 2-tone signal $u(t)=e^{j\omega_1 t}+e^{j\omega_2 t}$, the relevant contribution to the 2^{nd} order GFRF is given by

$$c_{20\ldots0}(12)[H^1_1(j\omega_1)H^1_1(j\omega_2)e^{-j(\omega_1k_1+\omega_2k_2)}+H^1_1(j\omega_2)H^1_1(j\omega_1)e^{j-(\omega_1k_2+\omega_2k_1)}]$$

It can be easily seen from this expression how the higher order GFRFs are recursively computed.

4.3.6 Input - Output Cross Terms

The terms in this class can be expressed as:

$$c_{pq_1\ldots q_r}(k_{l_1}\ldots k_{l_{p+q_1+\cdots+q_r}})\prod_{i=1}^{p}y(t-l_{l_i})\prod_{i=p+1}^{q_1}u_1(t-k_{l_i})\cdots\prod_{i=q_{r-1}+1}^{q_r}u_r(t-k_{l_i})$$

The contribution of this kind of terms to the n^{th} order GFRF, under the condition that $p+q_1+\cdots+q_r\leq n$, is given by the expression:

$$\sum_{q=1}^{n-1}\sum_{l_1,\ldots,l+p+q=0}^{L}e^{-j(\omega_{n-q+1}k_{l+p+1}+\cdots+\omega_n k_{l_{p+q}})}H_p^{n-q}(j\omega_1,\ldots,j\omega_{n-q})$$

For an example term given by $c_{11}(k_1k_2)y(t-k_1)u(t-k_2)$, the contribution to a 2^{nd} order GFRF, when the single input is split as a 2-tone $u(t)=e^{j\omega_1 t}+e^{j\omega_2 t}$, results from:

$$c_{11}(k_1k_2)[H_1^1(j\omega_1)e^{-j(\omega_1k_1+\omega_2k_2)}+H_1^1(j\omega_2)e^{-j(\omega_1k_2+\omega_2k_1)}]$$

Again the recursive nature of the higher-order transfer function is well emphasized by this example.

4.3.7 Data and Model Pre-Processing

The recursive probing algorithm presented in the sub-sections above is defined for a NARMAX models with zero mean inputs and without an internal constant. In practice however, the estimated model using the input-output data-set usually does not meet this criteria, and this is why further model processing techniques need to be applied.

When working with a set of inputs that have very different ranges, it is common practice to remove the mean of each input signal in order to bring all variables in proportion to each other. So removing the mean basically means centring the data. When the data is not corrected in this manner, the effects of each of the inputs on the system output are more difficult to interpret. This is clearly the case of the three orbital parameters inputs to the estimated NARMAX model, which have the means $\overline{u}_1=0.03$, $\overline{u}_2=23.34$ and $\overline{u}_3=181.96$.

Unlike the linear systems, where usually DC terms can be discarded without influencing the system behaviour (Astrom, 1980, Isermann, 1980), for nonlinear systems the DC term can be coupled within the recursive response of the system, and given the superposition principle is not applicable, simply discarding the term is not possible (Peyton-Jones and

Billings, 1993). A DC component usually appears due to a non-zero equilibrium state of the model.

A DC term present in the model brings various disadvantages to a recursively generated model. The behaviour of the system is affected by the increased number of additional terms and recursions (Peyton Jones and Choudharya, 2012). Early NARMAX algorithms did not consider systems with DC terms or just discarded them, but the extensions by Zhang and Billings (1993) and Peyton-Jones and Billings (1993) address this problem. The presence of an internal system constant also affects the frequency domain response and will give biased results in the analysis.

This subsection presents techniques used for working with zero mean inputs and for removing the internal constant for a NARX model defined as:

$$y(t) = f_0(y(t-1), \ldots, y(t-N_y), u_1(t-1), \ldots, u_1(t-N_{u_1}), \ldots, u_r(t-1), \ldots, u_r(N_{u_r})) \quad (4.13)$$

The NARMAX model is written in an alternative form by introducing the auxiliary input variables $\widetilde{u}_i(t)$ as $\widetilde{u}_i(t) = u_i(t) - \overline{u}_i$, where $\overline{u}_i$ represents the mean value of $u_i(t)$, which for a data-set of N points is given by $\overline{u}_i = \frac{1}{N}\sum_{j=1}^{N} u_{ij}(t)$.

Substituting $u_i(t) = \widetilde{u}_i(t) + \overline{u}_i$in equation (4.13), gives the following equivalent description:

$$\begin{aligned} y(t) &= f_0(y(t-1), \ldots, y(t-N_y), \widetilde{u}_1(t-1) + \overline{u}_1, \ldots, \widetilde{u}_1(t-N_{u_1}) + \overline{u}_1, \\ &\quad \ldots \widetilde{u}_r(t-1) + \overline{u}_r, \ldots, \widetilde{u}_r(t-N_{u_r}) + \overline{u}_r) \end{aligned} \quad (4.14)$$

Usually, the DC component is considered to be an additive term to the model, as: $\widetilde{y}(t) = y(t) + y_0$, where y_0 represents the system's internal constant (Peyton Jones and Choudharya, 2012). In order to remove the internal constant, at this stage $c\ \underbrace{00\ldots0}_{(r+1)\ times}$, equation (4.13) is re-written by making the variable substitution $y(t) = \widetilde{y}(t) - y_0$, as:

$$\begin{aligned} y(t) - y_0 &= f_0(y(t-1) - y_0, \ldots, y(t-N_y) - y_0, u_1(t-1), \ldots, u_1(t-N_{u_1}), \\ &\quad \ldots, u_r(t-1), \ldots, u_r(t-N_{u_r})) \end{aligned} \tag{4.15}$$

In this case as well, the model's terms need to be rearranged and the coefficients recalculated. This procedure will also introduce new terms, but these will not change the system behaviour and model's response, but only its structure.

The value of the internal constant is found as the solution to $c^*_{\underbrace{00\ldots0}_{(r+1)\,times}} = 0$, where $c^*_{\underbrace{00\ldots0}_{(r+1)\,times}}$ is the newly calculated value for the constant term.

Example

Next an example illustrating the two model changes explained above is given. The second degree of nonlinearity model with two inputs is considered as:

$$y(t) = 2y(t-1) + u_1(t-1)u_2(t-2) + 3y(t-2)u_1(t-2) + 2u_2(t-1) - 5 \tag{4.16}$$

For this example consider: $\overline{u}_1 = 3$ and $\overline{u}_2 = 2$. The identified model coefficients according to (4.16) are:

$$c_{100}(1) = 2 \qquad c_{001}(1) = 2$$

$$c_{011}(12) = 1 \qquad c_{000} = -5$$

$$c_{110}(22) = 3$$

Step1 - zero mean inputs

As detailed in Section 4.3.7 in order to have a model with zero mean inputs, the model needs to go through the variable changes: $u_1(t) = \widetilde{u}_1(t) + \overline{u}_1$ and $u_2(t) = \widetilde{u}_2(t) + \overline{u}_2$. The model in example (4.16) becomes:

$$\begin{aligned} y(t) &= 2y(t-1) + \widetilde{u}_1(t-1)\widetilde{u}_2(t-2) + \overline{u}_1\widetilde{u}_2(t-2) + \overline{u}_2\widetilde{u}_1(t-1) \\ &\quad +3y(t-2)\widetilde{u}_1(t-2) + 3\overline{u}_1 y(t-2) + 2\widetilde{u}_2(t-1) + \overline{u}_1\overline{u}_2 + 2\overline{u}_2 - 5 \end{aligned} \tag{4.17}$$

By rearranging the terms and recalculating the coefficients after substituting in the values of the input signals means, equation (4.17) becomes:

$$\begin{aligned} y(t) &= 2y(t-1) + 9y(t-2) + 3y(t-2)\tilde{u}_1(t-2) + \tilde{u}_1(t-1)\tilde{u}_2(t-2) \\ &\quad +2\tilde{u}_1(t-1) + 2\tilde{u}_2(t-1) + 3\tilde{u}_2(t-2) + 5 \end{aligned} \tag{4.18}$$

The new recalculated coefficients are:

$$c^*_{100}(1) = 2 \qquad c^*_{011}(12) = 1 \qquad c^*_{001}(2) = 3$$

$$c^*_{100}(2) = 9 \qquad c^*_{010}(1) = 2 \qquad c^*_{000} = 5$$

$$c^*_{110}(22) = 3 \qquad c^*_{001}(1) = 2$$

Three new coefficients, corresponding to three new terms, appear in the expansion in equation (4.18) as: $c^*_{100}(2)$, $c^*_{010}(1)$ and $c^*_{001}(2)$. The coefficient c_{000} has changed its value and was reassigned as c^*_{000}.

Step 2 - removing the internal constant

The model needs to be re-written with the variable change $y(t) = \tilde{y}(t) - y_0$ as explained in sub-section 4.3.7. In this case, the model equation (4.18) after the substitution and terms rearrangement, becomes:

$$\begin{aligned} \tilde{y}(t) &= 2\tilde{y}(t-1) + 9\tilde{y}(t-2) + 3\tilde{y}(t-2)\widetilde{u}_1(t-2) + \widetilde{u}_1(t-1)\widetilde{u}_2(t-2) \\ &\quad +2\widetilde{u}_1(t-1) - 3y_0\widetilde{u}_1(t-2) + 2\widetilde{u}_2(t-1) + 3\widetilde{u}_2(t-2) - 10y_0 + 5 \end{aligned} \tag{4.19}$$

y_0 is calculated from $c^{**}_{000} = 0$, so $-10y_0 + 5 = 0$. This gives the value $y_0 = 0.5$. By substituting this into the output model in equation (4.19) gives

$$\begin{aligned}\tilde{y}(t) &= 2\tilde{y}(t-1) + 9\tilde{y}(t-2) + 3\tilde{y}(t-2)\widetilde{u}_1(t-2) + \widetilde{u}_1(t-1)\widetilde{u}_2(t-2) \\ &\quad +2\widetilde{u}_1(t-1) - 1.5\widetilde{u}_1(t-2) + 2\widetilde{u}_2(t-1) + 3\widetilde{u}_2(t-2)\end{aligned}$$

The new coefficients are:

$$c^{**}_{100}(1) = 2 \qquad c^{**}_{011}(12) = 1 \qquad c^{**}_{001}(1) = 2$$

$$c^{**}_{100}(2) = 9 \qquad c^{**}_{010}(1) = 2 \qquad c^{**}_{001}(2) = 3$$

$$c^{**}_{110}(22) = 3 \qquad c^{**}_{010}(2) = -1.5 \qquad c^{**}_{000} = 0$$

It can be seen that compared to equation (4.18), one extra term is also introduced by this procedure.

4.4 Computation of the n^{th} Output Frequency Responses

Because of their dimensionality the GFRFs of order higher than three are difficult to visualise and interpret (Yue et al., 2005). In practice however, the first, second and third order transfer functions are often sufficient to characterize the system in the frequency domain (Zhang and Billings, 1993). Given the GFRFs are multi-dimensional functions they are difficult to interpret. In contrast, the OFRs, which are functions of a single complex variable, characterize completely the contribution made by the input to the output spectrum, through a particular GFRF. The evaluation of the OFRs requires knowledge of the GFRFs $H^{(n)}(j\omega_1, \ldots, j\omega_n)$ and the input spectrum $U_j(j\omega_i)$, $j = 1, \ldots, r$.

In order to obtain the nonlinear OFRs, the product of GFRFs and input spectrum needs to be integrated over the hyper-plane $\omega_1 + \cdots + \omega_n = \omega$, as shown by equation (4.8). This is computed for each output frequency ω of the output spectrum $Y(j\omega)$. The way each of the

input frequencies contribute to the OFR value at each output frequency for the second order function is illustrated in Figure 4.3 and explained in what follows.

In practice, the integration is replaced by a summation because the discrete Fourier Transform is computed. This means that equation (4.8) is replaced by:

$$Y^{(n)}(j\omega) = \frac{1}{2^{n-1}} \sum_{n_1+\cdots+n_m=n} \sum_{\omega_1+\cdots+\omega_n=\omega} H^{(n)}_{(n_1,\ldots,n_m)}(j\omega_1 \ldots j\omega_n) \prod_{j=1}^{m} \prod_{i=n_0+\cdots+n_{j-1}+1}^{n_0+\cdots+n_j} U_j(j\omega_i) d\tau_{n\omega} \tag{4.20}$$

For a third order system the output spectrum in equation (4.5) is written as:

$$Y(j\omega) = Y^1(j\omega) + Y^2(j\omega) + Y^3(j\omega) \tag{4.21}$$

By writing equation (4.20) for a third order nonlinear system with three inputs, each of the output frequency responses $Y^{(n)}(j\omega)$ in equation (4.21) is written as:

$$
\begin{cases}
Y^1(j\omega) = \sum\limits_{\omega_1=\omega} H_1^1(j\omega_1)U_1(j\omega_1) + \sum\limits_{\omega_1=\omega} H_2^1(j\omega_1)U_2(j\omega_1) + \sum\limits_{\omega_1=\omega} H_3^1(j\omega_1)U_3(j\omega_1) \\
\\
\begin{aligned}
Y^2(j\omega) = {} & \tfrac{1}{2}\sum\limits_{\omega_1+\omega_2=\omega} H_1^2(j\omega_1, j\omega_2)U_1(j\omega_1)U_1(j\omega_2) + \tfrac{1}{2}\sum\limits_{\omega_1+\omega_2=\omega} H_2^2(j\omega_1, j\omega_2)U_2(j\omega_1)U_2(j\omega_2) \\
& + \tfrac{1}{2}\sum\limits_{\omega_1+\omega_2=\omega} H_3^2(j\omega_1, j\omega_2)U_3(j\omega_1)U_3(j\omega_2) + \tfrac{1}{2}\sum\limits_{\omega_1+\omega_2=\omega} H_{12_{avg}}^2(j\omega_1, j\omega_2)U_1(j\omega_1)U_2(j\omega_2) \\
& + \tfrac{1}{2}\sum\limits_{\omega_1+\omega_2=\omega} H_{13_{avg}}^2(j\omega_1, j\omega_2)U_1(j\omega_1)U_3(j\omega_2) + \tfrac{1}{2}\sum\limits_{\omega_1+\omega_2=\omega} H_{23_{avg}}^2(j\omega_1, j\omega_2)U_2(j\omega_1)U_3(j\omega_2)
\end{aligned} \\
\\
\begin{aligned}
Y^3(j\omega) = {} & \tfrac{1}{4}\sum\limits_{\omega_1+\omega_2+\omega_3=\omega} H_1^3(j\omega_1, j\omega_2, j\omega_3)U_1(j\omega_1)U_1(j\omega_2)U_1(j\omega_3) \\
& + \tfrac{1}{4}\sum\limits_{\omega_1+\omega_2+\omega_3=\omega} H_2^3(j\omega_1, j\omega_2, j\omega_3)U_2(j\omega_1)U_2(j\omega_2)U_2(j\omega_3) \\
& + \tfrac{1}{4}\sum\limits_{\omega_1+\omega_2+\omega_3=\omega} H_3^3(j\omega_1, j\omega_2, j\omega_3)U_3(j\omega_1)U_3(j\omega_2)U_3(j\omega_3) \\
& + \tfrac{1}{4}\sum\limits_{\omega_1+\omega_2+\omega_3=\omega} H_{112_{avg}}^3(j\omega_1, j\omega_2, j\omega_3)U_1(j\omega_1)U_1(j\omega_2)U_2(j\omega_3) \\
& + \tfrac{1}{4}\sum\limits_{\omega_1+\omega_2+\omega_3=\omega} H_{122_{avg}}^3(j\omega_1, j\omega_2, j\omega_3)U_1(j\omega_1)U_2(j\omega_2)U_2(j\omega_3) \\
& + \tfrac{1}{4}\sum\limits_{\omega_1+\omega_2+\omega_3=\omega} H_{113_{avg}}^3(j\omega_1, j\omega_2, j\omega_3)U_1(j\omega_1)U_1(j\omega_2)U_3(j\omega_3) \\
& + \tfrac{1}{4}\sum\limits_{\omega_1+\omega_2+\omega_3=\omega} H_{133_{avg}}^3(j\omega_1, j\omega_2, j\omega_3)U_1(j\omega_1)U_3(j\omega_2)U_3(j\omega_3) \\
& + \tfrac{1}{4}\sum\limits_{\omega_1+\omega_2+\omega_3=\omega} H_{223_{avg}}^3(j\omega_1, j\omega_2, j\omega_3)U_2(j\omega_1)U_2(j\omega_2)U_3(j\omega_3) \\
& + \tfrac{1}{4}\sum\limits_{\omega_1+\omega_2+\omega_3=\omega} H_{233_{avg}}^3(j\omega_1, j\omega_2, j\omega_3)U_2(j\omega_1)U_3(j\omega_2)U_3(j\omega_3) \\
& + \tfrac{1}{4}\sum\limits_{\omega_1+\omega_2+\omega_3=\omega} H_{123_{avg}}^3(j\omega_1, j\omega_2, j\omega_3)U_1(j\omega_1)U_2(j\omega_2)U_3(j\omega_3)
\end{aligned}
\end{cases}
\tag{4.22}
$$

Equation (4.22) is written in compact form as:

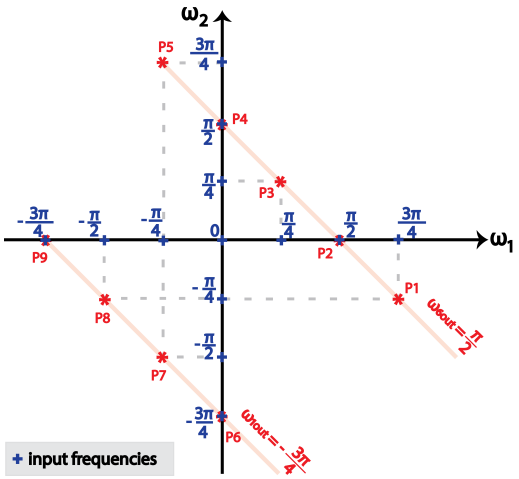

Point	Term in summation $Y^2(j\omega_{lout})=\sum_{\omega_1+\omega_2=\omega_{lout}} H^2(j\omega_1,j\omega_2)U(j\omega_1)U(j\omega_2)$	Result
P1	$H^2(j\frac{3\pi}{4},j\text{-}\frac{\pi}{4})U(j\frac{3\pi}{4})U(j\text{-}\frac{\pi}{4})$	
P2	$H^2(j\frac{\pi}{2},j0)U(j\frac{\pi}{2})U(j0)$	
P3	$H^2(j\frac{\pi}{4},j\frac{\pi}{4})U(j\frac{\pi}{4})U(j\frac{\pi}{4})$	$Y^2(j\omega_{6out})$
P4	$H^2(j0,j\frac{\pi}{2})U(j0)U(j\frac{\pi}{2})$	
P5	$H^2(j\text{-}\frac{\pi}{4},j\frac{3\pi}{4})U(j\text{-}\frac{\pi}{4})U(j\frac{3\pi}{4})$	
P6	$H^2(j0,j\text{-}\frac{3\pi}{4})U(j0)U(j\text{-}\frac{3\pi}{4})$	
P7	$H^2(j\text{-}\frac{\pi}{4},j\text{-}\frac{\pi}{2})U(j\text{-}\frac{\pi}{4})U(j\text{-}\frac{\pi}{2})$	
P8	$H^2(j\text{-}\frac{\pi}{2},j\text{-}\frac{\pi}{4})U(j\text{-}\frac{\pi}{2})U(j\text{-}\frac{\pi}{4})$	$Y^2(j\omega_{1\,out})$
P9	$H^2(j\text{-}\frac{3\pi}{4},j0)U(j\text{-}\frac{3\pi}{4})U(j0)$	

Figure 4.3: Combinations of frequencies $\omega_1+\omega_2=\omega_{iout}$ contributing to $Y^2(j\omega_{iout})$.

$$\begin{cases} Y^1(j\omega) = Y_1^1(j\omega)+Y_2^1(j\omega)+Y_3^1(j\omega) \\ Y^2(j\omega) = Y_1^2(j\omega)+Y_2^2(j\omega)+Y_3^2(j\omega)+Y_{12}^2(j\omega)+Y_{13}^2(j\omega)+Y_{23}^2(j\omega) \\ Y^3(j\omega) = Y_1^3(j\omega)+Y_2^3(j\omega)+Y_3^3(j\omega)+Y_{112}^3(j\omega)+Y_{122}^3(j\omega)+Y_{113}^3(j\omega)+Y_{133}^3(j\omega) \\ \quad +Y_{223}^3(j\omega)+Y_{233}^3(j\omega)+Y_{123}^3(j\omega) \end{cases} \tag{4.23}$$

In order to calculate the value of each Output Frequency Response $Y^{(n)}_{(n_1\ldots n_m)}(j\omega)$ with $n_1+\cdots+n_m=n$, all the frequency $\omega_1,\ldots,\omega_n$ contributing to each of the output frequencies $\omega=\omega_1+\cdots+\omega_n$ need to be determined. .

The procedure is illustrated in Figure 4.3 for a second order response $Y^2_{n_1n_2}(j\omega)$ and for a two-tone input given by the sum $u(t)=e^{j\omega_1 t}+e^{j\omega_2 t}$, $\omega_{1,2}=\{-\frac{3\pi}{4}-\frac{\pi}{2},-\frac{\pi}{4},0,\frac{\pi}{4},\frac{\pi}{2},\frac{3\pi}{4}\}$. For the given input, the output spectrum will be evaluated for all the frequencies $\omega_{i_{out}}=\omega_1+\omega_2$.

The full methodology for deriving the GFRFs and OFRs of a nonlinear dynamical system can be summarized as follows:

1. Identify a polynomial NARMAX model from data.

2. Compute the discrete Fourier Transforms $U_i(j\omega)$ and $Y(j\omega)$ of the input and outputs, respectively.

3. Compute the GFRFs $H^{(n)}(j\omega_1, \ldots, j\omega_n)$ using the probing approach.

4. Compute the OFRs of different orders $Y^{(n)}(j\omega_k)$.

5. Compute the combined OFR $Y(j\omega)$ corresponding to the GFRFs evaluated in step 3.

The time domain model estimation and frequency domain analysis of the NARMAX model is summarized in Figure 4.4.

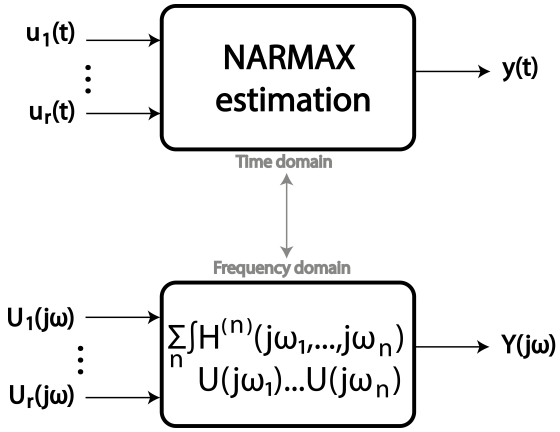

Figure 4.4: Diagram presenting the model analysis procedure.

4.5 Conclusions

This chapter introduced the concepts of Generalized Frequency Response Functions and Output Frequency Responses of nonlinear dynamical systems as well as methods to compute these functions for a general polynomial NARX model. The frequency domain methods presented in this chapter are powerful tools that allow the analysis of the underlying nonlinear mechanisms which contribute to the observed output spectrum (Zhang and Billings, 1993, Boaghe, 2000).

These methods will be used to analyse and compare the models estimated using the NARMAX methodology described in the previous chapter and the paleoclimate data-set. The application of the analysis tools presented in this chapter will be used to provide for

the first time a rigorous characterization of the nonlinear relationship between orbital forcing parameters and the paleoclimate proxy data. Also, it will be possible for the first time to characterize in the frequency domain how this dynamic relationship changed during and following the Mid-Pleistocene Transition by comparing the functions and graphical representations of the GFRFs and OFRs for the time periods ***before*** and ***after MPT***.

The higher-order OFRs allow identifying which frequencies and combinations of frequencies contribute most significantly in the output spectrum such as the peak corresponding to the $\sim 1/100$ cycles/kyr frequency. An important advantage of the frequency domain approach is that the GFRFs allow to uniquely characterize the dynamics of the system. Therefore GFRFs provide an effective way to compare the dynamical properties of the studied system ***before*** and ***after MPT***.

Chapter 5

Palaeoclimate Data Modelling Using the NARMAX Methodology

5.1 Introduction

The objective of this chapter is to apply the nonlinear system identification methods presented in Chapter 3 to infer NARMAX models which capture the dynamic relationship between the oxygen isotope measurements taken from deep-sea cores (model output) and the three orbital parameters *eccentricity*, *obliquity* and *longitude of perihelion* (model inputs) ***before*** and ***after MPT***. Specifically, the proxy data consists of measurements of oxygen isotope ratio taken from deep-sea sediment cores drilled at Site 806B. This is the first time such an approach has been used to model and analyse the relationship between palaeoclimate proxies and orbital forcing.

Although the resulting NARMAX models cannot be mapped directly on known physical processes, such models can reveal the nonlinear mechanisms by which orbital forcing modulated the paleoclimate ***before*** and ***after MPT***.

This chapter is organized as follows. Section 5.2 presents the data sets used to estimate and validate the models. The identification of the two NARMAX models based on paleoclimate proxy data ***before*** and ***after MPT*** is presented in Section 5.3. Section 5.4 presents model validation results. Conclusions are presented in Section 5.5.

5.2 Palaeoclimatic Proxy Data

The data used in this work is available from the National Climatic Data Center website (http://www.ncdc.noaa.gov). The output data set chosen for this study consists of $N_{out} = 536$ samples of the $\delta^{18}O$ *time-series*, which covers the time interval between the present time (year 0 is considered year 1950) and 5 Myr before present. The input data set consist of $N_{in} = 2140$ samples of *eccentricity*, *obliquity* and *longitude of perihelion* covering the interval between year 0 and 2.14 Myr BP. The inputs and output data sets have been discussed in more detail in Chapter 2 Sections 2.3 and 2.4, and are shown in Figures 2.4 - 2.6 and 2.13. Out of the entire data set available, in order to study the MPT, only the data corresponding to the Pleistocene time period was extracted.

The $\delta^{18}O$ time-series stored in the NCDC repository was obtained by first interpolating the raw isotope data and then resampling it (Berger et al., 1993a). The sampling period of the data is 4 kyr. The time series of orbital parameters were calculated following the equations (Berger and Loutre, 1992):

$$
\begin{aligned}
e\sin\overline{\omega} &= \textstyle\sum_i P_i \sin(\alpha_i t + \eta_i) \\
\epsilon &= \epsilon^* + \textstyle\sum_i A_i \cos(\gamma_i t + \zeta_i) \\
e &= e^* + \textstyle\sum_i E_i \cos(\lambda_i t + \phi_i)
\end{aligned}
$$

where e is the *eccentricity*, $e\sin\overline{\omega}$ is the climatic *precession*, ϵ is the *obliquity* and the amplitudes (P_i, A_i, E_i), frequencies (α_i, γ_i, λ_i) and phases (η_i, ζ_i, ϕ_i) are given in Berger and Loutre (1992) Table1.

The orbital parameters data was initially sampled at 1 kyr and, in this work, it was resampled at 4 kyr to match the sampling time of the $\delta^{18}O$ data set.

As the MPT was identified by most authors (Imbrie et al., 1992, Pisias and Moore Jr., 1981) around $900 - 850$ kyr BP, the data available was split into two data subsets D_1 and D_2, shown in Figure 5.1, as:

- D_1 marks the time period ***before MPT*** given by the time interval $[1400 - 852]$ kyr BP and consists of 138 data points in total.
- D_2 marks the time period ***after MPT*** given by the time interval $[852 - 0]$ kyr BP and

consists of 214 data points in total.

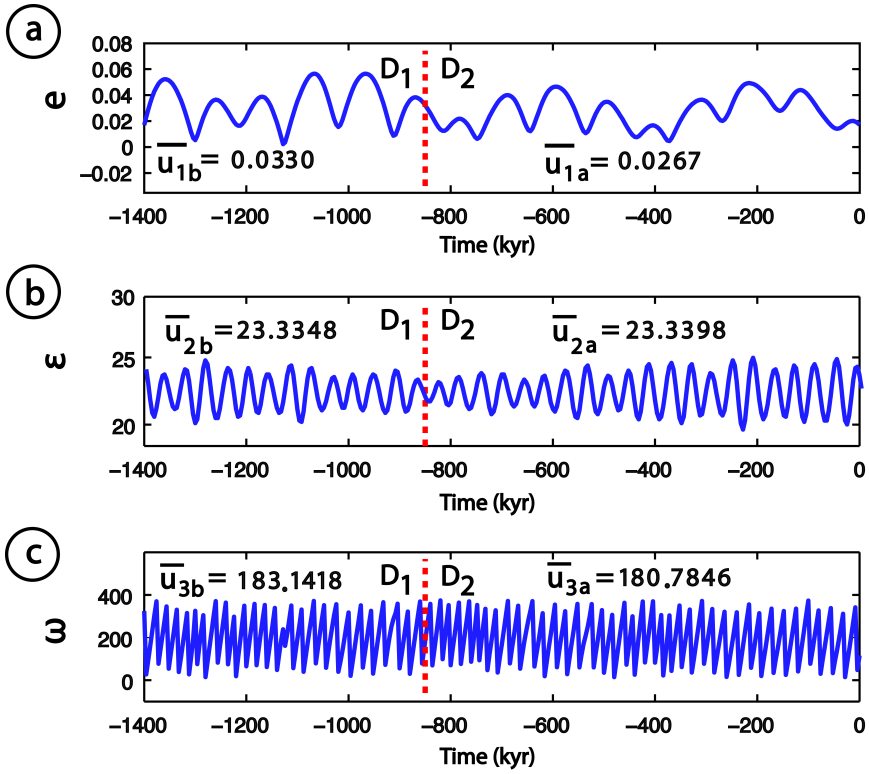

Figure 5.1: Inputs time-series: a. *eccentricity*, b. *obliquity*, c. *longitude of perihelion*; the vertical red dotted line represents the MPT time separating the subsets D_1 (***before MPT***) and D_2 (***after MPT***).

The system output is the time-series of *oxygen isotope ratio* $\delta^{18}O$ (hereafter referred to as y) and the system inputs are *eccentricity* (u_1), *obliquity* (u_2) and *longitude of perihelion* (u_3). The input is written in vector form as $u = [u_1\ u_2\ u_3]$.

For modelling purposes the inputs and output were split into an *estimation (training)* data set and a *validation* data set. These data sets were as:

- D_{1E} is the estimation data set for the time interval $[1126, 852]$ kyr BP ***before MPT***.
- D_{1V} is the validation data set for the time interval $[1400, 1126]$ kyr BP ***before MPT***.
- D_{2E} is the estimation data set for the time interval $[568, 0]$ kyr BP ***after MPT***.
- D_{2V} is the validation data set for the time interval $[852, 568]$ kyr BP ***after MPT***.

5.3 Model Structure Selection and Parameter Estimation

In this section, the NARMAX methodology is used to develop polynomial models which relate the proxy for *insolation*, which is the output of the system, to the three orbital parameters *eccentricity*, *obliquity* and *longitude of perihelion*, which represent the inputs for the system, in the cases ***before*** and ***after MPT***. The methodology presented here is applied similarly to the two separate sets of data.

In order to find the best model structure and parameters to fit the available data for each of the two time periods, the model degrees were varied ranging from 1 to 4. The lags values were set as: for first and second order models $N_y = 8$, $N_{u_i} = 8$, $i = 1, 2, 3$ and $N_e = 8$, for third order models $N_y = 4$, $N_{u_i} = 8$, $i = 1, 2, 3$ and $N_e = 4$ and for forth order models $N_y = 3$, $N_{u_i} = 4$, $i = 1, 2, 3$ and $N_e = 3$.

The full polynomial model structures include very large number of terms. For example, using the above lag values, the full models using all three inputs have 41 terms for the first order model, 861 terms for the second order model, 6545 terms for the cubic model and 7315 terms for the fourth order model. Given usually 15-20 terms are needed to fit the data accurately (Billings and Leontaritis, 1980), the strategy for reducing the number of terms using cross-validation is presented next. Also, the procedure establishes which of the three inputs or combinations of them are necessary to accurately fit the output data. To this end, for each model order 1 to 4, models with one input only (either u_1, u_2 or u_3), combinations of two ($[u_1\, u_2]$, $[u_1\, u_3]$ or $[u_2\, u_3]$) or all three inputs ($[u_1\, u_2\, u_3]$) were estimated.

For the structure detection procedure, the number of noise terms n_{no} were varied from 1 to 10 and the number of iterations of the noise model ranged from 5 to 25. For each value of n_{no} and noise iteration, the number of process terms n_{pr} was varied through from 1 to 30. Using the OFR procedure 30 polynomial models were obtained for each combination of n_{no} and iteration values. Using cross-validation it is possible to obtain the optimum number of n_{pr}, out of the total 30 considered, by plotting the estimation errors superimposed on the prediction errors (Figures 5.4a and 5.5a).

Model degree	$d = 1$		$d = 2$	
Input(s)	***Before MPT***	***After MPT***	***Before MPT***	***After MPT***
u_1	23.06%	18.83%	17.65%	19.51%
u_2	53.87%	20.63%	17.31%	**16.19%**
u_3	17.35%	21.43%	18.40%	22.82%
$[u_1\ u_2]$	38.67%	17.34%	**14.50%**	16.73%
$[u_1\ u_3]$	16.46%	17.90%	18.18%	19.87%
$[u_2\ u_3]$	**15.29%**	19.39%	17%	20.82%
$[u_1\ u_2\ u_3]$	17.95%	**16.10%**	14.91%	16.38%

Model degree	$d = 3$		$d = 4$	
Input(s)	***Before MPT***	***After MPT***	***Before MPT***	***After MPT***
u_1	17.84%	19.49%	26.92%	19.16%
u_2	15.60%	19.81%	**22.10%**	29.96%
u_3	19.80%	21.43%	31.21%	22.21%
$[u_1\ u_2]$	18.70%	18.41%	24.95%	**17.75%**
$[u_1\ u_3]$	25.95%	19.31%	26.80%	19.07%
$[u_2\ u_3]$	15.02%	21.75%	29.43%	20.94%
$[u_1\ u_2\ u_3]$	**13.93%**	**16%**	25.86%	18.40%

Table 5.1: *NRMSE* values for the best models for each degree of nonlinearity (d) and combination of input terms to the model. The emphasized values represent the smallest *NRMSE* for each order model.

Table 5.1 shows the *normalized root mean squared errors* for linear, quadratic, cubic and quartic polynomials models with one, two and three inputs fitted ***before*** and ***after MPT***. The values in Table 5.1 are *normalized root mean squared errors* calculated for the *mpo* on the entire time period used (D_1 or D_2), whereas the values used in cross-validation are *mean squared error* values calculated on the estimation and validation data sets (D_{1E}, D_{1V}, D_{2E}, D_{2V}) corresponding to each time period. The characteristics of the best model obtained for each model order for both time periods are summarized in Table 5.2.

Model type	***Before MPT***		***After MPT***	
	No of terms	Input	No of terms	Input
Linear	9	$[u_2\ u_3]$	22	$[u_1\ u_2\ u_3]$
Quadratic	17	$[u_1\ u_2]$	24	u_2
Cubic	21	$[u_1\ u_2\ u_3]$	20	$[u_1\ u_2\ u_3]$
Quartic	9	u_2	11	$[u_1\ u_2]$

Table 5.2: Number of terms and inputs used for the best linear, quadratic, cubic and quartic models ***before*** and ***after MPT.***

The simulation results of the best models for each order are shown for ***before MPT*** in Figure 5.2 and for ***after MPT*** in Figure 5.3. It is observed from the *NRMSE* values in Table 5.1 that for both time periods the overall best models are the third order ones which have all three orbital parameters as inputs. The *model predicted output* $\hat{y}$ corresponding to these two models is shown in Figures 5.2c and 5.3c. On the plots in Figures 5.2a, 5.2b, 5.2d and 5.3a, 5.3b, 5.3d it is emphasized where the first, second and fourth order models are outperformed by the third order models in Figures 5.2c and 5.3c, respectively.

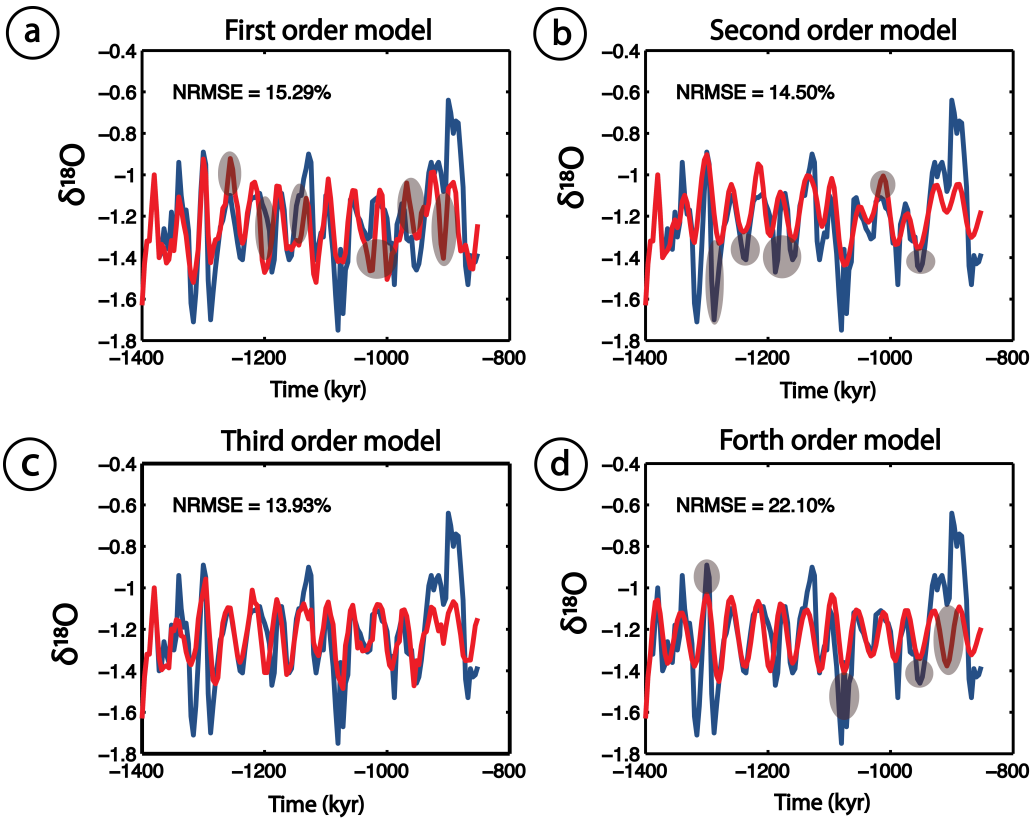

Figure 5.2: Best a. linear, b. quadratic, c. cubic and d. quartic *model predicted output* (red) superimposed on the $\delta^{18}O$ time-series (blue) ***before MPT***. The grey areas mark where the third order model outperforms the first, second and fourth order models.

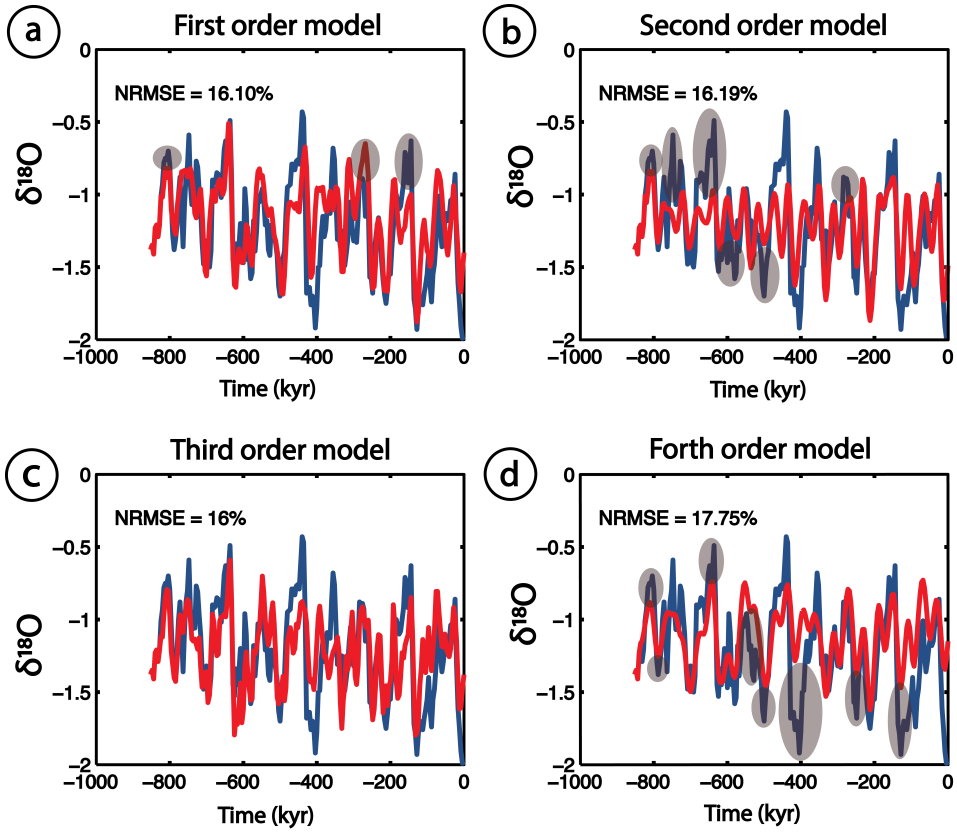

Figure 5.3: Best a. linear, b. quadratic, c. cubic and d. quartic *model predicted output* (red) superimposed on the $\delta^{18}O$ time-series (blue) ***after MPT***. The grey areas mark where the third order model outperforms the first, second and fourth order models.

Figures 5.4a and 5.5a present the cross-validation procedure results as it was explained above. These figures show the validation error (green) and the estimation error (black). The point marked with a red star represents the minimum value for the validation error. ***Before MPT*** (Figure 5.4a), for $n_{no} = 10$ the minimum estimation error is found for $n_{pr} = 11$. The best model ***before MPT*** has therefore a total of 21 terms. For the model ***after MPT***, the graphic shown in Figure 5.5a is for $n_{no} = 9$ and the minimum validation error is given by $n_{pr} = 11$. The best model ***after MPT*** has a total of 20 terms.

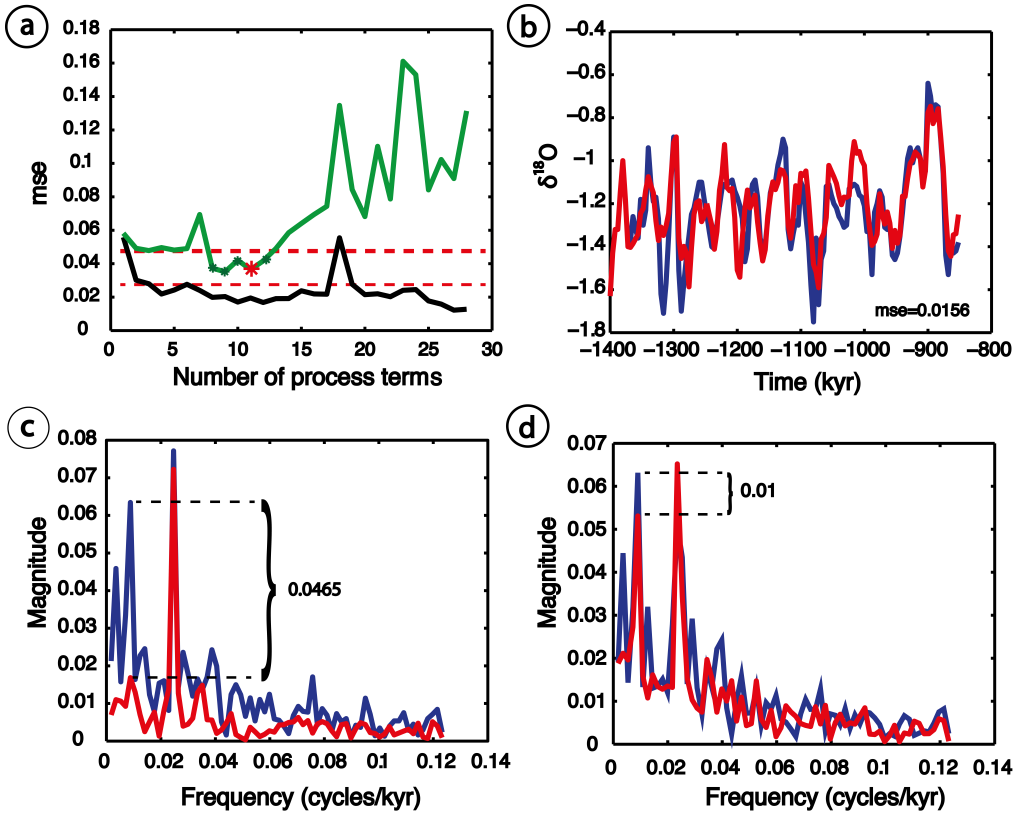

Figure 5.4: ***Before MPT*** a. cross-validation *mse* values for noise iteration 4 and $n_{no} = 10$ for estimation data set (black) and validation data set (green), b. model with $n_{pr} = 16$ and $n_{no} = 5$ (red) superimposed on $\delta^{18}O_{D_1}$ (blue), c. spectrum of the model with $n_{pr} = 11$ and $n_{no} = 10$ terms (red) superimposed on the spectrum of $\delta^{18}O_{D_1}$ (blue) and d. spectrum of model with $n_{pr} = 16$ and $n_{no} = 5$ (red) superimposed on spectrum of $\delta^{18}O_{D_1}$ (blue).

The dotted red lines in Figures 5.4a and 5.5a define an arbitrary interval in which the validation error vary insignificantly. ***Before MPT*** the validation error value for the best model is 0.038 and the arbitrary interval is considered [$\sim$ 0.03, $\sim$ 0.05] with the maximum validation error value 0.16. ***After MPT*** the validation error value for the best model is $\sim$ 0.1, the largest validation error value is 1.45 and the arbitrary interval was chosen as [0.07, 0.2]. These intervals will provide alternative values for n_{pr} and thus alternative model structures which will retain small error values.

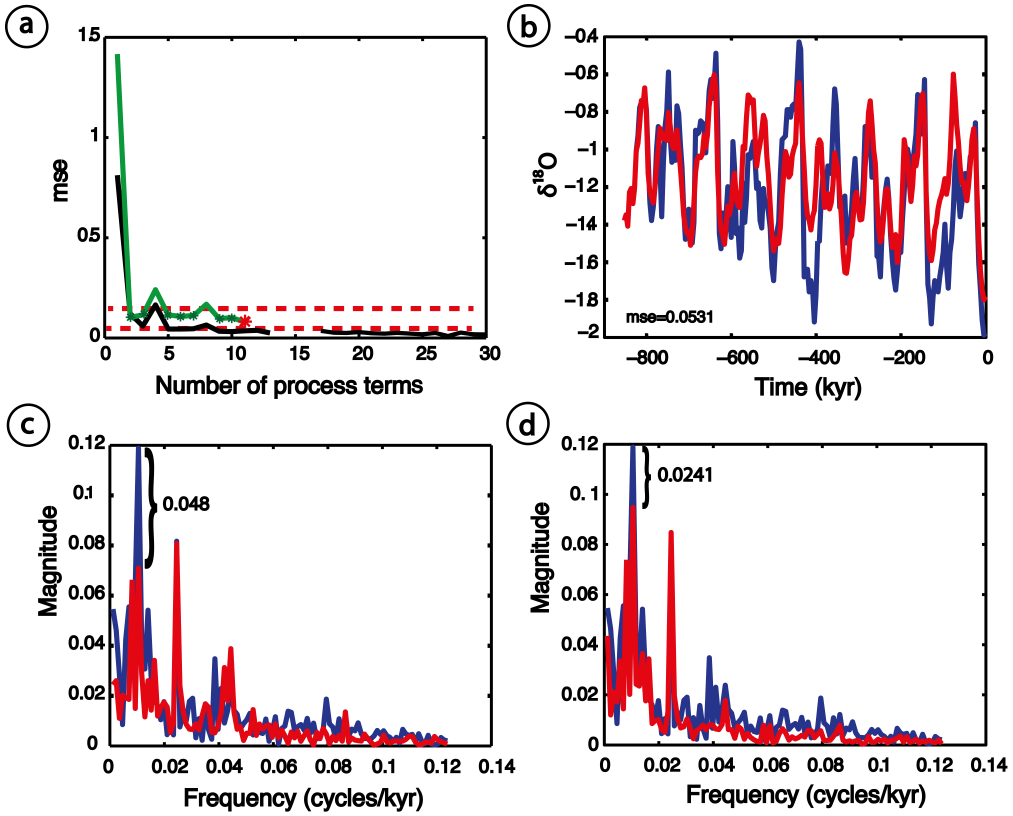

Figure 5.5: ***After MPT*** a. cross-validation *mse* values for noise iteration 9 and $n_{no} = 9$ for estimation data set (black) and validation data set (green), b. final selected model with 32 terms (red) superimposed on $\delta^{18}O_{D_2}$ (blue), c. spectrum of the selected model with 20 terms (red) superimposed on the spectrum of $\delta^{18}O_{D_2}$ (blue) and d. spectrum of model with 32 terms (red) superimposed on the spectrum of $\delta^{18}O_{D_2}$ (blue).

This study shows that all three orbital parameters (*eccentricity*, *obliquity* and *longitude of the perihelion*) and a cubic polynomial model structure are needed to best fit the data. This supports the theory that the climatic response is influenced by the three parameters simultaneously. This is accepted by most scientists (Pisias and Moore Jr., 1981, Clemens and Tiedemann, 1997, Muller and MacDonald, 2005) and, although some argue that orbital parameters may not represent the main drive for climate change (Muller and MacDonald, 1997, Imbrie et al., 1993, Ganopolski and Calov, 2011), it is widely accepted that all three parameters have a significant influence on the long term climate variations (Crucifix et al., 2007).

It is important for fitting accuracy to ensure that the model simulations fit the data in

time domain but also in the frequency domain. This is essential in the studied case when the main interest is to analyse two specific frequencies in the output spectrum. This means comparing the spectrum of the *mpo* with the spectrum of the output signal, the $\delta^{18}O$ time-series. Figures 5.4c and 5.5c show the spectrum of the output (blue) superimposed on the spectrum of the *mpo* (red). It can be seen that for both time periods the spectrum of the *mpo* reproduces well the frequency at 0.0244 cycles/kyr corresponding to the 41 kyr period, but it fails in both cases to reach the peak at the frequency corresponding to the $\sim$ 100 kyr period.

The analysis done so far proves that the modelling procedure needs to incorporate spectrum validation as well. This was done by starting from the cross-validation results for the third order models with three inputs and selecting models that provide close validation errors to the model that was firstly selected, shown between the dotted red lines in Figures 5.4a and 5.5a. For each model structure, the spectrum of the model response is compared with the spectrum of the $\delta^{18}O$ in order to obtain good magnitude match at the frequencies of interest. This procedure involves cross-validation structure detection, but also provides good frequency domain fitting of the data spectrum.

The model ***before MPT*** obtained using this combined procedure has 16 process terms and 5 noise terms. The *mean squared error* value in this case is $mse = 0.0159$, which is smaller than the best model obtained by cross-validation alone, which had $mse = 0.0239$. The magnitude spectrum difference at the frequency corresponding to the period of $\sim$ 100 kyr improves from 0.0465 to 0.0101, as seen in Figures 5.4c and 5.4d. The *mpo* for the model with 21 terms selected through the cross-validation and spectrum fitting combined procedure is shown in Figure 5.4b.

A similar analysis is done ***after MPT*** and presented in Figure 5.5. In this case, the cross-validation method returns the best model with $n_{pr} = 11$ and $n_{no} = 9$. The magnitude spectrum comparison in Figure 5.5c shows a difference of 0.048 between the $\delta^{18}O$ and *mpo* at the frequency corresponding to the $\sim$ 100 kyr period. Using the combined cross-validation and spectrum comparison procedure, a model with $n_{pr} = 25$ and $n_{no} = 7$ is found to give a magnitude spectrum difference of 0.0241. This value is half of the one given by the model obtained using cross-validation alone. The *mean squared error* value for the model obtain by

cross-validation alone is $mse = 0.0623$, and the one obtained using the combined procedure is $mse = 0.0531$. As it can be seen from these values and Figures 5.5b, 5.5c and 5.5d the final selected model brings a big improvement in fitting accuracy. The selected model ***after MPT*** has 32 terms.

For both models, ***before*** and ***after MPT***, the increase in the magnitude spectrum peak fitting accuracy is important and at no fitting loss to the time domain signal.

Figure 5.6 shows the two final selected models, with 21 terms ***before MPT*** and 32 terms ***after MPT***, simulated on the corresponding time periods. On the same figure are shown the estimation and validation errors obtained by using cross-validation. These simulated results provide us with visual confirmation on how well the models fit the data.

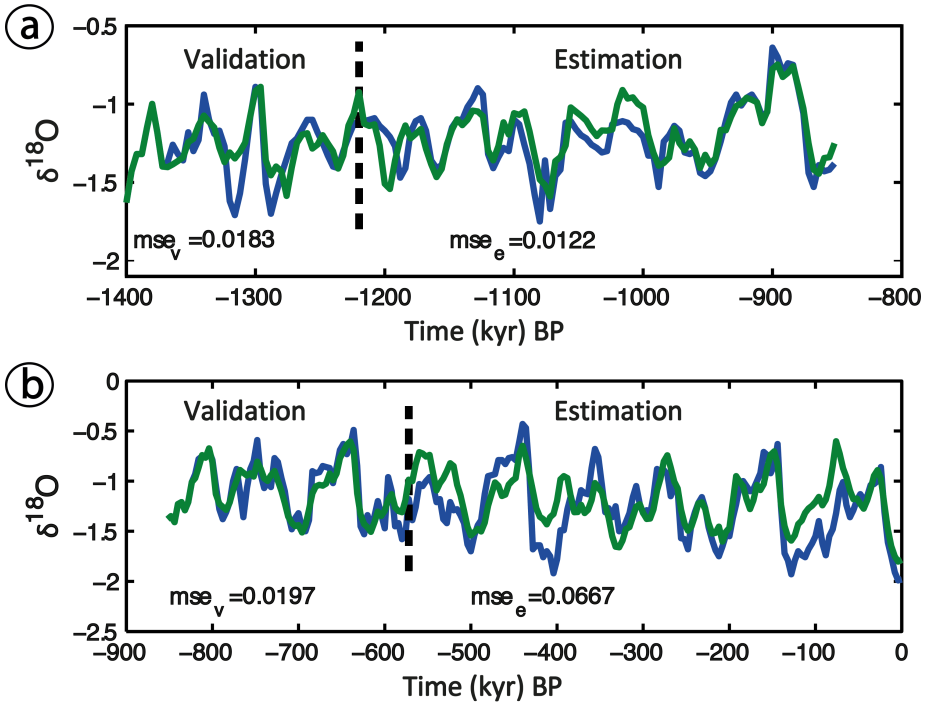

Figure 5.6: Model predicted output (green) superimposed on $\delta^{18}O$ (blue) and the estimation and prediction errors for the estimation and validation dataset for: a. ***before MPT***, b. ***after MPT***.

Figure 5.7 shows the simulations of the identified models on the entire studied Pleistocene time period $[1400 - 0]$ kyr BP and that the models are stable outside the estimation data range. This analysis shows how well the models are able to predict the validation data. The *normalized root mean squared error* when the model ***before MPT*** is used to simulate

on the entire time period is $NRMSE_{total_B} = 16.05\%$, and when the model ***after MPT*** is used to simulate on the entire time period is $NRMSE_{total_A} = 16.95\%$. The *normalized root mean squared errors* in the case of each models for the data that was not used for estimation or validation is for the model ***before MPT*** (the time period considered is $[852 - 0]$ kyr BP) $mse_{unseen_B} = 19.51\%$ and for the model ***after MPT*** (the time period considered is $[1400 - 852]$ kyr BP) $mse_{unseen_A} = 27.44\%$.

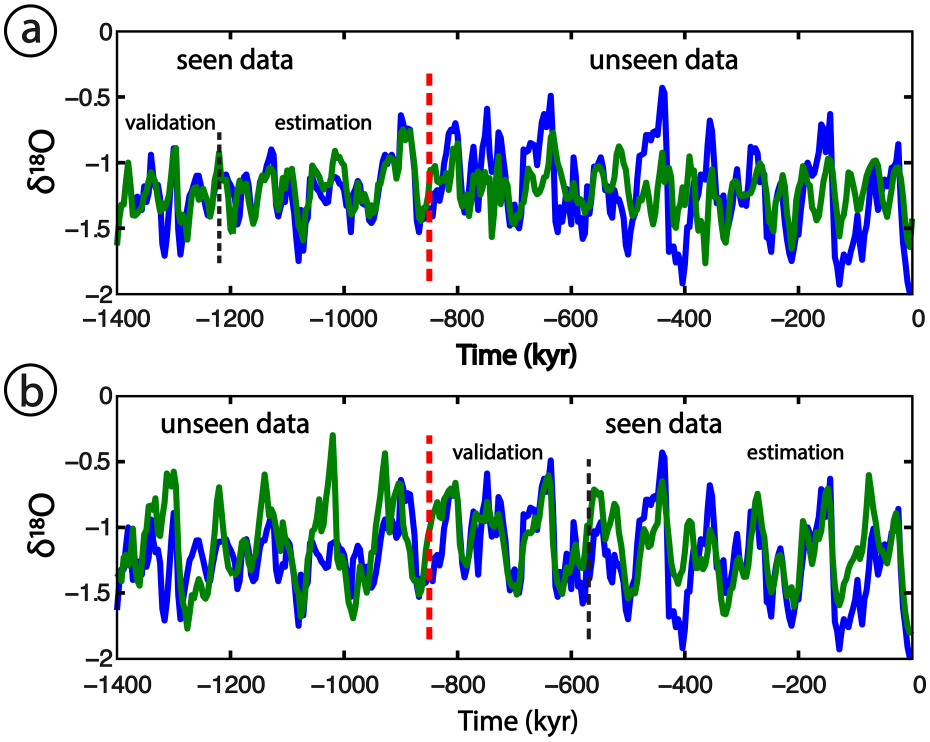

Figure 5.7: Model predicted output (green) superimposed on $\delta^{18}O$ (blue) for the time period $[1400 - 0]$ kyr BP using the estimated models: a. ***before MPT*** and b. ***after MPT.***

This analysis confirms that the *mpo* remains stable on the entire studied Pleistocene time period. However, Figure 5.7 and the *NRMSEs* show that the models fitted for each time period predict better on the data set used for estimation than they do on the entire time period. This shows that two different models are needed for each time period. The two different models facilitate the study of the difference observed in the simulations in Figure 5.7 and what triggers it.

Figure 5.8 shows the residuals calculated as $\hat{\varepsilon}(t) = y(t) - \hat{y}(t)$, where $\hat{y}(t)$ is the *model*

predicted output, calculated as in equation (3.12), for the entire studied Pleistocene time period $[1400 - 0]$ kyr BP. The horizontal green dotted lines represent the points of the minimum and maximum residual values for the data set used in the estimation procedure. In both cases, the residuals for the unseen data are, as expected, larger in value as the ones calculated on the data used for estimation. The difference is more noticeable for the simulation using the model ***before MPT***.

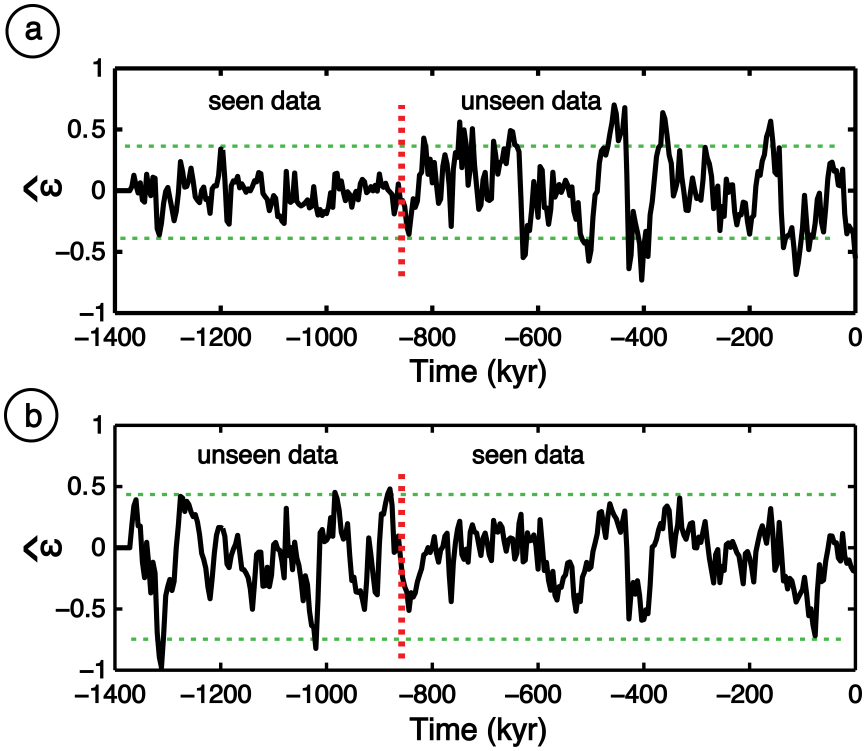

Figure 5.8: Residuals for the entire studied Pleistocene time period $[1400 - 0]$ kyr BP using the estimated model a. ***before MPT*** and b. ***after MPT***. The dotted red lines represent the MPT point and the dotted green lines represent the minimum and maximum residual values for the time period used for the estimation of each model.

The simulation results and analysis performed in this chapter confirm that there was a dramatic change to the nonlinear dynamic relationship between orbital parameters and climate proxies during MPT. This is supported by the following:

- Two different models were fitted for each period and, although both models gave stable simulations they did not perform as well on the entire Pleistocene time period.

- The models reproduce the dramatic frequency shift, by accurately fitting the data spectrum.
- Both models require all three inputs to give accurate results, but the model ***before MPT*** has 21 terms, whereas the model ***after MPT*** has 32 terms.
- The maximum lags required for each model terms were $N_y = 4$, $[N_{u_1}\ N_{u_2}\ N_{u_3}] = [8\ 8\ 6]$ ***before MPT*** and $N_y = 4$, $[N_{u_1}\ N_{u_2}\ N_{u_3}] = [7\ 8\ 8]$ ***after MPT***.

Tables 5.3 and 5.4 give the coefficients and terms for the selected models for the two studied time periods.

Before MPT			
Count	Coefficient	Coefficient symbol	Term
1	0.001795	$\theta_b(1)$	$y(t-1)u_2(t-8)^2$
2	−0.000125	$\theta_b(2)$	$u_2(t-1)^3$
3	0.000117	$\theta_b(3)$	$u_2(t-1)u_2(t-3)u_2(t-8)$
4	0.000130	$\theta_b(4)$	$u_1(t-8)u_3(t-1)u_3(t-4)$
5	−0.000086	$\theta_b(5)$	$u_1(t-6)u_3(t-1)u_3(t-4)$
6	0.000233	$\theta_b(6)$	$y(t-2)^2u_3(t-4)$
7	0.000124	$\theta_b(7)$	$y(t-3)u_2(t-4)u_3(t-4)$
8	0.000000025	$\theta_b(8)$	$u_3(t-2)u_3(t-3)u_3(t-5)$
9	−0.000327	$\theta_b(9)$	$y(t-4)^2u_3(t-2)$
10	−0.000694	$\theta_b(10)$	$u_1(t-1)u_2(t-3)u_3(t-5)$
11	−0.009606	$\theta_b(11)$	$y(t-1)u_1(t-1)u_3(t-6)$
12	−0.000000025	$\theta_b(12)$	$u_3(t-2)^2u_3(t-6)$
13	0.000000233	$\theta_b(13)$	$u_2(t-1)u_3(t-2)u_3(t-6)$
14	0.001595	$\theta_b(14)$	$y(t-1)y(t-3)u_3(t-4)$
15	−0.0000446	$\theta_b(15)$	$y(t-4)u_2(t-8)u_3(t-4)$
16	0.0000102	$\theta_b(16)$	$y(t-1)u_2(t-3)u_3(t-4)$
17	−0.022436	$\theta_b(17)$	$u_3(t-5)e(t-3)^2$
18	0.001097	$\theta_b(18)$	$y(t-1)u_3(t-5)e(t-4)$
19	0.009699	$\theta_b(19)$	$u_3(t-2)e(t-3)^2$
20	0.000023	$\theta_b(20)$	$u_3(t-1)u_3(t-6)e(t-3)$
21	−0.000023	$\theta_b(21)$	$u_3(t-2)u_3(t-6)e(t-3)$

Table 5.3: Model coefficients and terms for the time period ***before MPT.***

After MPT			
Count	Coefficient	Coefficient symbol	Term
1	0.001384	$\theta_a(1)$	$y(t-1)u_2(t-8)^2$
2	0.023525	$\theta_a(2)$	$y(t-2)u_1(t-7)u_3(t-1)$
3	−0.000087	$\theta_a(3)$	$u_2(t-1)^3$
4	0.0000067	$\theta_a(4)$	$y(t-2)u_3(t-3)u_3(t-8)$
5	0.020046	$\theta_a(5)$	$y(t-1)^2y(t-3)$
6	0.000445	$\theta_a(6)$	$y(t-2)u_2(t-3)^2$
7	0.002059	$\theta_a(7)$	$u_1(t-7)u_2(t-1)u_3(t-1)$
8	−0.411117	$\theta_a(8)$	$y(t-2)^2y(t-3)$
9	−0.005230	$\theta_a(9)$	$y(t-2)u_2(t-2)u_2(t-7)$
10	−0.010973	$\theta_a(10)$	$u_1(t-1)u_2(t-8)^2$
11	0.369465	$\theta_a(11)$	$y(t-1)y(t-4)u_1(t-2)$
12	−0.020101	$\theta_a(12)$	$y(t-1)u_1(t-1)u_3(t-7)$
13	−0.0000000144	$\theta_a(13)$	$u_3(t-1)^2u_3(t-8)$
14	0.0000000216	$\theta_a(14)$	$u_3(t-1)u_3(t-2)u_3(t-4)$
15	−0.000164	$\theta_a(15)$	$u_1(t-1)u_3(t-2)u_3(t-4)$
16	−0.000101	$\theta_a(16)$	$u_1(t-1)u_3(t-4)u_3(t-7)$
17	0.001057	$\theta_a(17)$	$u_1(t-3)u_2(t-7)u_3(t-4)$
18	−0.053157	$\theta_a(18)$	$y(t-2)^2u_2(t-3)$
19	−0.027060	$\theta_a(19)$	$y(t-2)y(t-3)u_2(t-5)$
20	−0.000164	$\theta_a(20)$	$u_2(t-8)^3$
21	0.0000891	$\theta_a(21)$	$u_1(t-2)u_3(t-2)u_3(t-3)$
22	0.000133	$\theta_a(22)$	$u_2(t-3)u_2(t-8)^2$
23	−0.0000063	$\theta_a(23)$	$y(t-1)u_3(t-3)u_3(t-8)$
24	−0.0000966	$\theta_a(24)$	$y(t-2)u_2(t-5)u_3(t-8)$
25	0.0000734	$\theta_a(25)$	$y(t-1)u_2(t-3)u_3(t-8)$
26	0.0000100	$\theta_a(26)$	$u_3(t-5)u_3(t-6)e(t-1)$
27	−513.1434	$\theta_a(27)$	$u_1(t-2)u_1(t-5)e(t-2)$
28	−0.040774	$\theta_a(28)$	$u_1(t-1)u_3(t-2)e(t-1)$
29	0.1681874	$\theta_a(29)$	$u_2(t-7)e(t-4)^2$
30	−114.6774	$\theta_a(30)$	$u_1(t-4)e(t-4)^2$
31	0.0591374	$\theta_a(31)$	$u_1(t-1)u_3(t-5)e(t-2)$
32	13.417572	$\theta_a(32)$	$e(t-1)^2e(t-3)$

Table 5.4: Model coefficients and terms for the time period ***after MPT.***

5.4 Model Validation

This section presents the model validation results for the identified models, based on techniques presented in Chapter 3 Section 3.4.

5.4.1 Coherence Analysis

The coherence function results were obtained using 30-points Hanning windows with 20 points overlap. For the FFT the number of data points used were 142 ***before MPT*** and 214 ***after MPT***.

The results in Figure 5.9 show that the $\delta^{18}O$ time-series and *mpo* correspond well to one another at the frequencies of interest, as the values in Table 5.5 also prove. As explained in Chapter 3 Section 3.4, the closer the coherence function values are to 1 the closer the predicted output is to the real output. For the first frequency of interest (sometimes associated to the $\sim$ 100 kyr *eccentricity* period (Berger, 1988)) Figure 5.9 and Table 5.5 show that the coherence between the two signals is above 90%, which is a highly satisfying fit. For the frequency associated to the 41 kyr *obliquity* period, the fit of $\sim$ 80% is still a good fit for the complex and highly nonlinear system under investigation.

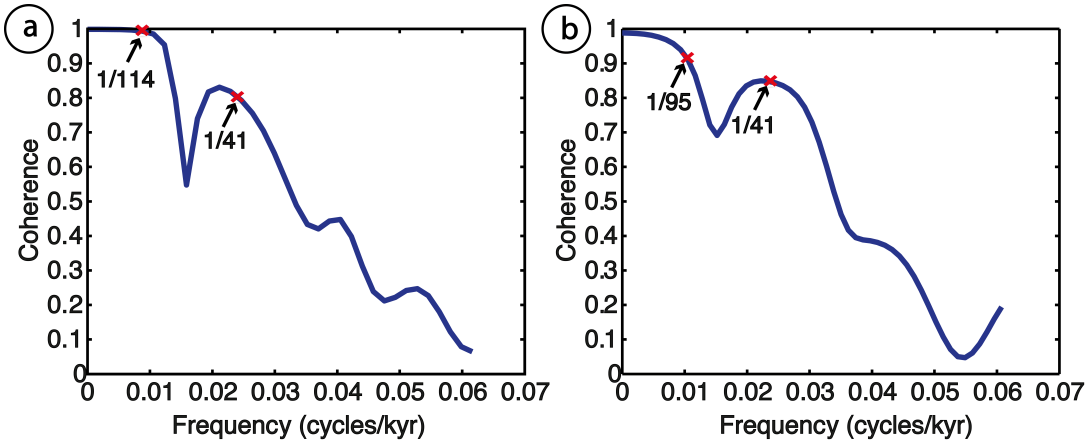

Figure 5.9: Coherence analysis between the model predicted output and the $\delta^{18}O$ time-series a. ***before MPT***, b. ***after MPT.***

Time period	Coherence value	
	$f \approx 1/100$ cycles/kyr	$f = 1/41$cycles/kyr
Before MPT	99.35%	79.28%
After MPT	91.10%	84.36%

Table 5.5: Coherence values ***before*** and ***after MPT*** at the two frequencies of interest.

5.4.2 Correlation Tests

The estimated models are also validated using the MIMO correlation tests developed using the SISO correlation tests detailed in Chapter 3 Section 3.4. The following correlation tests were computed for the fitted models having all three orbital parameters as inputs:

$$
\begin{array}{ccc}
 & \Phi_{E^2}(\tau) & \\
\Phi_{U_1E}(\tau) & \Phi_{U_2E}(\tau) & \Phi_{U_3E}(\tau) \\
\Phi_{U_1E^2}(\tau) & \Phi_{U_2E^2}(\tau) & \Phi_{U_3E^2}(\tau) \\
\Phi_{U_1^2E}(\tau) & \Phi_{U_2^2E}(\tau) & \Phi_{U_3^2E}(\tau) \\
\Phi_{U_1^2E^2}(\tau) & \Phi_{U_2^2E^2}(\tau) & \Phi_{U_3^2E^2}(\tau) \\
\Phi_{U_1U_2E}(\tau) & \Phi_{U_1U_3E}(\tau) & \Phi_{U_2U_3E}(\tau) \\
\Phi_{U_1U_2E^2}(\tau) & \Phi_{U_1U_3E^2}(\tau) & \Phi_{U_2U_3E^2}(\tau)
\end{array}
$$

where $E = \hat{\varepsilon} - \overline{\hat{\varepsilon}}$ and $E^2 = \hat{\varepsilon}^2(t) - \overline{\hat{\varepsilon}^2}$, $U_i = u_i(t) - \overline{u_i}$, $U_i^2 = u_i^2(t) - \overline{u_i^2}$, with $i = 1, 2, 3$.

Figures 5.10 and 5.11 show the results of the correlation functions for lag τ ranging from -5 to 5. All correlation tests, apart from $\Phi_{U_2E^2}(\tau)$ and $\Phi_{U_2^2E^2}(\tau)$ ***before MPT*** and $\Phi_{U_1U_3E^2}(\tau)$ ***after MPT***, are with the 95% confidence intervals defined by $\pm 1.96\sqrt{N}$, where N is the total number of data points. The correlation tests demonstrate that the residual error sequence is unpredictable from all linear and nonlinear combinations of past inputs and outputs (Billings and Zhu, 1994).

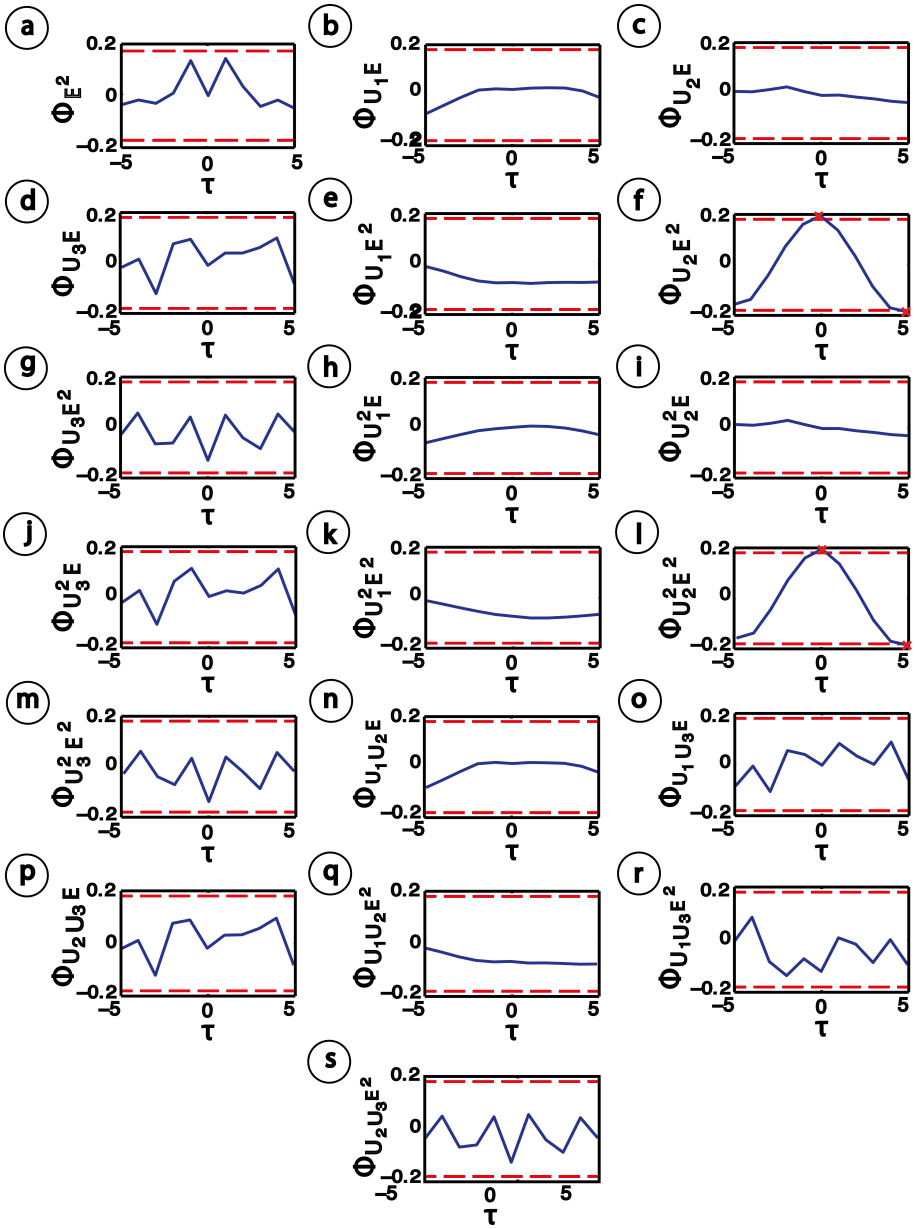

Figure 5.10: MIMO correlation tests for the model ***before MPT***: a. $\Phi_{E^2}(\tau)$, b. $\Phi_{U_1E}(\tau)$, c. $\Phi_{U_2E}(\tau)$, d. $\Phi_{U_3E}(\tau)$, e. $\Phi_{U_1E^2}(\tau)$, f. $\Phi_{U_2E^2}(\tau)$, g. $\Phi_{U_3E^2}(\tau)$, h. $\Phi_{U_1^2E}(\tau)$, i. $\Phi_{U_2^2E}(\tau)$, j. $\Phi_{U_3^2E}(\tau)$, k. $\Phi_{U_1^2E^2}(\tau)$, l. $\Phi_{U_2^2E^2}(\tau)$, m. $\Phi_{U_3^2E^2}(\tau)$, n. $\Phi_{U_1U_2E}(\tau)$, o. $\Phi_{U_1U_3E}(\tau)$, p. $\Phi_{U_2U_3E}(\tau)$, q. $\Phi_{U_1U_2E^2}(\tau)$, r. $\Phi_{U_1U_3E^2}(\tau)$, s. $\Phi_{U_2U_3E^2}(\tau)$.

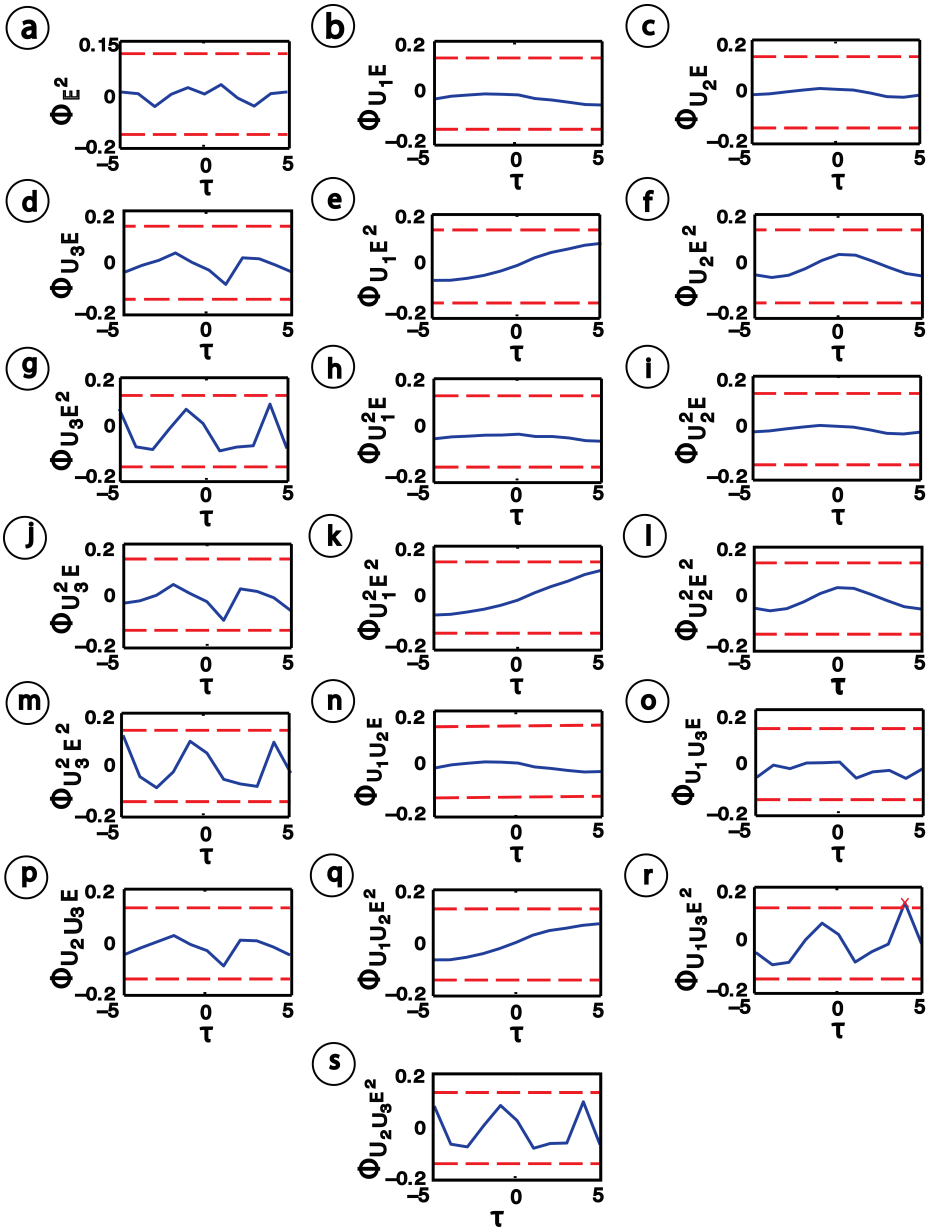

Figure 5.11: MIMO correlation tests for the model ***after MPT***: a. $\Phi_{E^2}(\tau)$, b. $\Phi_{U_1E}(\tau)$, c. $\Phi_{U_2E}(\tau)$, d. $\Phi_{U_3E}(\tau)$, e. $\Phi_{U_1E^2}(\tau)$, f. $\Phi_{U_2E^2}(\tau)$, g. $\Phi_{U_3E^2}(\tau)$, h. $\Phi_{U_1^2E}(\tau)$, i. $\Phi_{U_2^2E}(\tau)$, j. $\Phi_{U_3^2E}(\tau)$, k. $\Phi_{U_1^2E^2}(\tau)$, l. $\Phi_{U_2^2E^2}(\tau)$, m. $\Phi_{U_3^2E^2}(\tau)$, n. $\Phi_{U_1U_2E}(\tau)$, o. $\Phi_{U_1U_3E}(\tau)$, p. $\Phi_{U_2U_3E}(\tau)$, q. $\Phi_{U_1U_2E^2}(\tau)$, r. $\Phi_{U_1U_3E^2}(\tau)$, s. $\Phi_{U_2U_3E^2}(\tau)$.

5.5 Discussion

In this chapter the NARMAX methodology introduced in Chapter 3 was applied to identify models relating the three orbital parameters *eccentricity*, *obliquity* and *longitude of perihelion* to the oxygen isotope $\delta^{18}O$ time-series from the Pacific Site 806B, which is a proxy for Earth's insolation. A search over the space of polynomial model structures of different orders, with one, two and three inputs revealed that cubic models with three inputs performed best both ***before*** and ***after MPT***.

This chapter demonstrated for the first time that there is a direct causal link between the orbital forcing and oxygen isotope time-series. In contrast to previous attempts (Berger and Loutre, 1992, Imbrie et al., 1992, Rial and Anaclerio, 2000), the model derived in this chapter is the first model that can predict with such level of accuracy the evolution of the oxygen isotope time-series and that can reproduce the climate shift observed at the MPT point using only orbital parameters as inputs. Whilst there are clearly other factors that influence the response, the accuracy of the model predictions suggest that orbital parameters were by far the biggest drivers of the climate over the period covered by the studied data set.

The results of the study have confirmed that the underlying mechanism by which the orbital parameters affect the climate is nonlinear. This study also confirms that all three orbital parameters are needed to adequately model the data. Furthermore, simulations of the models over the entire analyzed period (***before*** and ***after MPT***) show clearly that the MPT represents a sudden change of nonlinear behaviour as the prediction of both models deteriorates when the models are simulated on the time period that was not used for estimation.

The models derived here will be subjected to further analysis in subsequent chapters in order to characterize and contrast the nonlinear interactions between orbital parameters and the oxygen isotope time-series ***before*** and ***after MPT***.

From the results presented in this section the above methodology proves to be very suited for modelling and prediction of this type of time-series. The models obtained in this chapter can be further used for frequency domain study. Although the models reproduce very well the time-domain signals, they do not offer great explanation for the changes occurred at

the MPT. Frequency domain mapping and analysis of these will offer a totally different perspective on the differences between the two estimated models.

Chapter 6

Higher-Order Frequency Domain Analysis of the Mid-Pleistocene Transition and the "100 kyr Problem"

6.1 Introduction

Frequency domain analysis provides an alternative analysis approach to the time domain methods. This chapter deals with the implementation and analysis of the GFRFs and of the OFRs, derived for the NARMAX models described in Chapter 5, which were estimated for each of the two time periods studied, namely ***before*** and ***after MPT***.

These frequency domain tools can help to investigate how energy is transferred between certain frequency bands of the inputs to frequency bands of in the output. The analysis explains the nonlinear mechanisms that gave rise to all frequencies in the output spectrum. Of particular interest is the frequency $\sim 1/100$ cycles/kyr associated with the so called "100 kyr Problem" described in Chapter 2.

Section 6.2 of this chapter starts with the model transformations which are required for the GFRF implementation. These involve converting the model into an equivalent representation that assumes zero mean inputs and has no internal constant. This section also deals with the computation of the GFRFs and OFRs and the analytical expressions derived using the theoretical concepts defined in Chapter 4. The GFRFs (Peyton-Jones and Billings, 1989,

Billings and Peyton Jones, 1990) are computed using the recursive probing algorithm (Li and Billings, 2005). The higher order OFRs (Output Frequency Responses) correspond to individual Volterra kernels of different orders which show explicitly the contributions of different inputs and nonlinear mechanisms to the overall frequency content of the output (Lang and Billings, 2005, Peng et al., 2011).

Section 6.3 presents a spectral analysis and comparison of the inputs, outputs and *mpos* for the two time periods. The GFRFs and OFRs are used to analyse and compare the properties of the two models obtained for the two time periods. A detailed analysis of the OFRs which contribute significantly to the $\sim 1/100$ cycles/kyr frequency is carried out. The analysis provides a rigorous characterization of the magnitude changes observed ***after MPT***.

6.2 Derivation of the Generalized Frequency Response Functions for the multi-input NARX model

6.2.1 Model transformations

The two models estimated using the NARMAX methodology in Chapter 5 Section 3.4 for each of the time periods ***before*** and ***after MPT***, were transformed using the two procedures detailed in Chapter 4 sub-section 4.3.7. The NARX model transformation procedures firstly involve writing the model as an equivalent one that works with zero mean inputs, and secondly removing the model's internal constant. The internal constants for each time period, corresponding to the fixed points of the models, are calculated as: $y_{0_{beforeMPT}} = 0.9533$ and $y_{0_{afterMPT}} = 0.9404$. It can be seen that both models operate within the neighborhoods of the same stable equilibrium point.

The model estimated and validated in Chapter 5 Section 3.4 for ***before MPT*** (Table 5.2), has 16 process terms and 5 noise terms and is a cubic model and will be denoted ***model B***. The best model for ***after MPT*** is a model of third order nonlinearity degree (Table 5.3) with 25 pure process terms and 7 noise terms and will be denoted ***model A***. After applying the model transformations, models that have equivalent response but different structure as the original ones were obtained. These have 73 terms in the case of ***model B*** and 95 terms

for ***model A***.

The models with zero mean inputs and without the internal constant, obtained by transforming the estimated models ***before*** and ***after MPT*** are listed in Tables A.1 and A.2 in Appendix A.

The procedures used to convert the model in the equivalent representations is illustrated on the 10^{th} term of the ***model B,*** Table A.2 in Appendix A, which is $\theta_b(10)u_1(t-1)u_2(t-3)u_3(t-5)$, where $\theta_b(10)$ is the model coefficient, $u_1(t)$ denotes *eccentricity*, $u_2(t)$ *obliquity* and $u_3(t)$ *longitude of perihelion*.

In order to have a model with zero mean inputs the following substitution is made:

$$\widetilde{u}_i(t) = u_i(t) - \overline{u}_i$$

where $\overline{u}_i$ represents the mean value of $u_i(t)$, which for a data-set of N points is given by $\overline{u}_i = \frac{1}{N}\sum_{j=1}^{N} u_{ij}(t)$.

When processing this term using the variable change $u_i(t) = \widetilde{u}_i(t) + \overline{u_i}$, with $\overline{u_1} = 0.0331$, $\overline{u_2} = 23.3348$ and $\overline{u_3} = 183.1418$, the resulting term becomes:

$$\begin{aligned}\theta_b(10)\widetilde{u}_1(t-1)\widetilde{u}_2(t-3)\widetilde{u}_3(t-5) + \theta_b(10)\overline{u_1}\widetilde{u}_2(t-3)\widetilde{u}_3(t-5) + \theta_b(10)\overline{u_2}\widetilde{u}_1(t-1)\widetilde{u}_3(t-5)\\ +\theta_b(10)\overline{u_3}\widetilde{u}_1(t-1)\widetilde{u}_2(t-3) + \theta_b(10)\overline{u_1u_2}\widetilde{u}_3(t-5) + \theta_b(10)\overline{u_1u_3}\widetilde{u}_2(t-3)\\ +\theta_b(10)\overline{u_2u_3}\widetilde{u}_1(t-1) + \theta_b(10)\overline{u_1u_2u_3}\end{aligned} \tag{6.1}$$

6.2.2 Computation of the Generalized Frequency Response Functions

The NARMAX model is mapped into the frequency domain by using the probing algorithm to compute the Generalized Frequency Response Functions (Peyton-Jones and Billings, 1989, Billings and Peyton Jones, 1990).

The output of a model with three inputs that includes kernels up to order of nonlinearity three can be written, as detailed in Chapter 4 Section 4.2, as:

$$
\begin{aligned}
y(t) &= \sum_{i=1}^{3}\int_{-\infty}^{\infty} h_i^{(1)}(\tau_1)u_i(t-\tau_1)d\tau_1 + \sum_{i=1}^{3}\int_{-\infty}^{\infty}\int_{-\infty}^{\infty} h_i^{(2)}(\tau_1,\tau_2)u_i(t-\tau_1)u_i(t-\tau_2)d\tau_1,d\tau_2 \\
&+ \sum_{i=1}^{3}\sum_{j=i+1}^{3}\int_{-\infty}^{\infty}\int_{-\infty}^{\infty}[h_{ij}^{(2)}(\tau_1,\tau_2)+h_{ji}^{(2)}(\tau_1,\tau_2)]u_i(t-\tau_1)u_j(t-\tau_2)d\tau_1,d\tau_2 \\
&+ \sum_{i=1}^{3}\sum_{j=i+1}^{3}[\int_{-\infty}^{\infty}\int_{-\infty}^{\infty}\int_{-\infty}^{\infty}[2h_{iij}^{(3)}(\tau_1,\tau_2,\tau_3)+2h_{iji}^{(3)}(\tau_1,\tau_2,\tau_3)+2h_{jii}^{(3)}(\tau_1,\tau_2,\tau_3)]u_i(t-\tau_1) \\
&\quad u_i(t-\tau_2)u_j(t-\tau_3)d\tau_1,d\tau_2,d\tau_3 \\
&+ \int_{-\infty}^{\infty}\int_{-\infty}^{\infty}\int_{-\infty}^{\infty}[2h_{ijj}^{(3)}(\tau_1,\tau_2,\tau_3)+2h_{jij}^{(3)}(\tau_1,\tau_2,\tau_3)+2h_{jji}^{(3)}(\tau_1,\tau_2,\tau_3)] \\
&\quad u_i(t-\tau_1)u_j(t-\tau_2)u_j(t-\tau_3)d\tau_1,d\tau_2,d\tau_3] \\
&+ \int_{-\infty}^{\infty}\int_{-\infty}^{\infty}\int_{-\infty}^{\infty}\sum_{i=1}^{3}\sum_{\substack{j=1\\ j\neq i}}^{3}\sum_{\substack{k=1\\ k\neq j,i}}^{3} h_{ijk}^{(3)}(\tau_1,\tau_2,\tau_3)\,u_1(t-\tau_1)u_2(t-\tau_2)u_3(t-\tau_3)d\tau_1,d\tau_2,d\tau_3
\end{aligned}
$$

Given that the GFRF definition is:

$$H^{(n)}(j\omega_1,\ldots,j\omega_n) = \int_{-\infty}^{\infty}\ldots\int_{-\infty}^{\infty} h^{(n)}(\tau_1,\ldots,\tau_n)e^{-j(\omega_1\tau_1+\cdots+\omega_n\tau_n)}d\tau_1\ldots d\tau_n$$

and that for any NARX model with one output and three inputs, the GFRFs have the general form: $H^{(n)}_{\underbrace{N_{u_1}\ldots N_{u_1}}_{n_1}\underbrace{N_{u_2}\ldots N_{u_2}}_{n_2}\underbrace{N_{u_3}\ldots N_{u_3}}_{n_3}}$ with n being the order of the computed GFRF and $n_1+n_2+n_3=n$, the GFRFs to be computed are:

1. First order GFRFs: $H_1^1(j\omega_1)$, $H_2^1(j\omega_1)$ and $H_3^1(j\omega_1)$.

2. Second order GFRFs:

$$
\begin{aligned}
&H_1^2(j\omega_1,j\omega_2)\\
&H_2^2(j\omega_1,j\omega_2)\\
&H_3^2(j\omega_1,j\omega_2)\\
H^2_{12_{avg}}(j\omega_1,j\omega_2) &= \tfrac{1}{2}[H_{12}^2(j\omega_1,j\omega_2)+H_{21}^2(j\omega_2,j\omega_1)]\\
H^2_{13_{avg}}(j\omega_1,j\omega_2) &= \tfrac{1}{2}[H_{13}^2(j\omega_1,j\omega_2)+H_{31}^2(j\omega_2,j\omega_1)]\\
H^2_{23_{avg}}(j\omega_1,j\omega_2) &= \tfrac{1}{2}[H_{23}^2(j\omega_1,j\omega_2)+H_{32}^2(j\omega_2,j\omega_1)]
\end{aligned}
$$

3. Third order GFRFs:

$$H_1^3(j\omega_1, j\omega_2, j\omega_3)$$
$$H_2^3(j\omega_1, j\omega_2, j\omega_3)$$
$$H_3^3(j\omega_1, j\omega_2, j\omega_3)$$

$$H^3_{112_{avg}}(j\omega_1, j\omega_2, j\omega_3) = \tfrac{1}{6}[2H^2_{112}(j\omega_1, j\omega_2, j\omega_3) + 2H^2_{121}(j\omega_1, j\omega_2, j\omega_3) + 2H^2_{211}(j\omega_1, j\omega_2, j\omega_3)]$$
$$H^3_{122_{avg}}(j\omega_1, j\omega_2, j\omega_3) = \tfrac{1}{6}[2H^2_{122}(j\omega_1, j\omega_2, j\omega_3) + 2H^2_{212}(j\omega_1, j\omega_2, j\omega_3) + 2H^2_{221}(j\omega_1, j\omega_2, j\omega_3)]$$
$$H^3_{113_{avg}}(j\omega_1, j\omega_2, j\omega_3) = \tfrac{1}{6}[2H^2_{113}(j\omega_1, j\omega_2, j\omega_3) + 2H^2_{131}(j\omega_1, j\omega_2, j\omega_3) + 2H^2_{311}(j\omega_1, j\omega_2, j\omega_3)]$$
$$H^3_{133_{avg}}(j\omega_1, j\omega_2, j\omega_3) = \tfrac{1}{6}[2H^2_{133}(j\omega_1, j\omega_2, j\omega_3) + 2H^2_{313}(j\omega_1, j\omega_2, j\omega_3) + 2H^2_{331}(j\omega_1, j\omega_2, j\omega_3)]$$
$$H^3_{223_{avg}}(j\omega_1, j\omega_2, j\omega_3) = \tfrac{1}{6}[2H^2_{223}(j\omega_1, j\omega_2, j\omega_3) + 2H^2_{232}(j\omega_1, j\omega_2, j\omega_3) + 2H^2_{322}(j\omega_1, j\omega_2, j\omega_3)]$$
$$H^3_{233_{avg}}(j\omega_1, j\omega_2, j\omega_3) = \tfrac{1}{6}[2H^2_{233}(j\omega_1, j\omega_2, j\omega_3) + 2H^2_{323}(j\omega_1, j\omega_2, j\omega_3) + 2H^2_{332}(j\omega_1, j\omega_2, j\omega_3)]$$
$$H^3_{123_{avg}}(j\omega_1, j\omega_2, j\omega_3) = \tfrac{1}{6}[H^2_{123}(j\omega_1, j\omega_2, j\omega_3) + H^2_{132}(j\omega_1, j\omega_2, j\omega_3) + H^2_{213}(j\omega_1, j\omega_2, j\omega_3)$$
$$+H^2_{231}(j\omega_1, j\omega_2, j\omega_3) + H^2_{312}(j\omega_1, j\omega_2, j\omega_3) + H^2_{321}(j\omega_1, j\omega_2, j\omega_3)]$$

For the estimated NARX models, the following transfer functions were computed: first order ($H_1^1(j\omega)$, $H_2^1(j\omega)$, $H_3^1(j\omega)$), second order self-kernel ($H_1^2(j\omega_1, j\omega_2)$, $H_2^2(j\omega_1, j\omega_2)$, $H_3^2(j\omega_1, j\omega_2)$), second order cross-kernel ($H_{12}^2(j\omega_1, j\omega_2)$, $H_{13}^2(j\omega_1, j\omega_2)$, $H_{23}^2(j\omega_1, j\omega_2)$) and third order self-kernel ones
($H_1^3(j\omega_1, j\omega_2, j\omega_3)$, $H_2^3(j\omega_1, j\omega_2, j\omega_3)$, $H_3^3(j\omega_1, j\omega_2, j\omega_3)$). In addition, only for ***model B*** the third order cross-kernel functions ($H^3_{112}(j\omega_1, j\omega_2, j\omega_3)$, $H^3_{122}(j\omega_1, j\omega_2, j\omega_3)$, $H^3_{113}(j\omega_1, j\omega_2, j\omega_3)$, $H^3_{133}(j\omega_1, j\omega_2, j\omega_3)$,
$H^3_{223}(j\omega_1, j\omega_2, j\omega_3)$, $H^3_{233}(j\omega_1, j\omega_2, j\omega_3)$, $H^3_{123}(j\omega_1, j\omega_2, j\omega_3)$) were also computed, for reasons presented in the analysis section.

The following cases describe the inputs used for the probing algorithm and the resulting GFRFS for different values of $n \leq 3$ and $\sum_{k=1}^{3} n_k = n$:

- Setting $n = 1$, the first order transfer functions are computed by defining the inputs as single tone ones. By setting each of the inputs at a time to $u_k(t) = e^{j\omega_1 t}$ and the rest to zero, as shown in Table 6.1, the first order transfer functions $H_k^1(j\omega_1)$ are calculated by expressing the output of the system as:

$$y(t) = H_k^1(j\omega_1)e^{j\omega_1 t}$$

GFRF	$u_1(t)$	$u_2(t)$	$u_3(t)$
$H_1^1(j\omega_1)$	$e^{j\omega_1 t}$	0	0
$H_2^1(j\omega_1)$	0	$e^{j\omega_1 t}$	0
$H_3^1(j\omega_1)$	0	0	$e^{j\omega_1 t}$

Table 6.1: Single-tone inputs used to compute the first order GFRFs $H_k^1(j\omega_1)$, $k = 1, 2, 3$.

By substituting the equations for the output and of each of the inputs at a time in the NARX model, the expressions for the first order transfer functions, $H_1^1(j\omega_1)$, $H_2^1(j\omega_1)$ and $H_3^1(j\omega_1)$ are obtained.

The resulting symbolical expressions for the first order GFRFs for ***model B*** (denoted by a subscript letter B) are:

$$H_{1B}^1(j\omega_1) = -\frac{2.91e^{-6jw_1} + 1.2e^{-1jw_1} - 4.36e^{-8jw_1}}{0.08e^{-2jw_1} - 0.68e^{-jw_1} - 0.25e^{-3jw_1} + 0.08e^{-4jw_1} + 1}$$

$$H_{2B}^1(j\omega_1) = -\frac{(0.19e^{-jw_1} - 0.06e^{-3jw_1} - 0.06e^{-2jw_1} + 0.02e^{-4jw_1} + 0.008e^{-8jw_1})}{(0.08e^{-2jw_1} - 0.68e^{-jw_1} - 0.25e^{-3jw_1} + 0.08e^{-4jw_1} + 1)}$$

$$H_{3B}^1(j\omega_1) = \frac{0.0008e^{-3jw_1} + 0.0005e^{-6jw_1} + 0.0003e^{-5jw_1} + 0.0003e^{-jw_1} - 0.0001e^{-2jw_1} - 0.00008e^{-4jw_1}}{0.08e^{-2jw_1} - 0.68e^{-jw_1} - 0.25e^{-3jw_1} + 0.08e^{-4jw_1} + 1}$$

The analytical expressions for the first order GFRFs for ***model A*** (denoted by a subscript letter A) are:

$$H_{1A}^1(j\omega_1) = \frac{4.69e^{-7jw_1} + 4.46e^{-3jw_1} - 11.23e^{-1jw_1} + 3.24e^{-2jw_1}}{0.48e^{-2jw_1} - 0.78e^{-1jw_1} - 0.25e^{-3jw_1} + 0.009e^{-4jw_1} + 1.0}$$

$$H_{2A}^1(j\omega_1) = -\frac{0.006e^{-3jw_1} - 0.12e^{-7jw_1} + 0.007e^{-5jw_1} + 0.133e^{-jw_1} - 0.115e^{-2jw_1} + 0.197e^{-8jw_1}}{0.48e^{-2jw_1} - 0.79e^{-jw_1} - 0.25e^{-3jw_1} + 0.009e^{-4jw_1} + 1}$$

$$H_{3A}^{1}(j\omega_1) = \frac{0.000017e^{-7jw_1} + 0.00036e^{-3jw_1} + 0.00046e^{-jw_1}}{0.48e^{-2jw_1} - 0.78e^{-jw_1} - 0.25e^{-3jw_1} + 0.009e^{-4jw_1} + 1} + \frac{0.00034e^{-2jw_1} + 0.00008e^{-4jw_1} - 0.00003e^{-8jw_1}}{0.48e^{-2jw_1} - 0.78e^{-jw_1} - 0.25e^{-3jw_1} + 0.009e^{-4jw_1} + 1}$$

- Setting $n = 2$ and $n_k = n$ provides the second order self-kernel transfer functions $H_k^2(j\omega_1, j\omega_2)$. These are calculated by defining each input at a time as a two-tone input as $u_k(t) = e^{j\omega_1 t} + e^{j\omega_2 t}$ and setting the rest of the inputs to zero, as in Table 6.2. The output is written as:

$$y(t) = H_k^1(j\omega_1)e^{j\omega_1 t} + H_k^1(j\omega_2)e^{j\omega_2 t} + 2!H_k^2(j\omega_1, j\omega_2)e^{j(\omega_1+\omega_2)t}$$

GFRF	$u_1(t)$	$u_2(t)$	$u_3(t)$
$H_1^2(j\omega_1, j\omega_2)$	$e^{j(\omega_1+\omega_2)t}$	0	0
$H_2^2(j\omega_1, j\omega_2)$	0	$e^{j(\omega_1+\omega_2)t}$	0
$H_3^2(j\omega_1, j\omega_2)$	0	0	$e^{j(\omega_1+\omega_2)t}$

Table 6.2: Two-tone inputs used to compute the second order self-kernel GFRFs $H_k^2(j\omega_1, j\omega_2)$, $k = 1, 2, 3$.

By substituting $y(t)$ and $u_k(t)$ into the NARX model, the expressions for the second order self-kernel functions, $H_1^2(j\omega_1, j\omega_2)$, $H_2^2(j\omega_1, j\omega_2)$ and $H_3^2(j\omega_1, j\omega_2)$, are obtained. The higher-order frequency response functions expressions for both models are listed in Appendix C. Direct interpretation of these functions is difficult and the relationship between the input and output spectra can be fully characterized by computing the OFRs.

- Setting $n = 2$, with $n_k = 1$ and $n_l = 1$, the second order cross-kernel averaged transfer functions $H_{kl}^2(j\omega_1, j\omega_2)$ are calculated. This is done by probing the NARX model with two single-tone inputs, $u_k(t) = e^{j\omega_1 t}$ and $u_l(t) = e^{j\omega_2 t}$, at a time and setting the rest of the inputs to zero, as in Table 6.3. In this case the output is written as:

$$y(t) = H_k^1(j\omega_1)e^{j\omega_1 t} + H_l^1(j\omega_2)e^{j\omega_2 t} + 2!H_{kl}^2(j\omega_1, j\omega_2)e^{j(\omega_1+\omega_2)t}$$

GFRF	$u_1(t)$	$u_2(t)$	$u_3(t)$
$H^2_{12}(j\omega_1)$	$e^{j\omega_1 t}$	$e^{j\omega_2 t}$	0
$H^2_{13}(j\omega_1)$	$e^{j\omega_1 t}$	0	$e^{j\omega_2 t}$
$H^2_{23}(j\omega_1)$	0	$e^{j\omega_1 t}$	$e^{j\omega_2 t}$

Table 6.3: Single-tone inputs used to compute the second order cross-kernels $H^2_{kl}(j\omega_1, j\omega_2)$, $k, l = 1, 2, 3$ and $k \neq l$.

By substituting the output and inputs expression into the NARX models the second order cross-kernel averaged transfer functions, $H^2_{12}(j\omega_1, j\omega_2)$, $H^2_{13}(j\omega_1, j\omega_2)$, $H^2_{23}(j\omega_1, j\omega_2)$ are obtained.

- Setting $n = 3$ and $n_k = n$, the third order self-kernel transfer functions $H^3_k(j\omega_1, j\omega_2, j\omega_3)$ are calculated. This is done by defining each input as a three-tone input as $u_k(t) = e^{j\omega_1 t} + e^{j\omega_2 t} + e^{j\omega_3 t}$ and setting the rest to zero, as in Table 6.4.

GFRF	$u_1(t)$	$u_2(t)$	$u_3(t)$
$H^3_1(j\omega_1, j\omega_2, j\omega_3)$	$e^{j(\omega_1+\omega_2+\omega_3)t}$	0	0
$H^3_2(j\omega_1, j\omega_2, j\omega_3)$	0	$e^{j(\omega_1+\omega_2+\omega_3)t}$	0
$H^3_3(j\omega_1, j\omega_2, j\omega_3)$	0	0	$e^{j(\omega_1+\omega_2+\omega_3)t}$

Table 6.4: Three-tone inputs used to compute the third order self-kernel GFRFs $H^3_k(j\omega_1, j\omega_2, j\omega_3)$, $k = 1, 2, 3$.

In this case the output is written as:

$$\begin{aligned} y(t) &= H^1_k(j\omega_1)e^{j\omega_1 t} + H^1_k(j\omega_2)e^{j\omega_2 t} + H^1_k(j\omega_3)e^{j\omega_3 t} + 2!H^2_k(j\omega_1, j\omega_2)e^{j(\omega_1+\omega_2)t} \\ &+ 2!H^2_k(j\omega_1, j\omega_3)e^{j(\omega_1+\omega_3)t} + 2!H^2_k(j\omega_2, j\omega_3)e^{j(\omega_2+\omega_3)t} + 3!H^3_k(j\omega_1, j\omega_2, j\omega_3)e^{j(\omega_1+\omega_2+\omega_3)t} \end{aligned}$$

By substituting the output and input expressions into the NARX model, the third order self-kernel transforms $H^3_1(j\omega_1, j\omega_2, j\omega_3)$, $H^3_2(j\omega_1, j\omega_2, j\omega_3)$ and $H^3_3(j\omega_1, j\omega_2, j\omega_3)$ are obtained.

- Setting $n = 3$ and $n_k = 2$ and $n_l = 1$ the third order cross-kernel averaged transfer functions $H^3_{kkl}(j\omega_1, j\omega_2, j\omega_3)$ are calculated. This is done by using one two-tone input $u_k(t) = e^{j\omega_1 t} + e^{j\omega_2 t}$ and one single-tone input $u_l(t) = e^{j\omega_3 t}$ and setting all the other inputs to zero, as in Table 6.5.

GFRF	$u_1(t)$	$u_2(t)$	$u_3(t)$
$H^3_{112}(j\omega_1, j\omega_2, j\omega_3)$	$e^{j(\omega_1+\omega_2)t}$	$e^{j\omega_3 t}$	0
$H^3_{122}(j\omega_1, j\omega_2, j\omega_3)$	$e^{j\omega_1 t}$	$e^{j(\omega_2+\omega_3)t}$	0
$H^3_{113}(j\omega_1, j\omega_2, j\omega_3)$	$e^{j(\omega_1+\omega_2)t}$	0	$e^{j\omega_3 t}$
$H^3_{133}(j\omega_1, j\omega_2, j\omega_3)$	$e^{j\omega_1 t}$	0	$e^{j(\omega_2+\omega_3)t}$
$H^3_{223}(j\omega_1, j\omega_2, j\omega_3)$	0	$e^{j(\omega_1+\omega_2)t}$	$e^{j\omega_3 t}$
$H^3_{233}(j\omega_1, j\omega_2, j\omega_3)$	0	$e^{j\omega_1 t}$	$e^{j(\omega_2+\omega_3)t}$

Table 6.5: Single- and two-tone inputs used to compute the third order cross-kernel GFRFs $H^2_{kkl}(j\omega_1, j\omega_2, j\omega_3)$, $k, l = 1, 2, 3$ and $k \neq l$.

In this case the output is written as

$$\begin{aligned} y(t) &= H^1_k(j\omega_1)e^{j\omega_1 t} + H^1_k(j\omega_2)e^{j\omega_2 t} + H^1_l(j\omega_3)e^{j\omega_3 t} + 2!H^2_k(j\omega_1, j\omega_2)e^{j(\omega_1+\omega_2)t} \\ &+ 2!H^2_{kl}(j\omega_1, j\omega_3)e^{j(\omega_1+\omega_3)t} + 2!H^2_{kl}(j\omega_2, j\omega_3)e^{j(\omega_2+\omega_3)t} + 3!H^3_{kkl}(j\omega_1, j\omega_2, j\omega_3)e^{j(\omega_1+\omega_2+\omega_3)t} \end{aligned}$$

The transfer functions computed in this case are $H^3_{112}(j\omega_1, j\omega_2, j\omega_3)$, $H^3_{122}(j\omega_1, j\omega_2, j\omega_3)$, $H^3_{113}(j\omega_1, j\omega_2, j\omega_3)$, $H^3_{133}(j\omega_1, j\omega_2, j\omega_3)$, $H^3_{223}(j\omega_1, j\omega_2, j\omega_3)$, $H^3_{233}(j\omega_1, j\omega_2, j\omega_3)$.

- Setting $n = 3$ and $n_1 = 1$, $n_2 = 1$ and $n_3 = 1$ the third order cross-kernel averaged transfer function, $H^3_{123}(j\omega_1, j\omega_2, j\omega_3)$, is calculated by probing the NARX model with three single-tone inputs: $u_1(t) = e^{j\omega_1 t}$, $u_2(t) = e^{j\omega_2 t}$ and $u_3(t) = e^{j\omega_3 t}$.

In this case the output is written as

$$\begin{aligned} y(t) &= H^1_1(j\omega_1)e^{j\omega_1 t} + H^1_2(j\omega_2)e^{j\omega_2 t} + H^1_3(j\omega_3)e^{j\omega_3 t} + 2!H^2_{12}(j\omega_1, j\omega_2)e^{j(\omega_1+\omega_2)t} \\ &+ 2!H^2_{13}(j\omega_1, j\omega_3)e^{j(\omega_1+\omega_3)t} + 2!H^2_{23}(j\omega_2, j\omega_3)e^{j(\omega_2+\omega_3)t} + 3!H^3_{123}(j\omega_1, j\omega_2, j\omega_3)e^{j(\omega_1+\omega_2+\omega_3)t} \end{aligned}$$

6.2.3 Computation of the Output Frequency Responses

This section deals with the evaluation and analysis of the Output Frequency Responses. The OFRs are one-dimensional complex functions of frequency, which makes them easily analysed and plotted. The OFRs are easier to analyse and interpret when compared to the multi-dimensional GFRFs. As it was shown in Section 6.2.2, the second or higher order GFRFs are difficult to interpret and analyse. The OFRs, due to their one-dimensional property, facilitate the analysis of the contributions of different input combinations to the output frequency. The OFRs are computed based on the GFRFs $H^{(n)}(j\omega_1 \dots j\omega_n)$ and the given frequency spectra $U_i(j\omega)$ corresponding to the inputs $u_i(t)$ with $i = 1, 2, 3$.

The output spectrum for a nonlinear system is written as:

$$Y(j\omega) = Y^1(j\omega) + Y^2(j\omega) + Y^3(j\omega) + higher\ order \tag{6.2}$$

Each OFR $Y^{(n)}(j\omega)$ can be written as (Lang and Billings, 1997):

$$\begin{aligned} Y^{(n)}(j\omega) \;=\; & \frac{1}{2^{n-1}} \sum_{N_1+\cdots+N_m=n} \sum_{\omega_1+\cdots+\omega_n=\omega} H^{(n)}_{(P_1=N_1,\dots,P_m=N_m)}(j\omega_1 \dots j\omega_n) \\ & \prod_{j=1}^{m} \prod_{i=N_0+\cdots+N_{j-1}+1}^{N_0+\cdots+N_j})U_j(j\omega_i) d\tau_{n\omega} \end{aligned} \tag{6.3}$$

Writing equation (6.3) for $n = 1$ yields the ***first order OFRs*** sum as:

$$Y^1(j\omega) = \sum_{\omega_1=\omega} H^1_1(j\omega_1)U_1(j\omega_1) + \sum_{\omega_1=\omega} H^1_2(j\omega_1)U_2(j\omega_1) + \sum_{\omega_1=\omega} H^1_3(j\omega_1)U_3(j\omega_1) \tag{6.4}$$

From (6.4) it follows that:

$$Y^1(j\omega) = Y^1_1(j\omega) + Y^1_2(j\omega) + Y^1_3(j\omega)$$

When substituting $n = 2$ in equation (6.3), the ***second order OFRs*** sum is computed

as:

$$\begin{aligned} Y^2(j\omega) &= \frac{1}{2}\sum_{\omega_1+\omega_2=\omega} H_1^2(j\omega_1, j\omega_2)U_1(j\omega_1)U_1(j\omega_2) + \frac{1}{2}\sum_{\omega_1+\omega_2=\omega} H_2^2(j\omega_1, j\omega_2)U_2(j\omega_1)U_2(j\omega_2) \\ &+ \frac{1}{2}\sum_{\omega_1+\omega_2=\omega} H_3^2(j\omega_1, j\omega_2)U_3(j\omega_1)U_3(j\omega_2) + \frac{1}{2}\sum_{\omega_1+\omega_2=\omega} H_{12}^2(j\omega_1, j\omega_2)U_1(j\omega_1)U_2(j\omega_2) \\ &+ \frac{1}{2}\sum_{\omega_1+\omega_2=\omega} H_{13}^2(j\omega_1, j\omega_2)U_1(j\omega_1)U_3(j\omega_2) + \frac{1}{2}\sum_{\omega_1+\omega_2=\omega} H_{23}^2(j\omega_1, j\omega_2)U_2(j\omega_1)U_3(j\omega_2) \end{aligned} \tag{6.5}$$

Equation (6.5) is then written as:

$$Y^2(j\omega) = Y_1^2(j\omega) + Y_2^2(j\omega) + Y_3^2(j\omega) + Y_{12}^2(j\omega) + Y_{13}^2(j\omega) + Y_{23}^2(j\omega)$$

The ***third order OFRs*** sum is obtained by substituting $n = 3$ in equation (6.3), as:

$$
\begin{aligned}
Y^3(j\omega) &= \frac{1}{4}\sum_{\omega_1+\omega_2+\omega_3=\omega} H_1^3(j\omega_1,j\omega_2,j\omega_3)U_1(j\omega_1)U_1(j\omega_2)U_1(j\omega_3) \\
&+ \frac{1}{4}\sum_{\omega_1+\omega_2+\omega_3=\omega} H_2^3(j\omega_1,j\omega_2,j\omega_3)U_2(j\omega_1)U_2(j\omega_2)U_2(j\omega_3) \\
&+ \frac{1}{4}\sum_{\omega_1+\omega_2+\omega_3=\omega} H_3^3(j\omega_1,j\omega_2,j\omega_3)U_3(j\omega_1)U_3(j\omega_2)U_3(j\omega_3) \\
&+ \frac{1}{4}\sum_{\omega_1+\omega_2+\omega_3=\omega} H_{112}^3(j\omega_1,j\omega_2,j\omega_3)U_1(j\omega_1)U_1(j\omega_2)U_2(j\omega_3) \\
&+ \frac{1}{4}\sum_{\omega_1+\omega_2+\omega_3=\omega} H_{122}^3(j\omega_1,j\omega_2,j\omega_3)U_1(j\omega_1)U_2(j\omega_2)U_2(j\omega_3) \\
&+ \frac{1}{4}\sum_{\omega_1+\omega_2+\omega_3=\omega} H_{113}^3(j\omega_1,j\omega_2,j\omega_3)U_1(j\omega_1)U_1(j\omega_2)U_3(j\omega_3) \\
&+ \frac{1}{4}\sum_{\omega_1+\omega_2+\omega_3=\omega} H_{133}^3(j\omega_1,j\omega_2,j\omega_3)U_1(j\omega_1)U_3(j\omega_2)U_3(j\omega_3) \\
&+ \frac{1}{4}\sum_{\omega_1+\omega_2+\omega_3=\omega} H_{223}^3(j\omega_1,j\omega_2,j\omega_3)U_2(j\omega_1)U_2(j\omega_2)U_3(j\omega_3) \\
&+ \frac{1}{4}\sum_{\omega_1+\omega_2+\omega_3=\omega} H_{233}^3(j\omega_1,j\omega_2,j\omega_3)U_2(j\omega_1)U_3(j\omega_2)U_3(j\omega_3) \\
&+ \frac{1}{4}\sum_{\omega_1+\omega_2+\omega_3=\omega} H_{123}^3(j\omega_1,j\omega_2,j\omega_3)U_1(j\omega_1)U_2(j\omega_2)U_3(j\omega_3) \qquad (6.6)
\end{aligned}
$$

Equation (6.6) can be written in compact form as:

$$
\begin{aligned}
Y^3(j\omega) &= Y_1^3(j\omega)+Y_2^3(j\omega)+Y_3^3(j\omega)+Y_{112}^3(j\omega)+Y_{122}^3(j\omega)+Y_{113}^3(j\omega)+Y_{133}^3(j\omega) \\
&+ Y_{223}^3(j\omega)+Y_{233}^3(j\omega)+Y_{123}^3(j\omega)
\end{aligned}
$$

6.3 Analysis of the GFRF and OFR Results

In this section the GFRFs expressions derived in Section 6.2.2 are used to plot the functions response. This is useful in order to generally compare the results of the GFRFs for the two time periods. Also, the planes $f_1 + f_2 = f$, where f is in turns the frequency corresponding

to the period of interest $\sim$ 100 and 41 kyr, are extracted. This is presented in order to see the magnitude spectrum and phase functions that can contribute to the output spectrum at the frequency f.

The OFR results analysis can tell which of the individual OFRs contribute significantly to the output spectrum. By knowing this it is then possible to know if a certain output frequency is a result of amplifying or dampening one or more input frequencies through the first order OFRs or if energy was transferred between frequency bands through the higher order OFRs.

6.3.1 Spectral Analysis of the Data

Many authors (Rial and Anaclerio, 2000, Lisiecki, 2010, Berger and Loutre, 1997a, Imbrie et al., 1993, Raymo, 1997) have explained the MPT dominant period shift from 41 kyr ***before MPT*** to $\sim$ 100 kyr ***after MPT*** and also the appearance of the $\sim$ 100 kyr period ***after MPT*** by coupling between frequencies associated to orbital parameters and energy transfer from some input frequency bands to other output frequency bands. It is therefore necessary for the analysis performed on the GFRFs and OFRs results that the input and output dataset spectrum be detailed first.

In order to compute and analyse the spectra of the input and output dataset, it is necessary to firstly define the frequency range used to compute the frequency response. For the time period ***before MPT***, a 142 points FFT was computed to evaluate the input and output spectrum. This gives the normalized frequency interval ω_B and a frequency sampling step of $\delta = 0.0442$. Given that $f_B = (\frac{f_s}{2\pi})\omega_B$, with $f_s = 0.25\, cycles/kyr$, the corresponding actual frequency range is

$$f_B = [-0.1232,\ 0.1232]\, cycles/kyr$$

In the case of the dataset for the time period ***after MPT***, a 214 points FFT was computed for the available data. The frequency sampling step for the normalized frequency interval ω_A was $\delta = 0.0294$. Following the same procedure as before, the corresponding actual frequency range is:

$$f_A = [-0.1238,\ 0.1238]\, cycles/kyr$$

For clarity, in this study, when referring to particular frequencies of interest the following notation is used:

$$f_T = \frac{1}{T} \tag{6.7}$$

where T is the period in kyr.

For example, for the period 95 kyr the corresponding frequency is 0.0105 cycles/kyr and the frequency notation will be f_{95}.

Figure 6.1 shows the magnitude spectrum of the three inputs (*eccentricity*, *obliquity* and *longitude of perihelion*) for each of the two studied time periods. For the input *eccentricity* (u_1) in Figures 6.1a and 6.1b, it can be seen that ***before MPT*** the dominant frequency is f_{95}, and the corresponding magnitude value of 0.0069. In the *eccentricity* spectrum ***after MPT*** there is also a significant peak located at f_{95}, but the magnitude value is 0.0038, which is almost half of the corresponding one ***before MPT***. Two other peaks with high magnitude values are found in the spectrum ***after MPT*** at the frequencies: f_{428} and the magnitude value of 0.0056 and f_{122} and the magnitude value of 0.0036.

Figures 6.1c and 6.1d show the spectrum of the input *obliquity* (u_2) ***before*** and ***after MPT***, respectively. From these plots it can clearly be seen that the spectrum of the signal does not change between the two time periods. The main peak in both signals is at f_{41} and the magnitude value is 0.32 for ***before MPT*** and 0.38 for ***after MPT***.

The spectra of the *longitude of perihelion* (u_3) ***before*** and ***after MPT***, illustrated in Figures 6.1e and 6.1f, show that the main peaks of the spectrum for both time periods are around the frequencies f_{23} and f_{19}. The magnitude value corresponding to the frequency $\sim f_{23}$ is 33.61 ***before MPT*** and 33.7 ***after MPT***. It can be observed that the magnitude value at this frequency does not change during and after the MPT. The magnitude values corresponding to $\sim f_{19}$ is 31.51 ***before MPT*** and 22.31 ***after MPT***, which shows a decrease in the magnitude value this frequency. The magnitude spectrum ***after MPT*** also shows a third high peak at tf_{12}, which has the respective magnitude value of 17.65.

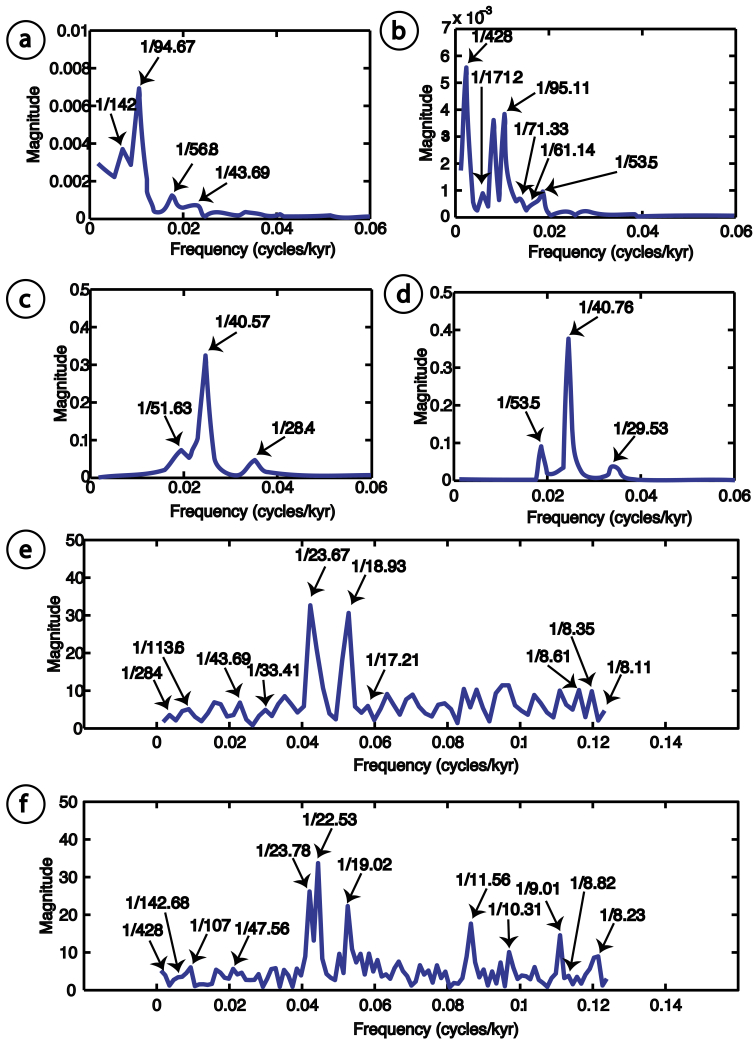

Figure 6.1: Spectrum of the orbital parameters: a., b. *eccentricity*, c., d. *obliquity*, e., f. *longitude of perihelion* for the time period: a., c., e. ***before MPT*** and b., d., f. ***after MPT***.

It can be seen from Figure 6.1 that the energy of these signals is concentrated in the same frequency bands for both time periods, which for *eccentricity* is $[f_{122}, f_{95}]$, for *obliquity* the dominant frequency is f_{41} and for *longitude of perihelion* the interval is $[f_{24}, f_{19}]$.

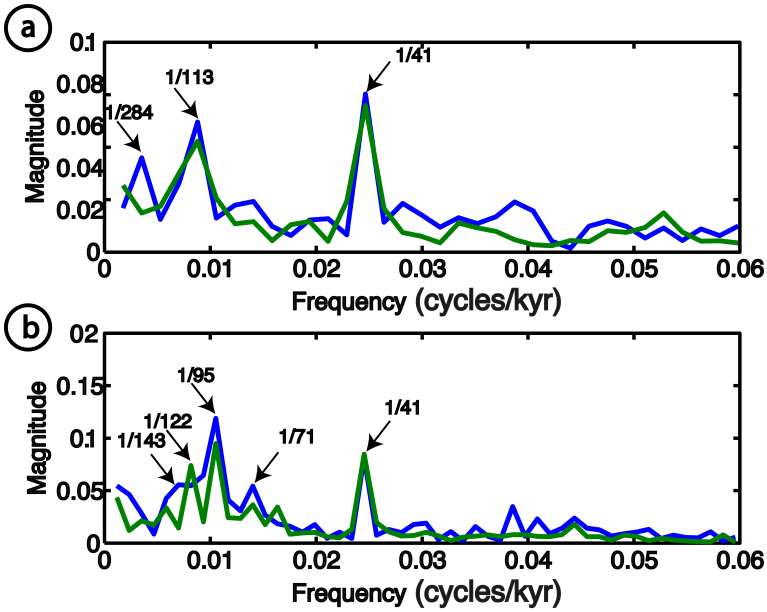

Figure 6.2: Spectrum of the $\delta^{18}O$ (blue) and *mpo* (green) a. ***before MPT*** (using 71 points to compute the positive FFT) and b. ***after MPT*** (using 107 points to compute the positive FFT).

Figure 6.2 shows for each of the time periods the magnitude spectrum of the oxygen isotope ratios data $\delta^{18}O$, denoted by $Z(j\omega)$, superimposed on the spectrum of the *model predicted output* calculated using the fitted NARX models. As it can be seen the magnitude spectra of the *mpo* matches closely the spectra of the two isotope ratio data sets. The dominant magnitude peak in the spectrum ***before MPT*** is clearly at the frequency f_{41}. ***After MPT*** the dominant magnitude peaks are located in the frequency band [f_{120}, f_{93}] band. ***Before MPT*** the exact magnitude peaks locations are at f_{113} ($\sim f_{100}$) and f_{41}, and ***after MPT*** at f_{95} ($\sim f_{100}$) and f_{41}.

It can be seen that the spectrum of the *mpo* reproduces well the change from a dominant output frequency f_{41} ***before MPT***, which also dominates the *obliquity* spectrum, to the frequency f_{95} ***after MPT***, which features strongly in the *eccentricity* spectrum. Also, from Figure 6.2 it can be seen that the magnitude of the spectrum of the *mpo* at the frequency f_{41} does not change significantly, from 0.0716 (0.0772 for $|Z_B(j\omega|)$ to 0.0848 (0.0817 for $|Z_A(j\omega)|$). At $\sim f_{100}$ the observed change in the *mpo* spectrum is more dramatic, to almost twice the magnitude value, from 0.0541 (0.0634 for $|Z_B(j\omega)|$) to 0.0948 (0.1188 for $|Z_A(j\omega)|$).

Other frequencies observed in the $\delta^{18}O$ spectrum (Figure 6.2) are either clearly harmonics of the orbital parameters frequencies, such as $f_{71} = 6f_{428}$ and $f_{142} = 3f_{428}$, or are their subharmonics, such as $f_{284} = \frac{f_{95}}{3}$.

The main frequency of interest will be referred to as $\sim f_{100}$ and the frequency functions information (magnitude and phase function values) necessary for the analysis will be extracted from f_{113} ***before MPT*** and f_{95} ***after MPT***.

6.3.2 Analysis and Comparison of the Generalized Frequency Response Functions Results

Using the expressions of the GFRFs derived in Section 6.2.2 and the frequencies ω defined in Section 6.3.1, the magnitude and phase functions for each GFRF are calculated and plotted.

Figures 6.3 and 6.4 show the plots of the magnitude and phase functions, respectively, for the first order GFRFs.

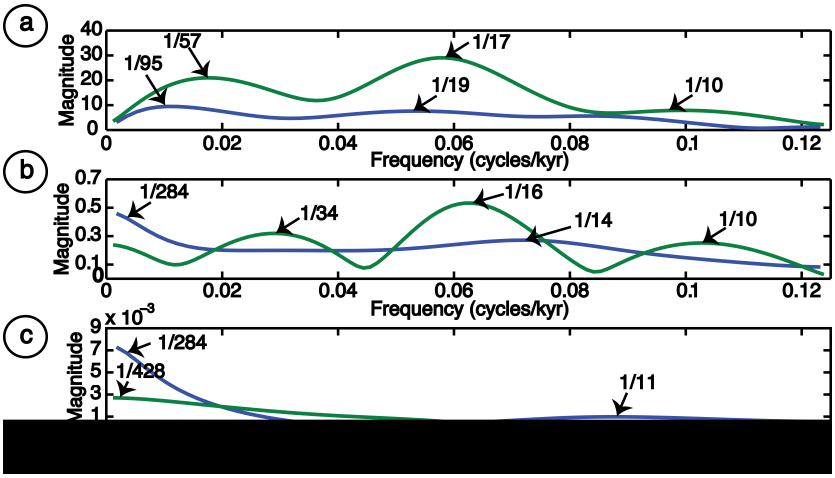

Figure 6.3: Magnitude functions for the first order GFRFs: a. $|H_1^1(j\omega_1)|$, b. $|H_2^1(j\omega_1)|$ and c. $|H_3^1(j\omega_1)|$ ***before MPT*** (blue) and ***after MPT*** (green).

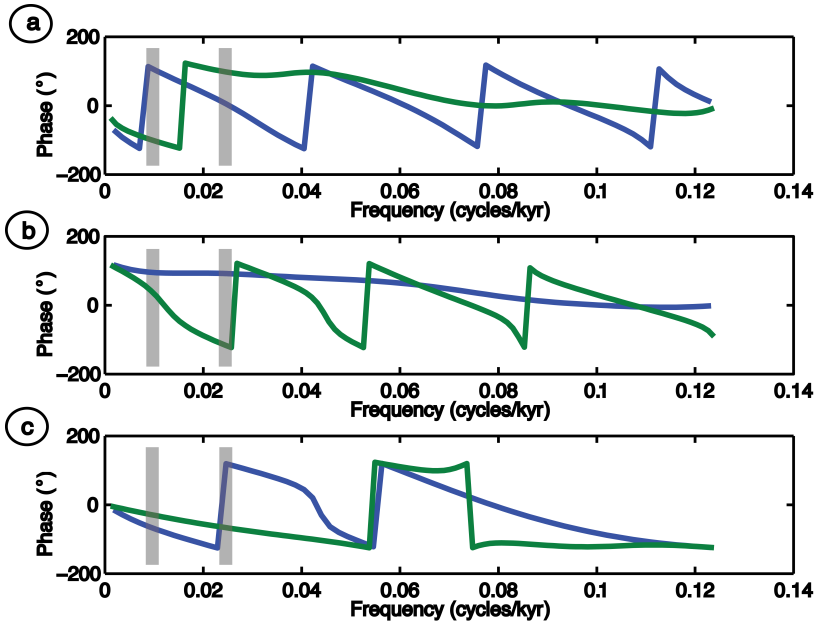

Figure 6.4: Phase functions for the first order GFRFs: a. $\angle H_1^1(j\omega_1)$, b. $\angle H_2^1(j\omega_1)$ and c. $\angle H_3^1(j\omega_1)$ for ***before MPT*** (blue) and ***after MPT.*** (green)

Figure 6.3a shows $H_1^1(j\omega)$ for ***models B*** (blue) and ***A*** (green). It can be seen that $|H_{1A}^1(j\omega)| > |H_{1B}^1(j\omega)|$. Also the location of the magnitude peaks changes. Frequencies corresponding to the magnitude peaks change as following: ***before MPT*** the two main peaks, located at the frequencies f_{95} and f_{19} have the magnitudes of 9.48 and 7.62. ***After MPT***, the three main magnitude peaks are located at the frequencies f_{17}, f_{57} and f_{10} and have the magnitudes of 28.83, 21.01 and 7.83, respectively. Given $H_1^1(j\omega)$ has the largest magnitude values of all the first order transfer functions, it is reasonable to assume that, through this linear FRF, the *eccentricity* contributes the most to the output spectrum, especially ***after MPT***.

Figure 6.3b, which shows $H_2^1(j\omega)$ for the two time periods, reveals that ***before MPT*** the major magnitude peaks are located at the frequencies f_{284} and f_{14} with the corresponding magnitudes of 0.43 and 0.53. ***After MPT*** the main magnitude peaks are located at the frequencies f_{34}, f_{16} and f_{10} and have the magnitudes 0.32, 0.53 and 0.25, respectively.

When analysing $|H_3^1(j\omega)|$ shown in Figure 6.3c, it can be seen that both magnitude curves have maximum values less than 10^{-3}, which implies that the contribution of $H_3^1(j\omega)$ to the

output spectrum will be small for both time periods.

The phase of the frequency transfer function was analyzed in a small interval of frequencies around the frequencies of interest, namely $\sim f_{100}$ and f_{41}. These intervals are marked with grey in Figure 6.4. For the interval $[f_1, f_2]$ providing the frequencies around $\sim f_{100}$, the most significant difference between the two time periods is in the phase functions corresponding to $H_1^1(j\omega)$, shown in Figure 6.4a, which are 162.71° ***before MPT*** and −149.35° ***after MPT***.

Around f_{41} both $H_2^1(j\omega)$, shown in Figure 6.4b, and $H_3^1(j\omega)$, shown in Figure 6.4c, show very dramatic difference between the phase functions. It is interesting to notice that in this interval of frequencies, $H_{2A}^1(j\omega)$ presents a large difference between the phase functions, from 131.59° ***before MPT*** to −166.75° ***after MPT***. A large difference also appears in the phase of $H_{3B}^1(j\omega)$ at f_{41}, with the phase functions value changing from 170.69° ***before MPT*** to −94.89° ***after MPT***. The fact that these differences appear in the interval of frequencies around f_{41} cycles/kyr could also contribute to the shift in frequencies of oscillation observed during the Mid-Pleistocene Transition.

Tables 6.6 and 6.7 summarize the magnitudes and phase values for the first order GFRFs ***before*** and ***after MPT*** at the frequencies of interest $\sim f_{100}$ and f_{41}, respectively.

i	$\lvert H_{iB}^1(j\omega)\rvert$	$\lvert H_{iA}^1(j\omega)\rvert$	$\angle H_{iB}^1(j\omega)$	$\angle H_{iA}^1(j\omega)$	Phase difference
1	9.2223	17.6665	162.71°	−149.35°	312.05°
2	0.3022	0.1063	137.55°	37.04°	100.52°
3	0.0046	0.0024	−89.70°	−45.63°	−44.07°

Table 6.6: Magnitude and phase functions values at the frequency $\sim f_{100}$ for the first order GFRFs.

i	$\lvert H_{iB}^1(j\omega)\rvert$	$\lvert H_{iA}^1(j\omega)\rvert$	$\angle H_{iB}^1(j\omega)$	$\angle H_{iA}^1(j\omega)$	Phase difference
1	5.9351	18.6693	7.24°	140.63°	−133.39°
2	0.1988	0.2954	131.59°	−166.75°	298.46°
3	0.0012	0.0017	170.69°	−94.89°	265.59°

Table 6.7: Magnitude and phase functions values at the frequency $\sim f_{41}$ for the first order GFRFs.

Figures 6.5, 6.7, 6.9, 6.11, 6.13 and 6.15 show the magnitudes for each of the second order GFRFs $H_1^2(j\omega_1, j\omega_2)$, $H_2^2(j\omega_1, j\omega_2)$, $H_3^2(j\omega_1, j\omega_2)$, $H_{12}^2(j\omega_1, j\omega_2)$, $H_{13}^2(j\omega_1, j\omega_2)$ and

$H^2_{23}(j\omega_1, j\omega_2)$ ***before*** and ***after MPT***. The figures also show sections through the magnitude functions along the lines $f_1 + f_2 =\sim f_{100}$ (red) and $f_1 + f_2 = f_{41}$ (green).

Figures 6.6, 6.8, 6.10, 6.12, 6.14 and 6.16 show the phase functions of each of the GFRFs $H^2_1(j\omega_1, j\omega_2)$, $H^2_2(j\omega_1, j\omega_2)$, $H^2_3(j\omega_1, j\omega_2)$, $H^2_{12}(j\omega_1, j\omega_2)$, $H^2_{13}(j\omega_1, j\omega_2)$ and $H^2_{23}(j\omega_1, j\omega_2)$, respectively, ***before*** and ***after MPT*** and also the corresponding phase of the section along $f_1 + f_2 =\sim f_{100}$ and $f_1 + f_2 = f_{41}$.

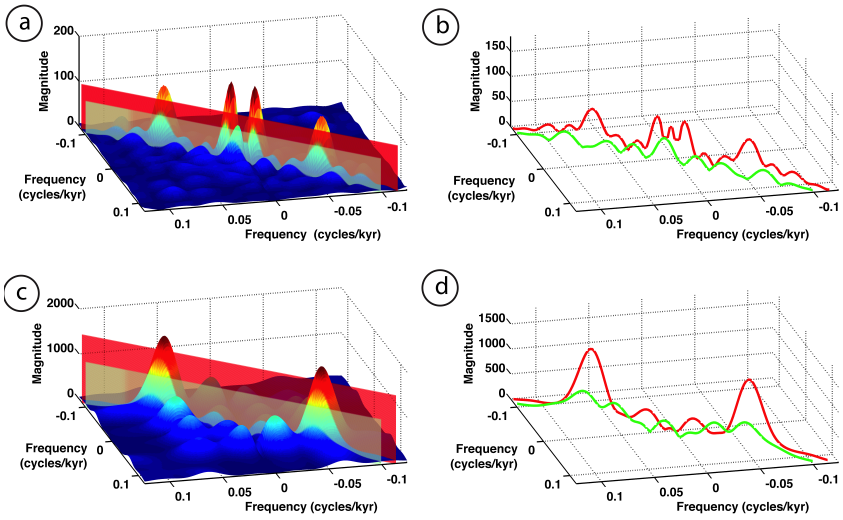

Figure 6.5: Magnitude functions for the second order self-kernel GFRFs: a. $|H^2_{1B}(j\omega_1)|$ c. $|H^2_{1A}(j\omega_1)|$, and the planes $f_1 + f_2 =\sim f_{100}$ (red) and $f_1 + f_2 = f_{41}$ (green) b. ***before MPT*** and d. ***after MPT.***

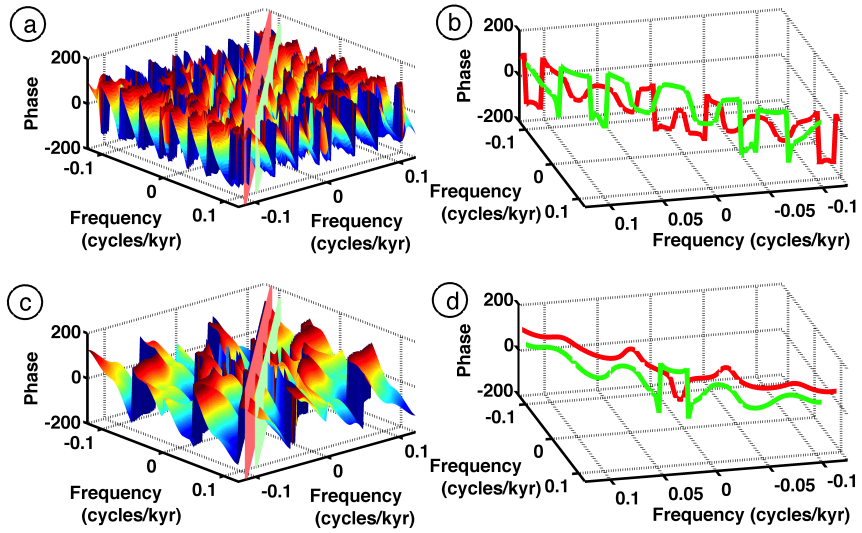

Figure 6.6: Phase functions for the second order self-kernel GFRFs: a. $\angle H^2_{1B}(j\omega_1, j\omega_2)$, c. $\angle H^2_{1A}(j\omega_1, j\omega_2)$, and the planes $f_1 + f_2 =\sim f_{100}$ (red) and $f_1 + f_2 = f_{41}$ (green) b. ***before MPT*** and d. ***after MPT***.

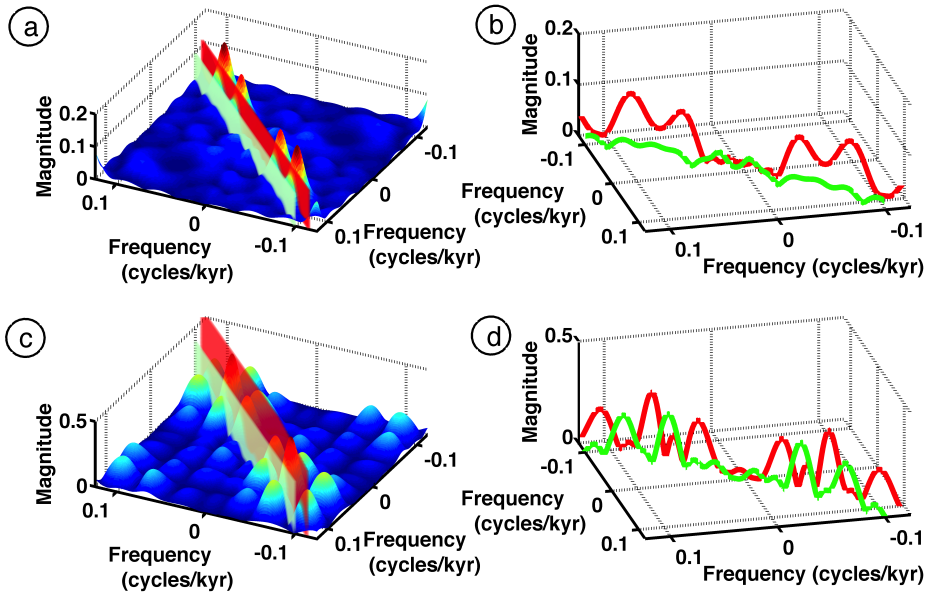

Figure 6.7: Magnitude functions for the second order self-kernel GFRFs: a. $|H^2_{2B}(j\omega_1)|$, c. $|H^2_{2A}(j\omega_1)|$, and the planes $f_1 + f_2 =\sim f_{100}$ (red) and $f_1 + f_2 = f_{41}$ (green) b. ***before MPT*** and d. ***after MPT***.

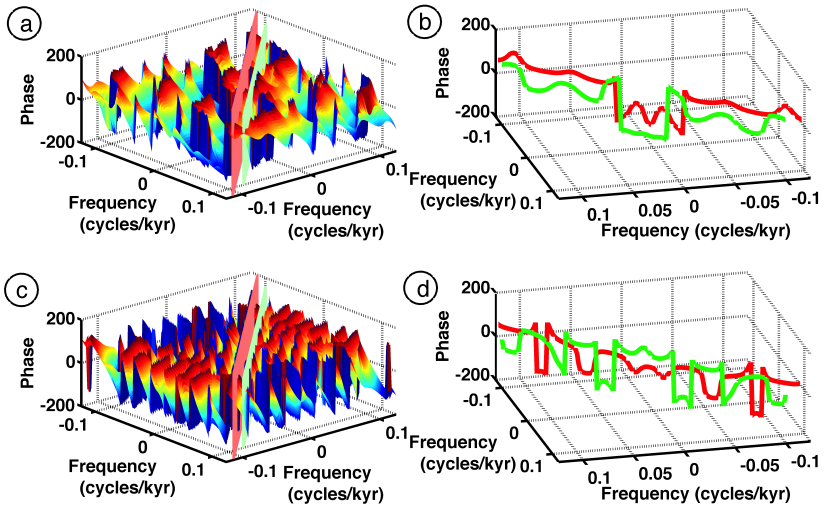

Figure 6.8: Phase functions for the second order self-kernel GFRFs: a. $\angle H^2_{2B}(j\omega_1, j\omega_2)$, c. $\angle H^2_{2A}(j\omega_1, j\omega_2)$, and the planes $f_1 + f_2 =\sim f_{100}$ (red) and $f_1 + f_2 = f_{41}$ (green) b. ***before MPT*** and d. ***after MPT***.

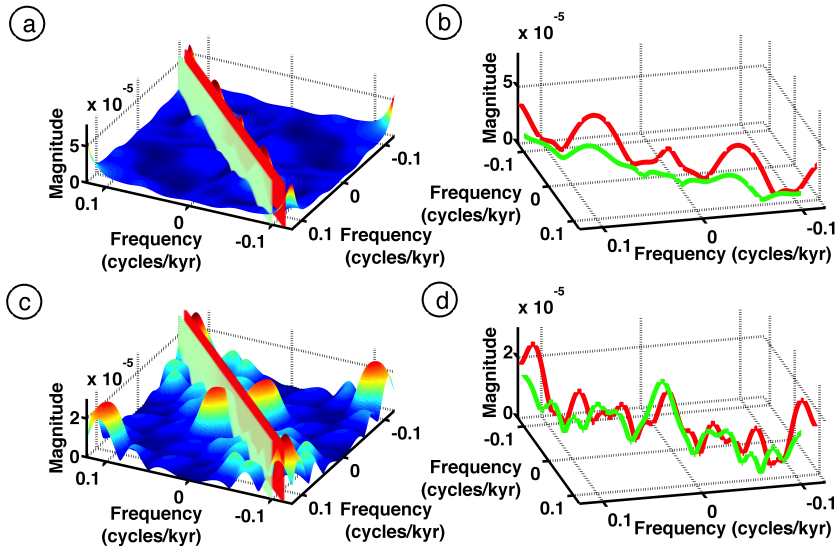

Figure 6.9: Magnitude functions for the second order self-kernel GFRFs: a. $|H^2_{3B}(j\omega_1)|$, c. $|H^2_{3A}(j\omega_1)|$, and the planes $f_1 + f_2 =\sim f_{100}$ (red) and $f_1 + f_2 = f_{41}$ (green) b. ***before MPT*** and d. ***after MPT***.

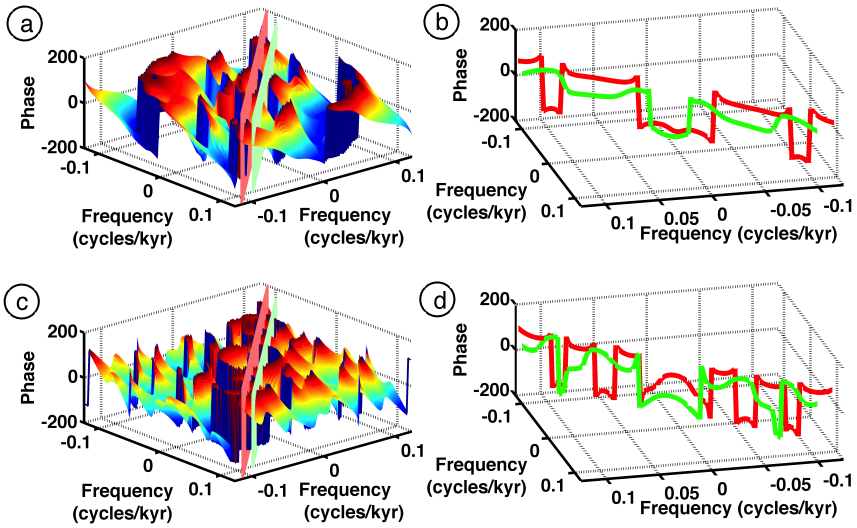

Figure 6.10: Phase functions for the second order self-kernel GFRFs: a. $\angle H^2_{3B}(j\omega_1, j\omega_2)$, c. $\angle H^2_{3A}(j\omega_1, j\omega_2)$, and the planes $f_1 + f_2 =\sim f_{100}$ (red) and $f_1 + f_2 = f_{41}$ (green) b. ***before MPT*** and d. ***after MPT***.

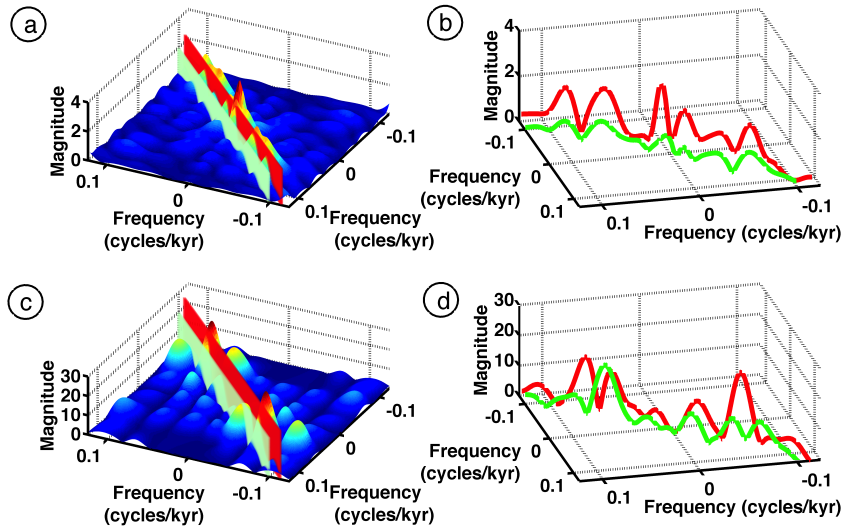

Figure 6.11: Magnitude functions for the second order self-kernel GFRFs: a. $|H^2_{12B}(j\omega_1)|$, c. $|H^2_{12A}(j\omega_1)|$, and the planes $f_1 + f_2 =\sim f_{100}$ (red) and $f_1 + f_2 = f_{41}$ (green) b. ***before MPT*** and d. ***after MPT***

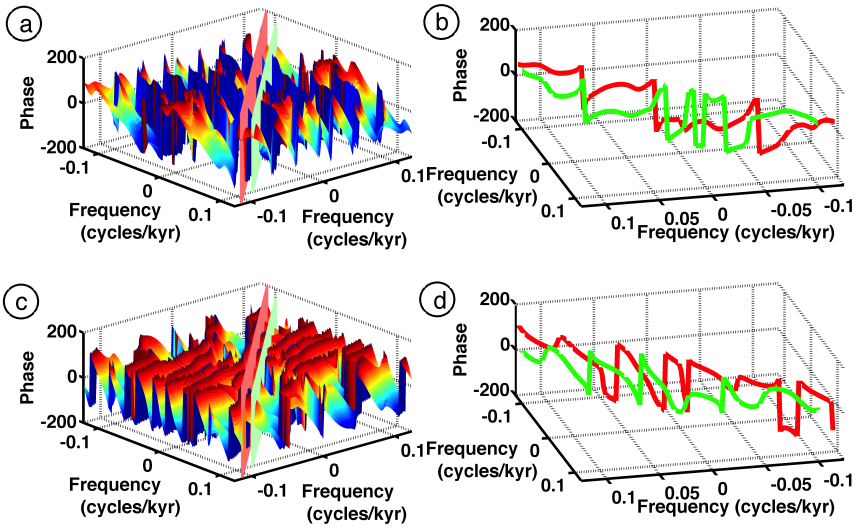

Figure 6.12: Phase functions for the second order self-kernel GFRFs: a. $\angle H^2_{12B}(j\omega_1, j\omega_2)$, c. $\angle H^2_{12A}(j\omega_1, j\omega_2)$, and the planes $f_1 + f_2 = \sim f_{100}$ (red) and $f_1 + f_2 = f_{41}$ (green) b. ***before MPT*** and d. ***after MPT***.

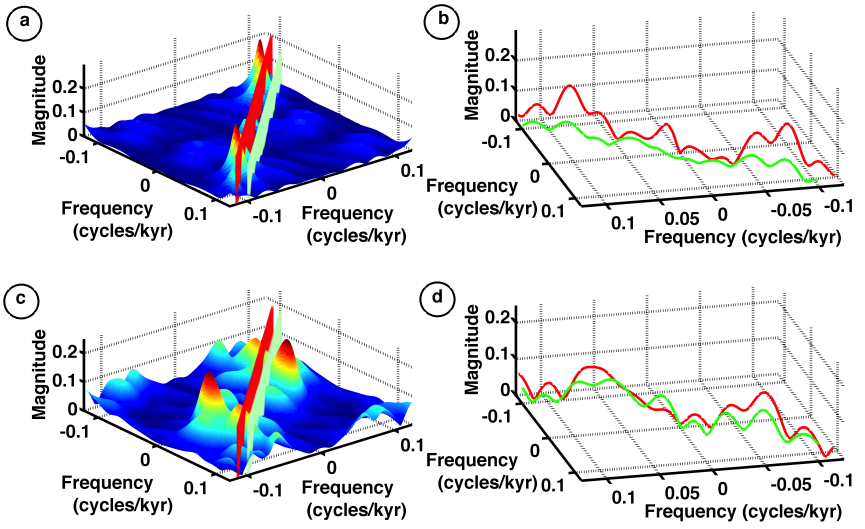

Figure 6.13: Magnitude functions for the second order self-kernel GFRFs: a. $|H^2_{13B}(j\omega_1)|$, c. $|H^2_{13A}(j\omega_1)|$, and the planes $f_1 + f_2 = \sim f_{100}$ (red) and $f_1 + f_2 = f_{41}$ (green) b. ***before MPT*** and d. ***after MPT***.

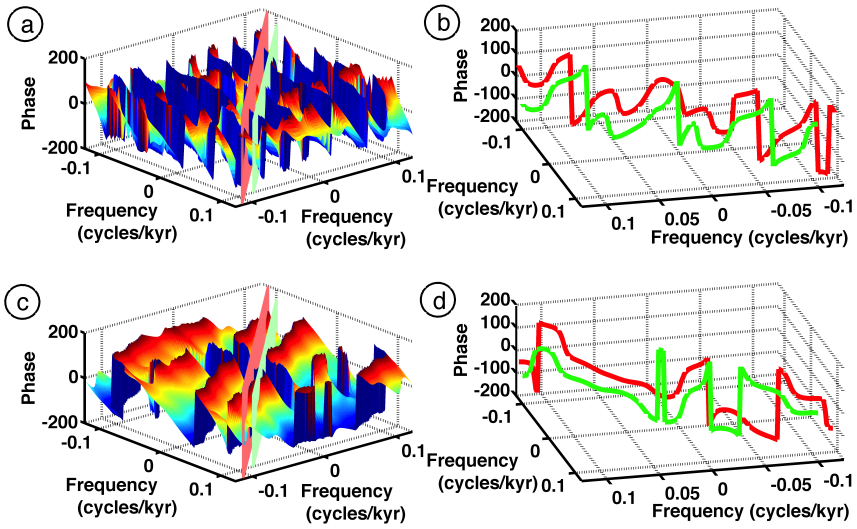

Figure 6.14: Phase functions for the second order self-kernel GFRFs: a. $\angle H^2_{13B}(j\omega_1, j\omega_2)$, c. $\angle H^2_{13A}(j\omega_1, j\omega_2)$, and the planes $f_1 + f_2 =\sim f_{100}$ (red) and $f_1 + f_2 = f_{41}$ (green) b. ***before MPT*** and d. ***after MPT***.

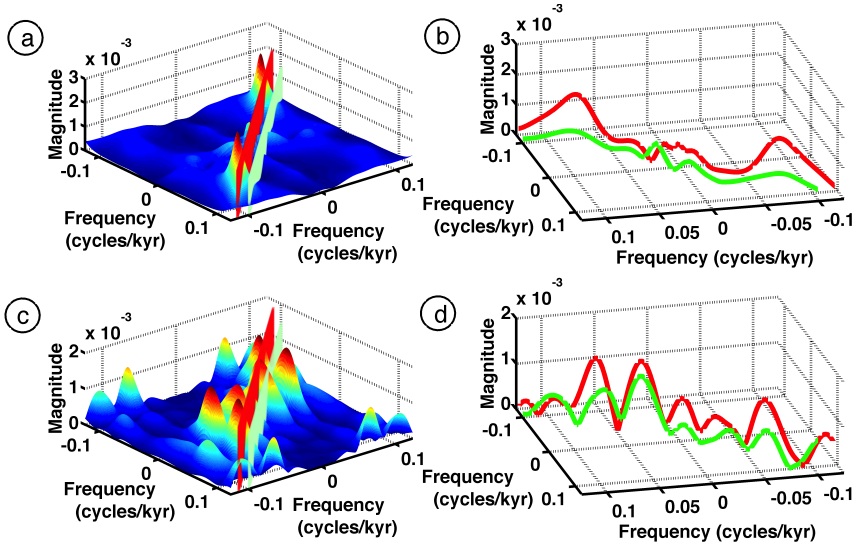

Figure 6.15: Magnitude functions for the second order self-kernel GFRFs: a. $|H^2_{23B}(j\omega_1)|$, c. $|H^2_{23A}(j\omega_1)|$, and the planes $f_1 + f_2 =\sim f_{100}$ (red) and $f_1 + f_2 = f_{41}$ (green) b. ***before MPT*** and d. ***after MPT***.

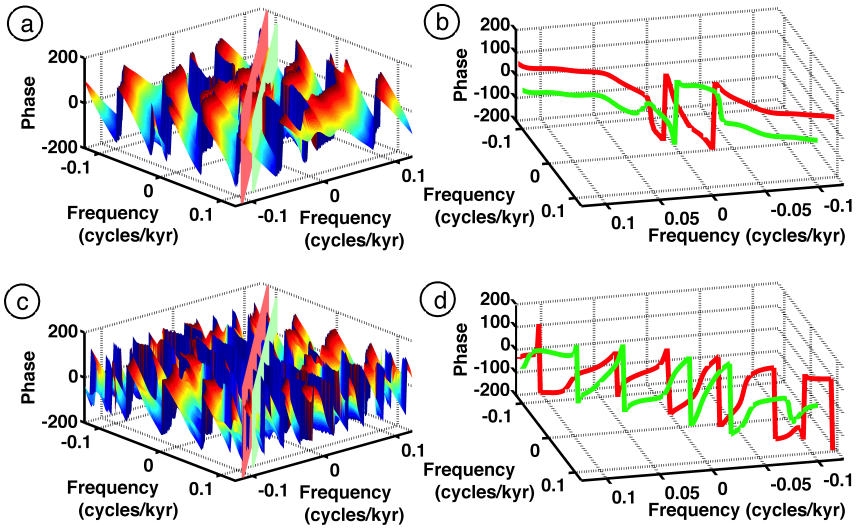

Figure 6.16: Phase functions for the second order self-kernel GFRFs: a. $\angle H^2_{23B}(j\omega_1, j\omega_2)$, c. $\angle H^2_{23A}(j\omega_1, j\omega_2)$, and the planes $f_1 + f_2 =\sim f_{100}$ (red) and $f_1 + f_2 = f_{41}$ (green) b. ***before MPT*** and d. ***after MPT***.

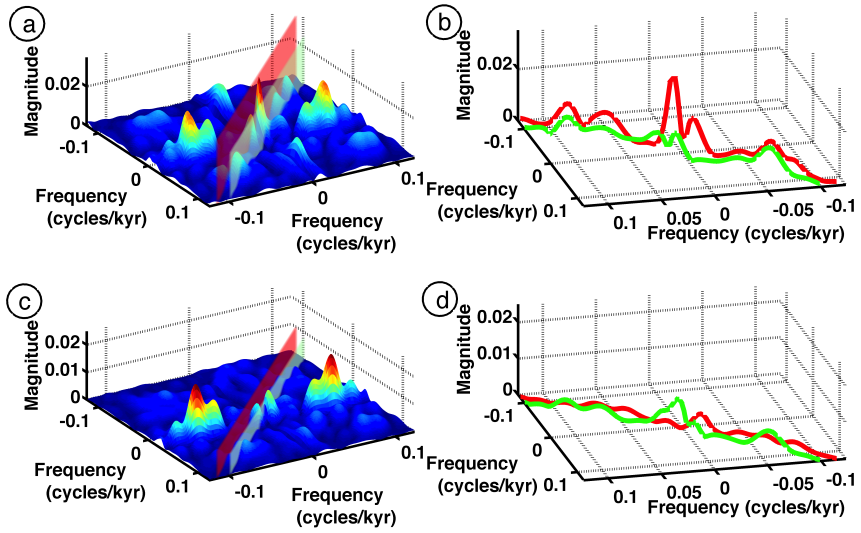

Figure 6.17: a., c. Magnitudes $|H^3_{123B}(j\omega_1, j\omega_2, j\omega_3)|$ for $f_3 = f - f_1 - f_2$ and b., d. the planes $f_1 + f_2 + f_3 = f$ with $f_3 = f_{100}$ (red) and $f_3 = f_{41}$(green) for a, b. $f = f_{100}$, c,d. $f = f_{41}$ for ***before MPT.***

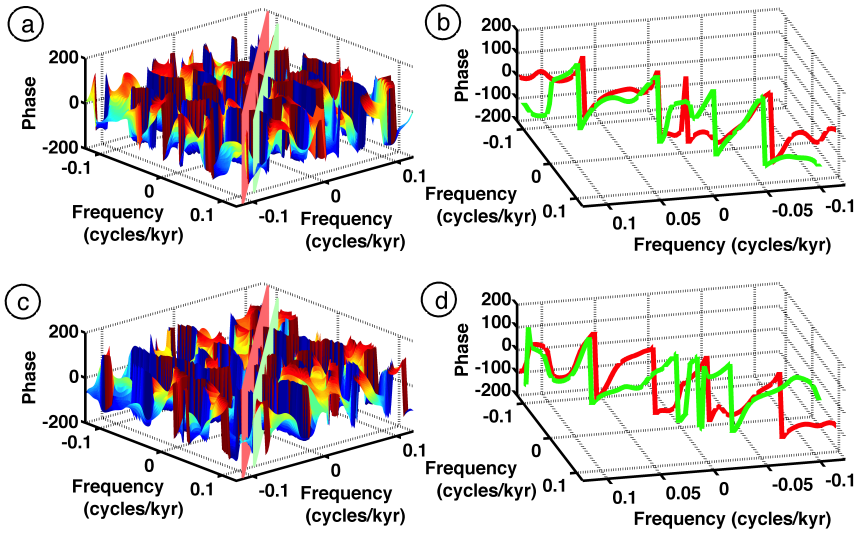

Figure 6.18: a., c. Phase functions $\angle H^3_{123b}(j\omega_1, j\omega_2, j\omega_3)$, for $f_3 = f - f_1 - f_2$ and b., d. the phase planes $f_1 + f_2 + f_3 = f$ with $f_3 = f_{100}$ (red) and $f_3 = f_{41}$(green) for a, b. $f = f_{100}$, c, d. $f = f_{41}$ for ***before MPT.***

The most significant magnitude peaks in the second order GFRFs are given in Table 6.8 and shown on the contour maps for each GFRF in Figures 6.19 and 6.20.

GFRF	Peaks (f_1, f_2)	Located on
$H^2_{1B}(j\omega_1, j\omega_2)$	$(f_{95}, -f_{95}), (-f_{95}, f_{95}), (f_{17}, -f_{17}), (-f_{17}, f_{17})$	$f_1 + f_2 = 0$
$H^2_{1A}(j\omega_1, j\omega_2)$	$(f_{17}, -f_{17}), (-f_{17}, f_{17})$	$f_1 + f_2 = 0$
	$(f_{61}, -f_{17}), (-f_{17}, f_{61}), (f_{17}, -f_{61}), (-f_{61}, f_{17})$	
$H^2_{2B}(j\omega_1, j\omega_2)$	$(f_{12}, -f_{12}), (-f_{12}, f_{12}), (f_{23}, -f_{23}), (f_{23}, -f_{23}),$ $(f_{10}, -f_{10}), (-f_{10}, f_{10})$	$f_1 + f_2 = 0$
$H^2_{2A}(j\omega_1, j\omega_2)$	$(f_{16}, -f_{16}), (-f_{16}, f_{16}), (f_{31}, -f_{31}),$	$f_1 + f_2 = 0$
	$(f_{16}, -f_{10}), (f_{10}, -f_{16})$ and $(-f_{16}, f_{10}), (-f_{10}, f_{16})$	$f_1 - f_2 = \pm\frac{1}{6}$
	$(f_{31}, -f_{16}), (f_{16}, -f_{31})$ and $(-f_{31}, f_{16}), (-f_{16}, f_{31})$	$f_1 - f_2 = \pm f_{10}$
$H^2_{3B}(j\omega_1, j\omega_2)$	$(f_{17}, -f_{17}), (-f_{17}, f_{17}), (f_8, -f_8), (f_8, -f_8),$ $(f_{555}, -f_{555}), (-f_{555}, f_{555})$	$f_1 + f_2 = 0$
	$(f_8, f_8), (-f_8, -f_8)$	$f_1 - f_2 = 0$
$H^2_{3A}(j\omega_1, j\omega_2)$	$(f_9, -f_9), (-f_9, f_9)$	$f_1 + f_2 = 0$
	$(f_9, f_9), (-f_9, -f_9), (f_{48}, f_{48}), (-f_{48}, -f_{48})$	$f_1 - f_2 = 0$
$H^2_{12B}(j\omega_1, j\omega_2)$	$(f_{142}, -f_{555}), (-f_{142}, f_{555}), (f_{17}, -f_{23}), (-f_{17}, f_{23}),$ $(f_{16}, -f_{16}), (-f_{16}, f_{16})$	$f_1 + f_2 \simeq 0$
$H^2_{12A}(j\omega_1, j\omega_2)$	f_1 is in the interval $\pm[f_{17}, f_{16}]$ and f_2 has the values: $f_2 = \{\mp f_{16}, \mp f_{31}, \mp f_{10}\}$	
$H^2_{13B}(j\omega_1, j\omega_2)$	$(f_{12}, -f_{12}), (-f_{12}, f_{12}), (f_{10}, -f_{10}), (-f_{10}, f_{10}),$ $(f_{17}, -f_{16}), (-f_{17}, f_{16})$	$f_1 + f_2 = 0$
	$(f_{142}, -f_{284}), (-f_{142}, f_{284})$	$f_1 + f_2 \simeq 0$
$H^2_{13A}(j\omega_1, j\omega_2)$	$(f_{17}, -f_{113}), (-f_{17}, f_{113}), (f_{16}, -f_{16}), (-f_{16}, f_{16})$	
$H^2_{23B}(j\omega_1, j\omega_2)$	$(f_{13}, -f_{13}), (-f_{13}, f_{13}), (f_{555}, -f_{555}), (-f_{555}, f_{555})$	$f_1 + f_2 = 0$
$H^2_{23A}(j\omega_1, j\omega_2)$	$(f_{16}, -f_{16}), (-f_{16}, f_{16}), (f_{856}, -f_{428}), (-f_{856}, f_{428})$	$f_1 + f_2 = 0$
	$(-f_{57}, f_{16}), (f_{57}, -f_{16}), (f_{50}, -f_{31}), (-f_{50}, f_{31}),$ $(f_8, -f_{16}), (-f_8, f_{16}), (f_8, f_{16}), (-f_8, -f_{16})$	

Table 6.8: Location of the main peaks in the second order GFRFs.

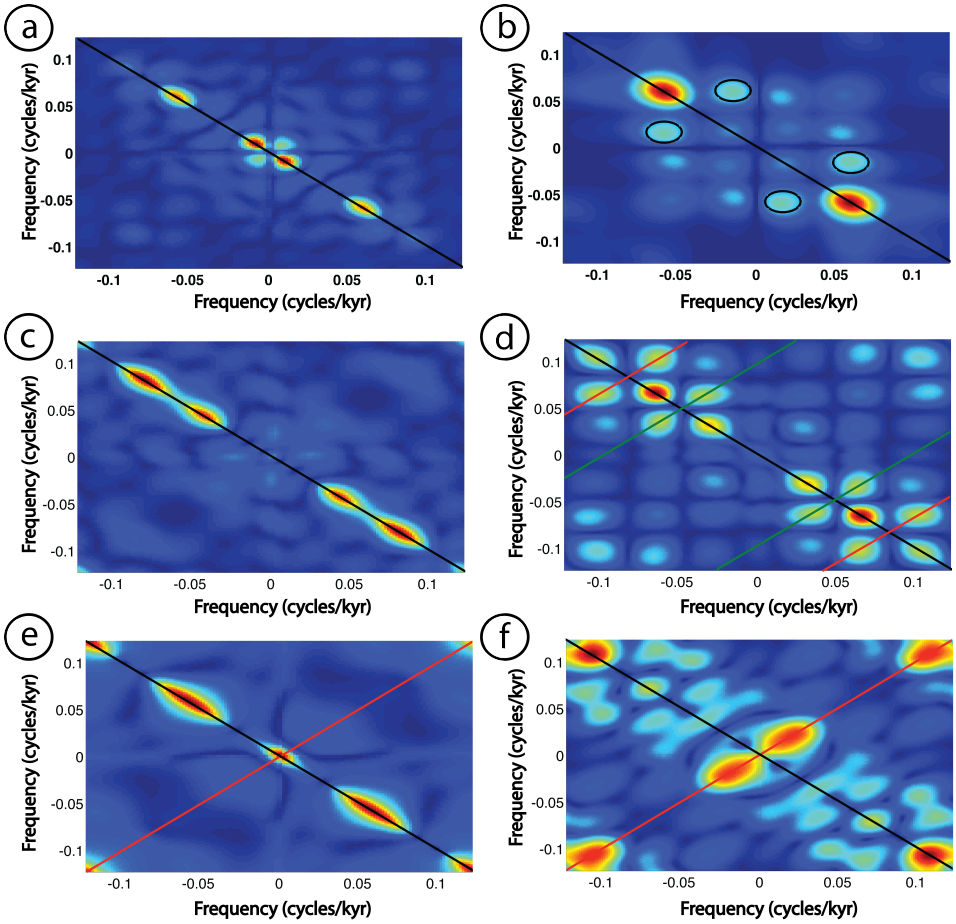

Figure 6.19: Contour maps showing the significant peaks locations for the second order self-kernel GFRFs: a. $H^2_{1B}(j\omega_1, j\omega_2)$, b. $H^2_{1A}(j\omega_1, j\omega_2)$, c. $H^2_{2B}(j\omega_1, j\omega_2)$, d. $H^2_{2A}(j\omega_1, j\omega_2)$, the green lines represent the planes $f_1 - f_2 = \pm f_{10}$ and the red lines represent the planes $f_1 - f_2 = \pm f_6$, e. $H^2_{3B}(j\omega_1, j\omega_2)$, the red line represents the plane $f_1 - f_2 = 0$, f. $H^2_{3A}(j\omega_1, j\omega_2)$, the red line represents the plane $f_1 - f_2 = 0$. In all plots diagonal black line represents the plane $f_1 + f_2 = 0$ and all the significant peaks locations (f_1, f_2) are listed in Table 6.8.

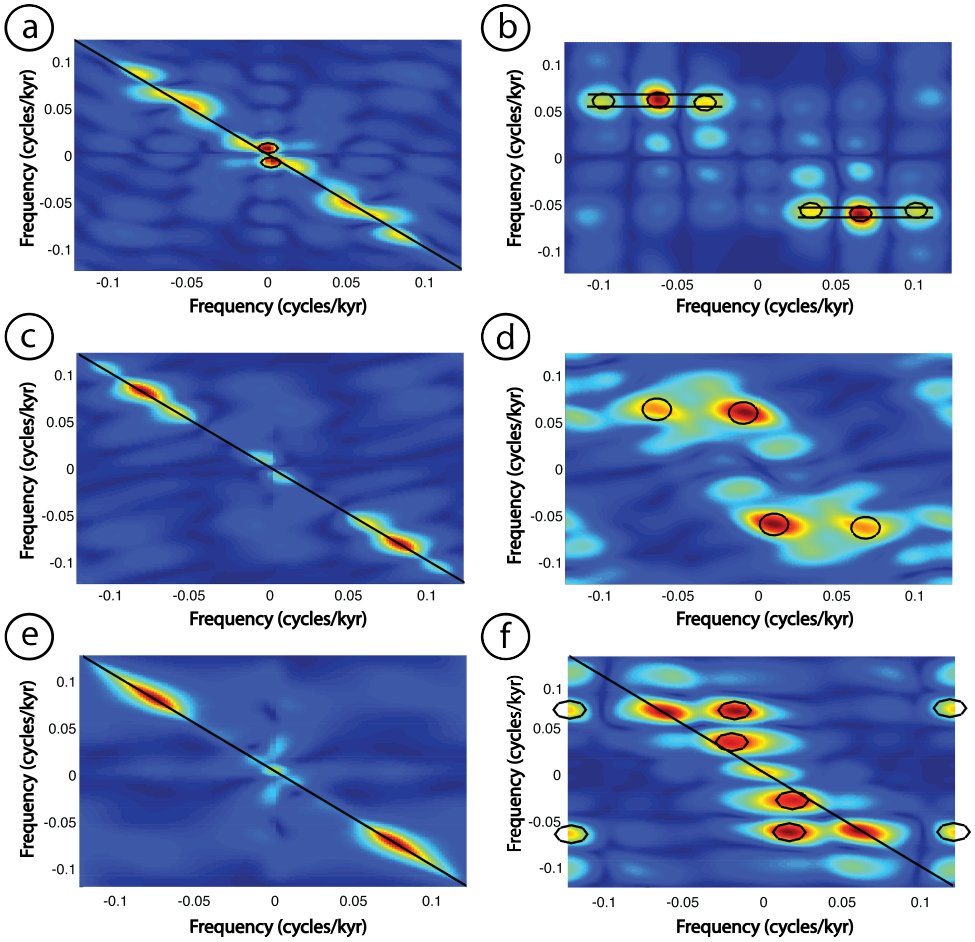

Figure 6.20: Contour maps showing the significant peaks locations for the second order cross-kernel GFRFs: a. $H^2_{12B}(j\omega_1, j\omega_2)$, b. $H^2_{12A}(j\omega_1, j\omega_2)$, c. $H^2_{13B}(j\omega_1, j\omega_2)$, d. $H^2_{13A}(j\omega_1, j\omega_2)$, e. $H^2_{23B}(j\omega_1, j\omega_2)$, f. $H^2_{23A}(j\omega_1, j\omega_2)$. Where present, the diagonal black line represents the plane $f_1 + f_2 = 0$ all the significant peaks locations (f_1, f_2) are listed in Table 6.8.

The third order GFRFs cannot be plotted in full so in order to visualise the results slices through $H^3(\omega_1, \omega_2, \omega_T - \omega_1 - \omega_2)$ were computed by setting $\omega_3 + \omega_2 + \omega_1 = \omega_T$, where $\omega_T = 2\pi f_T$ corresponds to a frequency of interest. Figure 6.17 presents for comparison the results of plotting the third order GFRF $H^3_{123}(j\omega_1, j\omega_2, j\omega_3)$ for f taking in turns the values of the frequencies of interest $f_T = f_{100}$ and $f_T = f_{41}$.

6.3.3 Analysis and Comparison of the Output Frequency Responses Results

Using the expressions of the OFRs as derived in Section 6.2.3, the magnitude and phase functions for each OFR are calculated and plotted for the frequency range given by ω.

Figures 6.21, 6.22 and 6.23 show the magnitudes and phase functions of each of the ***first order OFRs*** $Y_1^1(j\omega)$, $Y_2^1(j\omega)$ and $Y_3^1(j\omega)$, respectively.

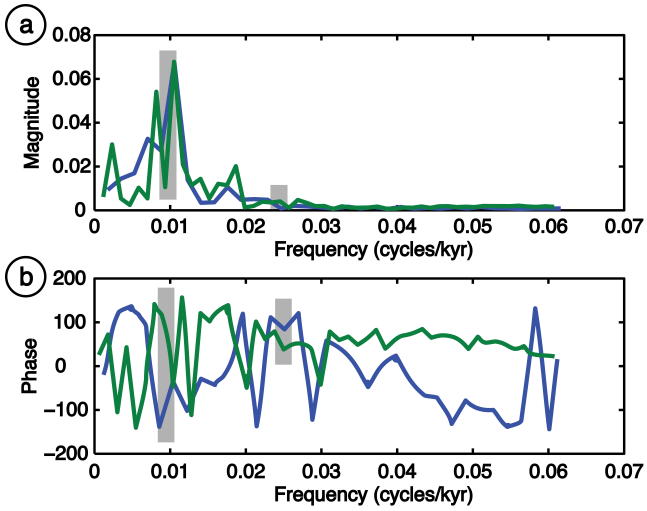

Figure 6.21: a. Magnitude $|Y_1^1(j\omega)|$ and b. Phase functions $\angle Y_1^1(j\omega)$ of $Y_1^1(j\omega)$ ***before MPT*** (blue) and ***after MPT*** (green).

Figure 6.21a shows that the maximum value of $|Y_1^1(j\omega)|$ has the same value of 0.068 and corresponds to the same frequency f_{95} for both periods. $|Y_{1A}^1(j\omega)|$ also has significant peaks located at the frequencies f_{122} and f_{428}.

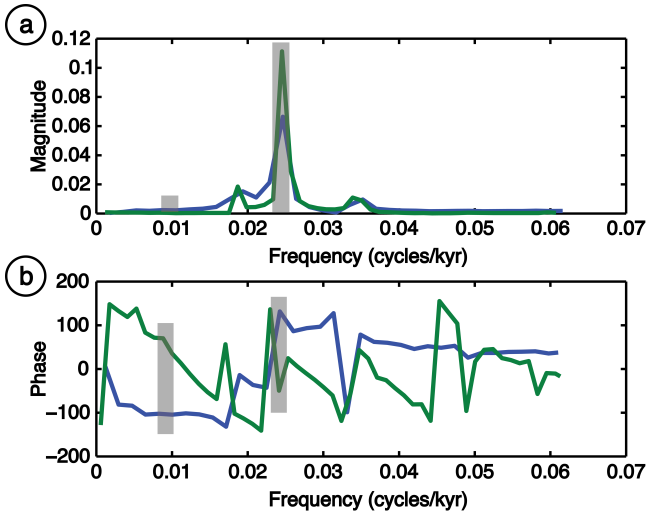

Figure 6.22: a. Magnitude $|Y_2^1(j\omega)|$ and b. Phase functions $\angle Y_2^1(j\omega)$ of $Y_2^1(j\omega)$ for ***before MPT*** (blue) and ***after MPT*** (green).

Figure 6.22a shows that the largest magnitudes of the OFRs $|Y_{1B}^2(j\omega)|$ and $|Y_{1A}^2(j\omega)|$ are located at the frequency f_{41}. There is an almost 100% increase in the magnitude of $Y_1^2(j\omega)$ at f_{41} from a value of 0.066 ***before MPT*** to 0.11 ***after MPT***.

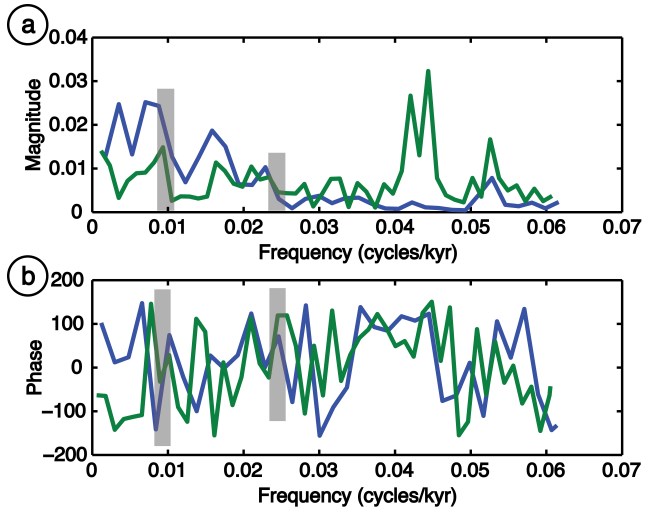

Figure 6.23: a. Magnitude $|Y_3^1(j\omega)|$ and b. Phase functions $\angle Y_3^1(j\omega)$ of $Y_3^1(j\omega)$ ***before MPT*** (blue) and ***after MPT*** (green).

Figure 6.23a shows that the largest magnitude of $|Y_{3B}^1(j\omega)|$ is 0.025 and is located at the frequency f_{142}, and the largest magnitude for $|Y_{3A}^1(j\omega)|$ is 0.032 and is located at the

frequency f_{23}. The magnitude values of $Y^1_{3B}(j\omega)$ in the interval of frequencies $[f_{115}, f_{93}]$ are roughly twice compared to the magnitude values of $Y^1_{3A}(j\omega)$, so a drastic decrease in magnitude is observed at the frequency $\sim f_{100}$.

Figures 6.24, 6.25 and 6.26 show the magnitude and phase functions of the ***second order self-kernel OFRs*** $Y^2_1(j\omega)$, $Y^2_2(j\omega)$ and $Y^2_3(j\omega)$, respectively.

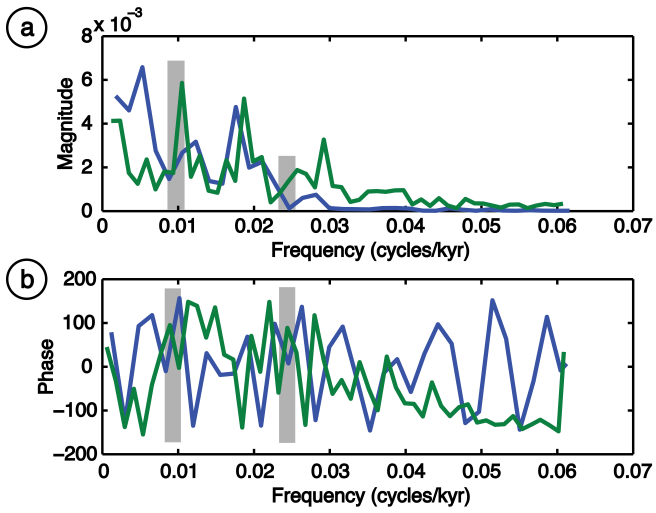

Figure 6.24: a. Magnitude $|Y^2_1(j\omega)|$ and b. Phase functions $\angle Y^2_1(j\omega)$ of $Y^2_1(j\omega)$ ***before MPT*** (blue) and ***after MPT*** (green).

The maximum $|Y^2_{1B}(j\omega)|$ is 0.0066 and is located at the frequency f_{189} and the largest $|Y^2_{1A}(j\omega)|$ is 0.0059 and is located at the frequency f_{95}. This latest value is considerably larger than the value 0.0027 of $|Y^2_{1B}(j\omega)|$ at the frequency $\sim f_{100}$. This shows that $Y^2_1(j\omega)$ at the frequency $\sim f_{100}$ has doubled ***after MPT***.

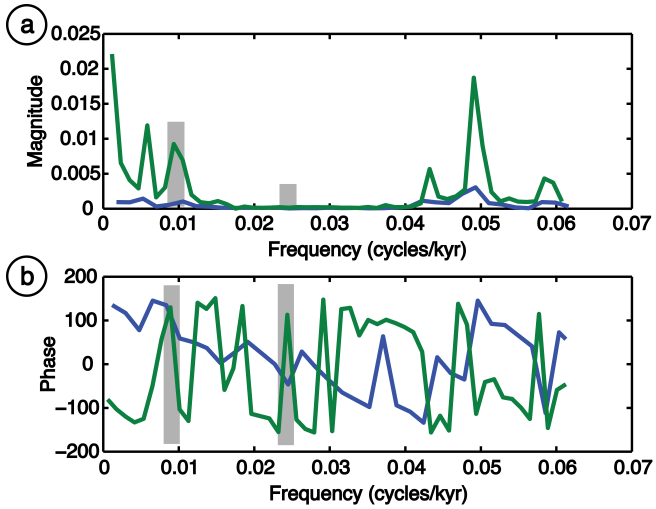

Figure 6.25: a. Magnitude $|Y_2^2(j\omega)|$ and b. Phase functions $\angle Y_2^2(j\omega)$ of $Y_2^2(j\omega)$ ***before MPT*** (blue) and ***after MPT*** (green).

The plot for $Y_2^2(j\omega)$ shows that for both of the time periods the highest peaks are at f_{21}. The magnitudes of $Y_{2B}^2(j\omega)$ and $Y_{2A}^2(j\omega)$ at this frequency are 0.0030 and 0.0187 respectively. Overall $|Y_{2A}^2(j\omega)| > |Y_{2B}^2(j\omega)|$. At the frequency f_{100} a major magnitude increase is observed from 0.0006 in $Y_{2B}^2(j\omega)$ to 0.0070 in $Y_{2A}^2(j\omega)$.

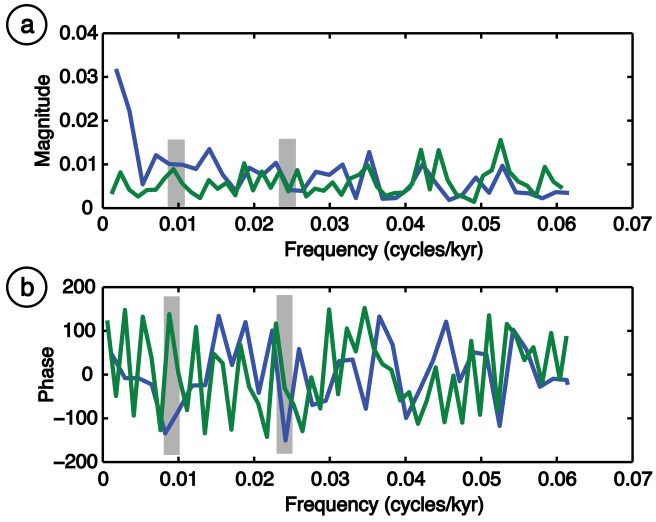

Figure 6.26: a. Magnitude $|Y_3^2(j\omega)|$ and b. Phase functions $\angle Y_3^2(j\omega)$ of $Y_3^2(j\omega)$ ***before MPT*** (blue) and ***after MPT*** (green).

$Y_3^2(j\omega)$ does not show significant differences between the magnitude values of the sig-

nals corresponding to the two time periods, and this hold for the two intervals of interest emphasized in Figure 6.26a.

Figures 6.27, 6.28 and 6.29 show the magnitudes and phase functions of the ***second order cross-kernel OFRs*** $Y_{12}^2(j\omega)$, $Y_{13}^2(j\omega)$ and $Y_{23}^2(j\omega)$, respectively.

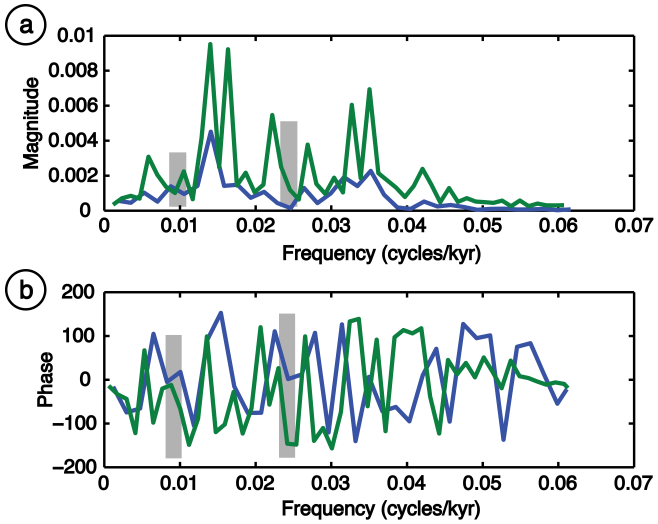

Figure 6.27: a. Magnitude $|Y_{12}^2(j\omega)|$ and b. Phase functions $\angle Y_{12}^2(j\omega)$ of $Y_{12}^2(j\omega)$ ***before MPT*** (blue) and ***after MPT*** (green).

For $Y_{12}^2(j\omega)$, in both cases, the largest magnitude is located at the frequency f_{71}, with $|Y_{12B}^2(j\omega)| = 0.0045$ and $|Y_{12A}^2(j\omega)| = 0.0095$. Overall, although the location of the main peaks are at similar frequencies in both spectra, $|Y_{12A}^2(j\omega)|$ shows significantly increased values compared to $|Y_{12B}^2(j\omega)|$.

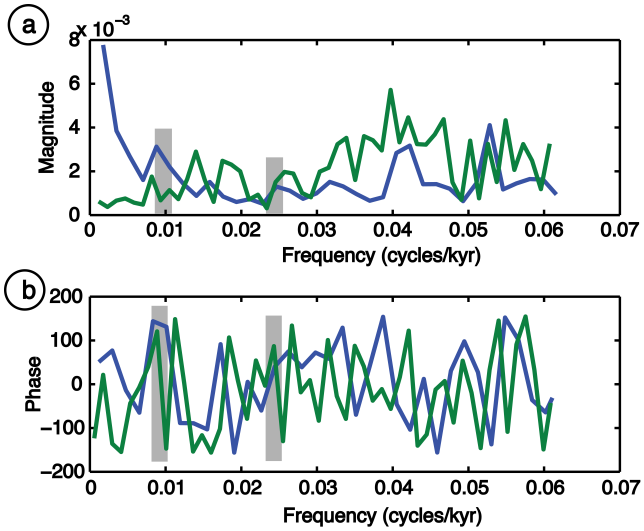

Figure 6.28: a. Magnitude $|Y_{13}^2(j\omega)|$ and b. Phase functions $\angle Y_{13}^2(j\omega)$ of $Y_{13}^2(j\omega)$ ***before MPT*** (blue) and ***after MPT*** (green).

When looking at the magnitude plot of $Y_{13}^2(j\omega)$ in Figure 6.28a, it can be seen that the main peaks are found at higher frequencies, starting at or after $\sim f_{27}$. The spectrum does not show a significant change at the frequency f_{41}. The change however is noticeable when analysing the interval $[f_{115} - f_{93}]$. Here the magnitude ***after MPT*** decreases to half the value of the magnitude ***before MPT***.

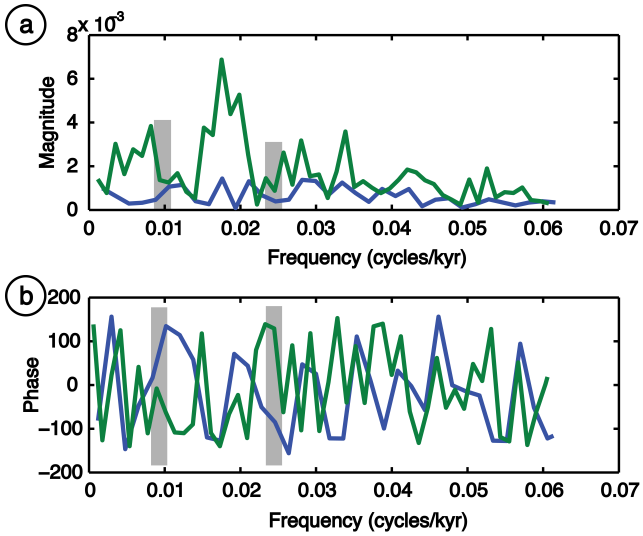

Figure 6.29: a. Magnitude $|Y_{23}^2(j\omega)|$ and b. Phase functions $\angle Y_{23}^2(j\omega)$ of $Y_{23}^2(j\omega)$ ***before MPT*** (blue) and ***after MPT*** (green).

Figure 6.29a shows that overall $|Y^2_{23B}(j\omega)| < |Y^2_{23A}(j\omega)|$. The largest magnitude of $Y^2_{23B}(j\omega)$ is 0.0014 and the one for $Y^2_{23A}(j\omega)$ is 0.0069. Both these values are located at the frequency f_{57}, which can be a subharmonic of f_{19}, a frequency found in the spectrum of $u_3(t)$, and can be written as $f_{57} = \frac{1}{3}f_{19}$.

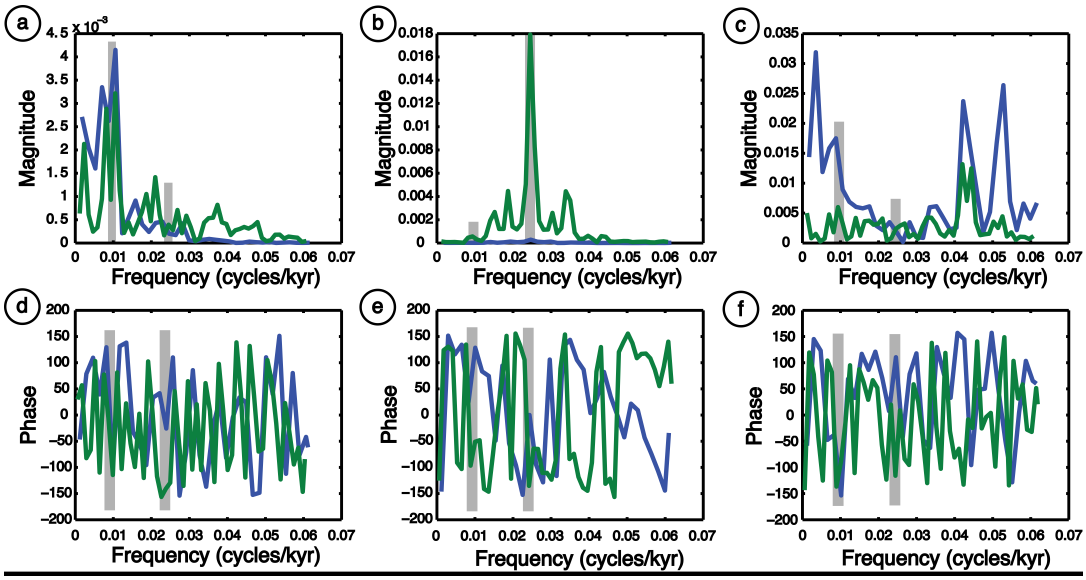

Figure 6.30: Magnitude a. $|Y^3_1(j\omega)|$, b. $|Y^3_2(j\omega)|$, c. $|Y^3_3(j\omega)|$ and Phase functions d. $\angle Y^3_1(j\omega)$, e. $\angle Y^3_2(j\omega)$, f. $\angle Y^3_3(j\omega)$ ***before MPT*** (blue) and ***after MPT*** (green).

Figure 6.30 shows the magnitudes and phase functions for the third order self-kernel OFRs $Y^3_1(j\omega)$, $Y^3_2(j\omega)$ and $Y^3_3(j\omega)$ ***before*** and ***after MPT***. Figure 6.30a shows that the maximum of both $|Y^3_{1B}(j\omega)|$ and $|Y^3_{1A}(j\omega)|$ is located at the frequency f_{95}, frequency found in the spectrum of $u_1(t)$. The values of the largest magnitudes are 0.0042 for $|Y^3_{1B}(j\omega)|$ and 0.0032 for $|Y^3_{1A}(j\omega)|$. As it can be observed, the values are very close. The second largest value for $|Y^3_{1B}(j\omega)|$ is 0.0033 and is located at the frequency f_{142} and for $|Y^3_{1A}(j\omega)|$ is 0.0029 and is located at the frequency f_{122}.

Figure 6.30b reveals that $|Y^3_{2B}(j\omega)| \ll |Y^3_{2A}(j\omega)|$. The largest $|Y^3_{1B}(j\omega)|$ is 0.00029 and the largest $|Y^3_{2A}(j\omega)|$ is 0.018 and are both located at the frequency f_{41}.

Figure 6.30c shows that for $|Y^3_{3B}(j\omega)|$ the four largest values are 0.032, 0.026, 0.024 and 0.018 and are located at the frequencies f_{284}, f_{19}, f_{23} and f_{113}, respectively. For $|Y^3_{3A}(j\omega)|$ the

largest values are 0.013, 0.012 and 0.006 and are located at the frequencies f_{23}, f_{22} and f_{107}, respectively. The phase functions for both $Y^3_{3B}(j\omega)$ and $Y^3_{3A}(j\omega)$ in the interval of frequency $[f_{115}, f_{93}]$ has similar values ($\sim -160°$).

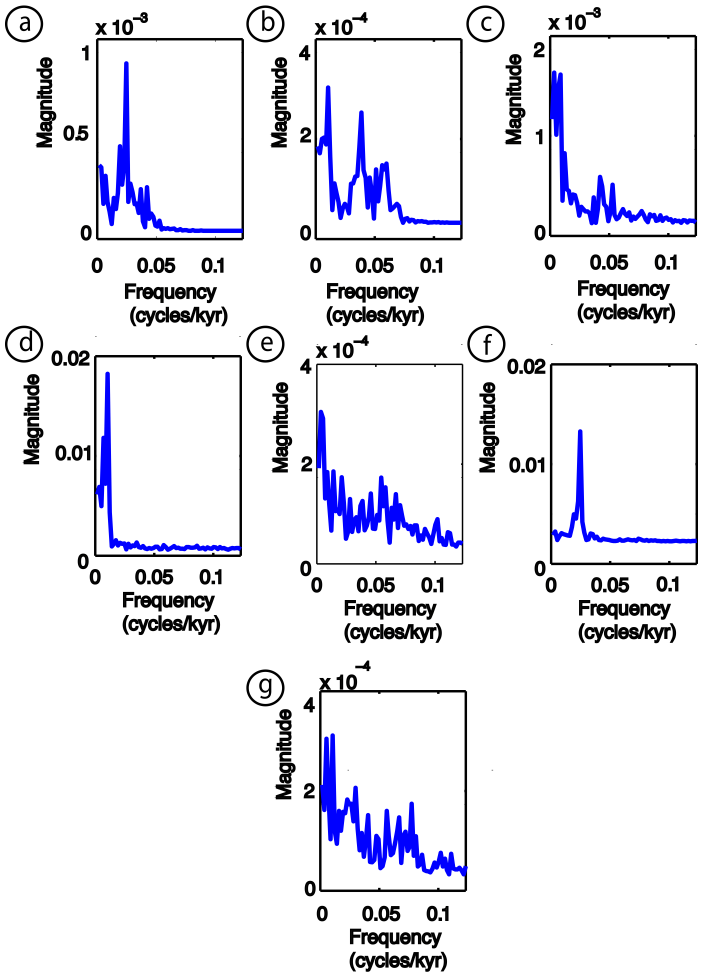

Figure 6.31: Magnitudes of the third order cross-kernel OFRs: a. $|Y^3_{112B}(j\omega)|$, b. $|Y^3_{122B}(j\omega)|$, c. $|Y^3_{113B}(j\omega)|$, d. $|Y^3_{133B}(j\omega)|$, e. $|Y^3_{223B}(j\omega)|$, f. $|Y^3_{233B}(j\omega)|$, g. $|Y^3_{123B}(j\omega)|$ ***before MPT***.

The ***third order cross-kernel OFRs*** $Y^3_{112B}(j\omega)$, $Y^3_{122B}(j\omega)$, $Y^3_{113B}(j\omega)$, $Y^3_{133B}(j\omega)$, $Y^3_{223B}(j\omega)$, $Y^3_{233B}(j\omega)$ and $Y^3_{123B}(j\omega)$ were computed for the time period ***before MPT*** only. They are shown in Figure 6.31 and the details of the major peaks are given in Table 6.9.

OFR	Peak 1		Peak 2 (if significant)	
	Magnitude	Frequency (cycles/kyr)	Magnitude	Frequency (cycles/kyr)
$Y^3_{112B}(j\omega)$	0.00084	f_{41}	-	
$Y^3_{122B}(j\omega)$	0.00027	f_{95}	0.00022	f_{26}
$Y^3_{113B}(j\omega)$	0.0015	f_{284}	0.0015	f_{113}
$Y^3_{133B}(j\omega)$	0.018	f_{95}	0.011	f_{142}
$Y^3_{223B}(j\omega)$	0.00027	f_{284}	-	
$Y^3_{233B}(j\omega)$	0.011	f_{41}	-	
$Y^3_{123B}(j\omega)$	0.00028	f_{95}	0.00028	f_{189}

Table 6.9: Magnitudes and location of the significant peaks in the third order cross-kernel OFRs ***before MPT***.

6.3.4 Analysis of the Changes Occurred During the MPT at $\sim f_{100}$ cycles/kyr Using the OFRs Results

As given in equation (6.2.3) the output spectrum $Y(j\omega)$ is the sum of the output frequency responses corresponding to all the GFRFs. For the time period ***before MPT***, $Y_B(j\omega)$ is approximated well, as seen in Figure 6.32a, by the sum:

$$\widetilde{Y}_B(j\omega) = \sum_{i=1}^{3} Y^1_{iB}(j\omega) + \sum_{i=1}^{3} Y^2_{iB}(j\omega) + Y^2_{12B}(j\omega) + Y^2_{13B}(j\omega) + Y^2_{23B}(j\omega) + \sum_{i=1}^{3} Y^3_{iB}(j\omega)$$

For the time period ***after MPT*** the third order cross-kernel OFRs $Y^3_{112}(j\omega)$, $Y^3_{122}(j\omega)$, $Y^3_{113}(j\omega)$, $Y^3_{133}(j\omega)$, $Y^3_{223}(j\omega)$,$Y^3_{233}(j\omega)$ and $Y^3_{123}(j\omega)$ had to be calculated additionally in order to approximate $Y_A(j\omega)$ by the OFR sum $\widetilde{Y}_A(j\omega)$.

The results can be seen overlapped in Figure 6.32. Figure 6.32a shows that, at the frequency f_{113}, $|\tilde{Y}_B(j\omega)|$ reproduces 92% of the magnitude spectrum of $|Y_B(j\omega)|$. At this frequency, the value of $|Y_B(j\omega)|$ is 0.059 and the value for $|\tilde{Y}_B(j\omega)|$ is 0.054. At the frequency f_{41}, the magnitude values of $|Y_B(j\omega)|$ and $|\tilde{Y}_B(j\omega)|$ are 0.0716 and 0.0739 which corresponds to an approximation error of 3.2%.

The results are also confirmed by the polar plots in Figure 6.33, which shows that the angle and magnitude of $\tilde{Y}(j\omega)$ at $\sim f_{100}$ correspond very well with those of $Y(j\omega)$ and the oxygen isotope spectrum for both ***before*** and ***after MPT***.

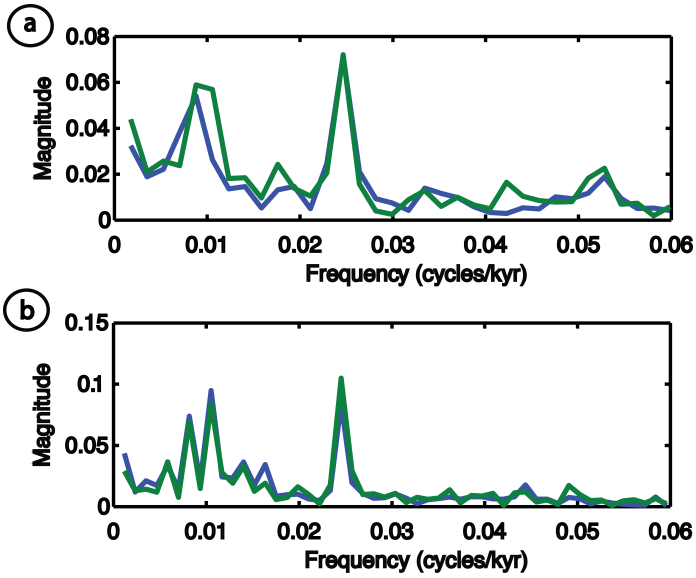

Figure 6.32: Spectra of the model predicted output $Y(j\omega)$ (blue) superimposed on $\widetilde{Y}(j\omega)$ (green) a. ***before MPT*** and b. ***after MPT***.

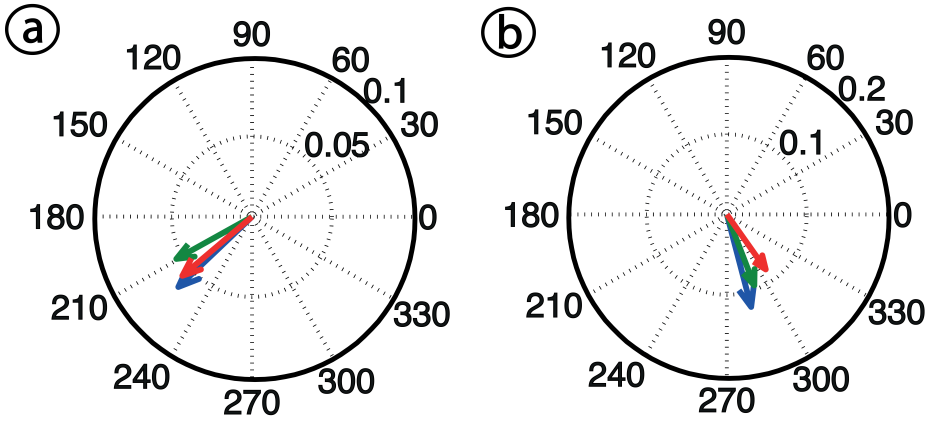

Figure 6.33: Polar plot at $\sim f_{100}$ of: a. $Z_B(j\omega)$ (blue), $Y_B(j\omega)$ (green) and $\widetilde{Y}_B(j\omega)$ (red), b. $Z_A(j\omega)$ (blue), $Y_A(j\omega)$ (green) and $\widetilde{Y}_A(j\omega)$ (red).

Figure 6.32b shows that, at the frequency f_{95}, $|\tilde{Y}_A(j\omega)|$ is 0.084, which represents 88% out of the 0.095 value of $|Y_A(j\omega)|$. At the frequency f_{41} the magnitude of $|Y_A(j\omega)|$ is 0.085, whilst the magnitude of $\tilde{Y}_A(j\omega)$ is 0.105. This gives an approximation error of 23.8%. This error could be improved further with the computation of many more higher order GFRFs, but this is not practical or required at this stage.

The contribution to the output spectrum of $Y(j\omega)$ at each frequency of interest is illustrated in Figure 6.34, which shows the magnitude spectrum of $Y(j\omega)$ superimposed on each $Y^i(j\omega)$, $i = 1, 2, 3$. The functions $Y^i(j\omega)$ were defined in Section 6.2.3. For the time interval $[f_{113}, f_{95}]$ the magnitude values and phase functions for $Y(j\omega)$ and each $Y^i(j\omega)$ are given in Table 6.10.

Before MPT, at the frequency f_{113}, the OFR $Y_B^1(j\omega)$ exceeds the magnitude spectrum value of $Y_B(j\omega)$ by 1.46%. The OFRs $Y_B^2(j\omega)$ and $Y_B^3(j\omega$ account for 18.73% and 28.06% out of the magnitude value of $Y(j\omega)$ at this frequency.

After MPT, at the frequency f_{95}, $Y_A^1(j\omega)$ represents 71.84% out of the total magnitude value of $Y_A(j\omega)$, and the second and third order OFRs $Y_A^2(j\omega)$ and $Y_A^3(j\omega)$ represent 13.15% and 6.95%, respectively.

From here it is seen that, at the frequency $\sim f_{100}$, the magnitude of the linear OFRs $Y^1(j\omega)$ explains most of the output spectrum $Y(j\omega)$ ***before*** and ***after MPT***. For the higher order OFRs however it is observed that the second largest contribution comes ***before MPT*** from $Y^3(j\omega)$ and ***after MPT*** from $Y^2(j\omega)$.

	Before MPT (f_{113})		***After MPT*** (f_{95})	
	$\lvert Y_B(j\omega)\rvert$	$\angle Y_B(j\omega)$	$\lvert Y_A(j\omega)\rvert$	$\angle Y_A(j\omega)$
$Y(j\omega)$	0.05328	-139.69	0.09478	-54.60
$Y^1(j\omega)$	0.05406	-158.54	0.06809	-50.63
$Y^2(j\omega)$	0.00998	-158.91	0.01246	-50.26
$Y^3(j\omega)$	0.01495	-41.52	0.00659	-113.66

Table 6.10: Magnitude and phase functions for the spectrum of the model predicted output $Y(j\omega)$ and each OFR $Y^i(j\omega)$, $i = 1, 2, 3$ for both time periods.

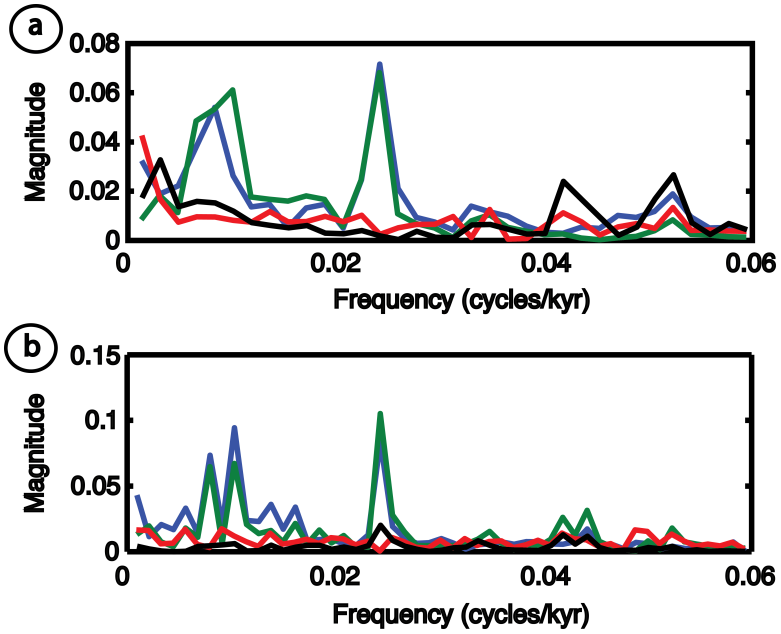

Figure 6.34: Magnitude of $Y(j\omega)$ (blue) superimposed on $Y^1(j\omega)$ (green), $Y^2(j\omega)$ (red) and $Y^3(j\omega)$ (black) a. ***Before MPT*** and b. ***After MPT***.

Table 6.11 summarizes the magnitude and phase changes at the frequency of interest around $\sim f_{100}$.

Function	***Before MPT***		***After MPT***	
	$\lvert Y_B(j\omega)\rvert$	$\angle Y_B(j\omega)$	$\lvert Y_A(j\omega)\rvert$	$\angle Y_A(j\omega)$
$Y(j\omega)$	0.0541	-151	0.0948	-69
$\widetilde{Y}(j\omega)$	0.0589	-140	0.0837	-55
$Y_1^1(j\omega)$	**0.0272**	-159	**0.0679**	-53
$Y_2^1(j\omega)$	0.0023	-117	0.0003	40
$Y_3^1(j\omega)$	**0.0243**	-162	0.0026	33
$Y_1^2(j\omega)$	0.0015	-11	**0.0059**	-3
$Y_2^2(j\omega)$	0.0006	155	**0.0070**	-118
$Y_3^2(j\omega)$	**0.0101**	-154	**0.0056**	5
$Y_{12}^2(j\omega)$	0.0014	-6	0.0022	-76
$Y_{13}^2(j\omega)$	0.0031	165	0.0011	-168
$Y_{23}^2(j\omega)$	0.0005	19	0.0013	-72
$Y_1^3(j\omega)$	0.0026	148	0.0032	-131
$Y_2^3(j\omega)$	0.0000	29	0.0003	-58
$Y_3^3(j\omega)$	**0.0175**	-43	0.0034	-102
$Y_{113}^3(j\omega)$	0.0015	156		
$Y_{133}^3(j\omega)$	0.0066	-30		
$Y_{112}^3(j\omega)$	0.0001	-13		
$Y_{122}^3(j\omega)$	0.0002	158		
$Y_{223}^3(j\omega)$	0.0002	113		
$Y_{233}^3(j\omega)$	0.0008	-50		
$Y_{123}^3(j\omega)$	0.0001	-0.6		

Table 6.11: Magnitudes and angles of each OFR at the frequency $\sim f_{100}$.

Figure 6.35 shows the magnitudes of the individual OFRs which contribute the most to the output spectrum. ***Before MPT*** these are $Y_{1B}^1(j\omega)$, $Y_{3B}^1(j\omega)$, $Y_{3B}^2(j\omega)$ and $Y_{3B}^3(j\omega)$ and ***after MPT*** these are $Y_{1A}^1(j\omega)$, $Y_{1A}^2(j\omega)$, $Y_{2A}^2(j\omega)$ and $Y_{3A}^2(j\omega)$. Figure 6.36 shows the main contributing frequency functions evaluated at the frequency $\sim f_{100}$ in polar coordinates.

Before MPT, the major contributions (Figures 6.35a and 6.36a) to the magnitude spectrum of the sum of OFRs $\tilde{Y}_B(j\omega)$ at the frequency f_{113} are from: $Y_{1B}^1(j\omega)$, representing 45.3%, $Y_{3B}^1(j\omega)$, representing 39.5%, $Y_{3B}^2(j\omega)$, representing 17.1% and $Y_{3B}^3(j\omega)$, representing 3.6%. The percentages of each contribution were calculated using the projections of each vector on $\widetilde{Y}_B(j\omega)$ seen in Figure 6.37a.

After MPT the main contributions (Figures 6.35b and 6.36b) to the magnitude spectrum of $\widetilde{Y}_A(j\omega)$ at the frequency f_{95} are from the OFRs: $Y_{1A}^1(j\omega)$, representing 81%, $Y_{1A}^2(j\omega)$, representing 4.3%, $Y_{2A}^2(j\omega)$, representing 3.7% and $Y_{3A}^2(j\omega)$, representing 3.4%. The percent-

ages of each contribution were calculated using the projections of each vector on $\widetilde{Y}_A(j\omega)$ seen in Figure 6.37b.

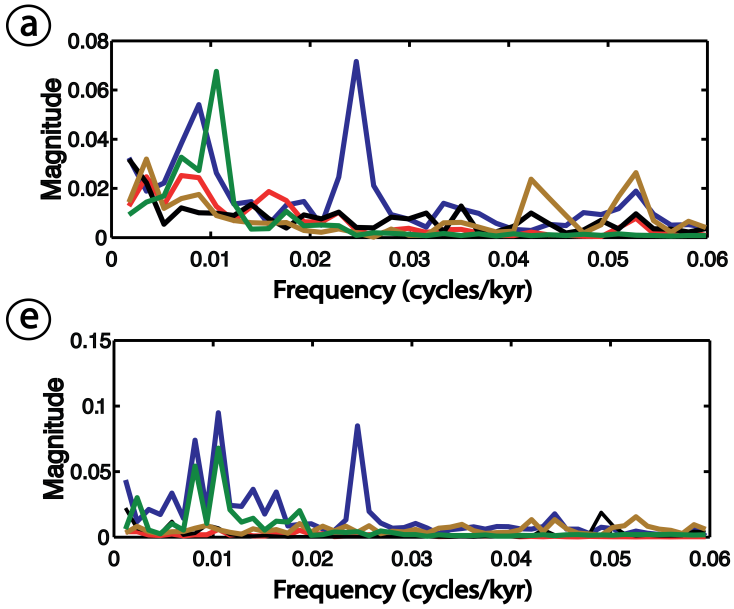

Figure 6.35: a. $|Y_B(j\omega)|$ (blue) superimposed on $|Y^1_{1B}(j\omega)|$ (green), $|Y^1_{3B}(j\omega)|$ (red), $|Y^2_{3B}(j\omega)|$ (black) and $|Y^3_{3B}(j\omega)|$ (brown), and b. $|\widetilde{Y}_A(j\omega)|$ (blue) superimposed on $|Y^1_{1A}(j\omega)|$ (green), $|Y^2_{1A}(j\omega)|$ (red), $|Y^2_{2A}(j\omega)|$ (black) and $|Y^2_{3A}(j\omega)|$ (brown).

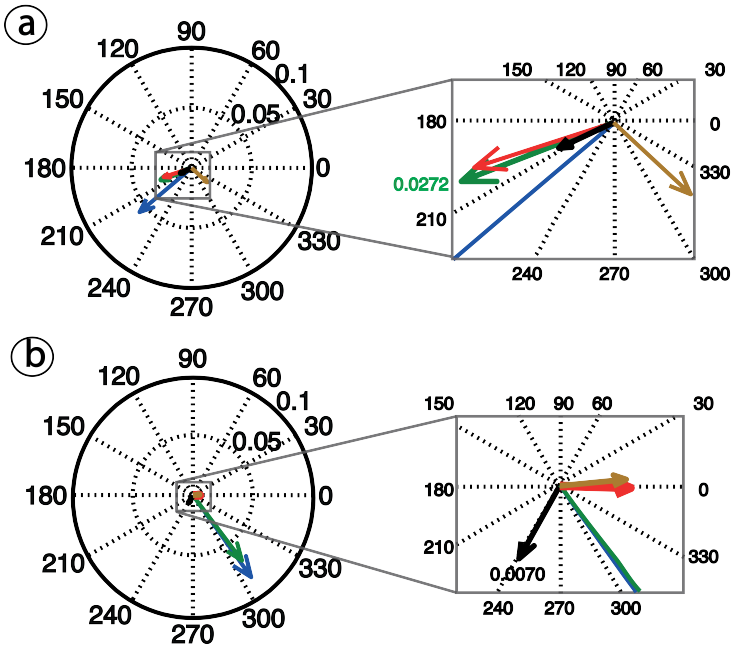

Figure 6.36: Polar plots at $\sim f_{100}$ of: a. $\widetilde{Y}_B(j\omega)$ (blue) superimposed on $Y^1_{1B}(j\omega)$ (green), $Y^1_{3B}(j\omega)$ (red), $Y^2_{3B}(j\omega)$ (black) and $Y^3_{3B}(j\omega)$ (brown), b. $\widetilde{Y}_A(j\omega)$ (blue) against $Y^1_{1A}(j\omega)$ (green), $Y^2_{1A}(j\omega)$ (red), $Y^2_{2A}(j\omega)$ (black) and $Y^2_{3A}(j\omega)$ (brown).

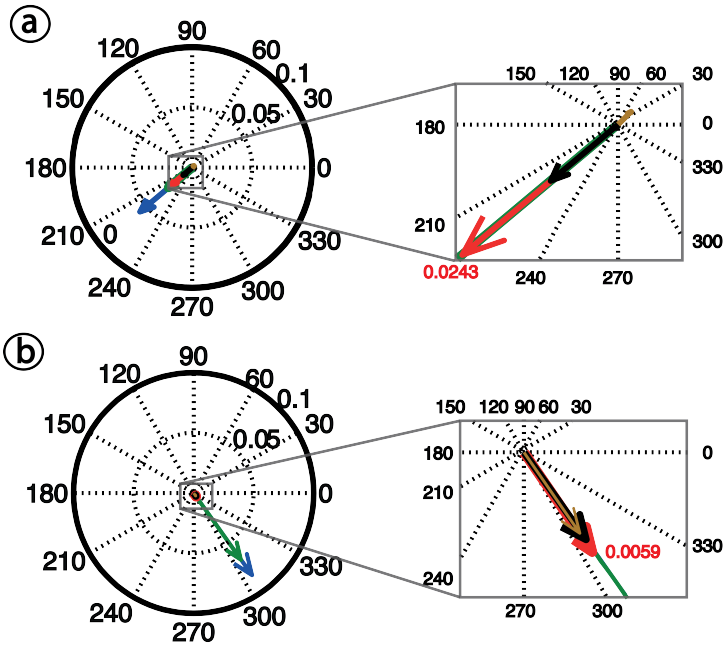

Figure 6.37: Polar plots at $\sim f_{100}$ of: a. Projections of the main contributions $Y^1_{1B}(j\omega)$ (green), $Y^1_{3B}(j\omega)$ (red), $Y^2_{3B}(j\omega)$ (black) and $Y^3_{3B}(j\omega)$ (brown) on the vector $\widetilde{Y}_B(j\omega)$ (blue), b. Projections of the main contributions $Y^1_{1A}(j\omega)$ (green), $Y^2_{1A}(j\omega)$ (red), $Y^2_{2A}(j\omega)$ (black) and $Y^2_{3A}(j\omega)$ (brown) on the sum vector $\widetilde{Y}_A(j\omega)$ of all calculated OFRs (blue).

This analysis shows that the most significant contributions to the output spectrum $Y(j\omega)$ at $\sim f_{100}$ ***before MPT*** are made by $Y^1_{1B}(j\omega)$, $Y^1_{3B}(j\omega)$ and $Y^2_{3B}(j\omega)$, whereas for ***after MPT*** the overwhelming contribution comes from the first order OFR $Y^1_{1A}(j\omega)$.

When analysing the first order functions, it can be observed from the Table 6.11 that the most dramatic change at the frequency $\sim f_{100}$ is in $Y^1_1(j\omega)$, from a magnitude of 0.0272 ***prior to the MPT*** to 0.0679 ***after MPT***. Given the first order OFRs are defined as $H(j\omega)U(j\omega)$ and that the input spectrum value of e*ccentricity* (Figure 6.1) does not change significantly (the value is 0.0035), the change must therefore come from the transfer function $H^1_1(j\omega)$ (Figure 6.38). The value of this magnitude increase is from 9.22 to 17.67, so the shift can be explained as a change in the system's linear response to *eccentricity* as observed in the transfer function. When looking at the GFRFs expression, we can see an increase of almost 10 times in the numerator term $u_1(t-1)$, which has lag 1 (4kyr).

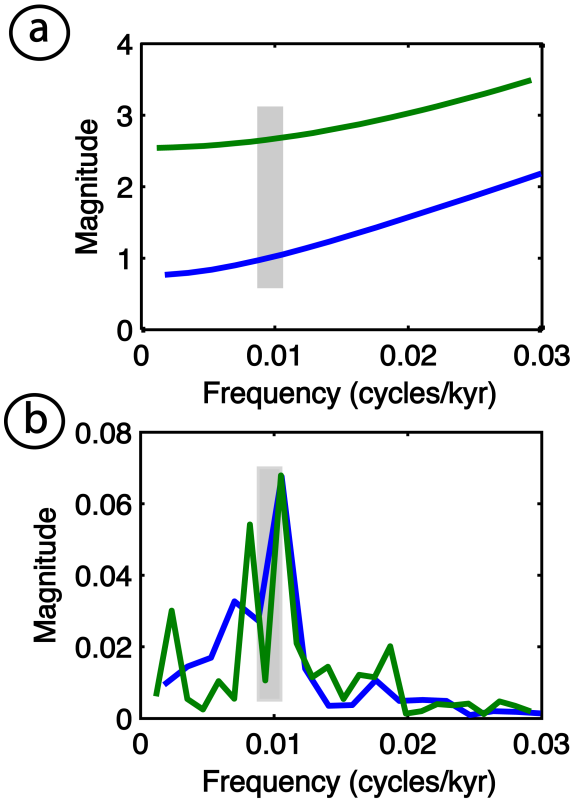

Figure 6.38: a. $H^1_{1B}(j\omega)|$ (blue) superimposed on $|H^1_{1A}(j\omega)|$ (green), b. $|Y^1_{1B}(j\omega)|$ (blue) superimposed on $|Y^1_{1A}(j\omega)|$ (green).

The second largest magnitude value for an OFR ***before MPT*** at the frequency f_{113} is the one given by $Y^1_{3B}(j\omega)$. In this case $H^1_{3B}(j\omega)$ has the magnitude value 0.0046 at this frequency and the input spectrum $U_{3B}(j\omega)$ has the large magnitude value 5.256.

When analysing the higher order OFRs, it is necessary to examine which pairs (ω_1, ω_2) give the largest contributions for each ω of interest to:

$$\frac{1}{2}\sum_{\omega_1+\omega_2=\omega} H^2(j\omega_1, j\omega_2)U(j\omega_1)U(j\omega_2) \tag{6.8}$$

For $Y^2_{3B}(j\omega)$ the magnitude value at the frequency f_{113} is 0.0101 and the $f_1+f_2 = f$ from equation (6.8) that give the largest magnitude values are $(f_1, f_2) = \{(-f_{25}, f_{20}), (-f_{20}, f_{17}), (-f_9, f_8)\}$. The magnitude values of $H^2_{3B}(\omega_1, \omega_2)$ for each pair (ω_1, ω_2) has the value in the order 10^{-5}, which is extremely small. From this it can be concluded that the value of the sum is mainly

given by the input spectrum values $U_{3B}(j\omega_1)$ and $U_{3B}(j\omega_2)$ in the interval of frequencies $[f_{25}, f_8]$ (Figure 6.1).

For the time period ***after MPT***, the major magnitude values in the summation in equation (6.8) for $Y_{1A}^2(j\omega)$ at the frequency f_{95} are given by the combinations $(f_1, f_2) = \{(f_{107}, f_{51}), (f_{95}, f_{48}),$

$(f_{214}, f_{171})\}$. The magnitude values of the input spectrum $U_1(j\omega)$ in each of the found ω_1 and ω_2 values are very small, in the orders 10^{-4} and 10^{-5}. The magnitude of the GFRFs $H_{1A}^2(j\omega_1, j\omega_2)$ for the given $(f_1, f_2) = \{(-f_{107}, f_{51}), (-f_{95}, f_{48}), (-f_{95}, f_{48})\}$ pairs are significantly higher and have the corresponding values: $|H_{1A}^2(j\omega_1, j\omega_2)| = \{349, 366, 119\}$. The extracted plane $f_1 + f_2 =\sim f_{100}$ from the GFRF $H_{1A}^2(j\omega_1, j\omega_2)$ can be seen in Figure 6.5b with red line.

For $Y_{2A}^2(j\omega)$ the largest magnitude values that contribute to the summation given by (6.8) at the frequency f_{95} are those corresponding to the frequency pairs $(f_1, f_2) = \{(-f_{41}, f_{29}),$ $(-f_{57}, f_{36})\}$. In this case, the largest contribution is given, for the first pair, by $|H_{2A}^2(j\omega_1, j\omega_2)| = 0.25$ and $|U_{2a}(j\omega_1)| = 0.38$.

In the case of $Y_{3A}^2(j\omega)$ the following combinations $(f_1, f_2) = \{(-f_{10}, f_9), (-f_{29}, f_{23}),$ $(-f_{23}, f_{19})\}$ are the largest contributions to the sum in equation (6.8) at the frequency f_{95}. The magnitude values of the GFRFs $H_{3A}^2(j\omega_1, j\omega_2)$ corresponding to the identified pairs are very small, in the orders of 10^{-5} and 10^{-6}. The largest contribution is $|U_{3A}(j\omega)| = 33.70$, peak shown in Figure 6.1c as corresponding to the frequency f_{23}.

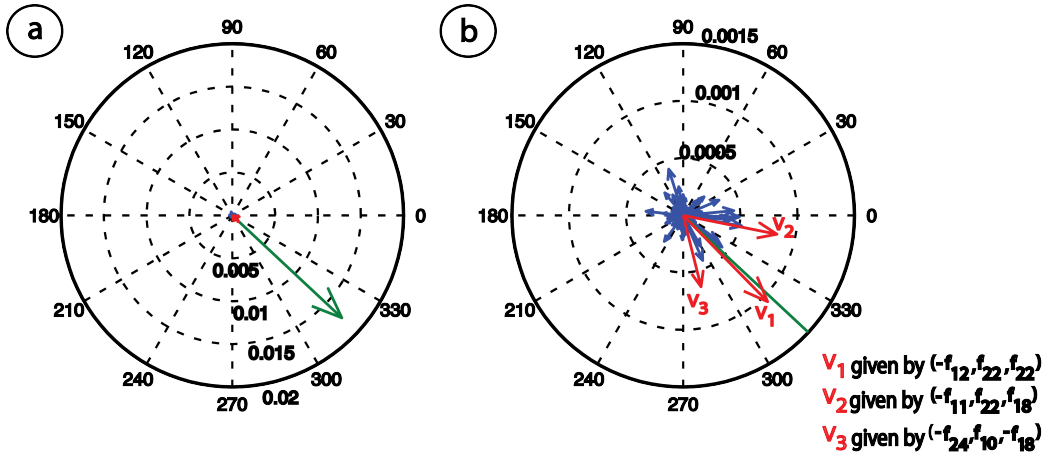

Figure 6.39: ***Before MPT***: a. Polar plot at $\sim f_{100}$ for each term in the summation $\sum_{\omega_1+\omega_2+\omega_3=\omega} H^3_{3B}(j\omega_1, j\omega_2, j\omega_3)U_3(\omega_1)U_3(\omega_2)U_3(\omega_3)$ (blue and red) and the resulting $Y^3_{3B}(j\omega)$ (green), and b. Zoom on the plot (a) showing in red the most significant terms contributing to $Y^3_{3B}(j\omega)$.

For $Y^3_{3B}(j\omega)$ the frequency combinations of interest $(\omega_1, \omega_2, \omega_3)$ at ω corresponding to the frequency f_{113} are those given by the terms in the summation:

$$\frac{1}{4} \sum_{\omega_1+\omega_2+\omega_3=\omega} H^3(j\omega_1, j\omega_2, j\omega_3)U(j\omega_1)U(j\omega_2)U(j\omega_3) \tag{6.9}$$

Each term that takes part in the summation in equation (6.9) is represented by one vector in Figure 6.39. The most significant ones, which are the ones having the largest magnitude values, are marked in Figure 6.39 with red colour and are found at the frequencies $(f_1, f_2, f_3) = \{(-f_{11}, f_{22}, f_{18}), (-f_{12}, f_{22}, f_{22}), (-f_{18}, f_{24}, f_{10})\}$. Each of the three red vectors represents 6 overlapped vectors each given by the 6 unique combinations given by each (f_1, f_2, f_3). All of these frequencies are present in the *longitude of perihelion* spectrum (Figure 6.1). The magnitude values of the GFRF $H^3_{3B}(j\omega_1, j\omega_2, j\omega_3)$ for each of the frequencies combinations $(\omega_1, \omega_2, \omega_3)$ are very small, in the order of 10^{-8}. The largest magnitudes of input spectrum that contribute to the summation in equation (6.9) are given by $|U_{3b}(j\omega)| = \{9.60, 11.02, 18.64\}$, with ω corresponding to the real frequencies $f = \{f_{11}, f_{22}, -f_{18}\}$, respectively.

Before MPT, the $\sim f_{100}$ cycles/kyr peak if obtained from the linear functions $Y^1_{1B}(j\omega)$ and $Y^1_{3B}(j\omega)$, so the influences are clearly *eccentricity* $(u_1(t))$ and the *longitude of the per-*

ihelion ($u_3(t)$), but also from the second and third order self-kernel functions based on the *longitude of the perihelion*, which are $Y^2_{3B}(j\omega)$ and $Y^3_{3B}(j\omega)$. The combinations of frequencies contributing are those from the spectrum $U_3(j\omega)$, as shown in the analysis.

After MPT, the main contributions change dramatically. The main contributions come from the *eccentricity* functions, although all three inputs appear to be needed. We can see from the results that the frequencies contributing to the $\sim f_{100}$ peak are from:

- *longitude of the perihelion* contribution given by $f_1 + f_2 = -f_{23} + f_{19}$ and found in $Y^2_{3A}(j\omega)$.
- *eccentricity* with $f_1 + f_2 = f_{214} + f_{171}$ and $f_1 + f_2 = -f_{95} + f_{48}$ and found in $Y^2_{1A}(j\omega)$.
- *obliquity* (u_2) with one combination: $f_1 + f_2 = -f_{41} + f_{29}$ and found in $Y^2_{2A}(j\omega)$.

As the analysis shows, the frequencies found contributing to the second and third order functions are either frequencies found in the spectrum of the inputs or frequencies that can be interpreted as harmonics or subharmonics of them, such as: $f_{214} = \frac{1}{4}f_{53.5}$, $f_{48} = 2f_{95}$, $f_{214} = \frac{1}{3}f_{71}$, $f_{24} = \frac{1}{2}f_{12}$.

6.4 Discussion

This chapter provided a detailed frequency domain analysis of the NARMAX models estimated in Chapter 5 Section 5.3. This was possible by computing the Generalized Frequency Response Functions and their associated Output Frequency Responses.

By decomposing the Output Frequency Response into individual contributions due to different GFRFs it was possible to determine the nonlinear mechanisms by which variations in the orbital parameters influence the output spectrum of the $\delta^{18}O$ time-series and also to study and identify the major changes in these mechanisms that occurred during MPT. This was done by comparing the results of each OFR and analyzing which functions and input spectrum frequencies or combination of frequencies changed from ***before*** to ***after MPT***. The focus of the study was on the frequency $\sim f_{100}$.

The frequency domain analysis demonstrated that most of the variability in the $\delta^{18}O$ records can be explained by the linear frequency responses generated by the *eccentricity* and

the *longitude of perihelion* inputs. There are also noticeable combinations of frequencies from the second and third order functions including frequencies found in the *eccentricity* and the *longitude of perihelion* bands but also frequencies that can be interpreted as their harmonics.

Chapter 7

Time Domain Analysis of the Identified Palaeoclimate Models

7.1 Introduction

This chapter presents a time domain analysis of the NARMAX models developed in Chapter 5 for each of the two periods of time studied. The aim is to characterize the performance of the models over different glacial and interglacial periods as well as study the stability of the equilibrium points of the system (fixed points of the two models).

The Chapter is organized as follows. Section 7.2 presents a detailed stability analysis of the two identified models which involves calculating the fixed points and the eigenvalues associated with the linearized systems around the fixed points. In Section 7.3, the *model predicted outputs* are compared with the $\delta^{18}O$ time-series in order to determine how well the models can reproduce dramatic climatic variability. Section 7.3.2 also provides a time domain decomposition of the responses of each model by mapping the individual Output Frequency Responses corresponding to different Generalized Frequency Response Functions back into the time domain. This allows to characterize the contribution of different linear and nonlinear mechanisms of energy transfer between the inputs and the output over different climatic periods, and mostly the effect of the nonlinear parts on the model response.

7.2 Stability Analysis of the Palaeoclimate Models

The fixed points of the NARX model representation

$$y(t) = f(y(t-1), \ldots, y(t-N_y), u_1(t-1), \ldots, u_1(t-N_{u_1}), \ldots, u_r(t-1), \ldots, u_r(t-N_{u_r})) \quad (7.1)$$

are defined as the points which satisfy

$$y_0 = y(t) = y(t+i),\ i \in \mathbb{Z} \quad (7.2)$$

In (7.2) the input is redefined as $u_j(t-i) = \overline{u_j},\ i = 0, 1, \ldots N_{u_j},\ j = 1, \ldots, r$, where $\overline{u_j}$ is the mean of the input $u_j(t)$ (Guckenheimer and Holmes, 1983, Wiggins, 1990, Mendes, 1995). Taking this into consideration, the NARX model in equation (7.1) is written as:

$$f_g(y(t-1), \ldots, y(t-N_y)) = f(y(t-1), \ldots, y(t-N_y), \overline{u_1}, \ldots, \overline{u_1}, \ldots, \overline{u_r}, \ldots, \overline{u_r}) \quad (7.3)$$

It follows that substituting equations (7.2) and (7.3) into equation (7.1) the following autonomous equation is obtained:

$$y_0 = f_g(y_0, \ldots, y_0) \quad (7.4)$$

Solving equation (7.4) gives the locations of the fixed points y_0 of the model.

In order to write the NARX model in equation (7.1) into a state space representation, the state variables are defined as:

$$\begin{bmatrix} x_1(k) \\ x_2(k) \\ \vdots \\ x_{N_y-1}(k) \\ x_{N_y}(k) \end{bmatrix} = \begin{bmatrix} y(k-N_y) \\ y(k-N_y+1) \\ \vdots \\ y(k-2) \\ y(k-1) \end{bmatrix} \quad (7.5)$$

where $X(k) = \begin{bmatrix} x_1(k) & x_2(k) & \dots & x_{N_y-1}(k) & x_{N_y}(k) \end{bmatrix}'$ represents the states vector.

Using the states given by $X(k)$ in equation (7.5), the input-output NARX representation can now be written as a state space model as:

$$\begin{aligned} x_1(k+1) &= x_2(k) \\ &\vdots \\ x_{N_y}(k+1) &= f(x_1(k), \dots, x_{N_y}(k)) \end{aligned} \tag{7.6}$$

To determine the behaviour of the model near a fixed point, the model has to be linearized around the fixed point. This can be done by using the Taylor expansion (and neglecting all terms of order higher than 1) as:

$$\begin{aligned} f_g(y(k-1), \dots, y(k-N_y)) &= f_g(y_0, \dots, y_0) + \frac{\partial f_g(y(k-1), \dots, y(k-N_y))}{y(k-1)}(y(k-1) - y_0) \\ &+ \dots + \frac{\partial f_g(y(k-1), \dots, y(k-N_y))}{y(k-N_y)}(y(k-N_y) - y_0) \end{aligned} \tag{7.7}$$

Equation (7.7) can now be written with regards to the states vector and the state space model derivates with regards to each state $x_i(k)$, $i = 1, \dots, N_y$ as:

$$\begin{bmatrix} x_1(k+1) \\ x_2(k+1) \\ \dots \\ x_{N_y-1}(k+1) \\ x_{N_y}(k+1) \end{bmatrix} = \begin{bmatrix} 0 & 1 & 0 & 0 & 0 \\ 0 & 0 & 1 & 0 & 0 \\ 0 & 0 & 0 & 1 & 0 \\ 0 & 0 & 0 & 0 & 1 \\ \frac{\partial f_g(y_0,\dots,y_0)}{\partial y(k-N_y)} & \frac{\partial f_g(y_0,\dots,y_0)}{\partial y(k-N_y-1)} & \frac{\partial f_g(y_0,\dots,y_0)}{\partial y(k-2)} & \dots & \frac{\partial f_g(y_0,\dots,y_0)}{\partial y(k-1)} \end{bmatrix} \begin{bmatrix} x_1(k) \\ x_2(k) \\ \vdots \\ x_{N_y-1}(k) \\ x_{N_y}(k) \end{bmatrix} + \begin{bmatrix} 0 \\ 0 \\ \vdots \\ 0 \\ y_0 \end{bmatrix} \tag{7.8}$$

The linearized model around the fixed point can be written in a concise way as:

$$X(k+1) = A(y_0)X(k) + \Gamma(y_0) \tag{7.9}$$

where $X(k+1)$ and $X(k)$ represent the state vectors and $A(y_0)$ is the Jacobian matrix.

Let λ be the eigenvalues, which are calculated by substituting each of the fixed points values as states values in equation (7.8).

The local stability of the fixed point of the nonlinear system in equation (7.1) can be decided in some cases by analysing the eigenvalues of the linearized system. This approach is known as Lyapunov's indirect (or first) method (Haddad and Chellaboina, 2011). An equilibrium of a dynamical system is said to be Lyapunov (locally) stable if all the solutions in its vicinity remain in some neighborhood of the equilibrium in the course of time (equation (7.2)). For asymptotic stability, the solutions are required, additionally, to converge to the equilibrium as time tends to infinity. The first (indirect) method of Lyapunov reduces the study of asymptotic stability of an autonomous system to the problem of location in the unit circle (for discrete-time systems) of the eigenvalues of the linearized system.

The equilibrium point y_0 for the nonlinear system is:

- *locally asymptotically stable* if all the eigenvalues of $A(y_0)$ are strictly inside the unit circle.
- *unstable* if at least one eigenvalue of $A(y_0)$ is strictly outside the unit circle.

The models used to compute the fixed points (Tables 7.1 and 7.2), were obtained by making the substitution $u_i = \overline{u_i}$, $i = 1, 2, 3$ in the NARX models in Tables A.1 and A.2 in Appendix A.

Term no	Term Coefficients θ_B	Model B terms	
1	0.9634	$y(t-1)$	0
2	0.0404	0	0
3	0.0428	$y(t-2)$	$y(t-2)$
4	0.5320	$y(t-3)$	0
5	−0.0599	$y(t-4)$	$y(t-4)$
6	0.2921	$y(t-1)$	$y(t-3)$
7	−0.1908	$y(t-4)$	0

Table 7.1: Model used to determine the fixed points ***before MPT.***

Term no	Term Coefficients θ_A	Model A terms		
1	0.7596	$y(t-1)$	0	0
2	-2.6803	$y(t-2)$	0	0
3	-1.4248	0	0	0
4	0.0200	$y(t-1)$	$y(t-1)$	$y(t-3)$
5	-0.4111	$y(t-2)$	$y(t-2)$	$y(t-3)$
6	0.0099	$y(t-1)$	$y(t-4)$	0
7	-1.2407	$y(t-2)$	$y(t-2)$	0
8	-0.6316	$y(t-2)$	$y(t-3)$	0

Table 7.2: Model used to determine the fixed points ***after MPT.***

The fixed points for ***models B*** and ***A*** were obtained by solving the following polynomial equations:

$$y_B = 0.2750y_B^2 + 0.3046y_B + 0.0404 \tag{7.10}$$

$$y_A = -0.3911y_A^3 - 1.8624y_A^2 - 2.9207y_A - 1.4248 \tag{7.11}$$

Model B has two fixed points which have the values $y_{01B} = -0.1542$, which is outside of the range of the data and appears to be a repeller, and $y_{02B} = -0.9533$. ***Model A*** has only one fixed point at $y_{01A} = -0.9404$. The other two solutions of the polynomial equation (7.11) are the complex conjugate values $y_{02A,03A} = -1.9109 \pm 0.4717i$.

Given that the maximum output lag for both models is 4, the state space variables are as follows:

$$\begin{bmatrix} x_1(k) \\ x_2(k) \\ x_3(k) \\ x_4(k) \end{bmatrix} = \begin{bmatrix} y(k-4) \\ y(k-3) \\ y(k-2) \\ y(k-1) \end{bmatrix} \tag{7.12}$$

The stability of ***model B*** is considered first. Substituting the states (7.12) into the model in Table 7.1 results in:

$$\begin{aligned} f_{g,B}(k) &= \theta_B(1)x_4(k) + \theta_B(2)x_3(k) + \theta_B(3) + \theta_B(4)x_4^2(k)x_2(k) + \theta_B(5)x_3^2(k)x_2(k) \\ &+ \theta_B(6)x_4(k)x_1(k) + \theta_B(7)x_3^2(k) + \theta_B(8)x_3(k)x_2(k) \end{aligned} \quad (7.13)$$

For the fixed point $y_{01B} = -0.1542$, the Jacobian matrix $A_B(y_{01B})$ is given by

$$A_B(y_{01B}) \begin{bmatrix} 0 & 1 & 0 & 0 \\ 0 & 0 & 1 & 0 \\ 0 & 0 & 0 & 1 \\ -0.1724 & 0.4869 & -0.0132 & 0.9184 \end{bmatrix}$$

The absolute values of the eigenvalues corresponding to $A_B(y_{01B})$ are $|\lambda_{01B}| = \begin{bmatrix} 1.1588 & 0.6847 & 0.6847 \end{bmatrix}$

Because not all the absolute values of the eigenvalues are inside the unit circle, the fixed point $y_{01B} = -0.1542$ is unstable.

For the fixed point $y_{02B} = -0.9533$, the Jacobian matrix $A_B(y_{02B})$ is given by

$$A_B(y_{02B}) = \begin{bmatrix} 0 & 1 & 0 & 0 \\ 0 & 0 & 1 & 0 \\ 0 & 0 & 0 & 1 \\ -0.0767 & 0.2535 & -0.0815 & 0.6850 \end{bmatrix}$$

The absolute values of the eigenvalues corresponding to $A_B(y_{02B})$ are $|\lambda_{02B}| = \begin{bmatrix} 0.8227 & 0.5656 & 0.5656 \end{bmatrix}$ and because all are inside the unit circle, the fixed point y_{02B} is locally asymptotically stable.

Substituting the states (7.12) into the ***model A*** in Table 7.1 results in:

$$f_{g,A}(k) = \theta_A(1)x_4(k) + \theta_A(2) + \theta_A(3)x_3^2(k) + \theta_A(4)x_2(k) + \theta_A(5)x_1^2(k) + \theta_A(6)x_4(k)x_2(k) + \theta_A(7)x_1(k) \quad (7.14)$$

For ***model A*** the fixed point is $y_{01A} = -0.9404$ and the Jacobian matrix $A_A(y_{01A})$ is given by

$$A_A(y_{01A}) = \begin{bmatrix} 0 & 1 & 0 & 0 \\ 0 & 0 & 1 & 0 \\ 0 & 0 & 0 & 1 \\ -0.0093 & 0.2481 & -0.4800 & 0.8059 \end{bmatrix}$$

The absolute values of the eigenvalues corresponding to $A_A(y_{01A})$ are $|\lambda_{01A}| = \begin{bmatrix} 0.6312 & 0.6036 & 0.6036 & (\end{bmatrix}$ Because all absolute values of the eigenvalues are inside the unit circle the fixed point y_{01A} is locally asymptotically stable.

It follows that for ***model B*** the fixed point in -0.9533 is locally asymptotically stable, whilst the fixed point -0.1542 is unstable. In contrast, ***model A*** has a single stable fixed point at -0.9404.

The fact that the maximum eigenvalue for the stable fixed point of ***model B*** is closer to the unit circle than the maximum eigenvalue of ***model A*** and the existence of an unstable fixed point suggests that the climate system was less robust ***before MPT***. Interestingly the MPT has resulted in the disappearance of an unstable equilibrium of the climate system whilst the position of the stable one has changed little. Such changes in the structural stability (number, position and type of equilibrium points) are associated with bifurcation phenomena resulting from changes in the system parameters.

7.3 Analysis and Comparison of the Model Responses with Palaeoclimatic Data

In order to place the data-set within the geological and climate timeline, a few concepts need to be defined. Traditionally, the terrestrial sediments sequences are divided, with respect to their type, into: glacial and non-glacial deposits. This will give corresponding periods called *glacial (cold)* and *interglacial (temperate) stages*, respectively (Gradstein et al., 2005). According to the American Commission (1961), a *glaciation* is a climatic episode during which extensive glaciers developed, attained a maximum extent, and then receded. An *interglacial* represents an episode during which the climate was incompatible with the wide extent of

glaciers that characterize the glaciation. In Europe, the interglacial represents a time period with a climate at least as warm as the present interglacial (the *Holocene*). Dividing the palaeoclimate into *glacial* and *interglacial* periods is mainly applied to the Middle and Late Pleistocene periods.

A second method of dividing the palaeoclimate is by using the $\delta^{16}O/\delta^{18}O$ ratios (Johnsen et al., 1972, Dansgaard, 1993). The stages resulting from using the marine isotope record are called Marine Isotope Stages (MIS). These are numbered starting from the present day (MIS1) backwards in time. The cold climate (*glacial*) is assigned even numbers and the warm climate (*interglacial*) is usually given odd numbers (Gradstein et al., 2005). The boundaries of the Marine Isotope Stages should show a major climate change, and are usually placed between temperature maxima and minima.

The beginning and the end time of geological periods and of MIS do not necessarily coincide, largely due to the fact that the ocean sediments give a global record whereas the terrestrial ones mostly account for the local climate events (Gradstein et al., 2005). This is why both dating methods are simultaneously needed.

7.3.1 Analysis of overall model responses

Figure 7.1 shows the *model predicted output* (green) superimposed on the $\delta^{18}O$ time-series (blue) for both time periods. The models are able to reproduce remarkably well the trends and periodicities of the data. The range of the model response ***before MPT*** is $[-1.66, -0.24]$ and ***after MPT*** is $[-1.80, -0.60]$.

On Figure 7.1 the MIS and the geological eras are identified for the studied time periods and also a temperature equivalent scale for the $\delta^{18}O$ values is given on the left of the $\delta^{18}O$ axis in both cases (Gradstein et al., 2005).

The values of the $NRMSE$ are $NRMSE_B = 7.2\%$ ***before MPT*** and it is $NMSE_A = 15.5\%$ ***after MPT***.

Chapter 6 sub-section 6.3.1 showed that both ***models B*** and ***A*** are able to reproduce very well the peaks at the frequencies of interest f_{41} and $\sim f_{100}$ and the overall change in dominant frequency from f_{41} to $\sim f_{100}$. Moreover, Figure 7.1 shows that the models are also able to follow remarkably the abrupt changes happening between each Marine Isotope Stage

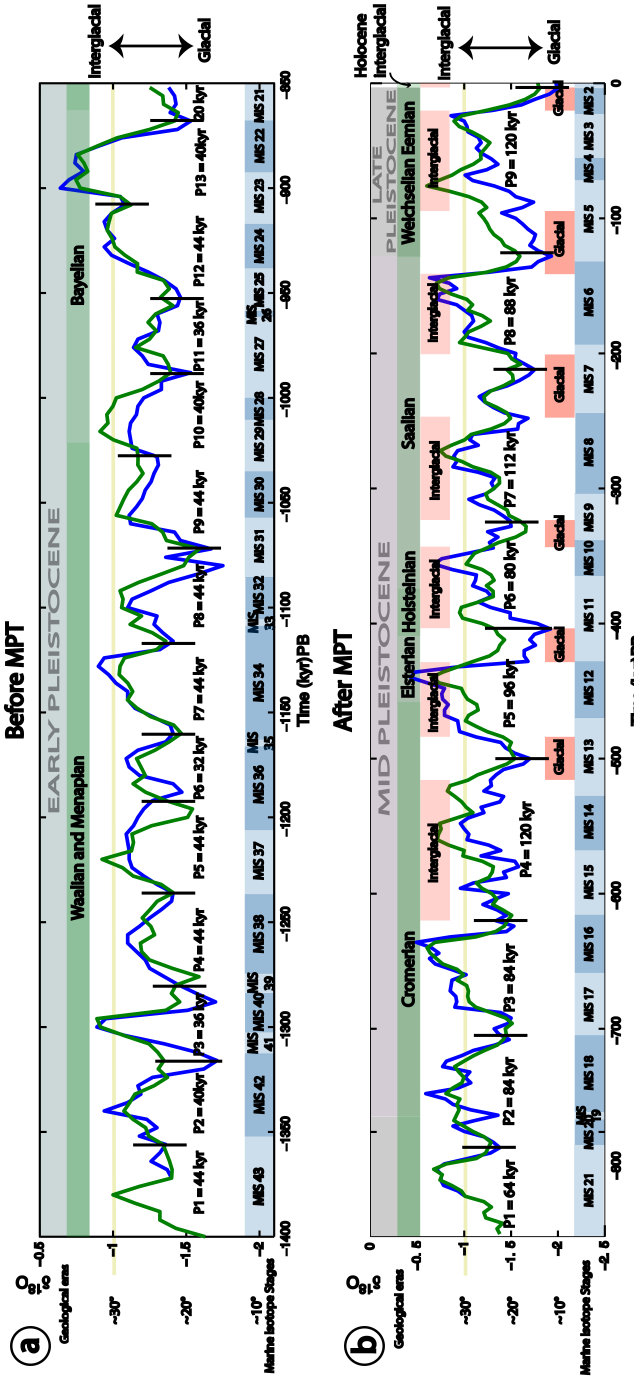

Figure 7.1: Geological Eras (top of figures in green) and Marine Isotope Stages (bottom of figures in blue) for the studied time periods. Blue is the $\delta^{18}O$ measured data and green represents the *mpo*. The vertical black lines show roughly the 41 kyr and $80 - 120$ kyr cycles observed for ***before*** and ***after MPT***, respectively. The available sequence of glacial and interglacial cycles is shows with red blocks. Image constructed using information from Gradstein et al. (2005).

(MIS), and is able to capture the peaks of the interglacials and the valleys of the glacial periods. The model outputs were compared with the $\delta^{18}O$ time-series for both time periods to analyse which peaks and MIS were matched and which were not. Results of this are shown in Tables 7.3, 7.4, 7.5 and 7.6. The error values were calculated as the percentage that $\hat{y}(t)$ does not explain of $\delta^{18}O(t)$ for each considered peak corresponding to the time t.

Peaks matched	
Peak location (kyr)	Error (%)
-1340 (MIS42)	14.25%
-1296 (MIS40)	-6.3%
-1260 (MIS38)	7.9%
-1208 (MIS37-36)	3.58%
-1172 (MIS35)	6.5%
-1100 (MIS32)	-3.7%
-1056 (MIS31-30 transition)	-7.9%
interval [-976, -864] (MIS26-21)	4.76% (average over the interval)

Table 7.3: The location of the peaks reproduced well by the model output $\hat{y}_B(t)$ and the fitting accuracy.

Peaks not matched	
Peak location (kyr)	Error (%)
-1316 (MIS42-41 transition)	21.17%
-1288 (MIS40-39 transition)	14.4%
-1196 (MIS36)	27.4%
-1128 (MIS34)	16.3%
-1080 (MIS31)	15.25%
interval [-1016, -1000] (MIS28)	15.85% (average over the interval)

Table 7.4: The location of the peaks that the model output $\hat{y}_B(t)$ did not reach and the fitting accuracy.

Peaks matched	
Peak location (kyr)	Error (%)
[-824,-776] (MIS21-20 transition)	4.32% (average over the interval)
the interval [-728, -684] (MIS17)	10.31% (average over the interval)
the interval [-660, -608] (MIS16)	11.88% (average over the interval)
-276 (MIS8)	-9.75%
-232 (MIS7)	4.4%
-184 (MIS6)	4.9%
-144 (MIS6)	16.18%
the interval [-52, -12] (MIS3 and MIS2)	6.95% (average over the interval)

Table 7.5: The location of the peaks reproduced well by the model output $\hat{y}_A(t)$ and the fitting accuracy.

Peaks not matched	
Peak location (kyr)	Error (%)
-764 (MIS19)	32.52%
-748 (MIS19-18 transition)	36.5%
[-684, -668] (MIS17)	19.13% (average over the interval)
[-572, -520] (MIS14)	25.38% (average over the interval)
[-468, -436] (MIS12)	37.5% (average over the interval)
[-420, -388] (MIS11)	26.15% (average over the interval)
[-128, -72] (MIS5 and MIS4)	26.5% (average over the interval)

Table 7.6: The location of the peaks that the model output $\hat{y}_A(t)$ did not reach and the fitting accuracy.

Before MPT the mean of the absolute value of the residuals is 0.0918, with the minimum being 0 and the maximum value of 0.3622. 60.15% of all the 138 absolute values of residuals are below the mean value.

After MPT the largest value of the absolute residuals value is 0.7186, the minimum is 0 and the mean value is 0.1734. The percentage of absolute values of residuals, out of 214

data points, below the mean value in this case is 57.94%.

It can be seen from the analysis above and Figure 7.1 that the models capture very well a rough cycle of $40 - 44$ kyr ***before MPT*** and a cycle of $80 - 120$ kyr ***after MPT***. This confirms the results of the spectrum analysis in Chapter 6 Section 6.3.1. Also, the same figure shows that both models are able to reproduce very well the succession of glacial and interglacial stages of the geological eras and the Marine Isotope Stages identified by many authors (Gradstein et al., 2005, Dawson, 1994, Pomerol, 1982). The succession of warm and cold periods indicated by the high and low concentrations of the $\delta^{18}O$ time-series have a characteristic saw-tooth shape (Rial, 2004a).

7.3.2 Time Domain Response Decomposition using Output Frequency Response

The Output Frequency Functions computed in Chapter 6 sub-section 6.2.3 explain the contribution, frequency coupling and energy transfer between the orbital parameters and temperature proxy data. Mapping the OFR corresponding to different GFRF's back into the time domain gives a time-domain decomposition of the model responses into individual components that correspond to different linear and nonlinear mechanisms of energy transfer between the inputs and the output.

Specifically, the output spectrum $Y(j\omega)$ is given by

$$Y(j\omega) = \sum_{k=1}^{n} Y^k(j\omega)$$

where $Y^k(j\omega)$ are the k^{th} order OFR sums.

By applying the inverse Fourier Transform, the above equation can be mapped back into the time-domain such that

$$\hat{y}(t) = \sum_{k=0}^{n} y^{(k)}(t)$$

where $\hat{y}(t)$ is the *mpo* and $y^{(k)}(t)$ denotes the k^{th} order output component, characterized by an k^{th} order kernel in the Volterra expansion, which is obtained by applying the inverse

Fourier Transform to $Y^k(j\omega)$ and $y^{(0)}$ is the mean value of $\hat{y}(t)$.

Figures 7.2 and 7.3 show the linear, quadratic and cubic components of the response ***before*** and ***after MPT***, respectively. This shows that the main contribution to the model response is made in both cases by the first order component $y^{(1)}(t)$ of the output which correspond to the linear OFR $Y^1(j\omega)$. However, the second and third order components of the response are also needed.

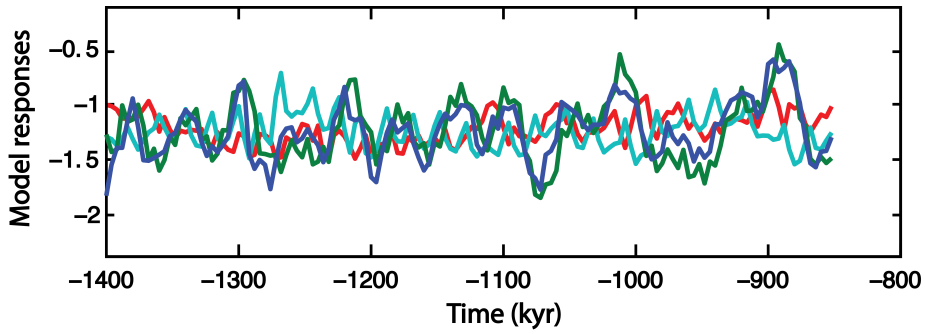

Figure 7.2: $\hat{y}_B(t)$ (blue) superimposed on the $y_B^{(1)}(t)$ (green), $y_B^{(2)}(t)$ (red) and $y_B^{(3)}(t)$ (cyan), corresponding to ***model B.***

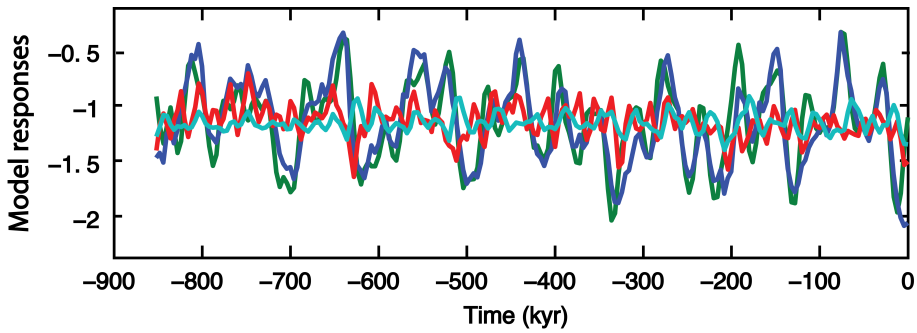

Figure 7.3: $\hat{y}_A(t)$ (blue) superimposed on the $y_A^{(1)}(t)$ (green), $y_A^{(2)}(t)$ (red) and $y_A^{(3)}(t)$ (cyan), corresponding to ***model A.***

Figures 7.4a and 7.5a show $\hat{y}(t)$ superimposed on $y^{(1)}(t)$ ***before*** and ***after MPT***. It can be seen that the first order response $y^{(1)}(t)$ largely contributes in both cases to the production of interglacial maxima and glacial minima in the data and once more that the linear response is imperative in obtaining a good fit for the $\delta^{18}O$ data ***before*** and ***after MPT***.

Figures 7.4b and 7.5b show the $\hat{y}(t) - y^{(1)}(t)$ superimposed on $y^{(2)}(t)$ ***before*** and ***after MPT***. This analysis is useful because the overwhelming contribution of $y^{(1)}(t)$ to $\hat{y}(t)$ can

mask the nonlinear contributions. The figures show that ***after MPT*** $y^{(2)}(t)$ and $\hat{y}(t) - y^{(1)}(t)$ almost overlap, which indicates that $y^{(2)}(t)$ contributes almost entirely to $\hat{y}(t) - y^{(1)}(t)$. Compared to the contribution of $y^{(1)}(t)$, in both cases $y^{(2)}(t)$ has lower impact on the residuals $\hat{y}(t) - y^{(1)}(t)$, which could indicate that $y^{(2)}(t)$ just aids $y^{(1)}(t)$ in reaching the interglacial maxima and glacial minima, but does not have a dramatic contribution itself.

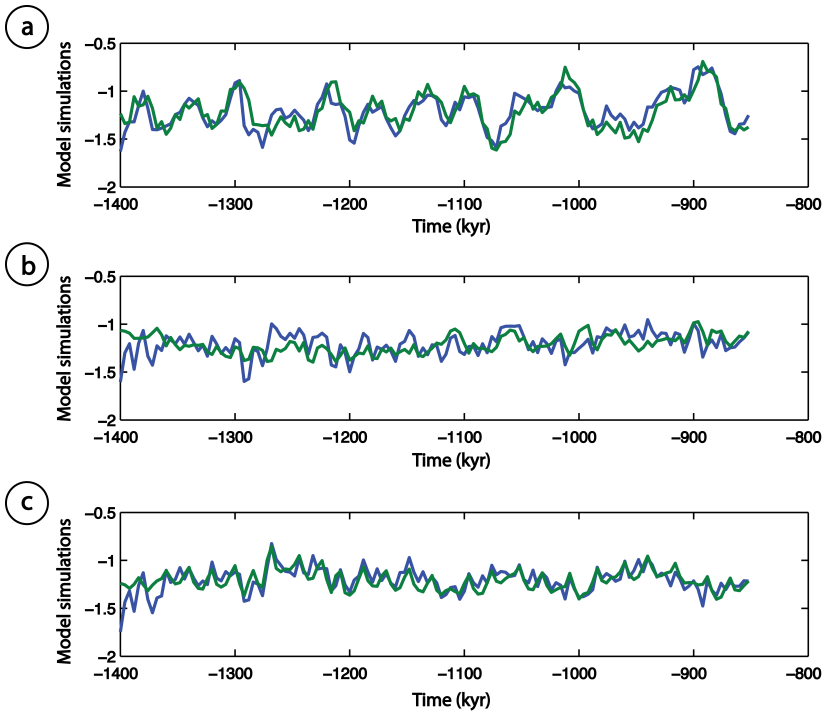

Figure 7.4: Time-series of: a. $\hat{y}_B(t)$ (blue) and $y_B^{(1)}(t)$ (green), b. $\hat{y}_B(t) - y_B^{(1)}(t)$ (blue) and $y_B^{(2)}(t)$ (green), c. $\hat{y}_B(t) - y_B^{(1)}(t) - y_B^{(2)}(t)$ (blue) and $y_B^{(3)}(t)$ (green) ***before MPT.***

Figures 7.4c and 7.5c show the $\hat{y}(t) - y^{(1)}(t) - y^{(2)}(t)$ superimposed on $y^{(3)}(t)$ ***before*** and ***after MPT***. Figure 7.5c shows more differences in the two signals ***after MPT*** when compared to ***before MPT***, when $\hat{y}(t) - y^{(1)}(t) - y^{(2)}(t)$ and $y^{(3)}(t)$ almost overlap. This proves that ***before MPT*** the third order response $y^{(3)}(t)$ has a greater contribution to the model output and that the impact of this contribution changes ***after MPT***.

The first, second and third order components explain 94.45% and 96.55% of the ***models B*** and ***A*** responses, respectively. As seen in Figure 7.6, the combined contribution from the components of orders $n \geq 4$, given by $\hat{y}(t) - y^{(1)}(t) - y^{(2)}(t) - y^{(3)}(t)$, is relatively small. This was obtained by extracting from the *mpo* the sum of the first three order functions. It can

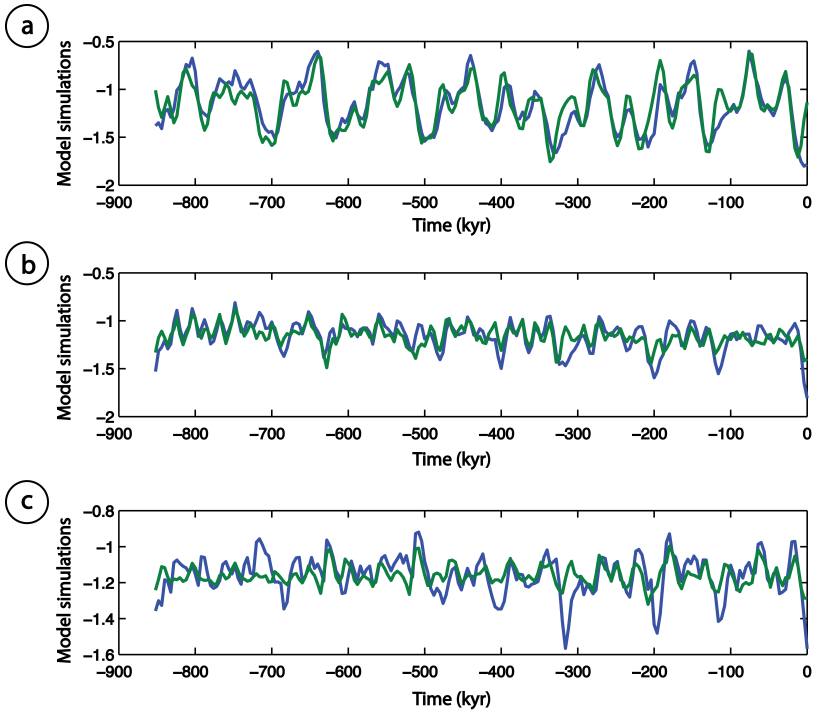

Figure 7.5: Time-series of: a. $\hat{y}_A(t)$ (blue) and $y_A^{(1)}(t)$ (green), b. $\hat{y}_A(t) - y_A^{(1)}(t)$ (blue) and $y_A^{(2)}(t)$ (green), c. $\hat{y}_A(t) - y_A^{(1)}(t) - y_A^{(2)}(t)$ (blue) and $y_A^{(3)}(t)$ (green) ***after MPT***.

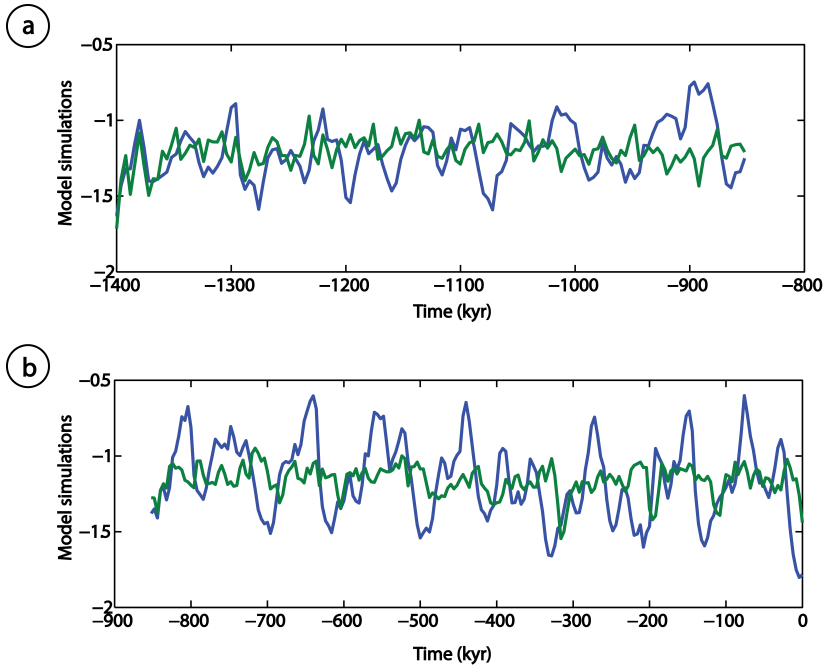

Figure 7.6: Time-series of $\hat{y}(t)$ (blue) and $y^{(n\geq 4)}(t)$ (green) a. ***Before MPT*** and b. ***After MPT***.

be seen from the plot that compared to the range of the signal and the contribution of the first three order signals, the forth and higher order time domain contribution is small.

The results provided by the analysis in this section confirm the frequency domain analysis in Chapter 6, that the largest output contribution is given by the first order component. In the frequency domain analysis, the largest contribution was also given by $Y^1(j\omega)$, and more specifically by the *eccentricity* based OFR $Y_1^1(j\omega)$, for both time periods.

7.4 Comparison of the NARMAX and Frequency Modulation Model Results

Comparing modelling results with other climatic models developed is not an easy task. This is due to different studied time periods, different data-sets used, different variables involved in the models, different error measurements or a lack of a mathematical model that can be simulated. In this section however, the NARMAX modelling results analysed in this chapter

are compared with Rial's model (2000) from the paper "Understanding nonlinear responses of the climate system to orbital". Rial uses a simple frequency modulation model described by the equation:

$$\Phi_{FM}(t) = a\sin[\frac{2\pi t}{95}+\beta\sin(\frac{2\pi t}{413})+\beta^{'}\sin(\frac{\pi t}{413})]+b\sin[\frac{2\pi t}{100}+\beta\sin(\frac{2\pi t}{413})]+c\sin[\frac{2\pi t}{125}+\beta\sin(\frac{2\pi t}{413})] \tag{7.15}$$

where t is the time in kilo-years, and the constants a through c are adjustable parameters, with a typically three times greater than b or c. By matching spectra, Rial observed that $\beta \sim 1$ and $\beta' \sim 2$.

Rial's simulation of this equation is presented in Figure 7.7c and denoted $y_{FM}(t)$ (grey). The image is reproduced with permission from the paper. As stated in the paper, in order to maximize data fit, the simulated time series was shifted in phase.

By performing simulations of the model in equation (7.15), the following values were chosen for the constant parameters: $a = -0.5$, $b = -0.15$, $c = 0.09$ and $\beta = 0.8$, $\beta' = -1.8$. The model simulation $\hat{y}_{FM}(t)$ showed that the range of the output was not corresponding to the range of the $\delta^{18}O$ data because of an offset of $c = 1.2$. In order to correct this, equation (7.15) was written as:

$$\Phi_{FM1}(t) = \Phi_{FM}(t) - c \tag{7.16}$$

Even with the corrected offset, the model simulation output $\hat{y}_{FM1}(t)$ of equation (7.16) is out of phase with the $\delta^{18}O$ time-series. This is shown in Figure 7.7a. As in Rial and Anaclerio (2000), the model output was shifted in order to maximize the fit. The shift was done by $t = 92$ kyr . The shifted model output of equation (7.16) is $\hat{y}_{FM2}$ and shown with grey colour in Figure 7.7b.

The NARMAX model output (blue) shown in Figure 7.7b represents the concatenated output given by the NARMAX ***models B*** and ***A***.

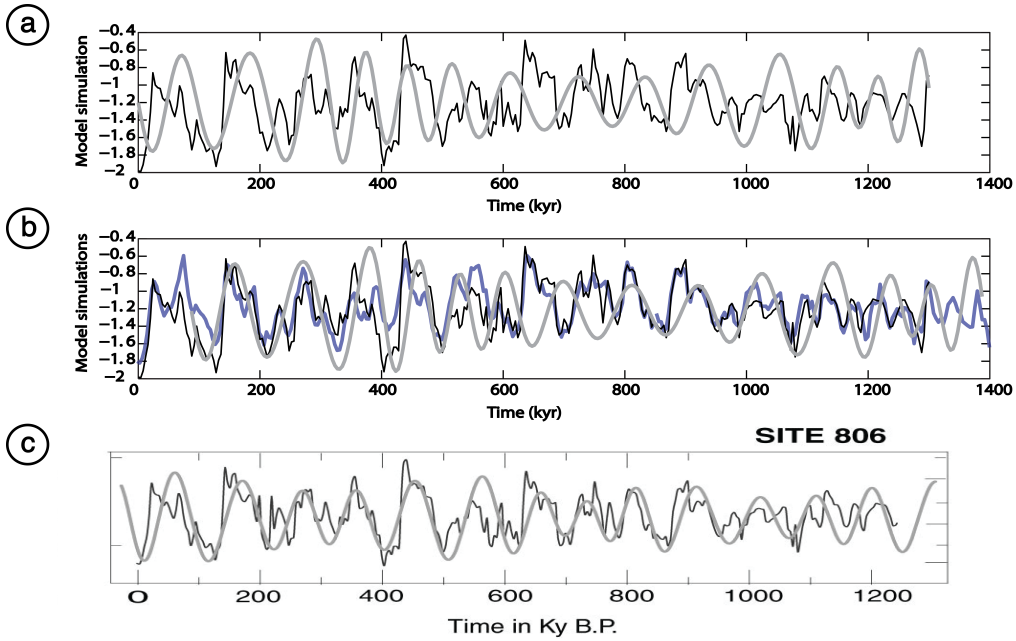

Figure 7.7: Time-series of: a. $\delta^{18}O$ (black) superimposed on $\hat{y}_{FM1}(t)$ (grey), b. $\delta^{18}O$ (black) superimposed on $\hat{y}_{FM2}(t)$ (grey) and NARMAX models outputs (blue) and c. $\delta^{18}O$ (black) superimposed on $y_{FM}(t)$ (grey). Figure 7.7c is taken from Rial and Anaclerio (2000).

Figure 7.7 shows that, although simple, Rial's model captures the periodicity of the data. However, it is not able to reproduce the subtle variability of the $\delta^{18}O$ data. This is reflected in the explained variance of just 48.07% given by the model output, measured on $\Phi_{FM2}(t)$.

In order to be able to compare the model performance, Table 7.7 gives explained variance of $\delta^{18}O$ for the two analysed models ***before*** and ***after MPT***. Rial's $\Phi_{FM2}(t)$ model simulation is clearly outperformed, by 41% ***before MPT*** and 39.21% ***after MPT***, by the NARMAX models.

	Before MPT	***After MPT***
$\Phi_{FM2}(t)$	51.80%	45.29%
$\hat{y}(t)$	92.8%	84.5%

Table 7.7: Explained variance (%) for $\Phi_{FM2}(t)$ and $\hat{y}(t)$.

7.5 Conclusions

This chapter provides for the first time a stability analysis of the climate system ***before*** and ***after MPT***.

The first part of the chapter covered theory and computation of the fixed points of each of the models. By calculating the fixed points location and their associated eigenvalues, the asymptotically stable fixed points were determined. It is shown that ***before MPT*** the climate system had two equilibrium points of which only one was stable and that following MPT the unstable equilibrium point has disappeared. ***After MPT*** the eigenvalues associated with the linearized system around the equilibrium point suggest that the system appears to be more robust. The interesting fact arising from this analysis is that both models have very similar (located closely to each other) fixed points.

In the second part of the chapter, model predictions were compared with the available paleoclimatic data by taking into account the important climatic periods and events during the Pleistocene and Quaternary eras.

The third part of the analysis used results of the frequency domain methods implemented in previous chapters in order to decompose the *model predicted* response into the linear, quadratic, cubic and higher order responses, which correspond to different kernels of the Volterra series expansion.

To further show the accurate fit that the NARMAX models developed in Chapter 5 provide for the $\delta^{18}O$, one other climatic model that uses frequency modulation was simulated. This showed the improved performance of the NARMAX models and how they can capture the subtle changes in the $\delta^{18}O$ time-series, which the frequency modulation model does not.

The time domain decomposition of the responses allowed identifying the time periods over which the contribution from second and third order kernels was significant, thus allowing to characterize the role of nonlinear interactions over different glacial and interglacial periods.

The analysis presented in this chapter provide further evidence that the two identified models not only predict well the oxygen isotope ratios, but also capture the dynamics of the underlying processes ***before*** and ***after MPT***. The models reproduce well the critical points in the data which correspond to climatic events, such as switching between a glacial

and interglacial period.

Chapter 8

Comparison, Modelling and Analysis on the Data-sets from Sites 806B and 805C

8.1 Introduction

Sites 806B and 805C are two extraction points part of Leg 130 in the ODP Ontong Java Plateau in the Western Pacific, as shown in Figure 8.1. The two Sites are located closely to each other and are well suited for comparison because they offer a continuous sediment record for the last 25 Myr (Berger et al., 1991c). Such a comparison can provide insight into the common features as well as the observed differences. This helps in validating the results of the dating performed on either of them and on the recorded sedimentation rate. The sedimentation rate of any Site is influenced by: the productivity of the forams, the rate of sinking of the biogenous sediments, solubility of the biogenous sediments in seawater or the bottom sea/ocean currents (Berger, 1969).

This chapter is aimed at describing the relationship between the oxygen isotope ratios of Sites 806B and 805C by using a NARMAX model. The model has one of the time-series as input and the other as output and uses only lagged terms in the input, so no lagged terms in the output are involved. Although the Sites are closely located to one another some differences are identified between the $\delta^{18}O$ time-series, as seen in Figure 8.2, and it is interesting to be able to account for these differences using a model.

Section 8.2 gives details with regards to the location of the two investigated Sites and

also some of their general characteristics. These refer to stratigraphy subdivisions and the composition of the foraminifera extracted from each Site. Section 8.3 presents an in depth comparison of the Sites aimed to find similarities and differences between them with regards to the chemical gradients of the interstitial waters and other sediments properties. This is useful because the benthic foraminifera may be sensitive to habitat, sediment, and water quality long-term and short-term changes (Berger, 1969). Section 8.4 deals with the strategies used to obtain a model relating the $\delta^{18}O$ data from the two Sites. Also in this section analysis of the model results and simulation is performed.

8.2 Location and General Comparison of the Sites

The distance between Site 806B and Site 805C is 164.6076km. The two Sites are part of Leg 130 in the Western Pacific, and their location within the leg and with respect to the Equator can be seen in Figure 8.1. Sites 803 to 805 are drilled in deeper water. The Site 805 represents the intermediate-to-deep member whilst Site 806 represents the shallow end member, in which sediments have experienced much less dissolution (Berger et al., 1993a).

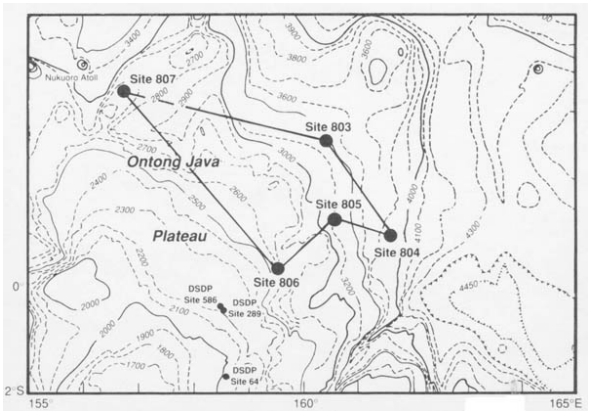

Figure 8.1: Map of the Sites of the ODP Leg 130 in Western Pacific, displaying the two Sites of interest 806 and 805 (Berger et al., 1991b).

Leg 130 Hole 806B is positioned at the coordinates $0°19.11' N$, $159°21.69' E$. The water depth until the sea floor is 2519.9 metres and the penetration using the drill is of 743.10 metres. The core recovery is of 89% (Kroenke et al., 1991b). The core is divided into two

subunits: *Subunit IA*, between 0 - 339 mbsf (metres below seafloor), which covers Pleistocene to upper middle Miocene and consists of foraminifer nannofossil ooze to nannofossil ooze with foraminifers, and *Subunit IB*, between 339 - 776 mbsf, which covers the eras lower upper Miocene to upper Oligocene and consists of foraminifer nannofossil chalk to nannofossil chalk with foraminifers, with a few intervals of nannofossil chalk.

Leg 130 Hole 805C is positioned at the coordinates $1°13.69' N$, $160°31.77' E$. The water depth until the sea floor is 3187.7 metres and the penetration using the drill is of 611 metres. Site 805 is positioned within a gently sloping valley about 3.5 km wide and flanked by low ridges along either side. The core recovery is of 81% (Kroenke et al., 1991a). The core is divided into two subunits: *Subunit IA*, between 0 - 293.7 mbsf, which covers Pleistocene to middle Miocene and consists of nannofossil ooze with foraminifers, and foraminifer nannofossil ooze, and *Subunit IB*, between 293.7 - 611 mbsf, which covers the middle Miocene to upper Oligocene and consists of nannofossil chalk, nannofossil chalk with foraminifers, and foraminifer nannofossil chalk.

The coarser grains (fine sand and coarse silt) at these Sites are foraminifers, so that fluctuations in the mean grain size are a good indicator of the relative abundances of foraminifers and nannofossils.

The sedimentation rates for the two Sites considered in this study are relatively high, with 12 - 13 m/m.y. (metres/million years) at Hole 805C and between 20 and 30 m/m.y. at Hole 806B (Berger et al., 1993a), and this permits the generation of high-resolution $\delta^{18}O$ and $\delta^{13}C$ records from the Western Equatorial Pacific Plateau back in time through to the middle Miocene. The sedimentation rates show a similar shape of the age/rate curve for all sites from Leg 130, however Site 806 averages a factor of 1.44 higher sedimentation rate than Site 805.

Sites 805 and 806 are similar with respect to their seismic records, except that the Site 805 record is compressed on average by a factor of 0.73 (Berger et al., 1993c).

8.3 Organic and Chemical Properties at the Sites

Chemical gradients of the interstitial waters at Site 806 tend to be slightly stronger when compared to Site 805, probably due to the higher supply of organic matter at the Site, because of its shallower depth (Berger et al., 1993b). Next a comparison between the two Sites with regards to the organic and chemical components will be presented. This comparison represents a brief summary of the extensive descriptions, analysis and comparison presented by W.H. Berger in the "Volume 130 Initial Reports" (Berger et al., 1993b, Berger et al., 1993a, Berger et al., 1993c, Kroenke et al., 1991a, Kroenke et al., 1991b).

- *Foraminifera content for Subunit 1A* for Site 806 is 15-30% and rarely below 10%, which is significantly higher than Site 805.
- *Foraminifera content (Subunit 1B)* for Site 806 varies between 10% and 50% and is relative higher compared to that of equivalent intervals at Site 805.
- *Sediment colour (Subunit 1A)* for Site 806 on uppermost several meters is brown, and grades rapidly to light gray then to white. Color banding for Site 806 appears to be less frequent, fainter, and more diffuse than at Site 805.
- *Lithification* at Site 806 shows the transition is at 340mbsf (lower upper Miocene), which is deeper and younger than the ooze-chalk transition at Site 805.
- *Sodium (Na) concentrations* at Site 806 below 300mbsf are higher than those at Site 805.
- *Alkalinity* maximum is deeper and broader with higher concentrations at Site 806 than Site 805, suggesting a larger supply of organic matter for oxidation at this fairly shallow site, the closest to the equator of those drilled on the Ontong Java Plateau.
- *Sulfate concentrations* show that the depletion at Site 806 is nearly a factor of 2 larger than at Site 805, and it is due to the influence of organic matter (Berger et al., 1993b).
- *Ammonia concentrations* at Site 806 are twice those at Site 805.

- *Strontium (Sr) concentrations* are, at the maximum, higher at Site 806 than at Site 805.
- *Lithium (Li) minimum concentrations* at Site 806 are lower and are persisting to somewhat greater depths than those at Site 805.
- *Potassium (K) concentrations* at Site 806 are smaller than those observed at Site 805.
- *Calcium concentrations* are smaller at Site 806 than those observed at Site 805. The differences between Site 806 and the first three Sites (803-805) drilled are that the magnitudes of Ca increases with depth and K and Rubidium (Rb) decreases with depth. This suggests that there must be differences in the history of basalt alteration at Site 806 compared with the others (Berger et al., 1993b).

Given there are dissimilarities between the two analysed Sites, as the synthesis done in this section shows, it is possible that these cause the difference in the oxygen isotope ratios values despite the fact that the two Sites are located very close to each other. These differences are shown in Figure 8.2.

In summary, there is good correlation between Sites 805 and 806, and good agreement in biostratigraphic dates for equivalent reflectors or reflector groups, regardless of the overall difference in sedimentation rates. The observed differences may be cause by palaeoceanographic events, that are of global significance and are reflected over a wide depth range, and/or by minor regional events (Kroenke et al., 1991a, Kroenke et al., 1991b).

8.4 Modelling Strategies and Results

Figure 8.2a shows that the two data-sets have very similar trends and share the same range of values. The difference between the data-sets with regards to the *mean squared error* is $NRMSE = 18.38\%$. In order to put this into perspective, it is useful to look at the amplitude ranges for the two data-sets, which are: $[-1.99, -0.43]$ for $\delta^{18}O\,(806)$ and $[-1.87, -0.15]$ for $\delta^{18}O\,(805)$. It is reasonable to expect similarities between the data, because the excavation Sites 806B and 805C are so closely located to one another. However, Figure 8.2a, shows that the two data-sets present a few differences outside of the main followed trend. These

variations could be explained by the differences, both due to location, organic material distribution and quantity and chemical gradients of the interstitial waters of the two Sites, detailed in Sections 8.2 and 8.3 of this chapter.

In order to inspect the similarities and differences in the frequencies of interest, $\sim f_{100}$ and f_{41}, it is also crucial to check the agreement of the two data-sets in the frequency domain. Figure 8.2b shows that most of the magnitude spectrum is very similar, except for the peaks at f_{254} and the $\sim f_{41}$, which is considerably higher for the $\delta^{18}O\,(806)$ data. Figure 8.2c shows the phase spectrum of the data from the two Sites. This shows that the two signals are in high agreement for the low frequencies, until $\sim f_{61}$. For the interval $[f_{61}, f_{41}]$ and the frequencies $f_{28.5}$ and $f_{21.5}$ the phase of the two signals does not correspond well, with the phase $\angle\delta^{18}O(805C)$ having larger angle values in the interval $[f_{61}, f_{41}]$. The phase spectrum of the two signals has again similar values after $f_{21.5}$.

The modelling and analysis presented next is targeted at establishing a relationship between the $\delta^{18}O$ data-sets from the two Sites, by fitting a NARMAX model. The NARMAX model has one input and no lagged terms in the output. The first problem encountered was which of the data to use as input to the model and which one as output. Figure 8.2a, shows a slight delay in the superimposed plots of the two data-sets, in the sense that generally the data-set from the Site 806 is "ahead" compared to the data-set from Site 805. On this figure, the red dots identify the delay between the two signals.

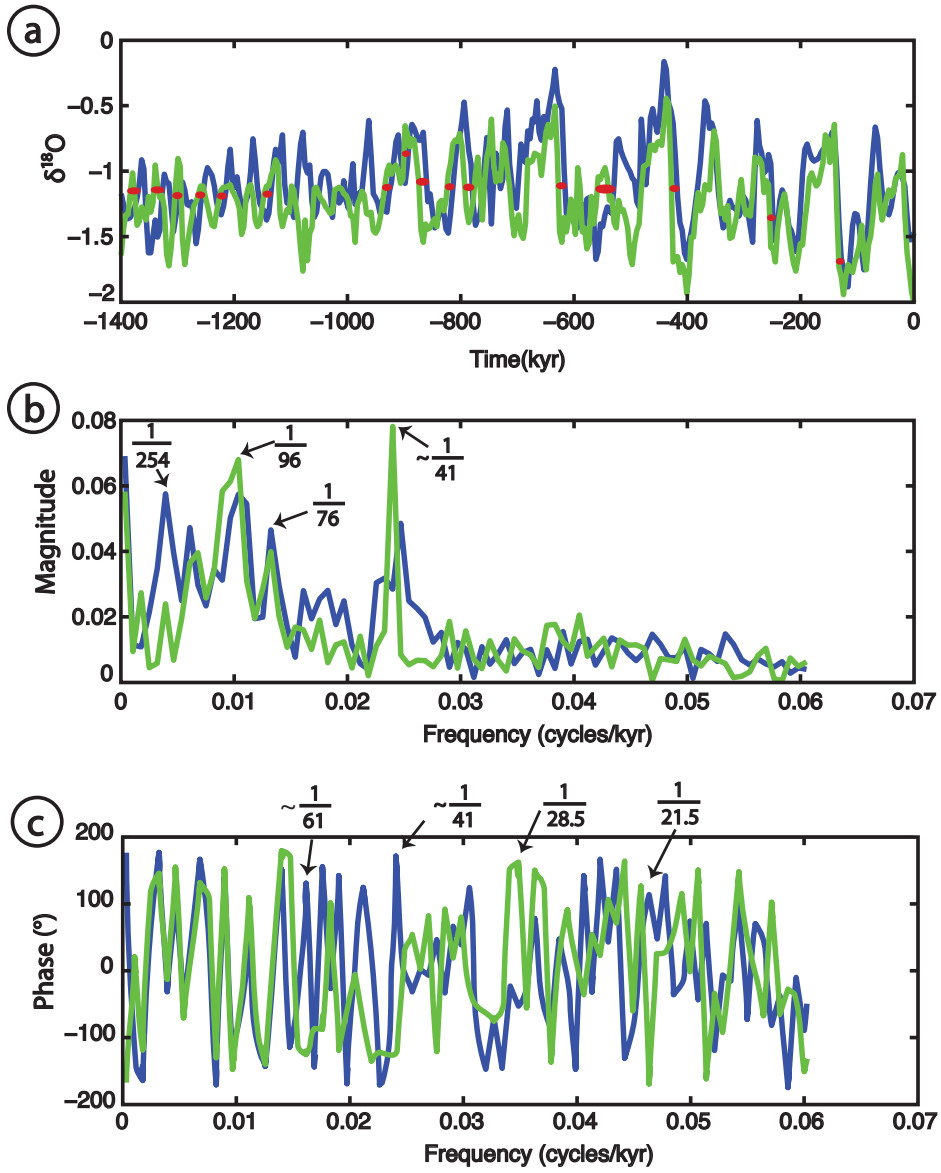

Figure 8.2: a. $\delta^{18}O(806)$ (green) and $\delta^{18}O(805)$ (blue), where the red dots mark the observed the delay between the signals b. Magnitude and c. Phase functions of $\delta^{18}O\,(806)$ (green) and $\delta^{18}O\,(805)$ (blue).

To further study this problem, six models were fitted. They correspond to the first three degrees of nonlinearity models for each of the two possible combinations of input-output. The maximum lag allowed for input and noise terms was eight. The *normalized root mean squared errors* for each of the possible full models is given in Table 8.1, and the model results

can be viewed in Figure 8.3.

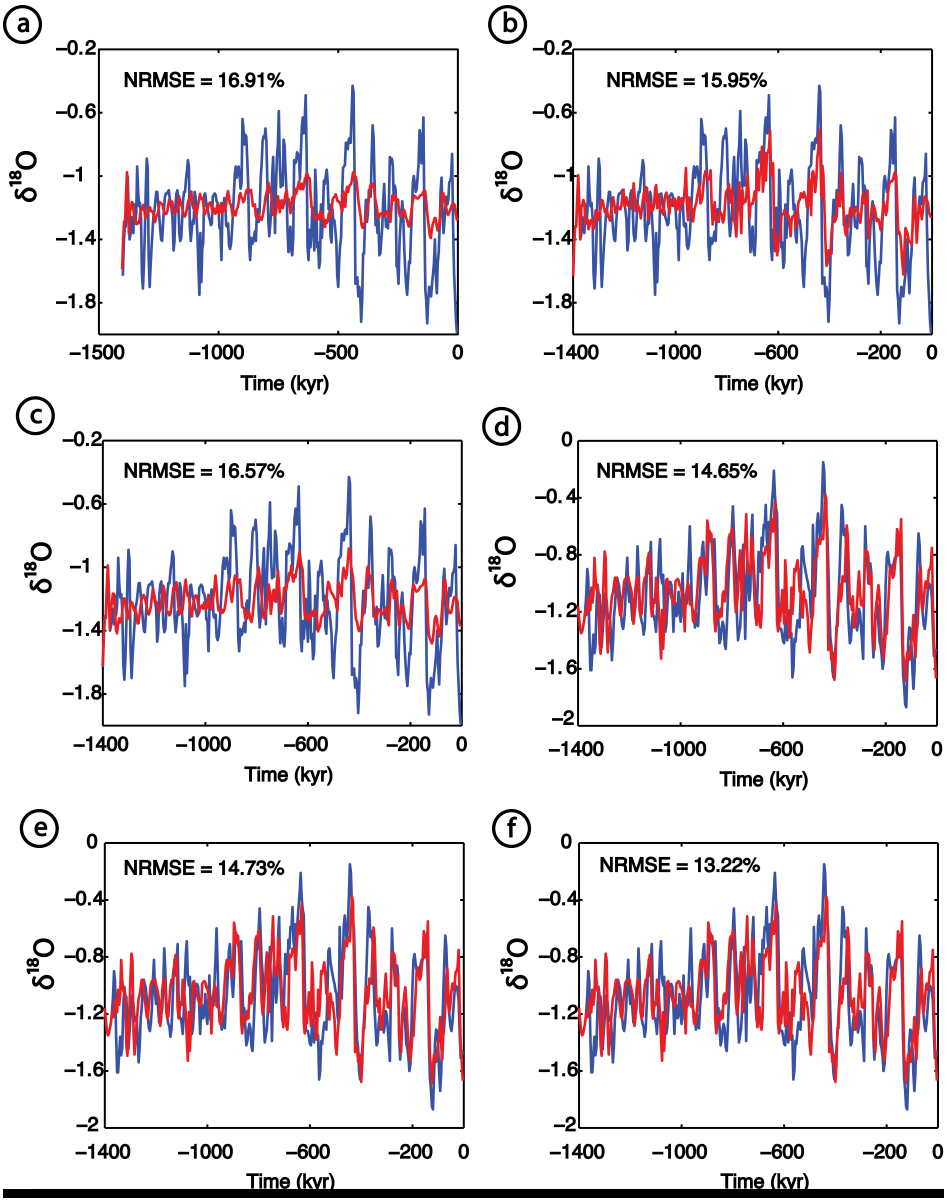

Figure 8.3: Modelling results and errors for: a, b, c. input $\delta^{18}O(805)$ and output $\delta^{18}O(806)$ and d, e, f. input $\delta^{18}O(806)$ and output $\delta^{18}O(805)$, for the following model degrees of nonlinearity: a, d. first order ($d = 1$); b, e. second order ($d = 2$) and c, f. third order ($d = 3$).

Case	degree = 1	degree = 2	degree = 3
$in = \delta^{18}O\,(805)$, $out = \delta^{18}O\,(806)$	16.91%	15.95%	16.57%
$in = \delta^{18}O\,(806)$, $out = \delta^{18}O\,(805)$	14.65%	14.73%	13.22%

Table 8.1: *NRMSE* values for the input-output studied cases.

This analysis revealed that the case with $\delta^{18}O(805)$ as input produced very poor model predicted outputs, as shown in Figures 8.3a, 8.3b and 8.3c. The smallest *NRMSE* value was for $\delta^{18}O(806)$ as input. For this case the model has the degree of nonlinearity three and its error value $NRMSE = 13.22\%$. Cross-validation was used to obtain the model structure giving the best fit.

The preliminary analysis suggested using the dataset from site 806 as input and the one from site 805 as output. The best model has 17 process terms and 10 noise terms. The model written for zero mean input is shown in Table 8.2. The *mpo* $y(t)$ superimposed on the output data $\delta^{18}O(805)$ is presented in Figure 8.4a. This shows that the *mpo* reproduces very well the time-series of the measured $\delta^{18}O\,(805)$. Furthermore, in the frequency domain the spectrum of the *mpo* fits well on the spectrum of the $\delta^{18}O\,(805)$ with the exception of the peak at $\sim f_{254}\,cycles/kyr$. The correlations tests in Figure 8.5 also show that the fitted model performs well within acceptable limits.

	Model coefficients	Model terms		
1	**0.1227**	u(t-1)	0	0
2	**-0.0805**	u(t-3)	0	0
3	0.2511	u(t-3)	u(t-3)	u(t-8)
4	0.1967	u(t-4)	u(t-8)	0
5	-1.0972	0	0	0
6	1.0284	u(t-1)	u(t-3)	0
7	0.2003	u(t-1)	u(t-2)	u(t-2)
8	-0.3075	u(t-1)	u(t-2)	0
9	-0.6319	u(t-1)	u(t-3)	u(t-8)
10	**0.2442**	u(t-4)	0	0
11	1.0719	u(t-3)	u(t-4)	0
12	0.7121	u(t-3)	u(t-3)	u(t-4)
13	0.1621	u(t-1)	u(t-2)	u(t-8)
14	0.1340	u(t-1)	u(t-8)	0
15	0.0588	u(t-4)	u(t-4)	u(t-8)
16	0.4317	u(t-1)	u(t-3)	u(t-3)
17	-0.2654	u(t-3)	u(t-3)	u(t-3)
18	-0.7294	u(t-3)	u(t-3)	0
19	0.1579	u(t-3)	0	u(t-8)
20	**-0.1175**	0	0	u(t-8)
21	-0.2439	0	u(t-2)	u(t-2)
22	**0.3745**	0	0	u(t-2)
23	-0.1974	0	u(t-2)	u(t-8)
24	-0.0716	u(t-4)	u(t-4)	0

Table 8.2: Model terms and coefficients describing the relationship between $\delta^{18}O$ (806) and $\delta^{18}O$ (805).

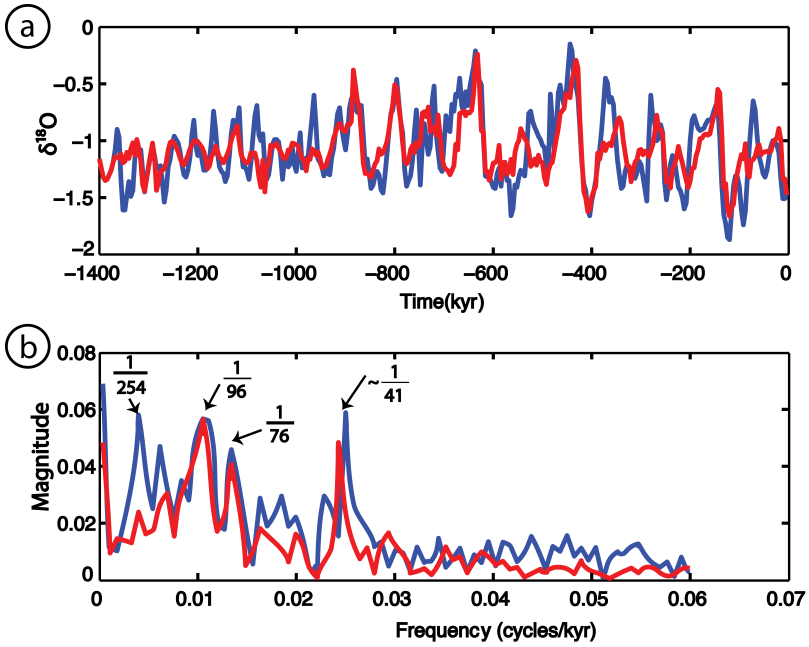

Figure 8.4: a. $\delta^{18}O(805)$ (blue) superimposed on the *mpo* $y(t)$ (red) b. Magnitude spectrum of $\delta^{18}O\,(805)$ (blue) and of $y(t)$ (red).

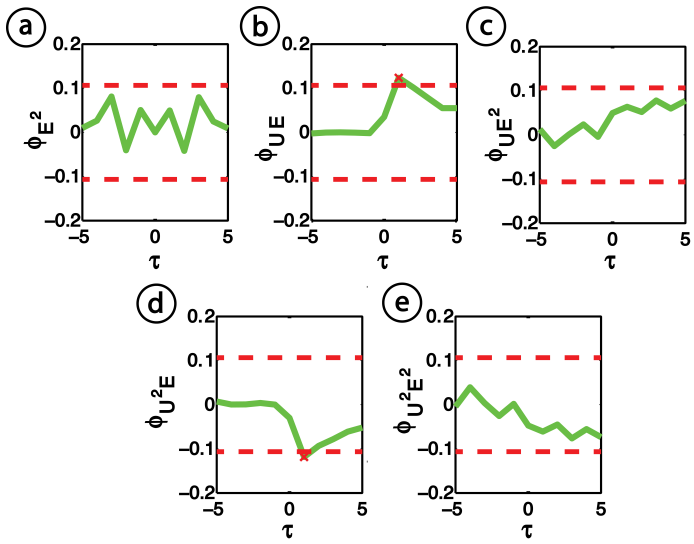

Figure 8.5: Correlation tests: a. ϕ_{E^2}, b. ϕ_{UE}, c. ϕ_{UE^2}, d. ϕ_{U^2E} and e. $\phi_{U^2E^2}$ for the fitted model with input $\delta^{18}O(806)$ and output $\delta^{18}O(805)$.

After the model was fitted and validated, the next step was to obtain the Output Frequency Responses (OFRs) by using the model's Generalized Frequency Response Func-

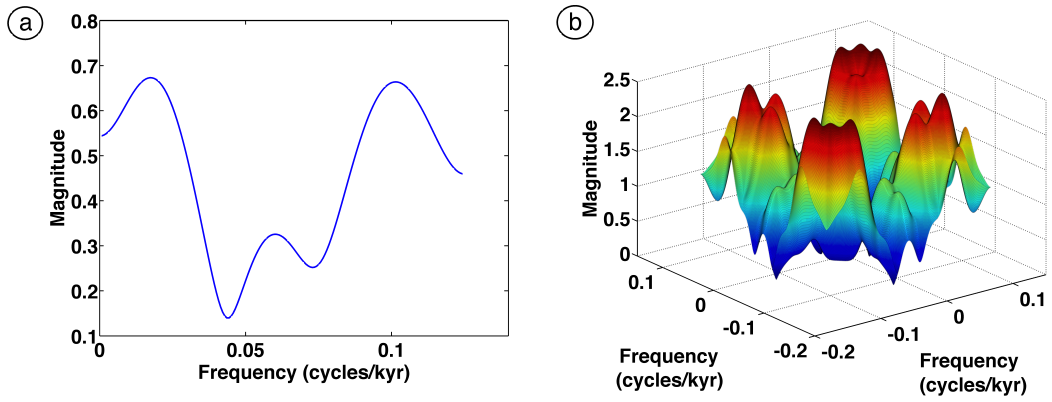

Figure 8.6: a. First and b. Second order Generalized Frequency Response Functions corresponding to the model in Table 8.2.

tions (GFRFs) and the input spectrum. Given the model is a third order SISO model, compared to the three inputs MIMO model studied in the previous chapters, it is easier to calculate the OFRs, because all of the functions are self-kernel functions. So the *mpo* spectrum can be defined as: $Y(j\omega) = \sum_{j=1}^{n} Y^j(j\omega)$, where n is the model nonlinearity order. So for the SISO model under investigation, the output spectrum is given by: $Y(j\omega) = Y^1(j\omega) + Y^2(j\omega) + Y^3(j\omega)$.

$$H^1(j\omega_1) = 0.1227e^{-j\omega_1} + 0.3745e^{-2j\omega_1} - 0.0805e^{-3j\omega_1} + 0.2442e^{-4j\omega_1} - 0.1175e^{-8j\omega_1}$$

$$\begin{aligned} H^2(j\omega_1, j\omega_2) \quad = \quad & -0.1538[e^{-j(\omega_1+2\omega_2)} + e^{-j(2\omega_1+\omega_2)} + 0.5142[e^{-j(\omega_1+3\omega_2)} + e^{-j(3\omega_1+\omega_2)}] \\ & -0.2439e^{-j(2\omega_1+2\omega_2)} - 0.7294e^{-j(3\omega_1+3\omega_2)} + 0.5360[e^{-j(3\omega_1+4\omega_2)} + e^{-j(4\omega_1+3\omega_2)}] \\ & -0.0716e^{-j(4\omega_1+4\omega_2)} + 0.0670[e^{-j(\omega_1+8\omega_2)} + e^{-j(8\omega_1+\omega_2)}] \\ & -0.0987[e^{-j(2\omega_1+8\omega_2)} + e^{-j(8\omega_1+2\omega_2)}] + 0.0790[e^{-j(3\omega_1+8\omega_2)} + e^{-j(8\omega_1+3\omega_2)}] \\ & +0.0983[e^{-j(4\omega_1+8\omega_2)} + e^{-j(8\omega_1+4\omega_2)}] \end{aligned}$$

The results of the OFR calculation is shown in Figure 8.7. This shows that the sum of the first three order functions perfectly fits on the output spectrum $Y(j\omega)$. Figure 8.7b presents separately each of the three functions $Y^1(j\omega)$ (blue), $Y^2(j\omega)$ (green) and $Y^3(j\omega)$ (red) in order to identify the main contributions to their sum.

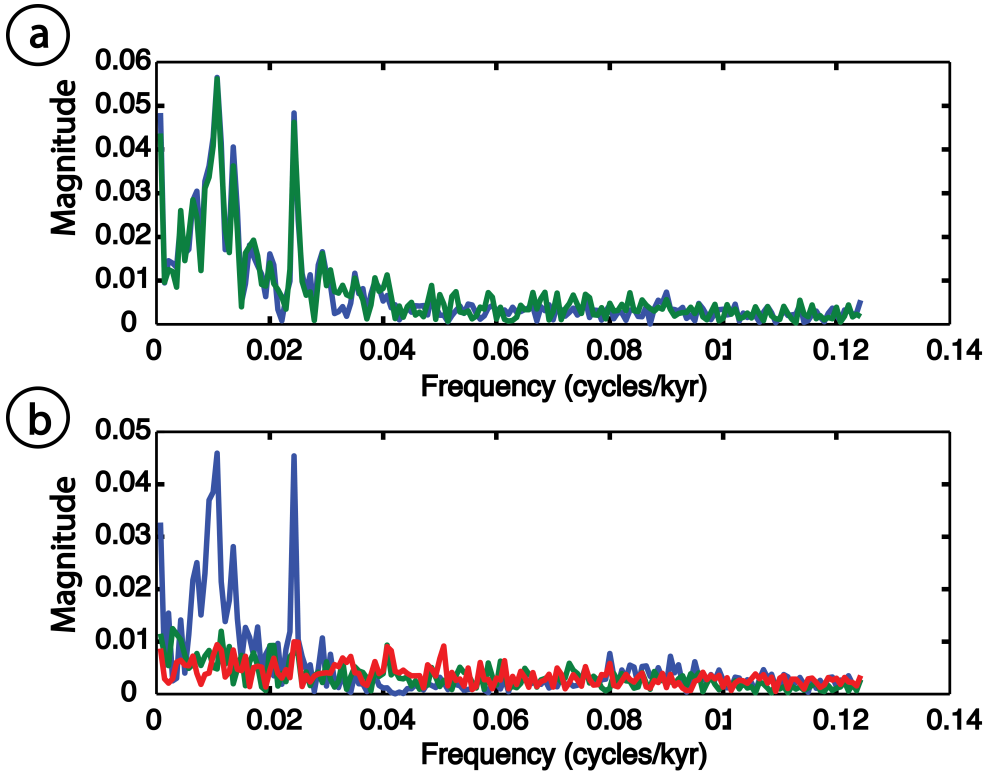

Figure 8.7: a. $Y(j\omega)$ (blue) superimposed on the sum of the first three order OFRs $Y^1(j\omega) + Y^2(j\omega) + Y^3(j\omega)$ (green); b. $Y^1(j\omega)$ (blue) superimposed on $Y^2(j\omega)$ (green) and $Y^3(j\omega)$ (red).

Figure 8.7 shows that the overwhelming contribution at the high magnitude peaks comes from $Y^1(j\omega)$. This is also confirmed by performing the inverse Fourier Transform frequency of the three calculated OFRs to obtain $\hat{y}^{(1)}(t)$, $\hat{y}^{(2)}(t)$ and $\hat{y}^{(3)}(t)$. The three signals add up to describe the mpo $y(t)$, as shown in Figure 8.8a.

Because the model was built without any lagged terms in the output, each order model part can be separated directly from the NARMAX model. The linear model is shown in bold font in Table 8.2 and its response $y^{(1)}(t)$ shown in Figure 8.8b. The model is:

$$y^{(1)}(t) = 0.1227\,u(t-1) + 0.3745\,u(t-2) - 0.0805\,u(t-3) - 0.1175\,u(t-8) + 0.2442\,u(t-4)$$

By analysing the response of $y^{(1)}(t)$ the terms that mostly contribute to the *mpo* were

identified as $y_s^{(1)}$as:

$$y_s^{(1)}(t) = 0.3745\, u(t-2) + 0.2442\, u(t-4)$$

The terms in the linear model $y_s^{(1)}(t)$ are $u(t-2)$, which involves a time delay of 8 kyr and $u(t-4)$, with a smaller term coefficient, which involves a time delay of 16 kyr. These terms can explain the small delay observed in the data-sets from the two Sites, which were identified in Figure 8.2a and discussed at the beginning of this section.

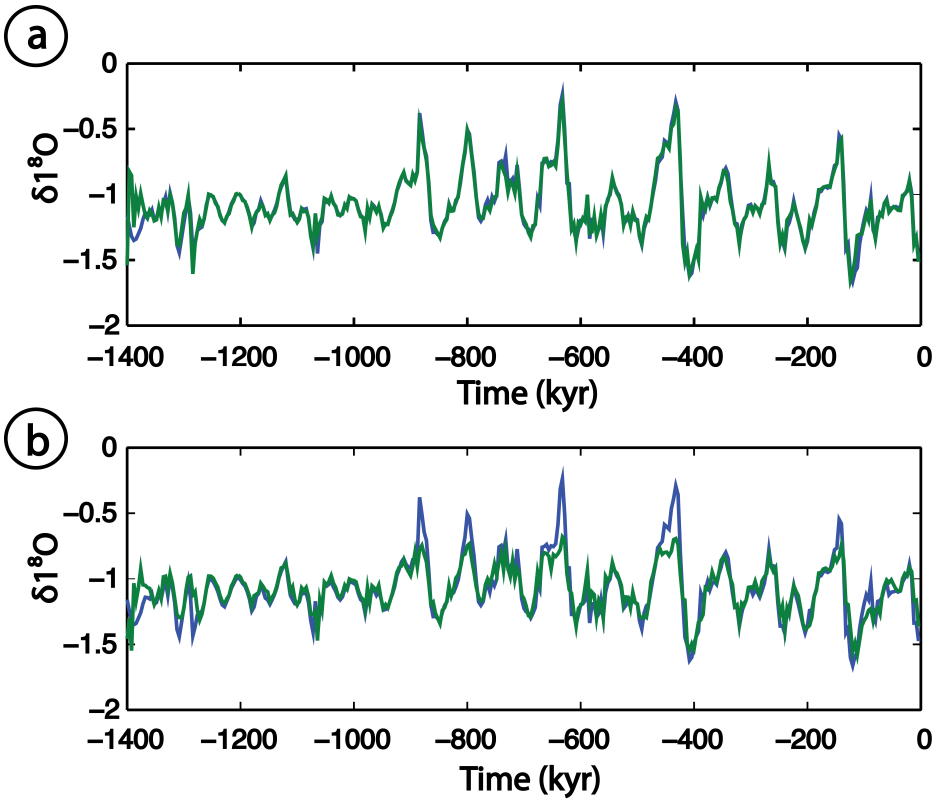

Figure 8.8: $y(t)$ (blue) superimposed on $\hat{y}(t)$, the time signal corresponding to the OFR sum $Y(j\omega) = Y^1(j\omega) + Y^2(j\omega) + Y^3(j\omega)$ (green); b. $y(t)$ (blue) superimposed on the time signal $\hat{y}^{(1)}(t)$ corresponding to the first order OFR $Y^{(1)}(j\omega)$ (green) and the model response $y_s^{(1)}(t)$ of the reduced first order model (red).

This confirms the frequency domain analysis from Figure 8.7b, which revealed that the linear model is enough to reproduce the model response.

The *normalized root mean squared error* Table 8.9 between the model response $y(t)$ and

$\delta^{18}O(805)$ is $NRMSE_{\delta^{18}O(805),y} = 13.22\%$ and the *normalized root mean squared error* between $y^{(1)}(t)$ and the mpo $y(t)$ is $NRMSE_{y,y^{(1)}} = 6.27\%$. This means $NRMSE_{y,y^{(1)}}$ is small (50%) compared to $NRMSE_{\delta^{18}O(805),y}$. The reduced linear model part $y_s^{(1)}(t)$ has a slightly larger $NRMSE_{y,y_s^{(1)}} = 7.71\%$ compared to $y(t)$, which represents 58% of the overall $NRMSE_{\delta^{18}O(805),y}$. By choosing the reduced linear model $y_s^{(1)}(t)$, only two model terms can represent the relationship between $\delta^{18}O(805)$ and $\delta^{18}O(806)$ and this brings only small increase in the error.

NRMSE relating	$\delta^{18}O(805)$	$y(t)$	$y^{(1)}(t)$	$y_s^{(1)}(t)$
$y(t)$	13.22%			
$y^{(1)}(t)$	16.38%	6.27%		
$y_s^{(1)}(t)$	14.49%	7.71%	2.63%	
$\hat{y}^{(1)}(t)$	14.07%	6.8%	4.7%	6.09%

Figure 8.9: *NRMSE* values relating each of the time-series: output $\delta^{18}O(805)$, *mpo* $y(t)$, linear model part $y^{(1)}(t)$, reduced size linear model part $y_s^{(1)}(t)$ and the linear model part corresponding to the first order Volterra kernel $\hat{y}^{(1)}(t)$.

8.5 Discussion

Sites 806B and 805C are two extraction points from Leg 130 in the ODP Ontong Java Plateau in the Western Pacific, that although are located closely to each other show differences in the $\delta^{18}O$ time-series. The slight differences are observed in the time-series and also in the spectra of the data. This is what triggered the investigation of the time-series and the similarities and differences that appear in the Sites conditions, sedimentation rates, types of foraminifera, geological and chemical gradients of the interstitial waters of the Sites. This analysis was taken further by using the NARMAX methodology to obtain a model of the relationship between the $\delta^{18}O$ time-series from the two Sites. The first step was to identify which of the time-series to use as the model input and which as the output. The $\delta^{18}O$ of Site 806B was used as the model inputs and $\delta^{18}O$ of Site 805C as model output.

The fitted NARMAX model was a third order of nonlinearity one with 24 terms.

Using the Output Frequency Responses the contribution of each order frequency response can be evaluated. This analysis revealed that the first order response explains most of the

model response. Given the model only has lagged terms in the input, the linear model can be separated directly from the time domain NARMAX model. This helped in finding which of the linear model terms have the largest influence on the model output. The largest coefficient was given by the term with lag 2, which involves a delay of 8 kyr between the data-sets. This means that the cause of the variability observed in the two data-sets could be a local Western Pacific parameter occurring on periods that are less than the orbital parameters. This parameter could be the influence of closure to the Equator (Hagelberg et al., 1995), deep water circulation (Hagelberg et al., 1995), gas exchanges processes at the surface (Bickert et al., 1995) or organic matter production (Bickert et al., 1995).

In this chapter NARMAX was used not only to establish a relationship between the orbital parameters and the $\delta^{18}O$, as in previous Chapters, but also to fit a mathematical relationship between two $\delta^{18}O$ time-series.

Chapter 9

Conclusions

9.1 Discussion

This thesis introduced a new methodology for studying long term climate data using nonlinear system identification techniques and time and frequency domain analysis approaches.

The main focus of the thesis is the study of the Mid-Pleistocene Transition, which was placed by many authors (Imbrie et al., 1992, Pisias and Moore Jr., 1981) around $900 - 850$ kyr BP. This point in palaeoclimate history brought a shift in the main period of oscillation of the oxygen isotope ratios time-series, which represents a proxy for insolation. The observed change was from the so called "41 kyr world", where the main cycle was of 41 kyr driven by obliquity, to the "100 kyr world". Many authors (Rial and Anaclerio, 2000, Rial, 2004b, Berger and Loutre, 1997a, Berger et al., 1998, Imbrie et al., 1993, Ganopolski et al., 2010, Muller and MacDonald, 2005, Pollard, 1983) analysed the possible cause that triggered the shift to the dominant 100 kyr cycle, but a unified theory could not be put forward. Some of the explanations for the appearance of the 100 kyr cycle include: ***external forcing*** through orbital inclination (Muller and MacDonald, 2005), ***internal feedbacks***: Northern Hemisphere ice sheets (Berger et al., 1999, DeBlonde and Peltier, 1991), CO_2 concentrations (Ganopolski and Calov, 2011, Berger and Loutre, 1997b, Loutre and Berger, 2000), dust feedback (Ganopolski and Calov, 2011), ***frequency modulation*** of the orbital parameters (Berger et al., 2005, Clemens and Tiedemann, 1997, Rial and Anaclerio, 2000) and a ***coupled response*** between the orbital forcing and an internal nonlinear amplification (Berger, 1988,

Imbrie et al., 1993).

The input - output data that was used are the three orbital parameters and the oxygen isotope ratios proxy data. The Earth's orbital parameters were linked to long term climatic changes by many authors (Hays et al., 1976, Imbrie et al., 1992, Raymo, 1997) because their main periods of oscillation are large enough (tens or hundreds of thousands of years) to be associated with the main shift observed at the MPT. Main theories proposing explanations for the appearance of the dominant 100 kyr cycle include: the climate sensitivity shifted from *obliquity* to *precession/eccentricity* (Liu et al., 2008), power is transferred from one frequency band into another through frequency modulation (Berger et al., 2005, Clemens and Tiedemann, 1997), a nonlinear amplification of *eccentricity* generates the observed periodicity ***after MPT*** (Clark et al., 2006).

In order to analyse the shift observed at the MPT, the NARMAX methodology was first used to derive two polynomial models, corresponding to the time periods ***before*** and ***after MPT***. The NARMAX methodology involves structure detection, parameter estimation and model validation. The structure detection and parameter estimation was done using the Orthogonal Forward Regression algorithm. The optimal number of process and noise terms were selected using cross-validation. The NARMAX models have the great advantages that they are versatile, can provide insight into the system's dynamics and they can be easily mapped in the frequency domain by computing the Generalized Frequency Response Functions.

For the modelling procedure a very large number of linear and nonlinear model structures of different orders and input combinations were considered as candidates. The identified best model structures for both time periods were third order polynomials using all three orbital parameters as inputs. The models were validated using coherence analysis results and correlation tests. The models are able to predict accurately the $\delta^{18}O$ time-series corresponding to the modeled time period. Given that the model gives such good prediction only using the three orbital parameters as inputs suggests that indeed the orbital forcing had a considerable impact on the studied Pleistocene time period. An important result of the NARMAX models simulations is the fact that two distinct models are required for each time period. When the models are used to predict the $\delta^{18}O$ data for the time period not used in modelling, the

prediction error increases considerably.

The stability analysis performed on the two identified NARMAX models involved calculating the location of the fixed points. By determining the associated eigenvalues, the asymptotically stable fixed points were determined. Each of the models had one stable equilibrium point, and the model ***before MPT*** also had one unstable equilibrium point. The location of the stable fixed points were found to be close to each other.

Although the time domain models predict with great accuracy the $\delta^{18}O$ time-series, the MPT cannot be easily analysed in the time domain. For this reason, the concepts of Generalized and Output Frequency Response Functions were used to map the estimated NARMAX models in the frequency domain (Billings and Tsang, 1989a, Billings and Tsang, 1989b) and to analyse their properties. Given the frequency domain representation of a system is unique, compared to the time domain one, the use of the GFRFs and OFRs provided a rigorous representation that was instrumental in analysing and comparing the models ***before*** and ***after MPT***. By analysing the results ***before*** and ***after MPT***, two problems that received great attention were tackled: what are the origins of the $\sim$ 100 kyr cycle and what changed during the MPT that can explain the frequency shift from a 41 kyr cycle ***before MPT*** to $\sim$ 100 kyr cycle ***after MPT***. This was done by analysing the contribution, with regards to both magnitude and phase spectrum, of each OFR at the frequency corresponding to $\sim$ 100 kyr. This showed how each contribution changed from ***before*** to ***after MPT***, and also which of them has the largest influence on the magnitude peak at this frequency of interest.

The frequency domain analysis showed that most of the variability observed in the output spectrum of the *model predicted output* comes ***before MPT*** from the linear OFR generated by *eccentricity* and *longitude of perihelion* and that ***after MPT*** the overwhelming contribution is given by the linear OFR generated by *eccentricity* alone.

Performing a frequency to time transform of the OFRs, it was also possible to decompose the model response into its linear, quadratic, cubic and higher order responses. This gave a different way of characterizing the role of the linear and nonlinear responses, and showed that the largest contribution ***before*** and ***after MPT*** is given by the linear model response.

The NARMAX models not only provide a novel approach to palaeoclimate data modelling, but they are also a very powerful tool for data fitting. This was proven by the comparison of

the NARMAX model prediction with a model proposed by Rial and Anaclerio (2000) that uses frequency modulation of the 95 kyr *eccentricity* signal to generate the saw-tooth shape of the $\delta^{18}O$ data-set from Site 806B. Even though this model is capable of reproducing the main periodicity of the data, it is not able to capture the subtle changes of the time-series. The NARMAX models perform better than Rial's model, as the simulations and analysis in Chapter 7 showed.

The NARMAX methodology was further used to fit a model based on the $\delta^{18}O$ time-series from two different drilling Sites in the Western Pacific, Site 806B and Site 805C. This analysis was triggered by the slight differences observed in the data-sets, even though the drilling Sites are located closely to one another. A preliminary analysis which showed a slight delay in the $\delta^{18}O$ time-series from Site 805C encouraged to choose it as model output. The NARMAX model structure detection showed that a third order model structure was the best suited to describe the relationship between the two data-sets. However, using the OFR analysis, it was proven that a linear model is sufficient to give good fitting results without a considerable increase in the prediction error.

9.2 Future Work

The analysis of the $\delta^{18}O$ spectrum ***before*** and ***after MPT*** showed that the MPT was a shift in the dominant frequency of oscillation from a 41 kyr cycle to a $\sim$ 100 kyr cycle. Although at the frequency corresponding to the $\sim$ 100 kyr period a dramatic increase in the magnitude spectrum is clearly observed, the change in the magnitude peak at the frequency corresponding to the 41 kyr period is not significant. The same methodology of analysis using the GFRFs and OFRs can also be used to analyse the individual contribution of each function to the frequency corresponding to the 41 kyr period. This can reveal if the magnitude and phase spectrum contributions remain the same or if they change. If the contributions change, it would be interesting to observe how they compare to the changes observed ***before*** and ***after MPT*** at the $\sim$ 100 kyr.

The computed GFRFs and OFRs for the two estimated NARMAX models can also be used to provide an explanation for the origin of the non-orbital frequencies observed in the

spectra of the oxygen isotope ratios data.

Cell-to-cell mapping is a method proposed by Hsu (1980), Hsu and Guttalu (1980), Hsu (1981), Hsu et al. (1982) and Hsu (1982), that analyzes the global behaviour of strongly nonlinear systems, by dividing the state space into a large number of cells. There are two types of cell mapping methods: *simple cell-to-cell mapping* (Hsu, 1980, Hsu and Guttalu, 1980), for which each cell has only one image cell, and *generalized cell-to-cell mapping* (Hsu, 1981, Hsu et al., 1982), case in which each cell can be mapped onto multiples cells, with different probabilities. The cell mapping technique can be used on the NARMAX models estimated ***before*** and ***after MPT*** in order to obtain for each of them the domains of attraction for asymptotically stable solutions and the periodic cells. This can provide an additional analysis tool that can aid in comparing the two studied time periods.

The NARMAX methodology can be further applied to estimate models that incorporate other inputs as well as the three orbital parameters *eccentricity*, *obliquity* and *longitude of perihelion*. This type of model can assess the impact of the orbital parameters when compared to the other inputs by looking at the model coefficients. Other parameters that could be considered, and are used in other studies (Berger et al., 1998, Gallee et al., 1992, Petoukhov et al., 2005, Saltzman and Maasch, 1991, Maslin and Ridgwell, 2005, Ghil and Tavantzis, 1983) as inputs, are the atmospheric CO_2 concentrations and the planetary albedo.

In a similar matter to the previous suggestion, the NARMAX methodology can be used to model the Vostok ice core data (or data recovered from other Sites than the Pacific Ocean ones) using the orbital parameters as inputs. This can give insight into the influence of orbital parameters on a palaeoclimate proxy data set recovered from an ice core and also, by using the GFRF and OFRs, further information on the MPT can be obtained.

The model developed in Chapter 8 can be re-estimated by using lagged terms in the output as well. This can help in distinguishing the effect these terms have on the simulated model response, and compare with the model only using lagged terms in the input. This analysis can maybe narrow down the possible causes of the slight differences observed in the proxy data extracted from Sites 806B and 805C.

An interesting prospect can be the analysis of the data from the Sites 806B/805C and the Vostok ice core in a similar manner to the analysis for the two Sites from ODP Leg 130

performed in Chapter 8. This can show if any relationship between these two data sets can be modeled and analyzed, given the two Sites are located at a great distance.

The NARMAX methodology can also be applied to a different time period than the Pleistocene one. This can prove once more the versatility and power of the NARMAX methodology. Also the impact of the orbital parameters on other time periods can be assessed and compared with the Pleistocene results.

Concluding Remark

The introduction of this thesis presented the aim of describing and explaining the relationship between orbital parameters and palaeoclimate proxy data using NARMAX models. This work targets a very controversial and intriguing question in the field of palaeoclimate, and system identification provided a novel approach on this subject. The modeling, prediction and analysis results presented in this thesis are superior compared to models previously presented in literature and show great promise for future development in understanding the long term environmental changes.

References

L. A. Aguirre. A tutorial introduction to nonlinear dynamics and chaos, Part II: Modelling and control. *SBA Controle & Automacao*, 7(1), 1996.

L.A. Aguirre and S.A. Billings. Dynamical effects of overparametrization in nonlinear models. *Physica D*, 80(1,2):26 – 40, 1995.

A.J Arnold, J.M. Bernhard, M. Buzas, S. Cooke, S.J. Culver, M. Fariduddin, S.T. Goldstein, P. Hallock, and H.J. Hansen. *Modern Foraminifera*. Springer, 2002.

K.J. Astrom. Maximum likelihood and prediction error methods. *Automatica*, 16:551 – 574, 1980.

J. Beer, M. Vonmoos, and R. Muscheler. Solar variability over the past several millennia. *Space Science Reviews*, 2006.

A. Berger. Long-term variations of daily insolation and quaternary climatic changes. *Journal of Atmospheric Sciences*, 35(12):2362 – 2367, December 1978a.

A. Berger. Long-term variations of caloric insolation resulting from the Earth's orbital elements. *Quaternary Research*, 9:139 – 167, 1978b.

A. Berger. Milankovitch theory and climate. *Rev. Geophys.*, 26(4):624 – 657, 1988.

A. Berger and M. F. Loutre. An exceptionally long interglacial ahead? *Science*, 297(5585): 1287 – 1288, 2002.

A. Berger and M.F. Loutre. Astronomical solutions for paleoclimate studies over the last 3 million years. *Earth and Planetary Science Letters*, 111:369 – 382, July 1992.

A. Berger and MF Loutre. Precession, eccentricity, obliquity, insolation and paleoclimates. *Long-Term Climatic Variations*, 122:107 – 151, 1994.

A. Berger and M.F. Loutre. Long-term variations in insolation and their effects on climate, the LLN experiments. *Surveys in Geophysics*, 18:147 – 161, 1997a. ISSN 0169-3298.

A. Berger and M.F. Loutre. Palaeoclimate sensitivity to CO2 and insolation. *Ambio*, 26(1): 32 – 37, February 1997b.

A. Berger and M.F. Loutre. Modeling the 100-kyr glacial-interglacial cycles. *Global and Planetary Change*, 72(4):275 – 281, July 2010.

A. Berger, H. Galle, T. Fichefet, I. Marsiat, and C. Tricot. Testing the astronomical theory with a coupled climate ice-sheet model. *Palaeogeography, Palaeoclimatology, Palaeoecology*, 89:125 – 141, October 1990.

A. Berger, J.L. Melice, and L. Hinnov. A strategy for frequency spectra of quaternary climate records. *Climate Dynamics*, 5:227 – 240, 1991a.

A. Berger, M. F. Loutre, and H. Gallee. Sensitivity of the LLN climate model to the astronomical and co2 forcings over the last 200 ky. *Climate Dynamics*, 14:615 – 629, 1998.

A. Berger, X.S. Li, and M.F. Loutre. Modelling Northern Hemisphere ice volume over the last 3Ma. *Quaternary Science Reviews*, 18(1):1 – 11, 1999.

A. Berger, J.L. Melice, and M.F. Loutre. On the origin of the 100-kyr cycles in the astronomical forcing. *Paleoceanography*, 2005.

W. H. Berger, T. Bickert, H. Schmidt, G. Wefer, and M. Yasuda. 22. Quaternary oxygen isotope record of pelagic foraminifers: Site 806, Ontong Java Plateau. *Proceedings ODP: Scientific Results*, 130:381 – 395, 1993a.

W.H. Berger. Planktonic foraminifera: Basic morphology and ecologic implications. *Journal of Paleontology*, pages 1369 – 1383, 1969.

W.H. Berger, L.W. Kroenke, L.A. Mayer, and Shipboard Scientific Party. 10. Ontong Java Plateau, Leg 130: Synopsis of major drilling results. *Proceedins of the Ocean Drilling Program, Initial Reports*, 130, 1991b.

W.H. Berger, L.W. Kroenke, L.A. Mayer, and Shipboard Scientific Party. 8. Site 806. *Proceedins of the Ocean Drilling Program, Initial Reports*, 130, 1991c.

W.H. Berger, L.W. Kroenke, and L.A. Mayer. 17. Oxygen and carbon isotope stratigraphy of the Middle Miocene, Holes 805B and 806B1. *Proceedins of the Ocean Drilling Program, Scientific Results*, 130, 1993b.

W.H. Berger, R.M. Leckie, T.R. Janecek, R. Stax, and T. Takayama. 44. Neogene carbonate sedimentationon Ontong Java Plateau: Highlights and open questions. *Proceedins of the Ocean Drilling Program, Scientific Results*, 130, 1993c.

W.H. Berger, M.K. Yasuda, T. Bickert, G. Wefer, and T. Takayama. Quaternary time scale for the Ontong Java Plateau: Milankovitch template for Ocean Drilling Program Site 806. *Geology*, 22(5):463 – 467, 1994.

K. Bhattacharya and M. Ghil. An energy-balance model with multiply-periodic and quasichaotic free oscillations, evolution of planetary atmospheres and climatology of the Earth. *Centre National d'Etudes Spatiales, Toulouse, France*, pages 299–310, 1978.

T. Bickert, W.B. Curry, and G. Wefer. 14. Spatial and temporal variability of late Neogene Equatorial Pacific. *Proceedings of the Ocean Drilling Program, Scientific Results*, 138, 1995.

S A Billings. *Nonlinear System Identification NARMAX Methods in the Time, Frequency and Spatio-Temporal Domains*. John Wiley and Sons, Ltd, 2013.

S.A. Billings and D. Coca. Identification of NARMAX and related models. Research Report 786, Department of Automatic control and Systems Engineering, The University of Sheffield, Sheffield, S1 3JD, March 2001.

S.A. Billings and I.J. Leontaritis. Identification of nonlinear systems using parameter estimation techniques. Research Report 117, The University of Sheffield, September 1980.

S.A Billings and J.C. Peyton Jones. Mapping non-linear integro-differential equations into the frequency domain. *Int J Control*, 52:863 – 879, 1990.

S.A. Billings and A.K. Swain. Reconstruction of multiple-input multiple-output non-linear differential equation models from the Generalized Frequency Response Function matrix. *Proceedings of the Institution of Mechanical Engineers, Part I: Journal of Systems and Control Engineering*, 214(1):35 – 52, February 2000.

S.A. Billings and K.M. Tsang. Spectral analysis for non-linear systems, part I: Parametric non-linear spectral analysis. *Mechanical Systems and Signal Processing*, 3(4):319 – 339, 1989a.

S.A. Billings and K.M. Tsang. Spectral analysis for non-linear systems, part II: Interpretation of non-linear frequency response functions. *Mechanical systems and signal processing*, 3(4): 341 – 359, 1989b.

S.A. Billings and W.S.F. Voon. Correlation based model validity tests for nonlinear models. Research Report 285, Department of Control Engineering, The University of Sheffield, Mappin Street, Sheffield, S1 3JD, October 1985.

S.A. Billings and M.I. Yusof. Decomposition of Generalized Frequency Response Functions for nonlinear systems using symbolic computation. *Int. J. Control*, 65(4):589 – 618, 1996.

S.A. Billings and Q.M. Zhu. A structure detection algorithm for nonlinear dynamic rational models. *International Journal of Control*, 59(6):1439 – 1463, June 1994.

S.A. Billings and Q.M. Zhu. Model validation tests for multivariable nonlinear models including neural networks. *Int. J. Control*, 62(4):749–766, 1995.

S.A. Billings, S. Chen, and M.J. Korenberg. Identification of mimo non-linear systems using a forward-regression orthogonal estimator. *International Journal of Control. J. Control*, 49 (6):2157 – 2189, 1989.

O. Boaghe. *Volterra Series: Modelling Limitations*. PhD thesis, Department of Automatic Control and Systems Engineering, The University of Sheffield, 2000.

O.M. Boaghe, S.A. Billings, L.M. Li, P.J. Fleming, and J. Liu. Time and frequency domain identification and analysis of a gas turbine engine. *Control Engineering Practice*, 10(12): 1347 – 1356, 2002.

R. J. Boynton, M. A. Balikhin, S. A. Billings, G. D. Reeves, N. Ganushkina, M. Gedalin, O. A. Amariutei, J. E. Borovsky, and S. N. Walker. The analysis of electron fluxes at geosynchronous orbit employing a NARMAX approach. *Journal of Geophysical Research: Space Physics*, 2013.

H.A. Bridgman. *The Global Climate System : Patterns, Processes, and Teleconnections*. Cambridge University Press, Cambridge, 2006.

M.W. Browne. Cross-validation methods. *J Math Psychol*, 44(1):108–132, March 2000.

J. Chappell and N.J. Shackleton. Oxygen isotopes and sea level. *Nature*, 324:137–140, 1986.

S. Chen and S. A. Billings. Representations of non-linear systems: The NARMAX model. *International Journal of Control*, 49(3):1013 – 1032, March 1989a.

S. Chen and S.A. Billings. Recursive prediction error parameter estimator for non-linear models. *International Journal of Control*, 49:569 – 594, 1989b.

S. Chen, S.A. Billings, C.F.N. Cowan, and P.M. Grant. Practical identification of NARMAX models using radial basis functions. *International Journal of Control*, 52(6):1327 – 1350, December 1990a.

S. Chen, S.A. Billings, and P.M. GRANT. Non-linear system identification using neural networks. *International Journal of Control*, 51:1191 – 1214, 1990b.

N. Chiras, C. Evans, and D. Rees. Nonlinear gas turbine modelling using NARMAX structures. *IEEE Transactions in Instrumentation and Measurement Technology*, 2001.

J. Chowning. The synthesis of complex audio spectra by means of frequency modulation. *Computer Music Journal*, 1:46 – 54, 1977.

P.U. Clark, D. Archer, D. Pollard, J.D. Blum, J.A. Rial, V. Brovkin, A.C. Mix, N.G. Pisias, and M. Roy. The Middle Pleistocene Transition: Characteristics, mechanisms, and implications for long-term changes in atmospheric pCO2. *Quaternary Science Reviews*, 25(23): 3150 – 3184, 2006.

S.C. Clemens and R. Tiedemann. Eccentricity forcing of Pliocene-Early Pleistocene climate revealed in a marine oxygen-isotope record. *Nature*, 385(6619):801 – 804, 1997.

D. Coca and S. A. Billings. Non-linear system identification using wavelet multiresolution models. *International Journal of Control*, 74(18):1718 – 1736, January 2001.

T.M. Cronin. *Paleoclimates: Understanding Climate Change Past and Present*. Columbia University Press, 2013.

M. Crucifix, M.F. Loutre, Tulkens, T. Fichefet, and A. Berger. Climate evolution during the Holocene: A study with an Earth system model of intermediate complexity. *Climate Dynamics*, 19:43 – 60, 2002.

M. Crucifix, M. F. Loutre, and A. Berger. The climate response to the astronomical forcing. In Y. Calisesi, R. M. Bonnet, L. Gray, J. Langen, and M. Lockwood, editors, *Solar Variability and Planetary Climates*, volume 23 of *Space Sciences Series of ISSI*, pages 213–226. Springer New York, 2007.

M. Crucifix, M. Claussen, G. Ganssen, J. Guiot, Z. Guo, T. Kiefer, Rousseau D.-D. Loutre, M.-F., and E. Wolff. Climate change: from the geological past to the uncertain future: A symposium honouring Andre Berger. *Climate Past*, 5:707 – 711, 2009.

W. Dansgaard. Stable isotopes in precipitation. *Tellus*, 16:436 – 468, 1964.

W. Dansgaard. Evidence for general instability of past climate from a 250-kyr ice-core record. *Nature*, 364:218 – 220, 1993.

A.G. Dawson. *Ice Age Earth - Late Quaternary Geology and Climate*. Routledge, 1994.

G. DeBlonde and W.R. Peltier. A one-dimensional model of continental ice volume fluctuations through the Pleistocene: Implications for the origin of the Mid-Pleistocene climate Transition. *Journal of Climate*, 4:318 – 344, 1991.

H. Diaz and A.A. Desrochers. Modeling of nonlinear discrete-time systems from input-output data. *Automatica*, 24(5):629 – 641, 1988.

A.B. Dobrucki and P. Pruchnicki. Application of the NARMAX method for modelling of the nonlinearity of dynamic loudspeakers. *106th Convention Audio Engineering Society, Munich, Germany*, 1999.

C. Emiliani. Pleistocene temperatures. *Journal of Geology*, 63:538–578, 1955.

C. Emiliani. Isotopic paleotemperatures. *Science*, 154:851–857, 1966.

D.B. Ericson and G. Wollin. *The Deep and the Past*. 1964.

M. Farina and L. Piroddi. An iterative algorithm for simulation error based identification of polynomial input-output models using multi-step prediction. *International Journal of Control*, 83(7):1442 – 1456, July 2010.

K.A. Farley and D.B. Patterson. A 100-kyr periodicity in the flux of extraterrestrial He to the sea floor. *NAture*, 378:600 – 603, 1995.

D. Finnegan. James Croll, metaphysical geologist. *Notes and Records of The Royal Society*, 2011.

U. Friederich. *Nonlinear System Identification and Analysis of Adaptive Neural Information Processing in the Fly Early Visual System*. PhD thesis, Dept. of Automatic Control and Systems Engineering, The University of Sheffield, 2011.

H. Gallee, J.P. Van Ypersele, T. Fichefet, C. Tricot, and A. Berger. Simulation of the last glacial cycle by a coupled 2D climate-ice sheet model. Part 2: Response to insolation and CO2. *J. Geophys. Res.*, 97:15713–15740, 1992.

A. Ganopolski and R. Calov. The role of orbital forcing, carbon dioxide and regolith in 100 kyr glacial cycles. *Climate of the Past Discussions*, 7(4):2391 – 2411, 2011.

A. Ganopolski, R. Calov, and M. Claussen. Simulation of the last glacial cycle with a coupled climate ice-sheet model of intermediate complexity. *Climate Past Past*, 6(2):229 – 244, 04 2010.

M. Ghil. Steady-state solutions of a diffusive energy-balance climate model and their stability. *J. Atmos. Sci.*, 33, 1976.

M. Ghil and K. Bhattacharya. An energy-balance model of glaciation cycles. *GARP Publ. Series*, 22:886–916, 1979.

M. Ghil and J. Tavantzis. Global Hopf bifurcation in a simple climate model. *SIAM Journal on Applied Mathematics*, 43(5):1019 – 1041, 1983.

F.M. Gradstein, J.G. Ogg, and A.G. Smith. *A Geologic Time Scale*, volume 86. Cambridge University Press, 2005.

J. Guckenheimer and P. Holmes. Nonlinear oscillations, dynamical systems, and bifurcations of vector fields. *Applied Mathematical Sciences*, 42, 1983.

L.Z. Guo and S.A. Billings. A modified orthogonal forward regression least-squares algorithm for system modelling from noisy regressors. *International Journal of Control*, 30(3):340–348, 2007.

R. Gutierrez-Osuna. Lecture 13: Validation, 2005.

Wassim Haddad and VijaySekhar Chellaboina. *Nonlinear Dynamical Systems and Control: A Lyapunov-Based Approach*. Princeton University Press, 2011.

T.K. Hagelberg, N.G. Pisias, L.A. Mayer, N.J. Shackleton, and A.C. Mix. 14. Spatial and temporal variability of Late Neogene Equatorial Pacific carbonate: Leg 1381. *Proceedings of the Ocean Drilling Program, Scientific Results*, 138, 1995.

J.D. Hays, J. Imbrie, and N.J. Shackleton. Variations in the Earth's orbit: Pacemaker of the ice ages. American Association for the Advancement of Science, 1976.

M.J. Head, B. Pillans, and S.A. Farquhar. The Early-Middle Pleistocene Transition: Characterization and a proposed guide for the defining boundary. *Episodes 31*, pages 234 – 238, 2008.

X. Hong and C.J. Harris. Nonlinear model structure detection using optimum experimental design and orthogonal least squares. *IEEE Trans. Neural Netw.*, 12(2):435 – 439, March 2001.

C.S. Hsu. A theory of cell-to-cell mapping dynamical systems. *Journal of Applied Mechanics*, 47:931–939, 1980.

C.S. Hsu. A generalized theory of cell-to-cell mapping for nonlinear dynamical systems. *ASME J. Appl. Mech.*, 48:634 – 842, 1981.

C.S. Hsu. A probabilistic theory of nonlinear dynamical systems based on the cell space concept. *ASME J. Appl. Mech.*, 49, 1982.

C.S. Hsu and R.S. Guttalu. An unraveling algorithm for global analysis of dynamical systems: An application of cell-to-cell mappings. *ASME Journal of Applied Mechanics*, 47:940 – 948, 1980.

C.S. Hsu, R.S. Guttalu, and W.H. Zhu. A method of analyzing generalized cell mappings. *ASME J. Appl. Mech.*, 49, 1982.

P. Huybers and C. Wunsch. Obliquity pacing of the Late Pleistocene glacial terminations. *Nature*, 434, 2005.

J. Imbrie and J.Z. Imbrie. Modeling the climatic response to orbital variations. *Science*, 207 (4434):943 – 953, 1980.

J Imbrie, , E.A Boyle, S.C. Clemens, A. Duffy, W.R. Howard, G Kukla, J Kutzbach, D.G. Martinson, A Mcintyre, A.C. Mix, B Molfino, J.J. Morley, L.C. Peterson, N.G. Pisias, W.L. Prell, M.E. Raymo, N.J. Shackleton, and J.R. Toggweiler. On the structure and origin of major glaciation cycles 1. Linear responses to Milankovitch forcing. *Paleoceanography*, 7 (6):701 – 738, 1992.

J. Imbrie, A. Berger, E.A. Boyle, S.C. Clemens, A. Duffy, W.R. Howard, G. Kukla, J. Kutzbach, D.G. Martinson, A. Mcintyre, A.C. Mix, B. Molfino, J.J. Morley, L.C. Peterson, N.G. Pisias, W.L. Prell, M.E. Raymo, N.J. Shackleton, and J.R. Toggweiler. On the structure and origin of major glaciation cycles 2. The 100,000-year cycle. *Paleoceanography*, 8(6):699 – 735, 1993.

R. Isermann. Practical aspects of process identification. *Automatica*, 16:575 – 587, 1980.

E. Jansen, J. Overpeck, K.R. Briffa, J.C. Duplessy, F. Joos, V. Masson-Delmotte, D. Olago, B. Otto-Bliesner, W.R. Peltier, S. Rahmstorf, R. Ramesh, D. Raynaud, D. Rind, O. Solomina, R. Villalba, and D. Zhang. *Climate Change 2007: The Physical Science Basis. Contribution of Working Group I to the Fourth Assessment Report of the Intergovernmental Panel on Climate Change*. Cambridge University Press, Cambridge, United Kingdom and New York, NY, USA., 2007.

S.J. Johnsen, W. Dansgaard, H.B. Clausen, and C.C. Jr. Langway. Oxygen isotope profiles through the Antarctic and Greenland ice sheets. *Nature*, 25:429 – 434, 1972.

J. Jouzel, N.I. Barkov, J.M. Barnola, M. Bender, J. Chappellaz, C. Genthon, and V.M. Kotlyakov. Extending the Vostok ice-core record of palaeoclimate to the penultimate glacial period. *Nature*, 364:407 – 412, 1993.

K.I. Kim and E.J. Powers. A digital method of modeling quadratically nonlinear systems with a general random input. *Acoustics, Speech and Signal Processing, IEEE Transactions on*, 36(11):1758 – 1769, 1988.

M.J. Korenberg, S.B. Bruder, and P.J. McLlroy. Exact orthogonal kernel estimation from finite data records: Extending Weiner's identification of nonlinear systems. *Annals of Biomedical Engineering Issue 2*, 16:201–214, 1988.

S.J. Kortenkamp and S.F. Dermott. A 100,000 year periodicity in the accretion rate of interplanetary dust. *Science*, 280:874 – 876, 1998.

L.W. Kroenke, W.H. Berger, and et al. Janecek, T.R. 7. Site 805. *Proceedings of the Ocean Drilling Program, Initial Reports*, 130, 1991a.

L.W. Kroenke, W.H. Berger, and et al. Janecek, T.R. 8. Site 806. *Proceedings of the Ocean Drilling Program, Initial Reports*, 130, 1991b.

G. Kukla, A. Berger, R. Lotti, and J. Brown. Orbital signature of interglacials. *Nature*, 290: 295 – 300, 1981.

S.L. Kukreja, Galiana H.L., and Kearney R.E. NARMAX representation and identification of ankle dynamics. *IEEE Trans Biomed Engineering*, 50:70 – 81, 2003.

Z.Q. Lang and S.A. Billings. Output frequencies of nonlinear systems. *International Journal of Control*, 67(5):713 – 730, 1997.

Z.Q. Lang and S.A. Billings. Evaluation of Output Frequency Responses of non-linear systems under multiple inputs. *IEEE Transactions on Circuits and Systems*, 47, 2000.

Z.Q. Lang and S.A. Billings. Energy transfer properties of non-linear systems in the frequency domain. *International Journal of Control*, 78(5):345 – 362, 2005.

Z.Q. Lang, S.A. Billings, R. Yue, and J. Li. Output frequency response function of nonlinear Volterra systems. *Automatica*, 43(5):805 – 816, 2007.

H. Le Treut, J. Portes, J. Jouzel, and M. Ghil. Isotopic modeling of climatic oscillations: Implications for a comparative study of marine and ice core records. *J. Geophys. Res.*, 93: 9365–9383, 1988.

I.J. Leontaritis and S.A. Billings. Input-output parametric models for non-linear systems Part I: Deterministic non-linear systems. *International Journal of Control*, 41(2):303 – 328, February 1985.

I.J. Leontaritis and S.A. Billings. Experimental design and identifiability for non-linear systems. *International Journal of Systems Science*, 18(1):189 – 202, 1987.

L.M. Li and S.A. Billings. Discrete time subharmonic modelling and analysis. *International Journal of Control*, 78(16):1265 – 1284, 2005.

X.S. Li, A. Berger, and M.F. Loutre. CO2 and Northern Hemisphere ice volume variations over the middle and late quaternary. *Climate Dynamics*, 14(7):537 – 544, 1998.

L. Lisiecki. Links between eccentricity forcing and the 100,000-year glacial cycle. *Nature Geoscience*, 3(5):349 – 352, May 2010.

J.J. Liu, Y.W. Lee, F.C. Wang, R. Uppala, and P.H. Chen. Time and frequency domain identification and analysis of a permanent magnet synchronous servo motor. *Journal of the Chinese Institute of Engineers*, 29(4):683 – 695, 2006.

Y.P. Liu. *Identification of Nonlinear Systems: The NARMAX Polynomial Model Approach.* PhD thesis, The University of Sheffield, Department of Automatic Control and Systems Engineering, 1998.

Z. Liu, L.C. Cleaveland, and T.D. Herbert. Early onset and origin of 100-kyr cycles in Pleistocene tropical SST records. *Earth and Planetary Science Letters*, 265(3 - 4):703 – 715, January 2008.

L. Ljung. *System identification - Theory for the User.* Prentice-Hall, 1999.

M.F. Loutre and A. Berger. Future climatic changes: Are we entering an exceptionally long interglacial? *Climatic Change*, 46(1 -2):61 – 90, 2000.

M.F. Loutre, A. Berger, P. Bretagnon, and P.L. Blanca. Astronomical frequencies for climate research at the decadal to century time scale. *Climate Dynamics*, 7:181 – 194, 1992.

K. Maasch and B. Saltzman. A low-order dynamical model of global climatic variability over the full Pleistocene. *J. Geophys. Res.*, 95:1955 – 1963, 1990.

K. A. Maasch. Statistical detection of the Mid-Pleistocene Transition. *Climate Dynamics*, 2 (3):133 – 143, 1988.

D. Macdougall. *Frozen Earth: The Once and Future Story of Ice Ages.* Berkeley (California): University of California Press, 2004.

D.G. Martinson, N.G. Pisias, J.D. Hays, J. Imbrie, T.C. Jr. Moore, and N.J. Shackleton. Age dating and the orbital theory of ice ages: Development of a high-resolution 0 to 300,000-year chronostratigraphy. *Quaternary Research*, 27:1 – 29, 1987.

M.A. Maslin and A.J. Ridgwell. Mid-Pleistocene Revolution and the "Eccentricity Myth". *Geological Society, London, Special Publications*, 247(1):19 – 34, 2005.

H. Mayer. Time-series analysis in cyclic stratigraphy: An example from the Cretaceous of the southern Alps, Italy. In special issue. Mathematical and statistical analysis of geological data. *Mathematical Geology*, 25:975 – 1001, 1993.

K. McGuffie and A. Henderson-Sellers. *A Climate Modelling Primer (Research and Developments in Climate and Climatology)*. John Wiley and Sons, 2005.

E. Mendes. *Identification of Nonlinear Discrete Systems with Intelligent Structure Detection*. PhD thesis, Dept. of Automatic Control and Systems Engineering, The University of Sheffield, 1995.

M. Mudelsee and M. Schulz. The Mid-Pleistocene climate Transition: Onset of 100ka cycle lags ice volume build-up by 280ka. *Earth and Planetary Science Letters*, 151(117 - 123), 1997.

R.A. Muller and G.J. MacDonald. Simultaneous presence of orbital inclination and eccentricity in proxy climate records from Ocean Drilling Program Site 806. *Geology*, 25(1):3 – 6, 1997.

R.A. Muller and G.J. MacDonald. Origin of the 100 kyr glacial cycle: Eccentricity or orbital inclination? 2, 2005.

J. Oerlemans. Glacial cycles and ice-sheet modelling. *Climatic Change*, 4(4):353 – 374, 1982.

J. Opsteegh, R. Haarsma, F. Selten, and A. Kattenberg. Ecbilt: A dynamic alternative to mixed boundary conditions in ocean models. 50(3), 1998.

D. Paillard. The timing of Pleistocene glaciations from a simple multiple-state climate model. *Nature*, 391, 1998.

D. Paillard. Glacial cycles: Toward a new paradigm. *Reviews of Geophysics*, 39(3):325 – 346, 2001.

J. Park and K.A. Maasch. Plio-Pleistocene time evolution of the 100-kyr cycle in marine paleoclimate records. *Journal of Geophysical Research*, 98(B1):447 – 461, 1993.

R.K. Pearson. Nonlinear input/output modelling. *Journal of Process Control*, 5(4):197 – 211, 1995.

Z.K. Peng, Z.Q. Lang, and S.A. Billings. Non-linear Output Frequency Response Functions for multi-input non-linear Volterra systems. *International Journal of Control*, 80(6):843 – 855, 2007.

Z.K. Peng, Z.Q. Lang, C. Wolters, S.A. Billings, and K. Worden. Feasibility study of structural damage detection using NARMAX modelling and Nonlinear Output Frequency Response Function based analysis. *Mechanical Systems and Signal Processing*, 25(3):1045 – 1061, 2011.

J.R. Petit, J. Jouzel, D. Raynaud, N.I. Barkov, J.M. Barnola, I. Basile, M. Bender, J. Chappellaz, M. Davis, and G. Delaygue. Climate and atmospheric history of the past 420,000 years from the Vostok ice core, Antarctica. *Nature*, 399(6735):429 – 436, 1999.

V. Petoukhov, M. Claussen, A. Berger, M. Crucifix, M. Eby, A.V. Eliseev, T. Fichefet, A. Ganopolski, H. Goosse, I. Kamenkovich, I.I. Mokhov, M. Montoya, L.A. Mysak, A. Sokolov, P. Stone, Z. Wang, and A.J. Weaver. EMIC Intercomparison Project (EMIC - CO2): Comparative analysis of EMIC simulations of climate, and of equilibrium and transient responses to atmospheric CO2 doubling. *Climate Dynamics*, 25:363 – 385, 2005.

J.C. Peyton Jones. Simplified computation of the Volterra frequency response functions of non-linear systems. *Mechanical Systems and Signal Processing*, 21:1452 – 1468, 2007.

J.C. Peyton-Jones and S.A. Billings. Recursive algorithm for computing the frequency response of a class of non-linear difference equation models. *International Journal of Control*, 50(5):1925–1940, 1989.

J.C Peyton-Jones and S.A. Billings. Mean levels in nonlinear analysis and identification. *Int. J. of Control*, 58(5):1033 – 1052, 1993.

J.C. Peyton Jones and K. Choudharya. Efficient computation of higher order frequency response functions for nonlinear systems with, and without, a constant term. *International Journal of Control*, 85(5):578 – 593, 2012.

N.G. Pisias and T.C. Moore Jr. The evolution of Pleistocene climate: A time series approach. *Earth and Scientific Letters*, 52:450 – 458, 1981.

D. Pollard. A coupled climate-ice sheet model applied to the Quaternary ice ages. *J. Geophys. Res*, 88(C12):7705 – 7718, 1983.

C. Pomerol. *The Cenozoic Era - Tertiary and Quaternary.* Ellis Horwood Limited, 1982.

D. Rapp. *Assessing Climate Change Temperatures, Solar Radiation, and Heat Balance.* Berlin ; New York : Springer ; Chichester, UK : Praxis, 2008.

M.E. Raymo. The timing of major climate terminations. *Paleoceanography*, 12:577 – 585, August 1997.

M.E. Raymo and K.H. Nisancioglu. The 41 kyr World: Milankovitch's other unsolved mystery. *Paleoceanography*, 18, 2003.

M.E. Raymo, L.E. Lisiecki, and K.H. Nisancioglu. Plio-Pleistocene ice volume, Antarctic climate, and the global d18O record. *Science*, 313:492 – 495, 2006.

P. Refaeilzadeh, L. Tang, and H. Liu. Cross-validation. Technical report, Arizona State University, 2008.

J. A. Rial. Pacemaking the ice ages by frequency modulation of Earth's orbital eccentricity. *Science*, 285(5427):564 – 568, July 1999.

J.A. Rial. Abrupt climate change: Chaos and order at orbital and millennial scales. *Global and Planetary Change*, 41(2):95 – 109, April 2004a.

J.A. Rial. Earth's orbital eccentricity and the rhythm of the Pleistocene ice ages: The concealed pacemaker. *Global and Planetary Change*, 41(2):81 – 93, April 2004b.

J.A. Rial and C.A. Anaclerio. Understanding non-linear responses of the climate system to orbital forcing. *Elsevier*, 2000.

W.F. Ruddiman. Orbital changes and climate. *Quaternary Science Reviews*, 25:3092 – 3112, 2006.

B. Saltzman and K. Maasch. A first-order global model of Late Cenozoic climate change II: A simplification of CO2 dynamics. *Climate Dynamics*, 5:201 – 210, 1991.

B. Saltzman and K.A. Maasch. A first-order global model of Late Cenozoic climatic change. *Transactions of the Royal Society of Edinburgh: Earth Sciences*, 81:315 – 325, 1990.

B. Saltzman and A. Sutera. The Mid-Quaternary climate Transition as the free response of a three-variable dynamical model. *Journal of the Atmospheric Science*, 44:236 – 241, 1987.

B. Saltzman and M. Verbitsky. Multiple instabilities and models of glacial rythmicity in the Plio-Pleistocene: A general theory of Late Cenozoic climate change. *Climate Dynamics*, 9: 1 – 15, 1993.

B. Saltzman and M. Verbitsky. Late Pleistocence climate trajectory in the phase space of global ice, ocean state, and CO2 : Observations and theory. *Paleoceanography*, 9(6):767 – 779, 1994.

I. Sandberg. Series expansions for nonlinear systems. *Circuits, Systems, and Signal Processing*, 2(1):77 – 87, 1983.

B. Satzman and M. Verbitsky. Asthenospheric ice-load effects in a global dynamical- system model of the Pleistocene climate. *Climate Dynamics*, 8, 1992.

M.W. Schmidt and J.E. Hertzberg. Abrupt climate change during the last ice age. *Nature Education Knowledge*, 3(10), 2011.

N.J. Shackleton and N.D. Opdyke. Oxygen isotope and palaeomagnetic stratigraphy of equatorial Pacific Core V28-238: Oxygen isotope temperatures and ice volumes on a 105 year and 106 year scale. *Quaternary Research*, 3(1):39 – 55, 1973.

N.J. Shackleton, H.H. Lamb, B.C. Worssam, J.M. Hodgson, A.R. Lord, F.W. Shotton, D.J. Schove, and L.H.N. Cooper. The oxygen isotope stratigraphic record of the Late Pleistocene. *Phil Trans R Soc B*, 280:169 – 182, 1977.

Shaw. *Time in Stratigraphy*. New York: McGraw-Hill, 1964.

E. Simeu and D. Georges. Modelling and control of an eddy current brake. *Control Engineering Practice (IFAC)*, 4(1):19 – 26, 1996.

T. Soderstrom and P. Stoica. *System Identification*. International Series in Systems and Control Engineering. Prentice Hall, 1989.

T.F. Stocker, D.G. Wright, and L.A. Mysak. A zonally averaged, coupled ocean-atmosphere model for paleoclimate studies. *J. Climate*, 5:773 – 797, 1992.

A.K. Swain and S.A. Billings. Generalized Frequency Response Function matrix for MIMO non-linear systems. *International Journal of Control*, 74(8):829 – 844, January 2001.

A.K. Swain, E. Mendes, and S.K. Nguang. Analysis of the effects of time delay in nonlinear systems using Generalised Frequency Response Functions. *Journal of Sound and Vibration*, 294(1):341 – 354, 2006.

L. Tarasov and W.R. Peltier. A high-resolution model of the 100-kyr ice age cycle. *Ann. Glaciol.*, 25:58 – 65, 1997.

M. Thomas. *Ocean Induced Variations of Earth's Rotation - Results from a Simultaneous Model of Global Circulation and Tides*. PhD thesis, Univ. of Hamburg, Hamburg, Germany, 2002.

K.E. Trenberth. *Observed Changes to the Climate and Their Causes*. Victoria Univ. Press, 2006.

Y.C. Tseng and D.A. Linebarger. Estimating transfer functions of quadratically nonlinear systems. *Signals, Systems and Computers*, 1991.

Y.C. Tseng and E.J. Powers. Identification of cubic systems using higher order moments of i.i.d signals. *IEEE Transactions of Signal Processing*, 43(7):1733 – 1735, 1995.

P. Wang, J. Tian, and X. Cheng. Transition of Quaternary glacial cyclicity in deep-sea records at Nansha, the South China Sea. *Science in China Series D: Earth Sciences*, 44 (10):926 – 933, 2001.

S. Wiggins. *Application to the Dynamics of the Damped, Forced Duffing Oscillator in Introduction to Applied Nonlinear Dynamical Systems and Chaos*. New York: Springer-Verlag, 1990.

T.M.L. Wigley. Spectral analysis and the astronomical theory of climatic change. *Nature*, 264, 1976.

D.F. Williams, R.C. Thunell, E. Tappa, D. Rio, and I. Raffi. Chronology of the Pleistocene oxygen isotope record: 0-1.88 m.y. B.P. *Palaeogeogr., Palaeoclimatol., Palaeoecol.*, 64: 221–240, 1988.

R. Yue, S.A. Billings, and Z.Q. Lang. An investigation into the characteristics of non-linear frequency response functions. Part 2: New analysis methods based on symbolic expansions and graphical techniques. *International Journal of Control*, 78(14):1130 – 1149, 2005.

J. Zachos, M. Pagani, L. Sloan, E. Thomas, and K. Billups. Trends, rhythms, and aberrations in global climate 65 Ma to present. *Science*, 292:686 – 693, 2001.

H. Zhang and S.A. Billings. Analysing non-linear systems on the frequency domain - I. The transfer function. *Mechanical Systems and Signal Processing*, 7(6):531 – 550, 1993.

L. Zhao. *System Identification for Complex Financial System*. PhD thesis, The University of Sheffield, Department of Automatic Control and Systems Engineering, 2010.

X. Zhao and V. Marmarelis. Nonlinear parametric models from Volterra kernels measurements. *Math. Comput. Model.*, 27(5):37 43, 1998.

Q.M. Zhu and S.A. Billings. A comparison of polynomial and rational NARMAX models for nonlinear system identification. Research Report 444, Department of Automatic control and Systems Engineering, The University of Sheffield, Mappin Street, Sheffield, S1 3JD, June 1992.

Q.M. Zhu, L.F. Zhang, and A. Longden. Development of omni-directional correlation functions for non-linear model validation. *Elsevier*, 2007.

Appendix A

Term number	Model coefficients	Model terms		
1	0.00179	$y_B(t-1)$	$u_{2B}(t-8)$	$u_{2B}(t-8)$
2	-0.000125	$u_{2B}(t-1)$	$u_{2B}(t-1)$	$u_{2B}(t-1)$
3	0.0001177	$u_{2B}(t-2)$	$u_{2B}(t-3)$	$u_{2B}(t-8)$
4	0.000130	$u_{1B}(t-8)$	$u_{3B}(t-1)$	$u_{3B}(t-4)$
5	-0.0000867	$u_{1B}(t-6)$	$u_{3B}(t-1)$	$u_{3B}(t-4)$
6	0.000234	$y_B(t-2)$	$y_B(t-2)$	$u_{3B}(t-4)$
7	0.0001245	$y_B(t-3)$	$u_{2B}(t-4)$	$u_{3B}(t-4)$
8	0.0000000249	$u_{3B}(t-2)$	$u_{3B}(t-3)$	$u_{3B}(t-5)$
9	-0.0003268	$y_B(t-4)$	$y_B(t-4)$	$u_{3B}(t-2)$
10	-0.0006939	$u_{1B}(t-1)$	$u_{2B}(t-3)$	$u_{3B}(t-5)$
11	-0.0009606	$y_B(t-1)$	$u_{1B}(t-1)$	$u_{3B}(t-6)$
12	-0.0000000249	$u_{3B}(t-2)$	$u_{3B}(t-2)$	$u_{3B}(t-6)$
13	0.00000023	$u_{2B}(t-1)$	$u_{3B}(t-2)$	$u_{3B}(t-6)$
14	0.001595	$y_B(t-1)$	$y_B(t-3)$	$u_{3B}(t-4)$
15	-4.465258e-005	$y_B(t-4)$	$u_{2B}(t-8)$	$u_{3B}(t-4)$
16	1.023898e-005	$y_B(t-1)$	$u_{2B}(t-3)$	$u_{3B}(t-4)$
17	0.08381	$y_B(t-1)$	$u_{2B}(t-8)$	
18	-0.00874	$u_{2B}(t-1)$	$u_{2B}(t-1)$	
19	0.002745	$u_{2B}(t-2)$	$u_{2B}(t-3)$	
20	0.002745	$u_{2B}(t-2)$	$u_{2B}(t-8)$	
21	0.002745	$u_{2B}(t-3)$	$u_{2B}(t-8)$	

22	0.02382	$u_{1B}(t-8)$	$u_{3B}(t-1)$	
23	0.02382	$u_{1B}(t-8)$	$u_{3B}(t-4)$	
24	0.00000143	$u_{3B}(t-1)$	$u_{3B}(t-4)$	
25	-0.01588	$u_{1B}(t-6)$	$u_{3B}(t-1)$	
26	-0.01588	$u_{1B}(t-6)$	$u_{3B}(t-4)$	
27	0.04276	$y_B(t-2)$	$y_B(t-2)$	
28	0.001384	$y_B(t-3)$	$u_{3B}(t-4)$	
29	0.022797	$y_B(t-3)$	$u_{2B}(t-4)$	
30	0.00000457	$u_{3B}(t-2)$	$u_{3B}(t-3)$	
31	0.00000457	$u_{3B}(t-2)$	$u_{3B}(t-5)$	
32	0.00000457	$u_{3B}(t-3)$	$u_{3B}(t-5)$	
33	-0.05985	$y_B(t-4)$	$y_B(t-4)$	
34	-0.127098	$u_{1B}(t-1)$	$u_{2B}(t-3)$	
35	-0.016194	$u_{1B}(t-1)$	$u_{3B}(t-5)$	
36	-0.00002295	$u_{2B}(t-3)$	$u_{3B}(t-5)$	
37	-0.0003176	$y_B(t-1)$	$u_{3B}(t-6)$	
38	-1.759253	$y_B(t-1)$	$u_{1B}(t-1)$	
39	-0.000004565	$u_{3B}(t-2)$	$u_{3B}(t-2)$	
40	-0.000003691	$u_{3B}(t-2)$	$u_{3B}(t-6)$	
41	0.00004269	$u_{2B}(t-1)$	$u_{3B}(t-2)$	
42	0.00004269	$u_{2B}(t-1)$	$u_{3B}(t-6)$	
43	0.29209	$y_B(t-1)$	$y_B(t-3)$	
44	-0.001042	$y_B(t-4)$	$u_{3B}(t-4)$	
45	-0.008178	$y_B(t-4)$	$u_{2B}(t-8)$	
46	-0.0012815	$y_B(t-1)$	$u_{3B}(t-4)$	
47	0.001875	$y_B(t-1)$	$u_{2B}(t-3)$	
48	-0.001712	$u_{2B}(t-8)$	$u_{2B}(t-8)$	
49	-0.0004452	$y_B(t-2)$	$u_{3B}(t-4)$	
50	-0.0001187	$u_{2B}(t-4)$	$u_{3B}(t-4)$	

51	0.0006231	$y_B(t-4)$	$u_{3B}(t-2)$	
52	0.0091572	$u_{1B}(t-1)$	$u_{3B}(t-6)$	
53	0.00004257	$u_{2B}(t-8)$	$u_{3B}(t-4)$	
54	-0.000009761	$u_{2B}(t-3)$	$u_{3B}(t-4)$	
55	0.68498	$y_B(t-1)$		
56	-0.19623	$u_{2B}(t-1)$		
57	-0.0080304	$u_{2B}(t-8)$		
58	0.058078	$u_{2B}(t-3)$		
59	0.064068	$u_{2B}(t-2)$		
60	-0.000079245	$u_{3B}(t-4)$		
61	0.0002626	$u_{3B}(t-1)$		
62	4.362359	$u_{1B}(t-8)$		
63	-2.907630	$u_{1B}(t-6)$		
64	0.2535	$y_B(t-3)$		
65	0.0003011	$u_{3B}(t-5)$		
66	0.0008365	$u_{3B}(t-3)$		
67	-0.0001365	$u_{3B}(t-2)$		
68	-1.288751	$u_{1B}(t-1)$		
69	0.0004629	$u_{3B}(t-6)$		
70	-0.076715	$y_B(t-4)$		
71	-0.08153	$y_B(t-2)$		
72	-0.02173	$u_{2B}(t-4)$		
73	1.110223e-016			

Table A.1: ***Model B*** with zero mean input and internal constant removed

Term number	Model coefficients	Model terms		
1	0.001384	$y_A(t-1)$	$u_{2A}(t-8)$	$u_{2A}(t-8)$
2	0.02355	$y_A(t-2)$	$u_{1A}(t-7)$	$u_{3A}(t-1)$
3	-0.00008768	$u_{2A}(t-1)$	$u_{2A}(t-1)$	$u_{2A}(t-1)$
4	0.00000678	$y_A(t-2)$	$u_{3A}(t-3)$	$u_{3A}(t-8)$
5	0.020046	$y_A(t-1)$	$y_A(t-1)$	$y_A(t-3)$
6	0.0004457	$y_A(t-2)$	$u_{2A}(t-3)$	$u_{2A}(t-3)$
7	0.0020592	$u_{1A}(t-7)$	$u_{2A}(t-1)$	$u_{3A}(t-1)$
8	-0.411117	$y_A(t-2)$	$y_A(t-2)$	$y_A(t-3)$
9	-0.005230	$y_A(t-2)$	$u_{2A}(t-2)$	$u_{2A}(t-7)$
10	-0.01097	$u_{1A}(t-1)$	$u_{2A}(t-8)$	$u_{2A}(t-8)$
11	0.369466	$y_A(t-1)$	$y_A(t-4)$	$u_{1A}(t-2)$
12	-0.020104	$y_A(t-1)$	$u_{1A}(t-1)$	$u_{3A}(t-7)$
13	-0.0000000144	$u_{3A}(t-1)$	$u_{3A}(t-1)$	$u_{3A}(t-8)$
14	0.0000000216	$u_{3A}(t-1)$	$u_{3A}(t-2)$	$u_{3A}(t-4)$
15	-0.0001644	$u_{1A}(t-1)$	$u_{3A}(t-2)$	$u_{3A}(t-4)$
16	-0.00010092	$u_{1A}(t-1)$	$u_{3A}(t-4)$	$u_{3A}(t-7)$
17	0.0010573	$u_{1A}(t-3)$	$u_{2A}(t-7)$	$u_{3A}(t-4)$
18	-0.053157	$y_A(t-2)$	$y_A(t-2)$	$u_{2A}(t-3)$
19	-0.02706	$y_A(t-2)$	$y_A(t-3)$	$u_{2A}(t-5)$
20	-0.00016383	$u_{2A}(t-8)$	$u_{2A}(t-8)$	$u_{2A}(t-8)$
21	0.00008908	$u_{1A}(t-2)$	$u_{3A}(t-2)$	$u_{3A}(t-3)$
22	0.0001331	$u_{2A}(t-3)$	$u_{2A}(t-8)$	$u_{2A}(t-8)$
23	-0.00000633	$y_A(t-1)$	$u_{3A}(t-3)$	$u_{3A}(t-8)$
24	-0.00009667	$y_A(t-2)$	$u_{2A}(t-5)$	$u_{3A}(t-8)$
25	0.00007341	$y_A(t-1)$	$u_{2A}(t-3)$	$u_{3A}(t-8)$
26	0.064598	$y_A(t-1)$	$u_{2A}(t-8)$	
27	0.0006278	$y_A(t-2)$	$u_{3A}(t-1)$	
28	4.253094	$y_A(t-2)$	$u_{1A}(t-7)$	

29	-0.006139	$u_{2A}(t-1)$	$u_{2A}(t-1)$	
30	-0.0010365	$y_A(t-2)$	$u_{3A}(t-8)$	
31	0.0012199	$y_A(t-2)$	$u_{3A}(t-3)$	
32	0.12078	$y_A(t-2)$	$u_{2A}(t-3)$	
33	0.372267	$u_{1A}(t-7)$	$u_{2A}(t-1)$	
34	0.025937	$u_{1A}(t-7)$	$u_{3A}(t-1)$	
35	0.00005495	$u_{2A}(t-1)$	$u_{3A}(t-1)$	
36	-0.12208	$y_A(t-2)$	$u_{2A}(t-7)$	
37	-0.12208	$y_A(t-2)$	$u_{2A}(t-2)$	
38	-0.51223	$u_{1A}(t-1)$	$u_{2A}(t-8)$	
39	-0.009958	$u_{2A}(t-8)$	$u_{2A}(t-8)$	
40	0.0098601	$y_A(t-1)$	$y_A(t-4)$	
41	-0.00053644	$y_A(t-1)$	$u_{3A}(t-7)$	
42	-3.633911	$y_A(t-1)$	$u_{1A}(t-1)$	
43	-0.0000026	$u_{3A}(t-1)$	$u_{3A}(t-1)$	
44	-0.0000052	$u_{3A}(t-1)$	$u_{3A}(t-8)$	
45	0.00000391	$u_{3A}(t-1)$	$u_{3A}(t-2)$	
46	0.00000391	$u_{3A}(t-1)$	$u_{3A}(t-4)$	
47	-0.00000048	$u_{3A}(t-2)$	$u_{3A}(t-4)$	
48	-0.0297	$u_{1A}(t-1)$	$u_{3A}(t-2)$	
49	-0.04797	$u_{1A}(t-1)$	$u_{3A}(t-4)$	
50	0.0006593	$u_{1A}(t-1)$	$u_{3A}(t-7)$	
51	-0.00000269	$u_{3A}(t-4)$	$u_{3A}(t-7)$	
52	0.19114	$u_{1A}(t-3)$	$u_{2A}(t-7)$	
53	0.02468	$u_{1A}(t-3)$	$u_{3A}(t-4)$	
54	0.00002822	$u_{2A}(t-7)$	$u_{3A}(t-4)$	
55	-0.85405	$y_A(t-2)$	$y_A(t-2)$	
56	0.14167	$y_A(t-2)$	$y_A(t-3)$	
57	0.01611	$u_{1A}(t-2)$	$u_{3A}(t-2)$	

58	0.01611	$u_{1A}(t-2)$	$u_{3A}(t-3)$	
59	0.00000238	$u_{3A}(t-2)$	$u_{3A}(t-3)$	
60	0.006214	$u_{2A}(t-3)$	$u_{2A}(t-8)$	
61	0.0005685	$y_A(t-1)$	$u_{3A}(t-8)$	
62	-0.001145	$y_A(t-1)$	$u_{3A}(t-3)$	
63	0.007971	$y_A(t-2)$	$u_{2A}(t-5)$	
64	0.01327	$y_A(t-1)$	$u_{2A}(t-3)$	
65	-0.00000039	$u_{3A}(t-3)$	$u_{3A}(t-8)$	
66	-0.018852	$y_A(t-1)$	$y_A(t-1)$	
67	-0.037704	$y_A(t-1)$	$y_A(t-3)$	
68	-0.0004191	$u_{2A}(t-3)$	$u_{2A}(t-3)$	
69	0.0049188	$u_{2A}(t-2)$	$u_{2A}(t-7)$	
70	-0.34745	$y_A(t-4)$	$u_{1A}(t-2)$	
71	-0.34745	$y_A(t-1)$	$u_{1A}(t-2)$	
72	0.025448	$y_A(t-3)$	$u_{2A}(t-5)$	
73	0.0000909	$u_{2A}(t-5)$	$u_{3A}(t-8)$	
74	-0.000069041	$u_{2A}(t-3)$	$u_{3A}(t-8)$	
75	0.78583	$y_A(t-1)$		
76	-0.480025	$y_A(t-2)$		
77	-0.133354	$u_{2A}(t-1)$		
78	0.00045796	$u_{3A}(t-1)$		
79	4.688946	$u_{1A}(t-7)$		
80	-0.19712	$u_{2A}(t-8)$		
81	-11.2316	$u_{1A}(t-1)$		
82	-0.000030359	$u_{3A}(t-8)$		
83	0.00008521	$u_{3A}(t-4)$		
84	0.000343	$u_{3A}(t-2)$		
85	0.000017595	$u_{3A}(t-7)$		
86	0.11990	$u_{2A}(t-7)$		

87	4.461101	$u_{1A}(t-3)$		
88	0.0003594	$u_{3A}(t-3)$		
89	3.238296	$u_{1A}(t-2)$		
90	-0.00654	$u_{2A}(t-3)$		
91	0.248089	$y_A(t-3)$		
92	-0.007496	$u_{2A}(t-5)$		
93	0.1148	$u_{2A}(t-2)$		
94	-0.009273	$y_A(t-4)$		
95	-2.220446e-016			

Table A.2: ***Model A*** with zero mean input and internal constant removed

Appendix B

Term	Contribution to GFRF
$cy(t-a)$	$ce^{-ia\omega}$
$cu_k(t-b)$	$ce^{-ia\omega}$

Table B.1: Model terms and their contribution to the first order GFRF $H_k^1(j\omega)$.

Term	Contribution to GFRF
$cy(t-a)$	$ce^{-ia(\omega_1+\omega_2)}$
$cy(t-a)y(t-b)$	$cH_k^1(j\omega_1)H_k^1(j\omega_2)[e^{-i(a\omega_1+b\omega_2)}+e^{-i(b\omega_1+a\omega_2)}]$
$cy(t-a)u_k(t-b)$	$c[H_k^1(j\omega_1)e^{-i(a\omega_1+b\omega_2)}+H_k^1(j\omega_2)e^{-i(b\omega_1+a\omega_2)}]$
$cu_k(t-a)u_k(t-b)$	$c[e^{-i(a\omega_1+b\omega_2)}+e^{-i(b\omega_1+a\omega_2)}]$

Table B.2: Model terms and their contribution to the second order self-kernel GFRF $H_k^2(j\omega_1, j\omega_2)$.

Term	Contribution to GFRF
$cy(t-a)$	$ce^{-ia(\omega_1+\omega_2)}$
$cy(t-a)y(t-b)$	$cH_k^1(j\omega_1)H_j^1(j\omega_2)[e^{-i(a\omega_1+b\omega_2)}+e^{-i(b\omega_1+a\omega_2)}]$
$cy(t-a)u_j(t-b)$	$cH_k^1(j\omega_2)e^{-i(b\omega_1+a\omega_2)}$
$cy(t-a)u_k(t-b)$	$cH_j^1(j\omega_1)e^{-i(a\omega_1+b\omega_2)}$
$cu_k(t-a)u_j(t-b)$	$ce^{-i(a\omega_1+b\omega_2)}$

Table B.3: Model terms and their contribution to the second order cross-kernel GFRF $H_{kj}^2(j\omega_1, j\omega_2)$.

FRF	$H_k^3(j\omega_1, j\omega_2, j\omega_3)$
$dy(t-a)$	$de^{-ia(\omega_1+\omega_2+\omega_3)}$
$dy(t-a)y(t-b)$	$d[2H_k^1(j\omega_1)H_k^2(j\omega_2, j\omega_3)[e^{-i(a\omega_1+b\omega_2+b\omega_3)} + e^{-i(b\omega_1+a\omega_2+a\omega_3)}]$ $+2H_k^1(j\omega_2)H_k^2(j\omega_1, j\omega_3)[e^{-i(b\omega_1+a\omega_2+b\omega_3)} + e^{-i(a\omega_1+b\omega_2+a\omega_3)}]$ $+2H_k^1(j\omega_3)H_k^2(j\omega_1, j\omega_2)[e^{-i(b\omega_1+b\omega_2+a\omega_3)} + e^{-i(a\omega_1+a\omega_2+b\omega_3)}]]$
$dy(t-a)y(t-b)y(t-c)$	$dH_k^1(j\omega_1)H_k^1(j\omega_2)H_k^1(j\omega_3)[e^{-i(a\omega_1+b\omega_2+c\omega_3)} + e^{-i(a\omega_1+c\omega_2+b\omega_3)}$ $+e^{-i(b\omega_1+a\omega_2+c\omega_3)}e^{-i(c\omega_1+a\omega_2+b\omega_3)} + e^{-i(b\omega_1+c\omega_2+a\omega_3)} + e^{-i(c\omega_1+b\omega_2+a\omega_3)}]$
$dy(t-a)y(t-b)u_k(t-c)$	$d[H_k^1(j\omega_1)H_k^1(j\omega_2)[e^{-i(a\omega_1+b\omega_2+c\omega_3)} + e^{-i(b\omega_1+a\omega_2+c\omega_3)}]$ $+H_k^1(j\omega_1)H_k^1(j\omega_3)[e^{-i(a\omega_1+c\omega_2+b\omega_3)} + e^{-i(b\omega_1+c\omega_2+a\omega_3)}]$ $+H_k^1(j\omega_2)H_k^1(j\omega_3)[e^{-i(c\omega_1+a\omega_2+b\omega_3)} + e^{-i(c\omega_1+b\omega_2+a\omega_3)}]]$
$dy(t-a)u_k(t-b)u_k(t-c)$	$d[H_k^1(j\omega_1)[e^{-i(a\omega_1+b\omega_2+c\omega_3)} + e^{-i(a\omega_1+c\omega_2+b\omega_3)}]$ $+[H_k^1(j\omega_2)[e^{-i(b\omega_1+a\omega_2+c\omega_3)} + e^{-i(c\omega_1+a\omega_2+b\omega_3)}]$ $+[H_k^1(j\omega_3)[e^{-i(b\omega_1+c\omega_2+a\omega_3)} + e^{-i(c\omega_1+b\omega_2+a\omega_3)}]$
$du_k(t-a)u_k(t-b)u_k(t-c)$	$d[e^{-i(a\omega_1+b\omega_2+c\omega_3)} + e^{-i(a\omega_1+c\omega_2+b\omega_3)}$ $+e^{-i(b\omega_1+a\omega_1+c\omega_3)} + e^{-i(c\omega_1+a\omega_2+b\omega_3)}$ $+e^{-i(b\omega_1+c\omega_2+a\omega_3)} + e^{-i(c\omega_1+b\omega_2+a\omega_3)}]$
$dy(t-a)u_k(t-b)$	$d[2H_k^2(j\omega_1, j\omega_2)e^{-i(a\omega_1+a\omega_2+b\omega_3)} + 2H_k^2(j\omega_1, j\omega_3)e^{-i(a\omega_1+b\omega_2+a\omega_3)}$ $+2H_k^2(j\omega_2, j\omega_3)e^{-i(a\omega_1+b\omega_2+b\omega_3)}]$

Table B.4: Model terms and their contribution to the third order self-kernel GFRF $H_k^3(j\omega_1, j\omega_2, j\omega_3)$.

Appendix C

$$\boldsymbol{H^2_{1B}(j\omega_1, j\omega_2)} =$$
$$\frac{-1.76H^1_{1B}(\omega_1)e^{-(i\omega_1+i\omega_2)} + 1.76H^1_{1B}(\omega_2)e^{-(i\omega_1+i\omega_2)} - 0.08H^1_{1B}(\omega_1)H^1_{1B}(\omega_2)e^{-(2i\omega_1+2i\omega_2)}}{(0.16e^{-(2i\omega_1+2i\omega_2)} - 1.37e^{-(i\omega_1+i\omega_2)} - 0.51e^{-(3i\omega_1+3i\omega_2)} + 0.15e^{-(4i\omega_1+4i\omega_2)} + 2)}$$
$$+\frac{-0.29H^1_{1B}(\omega_1)H^1_{1B}(\omega_2)(e^{-(3i\omega_1+i\omega_2)} + e^{-(i\omega_1+3i\omega_2)}) + 0.12H^1_{1B}(\omega_1)H^1_{1B}(\omega_2)e^{-(4i\omega_1+4i\omega_2)}}{(0.16e^{-(2i\omega_1+2i\omega_2)} - 1.37e^{-(i\omega_1+i\omega_2)} - 0.51e^{-(3i\omega_1+3i\omega_2)} + 0.15e^{-(4i\omega_1+4i\omega_2)} + 2)}$$

$$\boldsymbol{H^2_{2B}(j\omega_1, j\omega_2)} =$$
$$\frac{1}{2}\frac{(0.003e^{-(3i\omega_1+2i\omega_2)} + 0.003e^{-(2i\omega_1+3i\omega_2)} + 0.003e^{-(3i\omega_1+8i\omega_2)} + 0.003e^{-(8i\omega_1+3i\omega_2)}}{(0.08e^{-(2i\omega_1+2i\omega_2)} - 0.68e^{-(i\omega_1+i\omega_2)} - 0.25e^{-(3i\omega_1+3i\omega_2)} + 0.077e^{-(4i\omega_1+4i\omega_2)} + 1)}$$
$$+\frac{-0.017e^{-(i\omega_1+i\omega_2)} + 0.003e^{-(2i\omega_1+8i\omega_2)} + 0.003e^{-(8i\omega++2i\omega_2)} - 0.0034e^{-(8i\omega_1+8i\omega_2)}}{(0.08e^{-(2i\omega_1+2i\omega_2)} - 0.68e^{-(i\omega_1+i\omega_2)} - 0.25e^{-(3i\omega_1+3i\omega_2)} + 0.077e^{-(4i\omega_1+4i\omega_2)} + 1)}$$
$$+\frac{+0.002H^1_{2B}(\omega_1)e^{-(i\omega_1+3i\omega_2)}0.023H^1_{2B}(\omega_1)e^{-(3i\omega_1+4i\omega_2)} + 0.002H^1_{2B}(\omega_2)e^{-(3i\omega_1+i\omega_2)}}{(0.08e^{-(2i\omega_1+2i\omega_2)} - 0.68e^{-(i\omega_1+i\omega_2)} - 0.25e^{-(3i\omega_1+3i\omega_2)} + 0.077e^{-(4i\omega_1+4i\omega_2)} + 1)}$$
$$+\frac{+0.023H^1_{2B}(\omega_2)e^{-(4i\omega_1+3i\omega_2)} + 0.084H^1_{2B}(\omega_1)e^{-(i\omega_1+8i\omega_2)} - 0.008H^1_{2B}(\omega_1)e^{-(4i\omega_1+8i\omega_2)}}{(0.08e^{-(2i\omega_1+2i\omega_2)} - 0.68e^{-(i\omega_1+i\omega_2)} - 0.25e^{-(3i\omega_1+3i\omega_2)} + 0.077e^{-(4i\omega_1+4i\omega_2)} + 1)}$$
$$+\frac{+0.084H^1_{2B}(\omega_2)e^{-(8i\omega_1+i\omega_2)} - 0.008H^1_{2B}(\omega_2)e^{-(8i\omega_1+4i\omega_2)}}{(0.08e^{-(2i\omega_1+2i\omega_2)} - 0.68e^{-(i\omega_1+i\omega_2)} - 0.25e^{-(3i\omega_1+3i\omega_2)} + 0.077e^{-(4i\omega_1+4i\omega_2)} + 1)}$$
$$+\frac{+0.29H^1_{2B}(\omega_1)H^1_{2B}(\omega_2)(e^{-(3i\omega_1+i\omega_2)} + e^{-(i\omega_1+3i\omega_2)}) + 0.086H^1_{2B}(\omega_1)H^1_{2B}(\omega_2)e^{-(2i\omega_1+2i\omega_2)}}{(0.08e^{-(2i\omega_1+2i\omega_2)} - 0.68e^{-(i\omega_1+i\omega_2)} - 0.25e^{-(3i\omega_1+3i\omega_2)} + 0.077e^{-(4i\omega_1+4i\omega_2)} + 1)}$$
$$+\frac{-0.12H^1_{2B}(\omega_1)H^1_{2B}(\omega_2)e^{-(4i\omega_1+4i\omega_2)})}{(0.08e^{-(2i\omega_1+2i\omega_2)} - 0.68e^{-(i\omega_1+i\omega_2)} - 0.25e^{-(3i\omega_1+3i\omega_2)} + 0.077e^{-(4i\omega_1+4i\omega_2)} + 1)}$$

$$\boldsymbol{H^2_{3B}(j\omega_1, j\omega_2)} = \frac{1}{2}$$
$$\Big(\frac{0.0000045e^{-(3i\omega_1+5i\omega_2)} + 0.0000045e^{-(5i\omega_1+3i\omega_2)} + 0.0000045e^{-(3i\omega_1+2i\omega_2)}}{(0.08e^{-(2i\omega_1+2i\omega_2)} - 0.68e^{-(i\omega_1+i\omega_2)} - 0.25e^{-(3i\omega_1+3i\omega_2)} + 0.077e^{-(4i\omega_1+4i\omega_2)} + 1.0)}$$
$$+\frac{+0.0000045e^{-(2i\omega_1+3i\omega_2)} - 0.0000037e^{-(6i\omega_1+2i\omega_2)} - 0.0000037e^{-(2i\omega_1+6i\omega_2)}}{(0.08e^{-(2i\omega_1+2i\omega_2)} - 0.68e^{-(i\omega_1+i\omega_2)} - 0.25e^{-(3i\omega_1+3i\omega_2)} + 0.077e^{-(4i\omega_1+4i\omega_2)} + 1.0)}$$
$$+\frac{+0.0000045e^{-(5i\omega_1+2i\omega_2)} + 0.0000045e^{-(2i\omega_1+5i\omega_2)}0.0000014e^{-(i\omega_1+4i\omega_2)}}{(0.08e^{-(2i\omega_1+2i\omega_2)} - 0.68e^{-(i\omega_1+i\omega_2)} - 0.25e^{-(3i\omega_1+3i\omega_2)} + 0.077e^{-(4i\omega_1+4i\omega_2)} + 1.0)}$$
$$+\frac{-0.000009e^{-(2i\omega_1+2i\omega_2)} + 0.0000014e^{-(4i\omega_1+i\omega_2)} - 0.0003H^1_{3B}(\omega_1)e^{-(i\omega_1+6i\omega_2)}}{(0.08e^{-(2i\omega_1+2i\omega_2)} - 0.68e^{-(i\omega_1+i\omega_2)} - 0.25e^{-(3i\omega_1+3i\omega_2)} + 0.077e^{-(4i\omega_1+4i\omega_2)} + 1.0)}$$
$$+\frac{+0.0014H^1_{3B}(\omega_1)e^{-(3i\omega_1+4i\omega_2)} - 0.0003H^1_{3B}(\omega_2)e^{-(6i\omega_1+i\omega_2)} + 0.0014H^1_{3B}(\omega_2)e^{-(4i\omega_1+3i\omega_2)}}{(0.08e^{-(2i\omega_1+2i\omega_2)} - 0.68e^{-(i\omega_1+i\omega_2)} - 0.25e^{-(3i\omega_1+3i\omega_2)} + 0.077e^{-(4i\omega_1+4i\omega_2)} + 1.0)}$$
$$+\frac{-0.0013H^1_{3B}(\omega_1)e^{-(i\omega_1+4i\omega_2)} - 0.00044H^1_{3B}(\omega_1)e^{-(2i\omega_1+4i\omega_2)} + 0.0006H^1_{3B}(\omega_1)e^{-(4i\omega_1+2i\omega_2)}}{(0.08e^{-(2i\omega_1+2i\omega_2)} - 0.68e^{-(i\omega_1+i\omega_2)} - 0.25e^{-(3i\omega_1+3i\omega_2)} + 0.077e^{-(4i\omega_1+4i\omega_2)} + 1.0)}$$
$$+\frac{-0.001H^1_{3B}(\omega_1)e^{-(4i\omega_1+4i\omega_2)} - 0.0013H^1_{3B}(\omega_2)e^{-(4i\omega_1+1i\omega_2)} + 0.0006H^1_{3B}(\omega_2)e^{-(2i\omega_1+4i\omega_2)}}{(0.08e^{-(2i\omega_1+2i\omega_2)} - 0.68e^{-(i\omega_1+i\omega_2)} - 0.25e^{-(3i\omega_1+3i\omega_2)} + 0.077e^{-(4i\omega_1+4i\omega_2)} + 1.0)}\Big)$$
$$\frac{-0.00044H^1_{3B}(\omega_2)e^{-(4i\omega_1+2i\omega_2)} - 0.001H^1_{3B}(\omega_2)e^{-(4i\omega_1+4i\omega_2)} - 0.12H^1_{3B}(\omega_1)H^1_{3B}(\omega_2)e^{-(4i\omega_1+4i\omega_2)}}{(0.08e^{-(2i\omega_1+2i\omega_2)} - 0.68e^{-(i\omega_1+i\omega_2)} - 0.25e^{-(3i\omega_1+3i\omega_2)} + 0.077e^{-(4i\omega_1+4i\omega_2)} + 1.0)}$$
$$\frac{+0.29H^1_{3B}(\omega_1)H^1_{3B}(\omega_2)(e^{-(3i\omega_1+i\omega_2)} + e^{-(i\omega_1+3i\omega_2)}) + 0.08H^1_{3B}(\omega_1)H^1_{3B}(\omega_2)e^{-(2i\omega_1+2i\omega_2)}}{(0.08e^{-(2i\omega_1+2i\omega_2)} - 0.68e^{-(i\omega_1+i\omega_2)} - 0.25e^{-(3i\omega_1+3i\omega_2)} + 0.077e^{-(4i\omega_1+4i\omega_2)} + 1.0)}$$

$$\boldsymbol{H^2_{12B}(j\omega_1, j\omega_2)} =$$
$$\frac{0.00094H^1_{1B}(\omega_1)e^{-(i\omega_1+3i\omega_2)} - 0.064e^{-(i\omega_1+3i\omega_2)} + 0.011H^1_{1B}(\omega_1)e^{-(3i\omega_1+4i\omega_2)}}{0.08e^{-(2i\omega_1+2i\omega_2)} - 0.68e^{-(i\omega_1+i\omega_2)} - 0.25e^{-(3i\omega_1+i\omega_2)} + 0.077e^{-(4i\omega_1+4i\omega_2)} + 1.0}$$
$$+\frac{+0.04H^1_{1B}(\omega_1)e^{-(i\omega_1+8i\omega_2)} - 0.0041H^1_{1B}(\omega_1)e^{-(4i\omega_1+8i\omega_2)} - 0.88H^1_{2B}(\omega_2)e^{-(i\omega_1+i\omega_2)}}{0.08e^{-(2i\omega_1+2i\omega_2)} - 0.68e^{-(i\omega_1+i\omega_2)} - 0.25e^{-(3i\omega_1+i\omega_2)} + 0.077e^{-(4i\omega_1+4i\omega_2)} + 1.0}$$
$$+\frac{+0.15H^1_{1B}(\omega_1)H^1_{2B}(\omega_2)(e^{-(3i\omega_1+i\omega_2)} + e^{-(i\omega_1+3i\omega_2)})}{0.08e^{-(2i\omega_1+2i\omega_2)} - 0.68e^{-(i\omega_1+i\omega_2)} - 0.25e^{-(3i\omega_1+i\omega_2)} + 0.077e^{-(4i\omega_1+4i\omega_2)} + 1.0}$$
$$+\frac{+0.04H^1_{1B}(\omega_1)H^1_{2B}(\omega_2)e^{-(2i\omega_1+2i\omega_2)} - 0.06H^1_{1B}(\omega_1)H^1_{2B}(\omega_2)e^{-(4i\omega_1+4i\omega_2)}}{0.08e^{-(2i\omega_1+2i\omega_2)} - 0.68e^{-(i\omega_1+i\omega_2)} - 0.25e^{-(3i\omega_1+i\omega_2)} + 0.077e^{-(4i\omega_1+4i\omega_2)} + 1.0}$$

$$\boldsymbol{H^2_{13B}(j\omega_1, j\omega_2)} =$$

$$-\frac{0.0079e^{-(6i\omega_1+i\omega_2)} - 0.0046e^{-(i\omega_1+6i\omega_2)} + 0.0079e^{-(6i\omega_1+4i\omega_2)} + 0.0081e^{-(i\omega_1+5i\omega_2)}}{0.08e^{-(2i\omega_1+2i\omega_2)} - 0.68e^{-(i\omega_1+i\omega_2)} - 0.25e^{-(3i\omega_1+3i\omega_2)} + 0.077e^{-(4i\omega_1+4i\omega_2)} + 1.0}$$

$$-\frac{-0.012e^{-(8i\omega_1+i\omega_2)} - 0.012e^{-(8i\omega_1+4i\omega_2)} + 0.00016H^1_{1B}(\omega_1)e^{-(i\omega_1+6i\omega_2)}}{0.08e^{-(2i\omega_1+2i\omega_2)} - 0.68e^{-(i\omega_1+i\omega_2)} - 0.25e^{-(3i\omega_1+3i\omega_2)} + 0.077e^{-(4i\omega_1+4i\omega_2)} + 1.0}$$

$$-\frac{-0.0007H^1_{1B}(\omega_1)e^{-(3i\omega_1+4i\omega_2)} + 0.00064H^1_{1B}(\omega_1)e^{-(i\omega_1+4i\omega_2)}}{0.08e^{-(2i\omega_1+2i\omega_2)} - 0.68e^{-(i\omega_1+i\omega_2)} - 0.25e^{-(3i\omega_1+3i\omega_2)} + 0.077e^{-(4i\omega_1+4i\omega_2)} + 1.0}$$

$$-\frac{+0.0002H^1_{1B}(\omega_1)e^{-(2i\omega_1+4i\omega_2)} + 0.0003H^1_{1B}(\omega_1)e^{-(4i\omega_1+2i\omega_2)}}{0.08e^{-(2i\omega_1+2i\omega_2)} - 0.68e^{-(i\omega_1+i\omega_2)} - 0.25e^{-(3i\omega_1+3i\omega_2)} + 0.077e^{-(4i\omega_1+4i\omega_2)} + 1.0}$$

$$-\frac{+0.0005H^1_{1B}(\omega_1)e^{-(4i\omega_1+4i\omega_2)} - 0.88H^1_{3B}(\omega_2)e^{-(i\omega_1+i\omega_2)}}{0.08e^{-(2i\omega_1+2i\omega_2)} - 0.68e^{-(i\omega_1+i\omega_2)} - 0.25e^{-(3i\omega_1+3i\omega_2)} + 0.077e^{-(4i\omega_1+4i\omega_2)} + 1.0}$$

$$-\frac{-0.15H^1_{1B}(\omega_1)H^1_{3B}(\omega_2)(e^{-(3i\omega_1+i\omega_2)} + e^{-(i\omega_1+3i\omega_2)}) - 0.04H^1_{1B}(\omega_1)H^1_{3B}(\omega_2)e^{-(2i\omega_1+2i\omega_2)}}{0.08e^{-(2i\omega_1+2i\omega_2)} - 0.68e^{-(i\omega_1+i\omega_2)} - 0.25e^{-(3i\omega_1+3i\omega_2)} + 0.077e^{-(4i\omega_1+4i\omega_2)} + 1.0}$$

$$-\frac{+0.06H^1_{1B}(\omega_1)H^1_{3B}(\omega_2)e^{-(4i\omega_1+4i\omega_2)}}{0.08e^{-(2i\omega_1+2i\omega_2)} - 0.68e^{-(i\omega_1+i\omega_2)} - 0.25e^{-(3i\omega_1+3i\omega_2)} + 0.077e^{-(4i\omega_1+4i\omega_2)} + 1.0}$$

$$\boldsymbol{H^2_{23B}(j\omega_1, j\omega_2)} =$$

$$\frac{0.000021e^{-(i\omega_1+6i\omega_2)} - 0.000011e^{-(3i\omega_1+5i\omega_2)} - 0.000005e^{-(3i\omega_1+4i\omega_2)}}{0.08e^{-(2i\omega_1+2i\omega_2)} - 0.68e^{-(i\omega_1+i\omega_2)} - 0.25e^{-(3i\omega_1+3i\omega_2)} + 0.077e^{-(4i\omega_1+4i\omega_2)} + 1.0}$$

$$+\frac{+0.00002e^{-(i\omega_1+2i\omega_2)} - 0.00006e^{-(4i\omega_1+4i\omega_2)} + 0.00002e^{-(8i\omega_1+4i\omega_2)}}{0.08e^{-(2i\omega_1+2i\omega_2)} - 0.68e^{-(i\omega_1+i\omega_2)} - 0.25e^{-(3i\omega_1+3i\omega_2)} + 0.077e^{-(4i\omega_1+4i\omega_2)} + 1.0}$$

$$\frac{-0.00016H^1_{2B}(\omega_1)e^{-(i\omega_1+6i\omega_2)} + 0.0007H^1_{2B}(\omega_1)e^{-(3i\omega_1+4i\omega_2)} + 0.0009H^1_{3B}(\omega_2)e^{-(3i\omega_1+i\omega_2)}}{0.08e^{-(2i\omega_1+2i\omega_2)} - 0.68e^{-(i\omega_1+i\omega_2)} - 0.25e^{-(3i\omega_1+3i\omega_2)} + 0.077e^{-(4i\omega_1+4i\omega_2)} + 1.0}$$

$$+\frac{+0.011H^1_{3B}(\omega_2)e^{-(4i\omega_1+3i\omega_2)} - 0.0006H^1_{2B}(\omega_1)e^{-(i\omega_1+4i\omega_2)} - 0.0002H^1_{2B}(\omega_1)e^{-(2i\omega_1+4i\omega_2)}}{0.08e^{-(2i\omega_1+2i\omega_2)} - 0.68e^{-(i\omega_1+i\omega_2)} - 0.25e^{-(3i\omega_1+3i\omega_2)} + 0.077e^{-(4i\omega_1+4i\omega_2)} + 1.0}$$

$$\frac{+0.0003H^1_{2B}(\omega_1)e^{-(4i\omega_1+2i\omega_2)} - 0.0005H^1_{2B}(\omega_1)e^{-(4i\omega_1+4i\omega_2)} + 0.04H^1_{3B}(\omega_2)e^{-(8i\omega_1+i\omega_2)}}{0.08e^{-(2i\omega_1+2i\omega_2)} - 0.68e^{-(i\omega_1+i\omega_2)} - 0.25e^{-(3i\omega_1+3i\omega_2)} + 0.077e^{-(4i\omega_1+4i\omega_2)} + 1.0}$$

$$+\frac{-0.0041H^1_{3B}(\omega_2)e^{-(8i\omega_1+4i\omega_2)} + 0.043H^1_{2B}(\omega_1)H^1_{3B}(\omega_2)e^{-(2i\omega_1+2i\omega_2)}}{0.08e^{-(2i\omega_1+2i\omega_2)} - 0.68e^{-(i\omega_1+i\omega_2)} - 0.25e^{-(3i\omega_1+3i\omega_2)} + 0.077e^{-(4i\omega_1+4i\omega_2)} + 1.0}$$

$$+\frac{+0.15H^1_{2B}(\omega_1)H^1_{3B}(\omega_2)(e^{-(3i\omega_1+i\omega_2)} + e^{-(i\omega_1+3i\omega_2)}) - 0.06H^1_{2B}(\omega_1)H^1_{3B}(\omega_2)e^{-(4i\omega_1+4i\omega_2)}}{0.08e^{-(2i\omega_1+2i\omega_2)} - 0.68e^{-(i\omega_1+i\omega_2)} - 0.25e^{-(3i\omega_1+3i\omega_2)} + 0.077e^{-(4i\omega_1+4i\omega_2)} + 1.0}$$

$$\boldsymbol{H^2_{1A}(j\omega_1, j\omega_2)} =$$

$$-\frac{3.63H^1_{1A}(\omega_1)e^{-(i\omega_1+i\omega_2)} - 4.25H^1_{1A}(\omega_2)e^{-(7i\omega_1+2i\omega_2)} - 4.25H^1_{1A}(\omega_1)e^{-(2i\omega_1+7i\omega_2)}}{0.96e^{-(2i\omega_1+2i\omega_2)} - 1.57e^{-(i\omega_1+i\omega_2)} - 0.5e^{-(3i\omega_1+3i\omega_2)} + 0.019e^{-(4i\omega_1+4i\omega_2)} + 2.0}$$

$$-\frac{+0.35H^1_{1A}(\omega_1)e^{-(i\omega_1+2i\omega_2)} + 0.35H^1_{1A}(\omega_1)e^{-(4i\omega_1+2i\omega_2)} + 3.63H^1_{1A}(\omega_2)e^{-(i\omega_1+i\omega_2)}}{0.96e^{-(2i\omega_1+2i\omega_2)} - 1.57e^{-(i\omega_1+i\omega_2)} - 0.5e^{-(3i\omega_1+3i\omega_2)} + 0.019e^{-(4i\omega_1+4i\omega_2)} + 2.0}$$

$$-\frac{+0.35H^1_{1A}(\omega_2)e^{-(2i\omega_1+i\omega_2)} + 0.35H^1_{1A}(\omega_2)e^{-(2i\omega_1+4i\omega_2)}}{0.96e^{-(2i\omega_1+2i\omega_2)} - 1.57e^{-(i\omega_1+i\omega_2)} - 0.5e^{-(3i\omega_1+3i\omega_2)} + 0.019e^{-(4i\omega_1+4i\omega_2)} + 2.0}$$

$$-\frac{+0.038H^1_{1A}(\omega_1)H^1_{1A}(\omega_2)(e^{-(3i\omega_1+i\omega_2)} + e^{-(i\omega_1+3i\omega_2)})}{0.96e^{-(2i\omega_1+2i\omega_2)} - 1.57e^{-(i\omega_1+i\omega_2)} - 0.5e^{-(3i\omega_1+3i\omega_2)} + 0.019e^{-(4i\omega_1+4i\omega_2)} + 2.0}$$

$$-\frac{-0.14H^1_{1A}(\omega_1)H^1_{1A}(\omega_2)(e^{-(3i\omega_1+2i\omega_2)} + e^{-(2i\omega_1+3i\omega_2)}) + 0.038H^1_{1A}(\omega_1)H^1_{1A}(\omega_2)e^{-(i\omega_1+i\omega_2)}}{0.96e^{-(2i\omega_1+2i\omega_2)} - 1.57e^{-(i\omega_1+i\omega_2)} - 0.5e^{-(3i\omega_1+3i\omega_2)} + 0.019e^{-(4i\omega_1+4i\omega_2)} + 2.0}$$

$$-\frac{+1.71H^1_{1A}(\omega_1)H^1_{1A}(\omega_2)e^{-(2i\omega_1+2i\omega_2)} - 0.01H^1_{1A}(\omega_1)H^1_{1A}(\omega_2)(e^{-(i\omega_1+4i\omega_2)} + e^{-(i\omega_1+i\omega_2)})}{0.96e^{-(2i\omega_1+2i\omega_2)} - 1.57e^{-(i\omega_1+i\omega_2)} - 0.5e^{-(3i\omega_1+3i\omega_2)} + 0.019e^{-(4i\omega_1+4i\omega_2)} + 2.0}$$

$$\boldsymbol{H^2_{2A}(j\omega_1, j\omega_2)} = \frac{1}{2}$$

$$(\frac{0.005e^{-(7i\omega_1+2i\omega_2)} - 0.00084e^{-(3i\omega_1+3i\omega_2)} + 0.005e^{-(2i\omega_1+7i\omega_2)} + 0.006e^{-(3i\omega_1+8i\omega_2)}}{0.48e^{-(2i\omega_1+2i\omega_2)} - 0.79e^{-(i\omega_1+i\omega_2)} - 0.25e^{-(3i\omega_1+3i\omega_2)} + 0.009e^{-(4i\omega_1+4i\omega_2)} + 1.0}$$

$$+\frac{+0.006e^{-(8i\omega_1+3i\omega_2)} - 0.012e^{-(i\omega_1+i\omega_2)} - 0.02e^{-(8i\omega_1+8i\omega_2)} + 0.025H^1_{2A}(\omega_1)e^{-(3i\omega_1+5i\omega_2)}}{0.48e^{-(2i\omega_1+2i\omega_2)} - 0.79e^{-(i\omega_1+i\omega_2)} - 0.25e^{-(3i\omega_1+3i\omega_2)} + 0.009e^{-(4i\omega_1+4i\omega_2)} + 1.0}$$

$$+\frac{-0.12H^1_{2A}(\omega_1)e^{-(2i\omega_1+7i\omega_2)} - 0.12H^1_{2A}(\omega_2)e^{-(7i\omega_1+2i\omega_2)} + 0.025H^1_{2A}(\omega_2)e^{-(5i\omega_1+3i\omega_2)}}{0.48e^{-(2i\omega_1+2i\omega_2)} - 0.79e^{-(i\omega_1+i\omega_2)} - 0.25e^{-(3i\omega_1+3i\omega_2)} + 0.009e^{-(4i\omega_1+4i\omega_2)} + 1.0}$$

$$+\frac{+0.12H^1_{2A}(\omega_1)e^{-(2i\omega_1+3i\omega_2)} + 0.013H^1_{2A}(\omega_2)e^{-1(3i\omega_1+i\omega_2)} + 0.12H^1_{2A}(\omega_2)e^{-(3i\omega_1+2i\omega_2)}}{0.48e^{-(2i\omega_1+2i\omega_2)} - 0.79e^{-(i\omega_1+i\omega_2)} - 0.25e^{-(3i\omega_1+3i\omega_2)} + 0.009e^{-(4i\omega_1+4i\omega_2)} + 1.0}$$

$$+\frac{+0.008H^1_{2A}(\omega_1)e^{-(2i\omega_1+5i\omega_2)} + 0.008H^1_{2A}(\omega_2)e^{-(5i\omega_1+2i\omega_2)} - 0.12H^1_{2A}(\omega_1)e^{-(2i\omega_1+2i\omega_2)}}{0.48e^{-(2i\omega_1+2i\omega_2)} - 0.79e^{-(i\omega_1+i\omega_2)} - 0.25e^{-(3i\omega_1+3i\omega_2)} + 0.009e^{-(4i\omega_1+4i\omega_2)} + 1.0}$$

$$+\frac{+0.065H^1_{2A}(\omega_1)e^{-(i\omega_1+8i\omega_2)} - 0.12H^1_{2A}(\omega_2)e^{-(2i\omega_1+2i\omega_2)} + 0.065H^1_{2A}(\omega_2)e^{-(8i\omega_1+i\omega_2)}}{0.48e^{-(2i\omega_1+2i\omega_2)} - 0.79e^{-(i\omega_1+i\omega_2)} - 0.25e^{-(3i\omega_1+3i\omega_2)} + 0.009e^{-(4i\omega_1+4i\omega_2)} + 1.0}$$

$$+\frac{-0.038H^1_{2A}(\omega_1)H^1_{2A}(\omega_2)(e^{-(3i\omega_1+i\omega_2)} + e^{-(i\omega_1+3i\omega_2)})}{0.48e^{-(2i\omega_1+2i\omega_2)} - 0.79e^{-(i\omega_1+i\omega_2)} - 0.25e^{-(3i\omega_1+3i\omega_2)} + 0.009e^{-(4i\omega_1+4i\omega_2)} + 1.0}$$

$$+\frac{+0.14H^1_{2A}(\omega_1)H^1_{2A}(\omega_2)(e^{-(3i\omega_1+2i\omega_2)} + e^{-(2i\omega_1+3i\omega_2)}) - 0.038H^1_{2A}(\omega_1)H^1_{2A}(\omega_2)e^{-(i\omega_1+i\omega_2)}}{0.48e^{-(2i\omega_1+2i\omega_2)} - 0.79e^{-(i\omega_1+i\omega_2)} - 0.25e^{-(3i\omega_1+3i\omega_2)} + 0.009e^{-(4i\omega_1+4i\omega_2)} + 1.0}$$

$$+\frac{-1.71H^1_{2A}(\omega_1)H^1_{2A}(\omega_2)e^{-(2i\omega_1+2i\omega_2)} + 0.01H^1_{2A}(\omega_1)H^1_{2A}(\omega_2)(e^{-(i\omega_1+4i\omega_2)} + e^{-(4i\omega_1+i\omega_2)})}{0.48e^{-(2i\omega_1+2i\omega_2)} - 0.79e^{-(i\omega_1+i\omega_2)} - 0.25e^{-(3i\omega_1+3i\omega_2)} + 0.009e^{-(4i\omega_1+4i\omega_2)} + 1.0}$$

$$+\frac{+0.013H^1_{2A}(\omega_1)^{e-(i\omega_1+3i\omega_2)})}{0.48e^{-(2i\omega_1+2i\omega_2)} - 0.79e^{-(i\omega_1+i\omega_2)} - 0.25e^{-(3i\omega_1+3i\omega_2)} + 0.009e^{-(4i\omega_1+4i\omega_2)} + 1.0})$$

$$\boldsymbol{H_{3A}^{2}(j\omega_1, j\omega_2)} = -\frac{1}{2}$$
$$\Big(\frac{0.0000027e^{-(7i\omega_1+4i\omega_2)} + 0.0000027e^{-(4i\omega_1+7i\omega_2)} - 0.0000024e^{-(3i\omega_1+2i\omega_2)}}{0.48e^{-(2i\omega_1+2i\omega_2)} - 0.78e^{-(i\omega_1+i\omega_2)} - 0.25e^{-(3i\omega_1+3i\omega_2)} + 0.01e^{-(4i\omega_1+4i\omega_2)} + 1.0}$$
$$+\frac{-0.0000024e^{-(2i\omega_1+3i\omega_2)} + 0.0000004e^{-(3i\omega_1+8i\omega_2)} + 0.0000004e^{-(8i\omega_1+3i\omega_2)}}{0.48e^{-(2i\omega_1+2i\omega_2)} - 0.78e^{-(i\omega_1+i\omega_2)} - 0.25e^{-(3i\omega_1+3i\omega_2)} + 0.01e^{-(4i\omega_1+4i\omega_2)} + 1.0}$$
$$+\frac{+0.000005e^{-(i\omega_1+i\omega_2)} - 0.000004e^{-(i\omega_1+2i\omega_2)} - 0.000004e^{-(2i\omega_1+i\omega_2)}}{0.48e^{-(2i\omega_1+2i\omega_2)} - 0.78e^{-(i\omega_1+i\omega_2)} - 0.25e^{-(3i\omega_1+3i\omega_2)} + 0.01e^{-(4i\omega_1+4i\omega_2)} + 1.0}$$
$$+\frac{-0.000004e^{-(i\omega_1+4i\omega_2)} - 0.000004e^{-(4i\omega_1+i\omega_2)} + 0.000005e^{-(i\omega_1+8i\omega_2)} +}{0.48e^{-(2i\omega_1+2i\omega_2)} - 0.78e^{-(i\omega_1+i\omega_2)} - 0.25e^{-(3i\omega_1+3i\omega_2)} + 0.01e^{-(4i\omega_1+4i\omega_2)} + 1.0}$$
$$+\frac{0.00000048e^{-(2i\omega_1+4i\omega_2)} + 0.00000048e^{-(4i\omega_1+2i\omega_2)} + 0.000005e^{-(8i\omega_1+i\omega_2)}}{0.48e^{-(2i\omega_1+2i\omega_2)} - 0.78e^{-(i\omega_1+i\omega_2)} - 0.25e^{-(3i\omega_1+3i\omega_2)} + 0.01e^{-(4i\omega_1+4i\omega_2)} + 1.0}$$
$$+\frac{+0.0005H_{3A}^{1}(\omega_1)e^{-(i\omega_1+7i\omega_2)} + 0.0005H_{3A}^{1}(\omega_2)e^{-(7i\omega_1+i\omega_2)} + 0.001H_{3A}^{1}(\omega_1)e^{-(i\omega_1+3i\omega_2)}}{0.48e^{-(2i\omega_1+2i\omega_2)} - 0.78e^{-(i\omega_1+i\omega_2)} - 0.25e^{-(3i\omega_1+3i\omega_2)} + 0.01e^{-(4i\omega_1+4i\omega_2)} + 1.0}$$
$$+\frac{-0.001H_{3A}^{1}(\omega_1)e^{-(2i\omega_1+3i\omega_2)} + 0.001H_{3A}^{1}(\omega_2))e^{-(3i\omega_1+i\omega_2)} - 0.001H_{3A}^{1}(\omega_2)e^{-(3i\omega_1+2i\omega_2)}}{0.48e^{-(2i\omega_1+2i\omega_2)} - 0.78e^{-(i\omega_1+i\omega_2)} - 0.25e^{-(3i\omega_1+3i\omega_2)} + 0.01e^{-(4i\omega_1+4i\omega_2)} + 1.0}$$
$$+\frac{-0.0006H_{3A}^{1}(\omega_1)e^{-(2i\omega_1+i\omega_2)} - 0.00057H_{3A}^{1}(\omega_1)e^{-(i\omega_1+8i\omega_2)} + 0.001H_{3A}^{1}(\omega_1)e^{-(2i\omega_1+8i\omega_2)}}{0.48e^{-(2i\omega_1+2i\omega_2)} - 0.78e^{-(i\omega_1+i\omega_2)} - 0.25e^{-(3i\omega_1+3i\omega_2)} + 0.01e^{-(4i\omega_1+4i\omega_2)} + 1.0}$$
$$+\frac{-0.00063H_{3A}^{1}(\omega_2)e^{-(i\omega_1+2i\omega_2)} - 0.00057H_{3A}^{1}(\omega_2)e^{-(8i\omega_1+i\omega_2)} + 0.001H_{3A}^{1}(\omega_2)e^{-(8i\omega_1+2i\omega_2)}}{0.48e^{-(2i\omega_1+2i\omega_2)} - 0.78e^{-(i\omega_1+i\omega_2)} - 0.25e^{-(3i\omega_1+3i\omega_2)} + 0.01e^{-(4i\omega_1+4i\omega_2)} + 1.0}$$
$$+\frac{+0.038H_{3A}^{1}(\omega_1)H_{3A}^{1}(\omega_2)(e^{-(3i\omega_1+i\omega_2)} + e^{-(i\omega_1+3i\omega_2)})}{0.48e^{-(2i\omega_1+2i\omega_2)} - 0.78e^{-(i\omega_1+i\omega_2)} - 0.25e^{-(3i\omega_1+3i\omega_2)} + 0.01e^{-(4i\omega_1+4i\omega_2)} + 1.0}$$
$$+\frac{-0.14H_{3A}^{1}(\omega_1)H_{3A}^{1}(\omega_2)(e^{-(3i\omega_1+2i\omega_2)} + e^{-(2i\omega 1+3i\omega_2)}) + 0.038H_{3A}^{1}(\omega_1)H_{3A}^{1}(\omega_2)e^{-(i\omega_1+i\omega_2)}}{0.48e^{-(2i\omega_1+2i\omega_2)} - 0.78e^{-(i\omega_1+i\omega_2)} - 0.25e^{-(3i\omega_1+3i\omega_2)} + 0.01e^{-(4i\omega_1+4i\omega_2)} + 1.0}$$
$$+\frac{+1.71H_{3A}^{1}(\omega_1)H_{3A}^{1}(\omega_2)e^{-(2i\omega_1+2i\omega_2)} - 0.01H_{3A}^{1}(\omega_1)H_{3A}^{1}(\omega_2)(e^{-(i\omega_1+4i\omega_2)} + e^{-(4i\omega_1+i\omega_2)})}{0.48e^{-(2i\omega_1+2i\omega_2)} - 0.78e^{-(i\omega_1+i\omega_2)} - 0.25e^{-(3i\omega_1+3i\omega_2)} + 0.01e^{-(4i\omega_1+4i\omega_2)} + 1.0}\Big)$$

$$\boldsymbol{H^2_{12A}(j\omega_1, j\omega_2)} =$$

$$\frac{0.1e^{-(3i\omega_1+7i\omega_2)} + 0.19e^{-(7i\omega_1+i\omega_2)} - 0.26e^{-(i\omega_1+8i\omega_2)} + 0.013H^1_{1A}(\omega_1)e^{-(3i\omega_1+5i\omega_2)}}{0.48e^{-(2i\omega_1+2i\omega_2)} - 0.79e^{-(i\omega_1+i\omega_2)} - 0.25e^{-(3i\omega_1+3i\omega_2)} + 0.01e^{-(4i\omega_1+4i\omega_2)} + 1}$$
$$+\frac{-0.06H^1_{1A}(\omega_1)e^{-(2i\omega_1+7i\omega_2)} + 2.13H^1_{2A}(\omega_2)e^{-(7i\omega_1+2i\omega_2)} + 0.0067H^1_{1A}(\omega_1)e^{-(i\omega_1+3i\omega_2)}}{0.48e^{-(2i\omega_1+2i\omega_2)} - 0.79e^{-(i\omega_1+i\omega_2)} - 0.25e^{-(3i\omega_1+3i\omega_2)} + 0.01e^{-(4i\omega_1+4i\omega_2)} + 1}$$
$$+\frac{+0.06H^1_{1A}(\omega_1)e^{-(2i\omega_1+3i\omega_2)} + 0.004H^1_{1A}(\omega_1)e^{-(2i\omega_1+5i\omega_2)} - 0.06H^1_{1A}(\omega_1)e^{-(2i\omega_1+2i\omega_2)}}{0.48e^{-(2i\omega_1+2i\omega_2)} - 0.79e^{-(i\omega_1+i\omega_2)} - 0.25e^{-(3i\omega_1+3i\omega_2)} + 0.01e^{-(4i\omega_1+4i\omega_2)} + 1}$$
$$+\frac{+0.03H^1_{1A}(\omega_1)e^{-(i\omega_1+8i\omega_2)} - 1.82H^1_{2A}(\omega_2)e^{-(i\omega_1+i\omega_2)} - 0.17H^1_{2A}(\omega_2)e^{-(2i\omega_1+i\omega_2)}}{0.48e^{-(2i\omega_1+2i\omega_2)} - 0.79e^{-(i\omega_1+i\omega_2)} - 0.25e^{-(3i\omega_1+3i\omega_2)} + 0.01e^{-(4i\omega_1+4i\omega_2)} + 1}$$
$$+\frac{-0.17H^1_{2A}(\omega_2)e^{-(2i\omega_1+4i\omega_2)} - 0.019H^1_{1A}(\omega_1)H^1_{2A}(\omega_2)(e^{-(3i\omega_1+i\omega_2)} + e^{-(i\omega_1+3i\omega_2)})}{0.48e^{-(2i\omega_1+2i\omega_2)} - 0.79e^{-(i\omega_1+i\omega_2)} - 0.25e^{-(3i\omega_1+3i\omega_2)} + 0.01e^{-(4i\omega_1+4i\omega_2)} + 1}$$
$$+\frac{+0.071H^1_{1A}(\omega_1)H^1_{2A}(\omega_2)(e^{-(3i\omega_1+2i\omega_2)} + e^{-(2i\omega_1+3i\omega_2)})}{0.48e^{-(2i\omega_1+2i\omega_2)} - 0.79e^{-(i\omega_1+i\omega_2)} - 0.25e^{-(3i\omega_1+3i\omega_2)} + 0.01e^{-(4i\omega_1+4i\omega_2)} + 1}$$
$$+\frac{-0.019H^1_{1A}(\omega_1)H^1_{2A}(\omega_2)e^{-(i\omega_1+i\omega_2)} - 0.85H^1_{1A}(\omega_1)H^1_{2A}(\omega_2)e^{-(2i\omega_1+2i\omega_2)}}{0.48e^{-(2i\omega_1+2i\omega_2)} - 0.79e^{-(i\omega_1+i\omega_2)} - 0.25e^{-(3i\omega_1+3i\omega_2)} + 0.01e^{-(4i\omega_1+4i\omega_2)} + 1}$$
$$+\frac{+0.005H^1_{1A}(\omega_1)H^1_{2A}(\omega_2)(e^{-(i\omega_1+4i\omega_2)} + e^{-(4i\omega_1+i\omega_2)})}{0.48e^{-(2i\omega_1+2i\omega_2)} - 0.79e^{-(i\omega_1+i\omega_2)} - 0.25e^{-(3i\omega_1+3i\omega_2)} + 0.01e^{-(4i\omega_1+4i\omega_2)} + 1}$$

$$\boldsymbol{H^2_{13A}(j\omega_1, j\omega_2)} =$$

$$\frac{0.011e^{-(7i\omega_1+i\omega_2)} + 0.0003e^{-(i\omega_1+7i\omega_2)} + 0.0081e^{-(2i\omega_1+3i\omega_2)} + 0.012e^{-(3i\omega_1+4i\omega_2)}}{0.48e^{-(2i\omega_1+2i\omega_2)} - 0.78e^{-(i\omega_1+i\omega_2)} - 0.25e^{-(3i\omega_1+3i\omega_2)} + 0.009e^{-(4i\omega_1+4i\omega_2)} + 1}$$

$$+\frac{-0.015e^{-(i\omega_1+2i\omega_2)} - 0.024e^{-(i\omega_1+4i\omega_2)} + 0.008e^{-(2i\omega_1+2i\omega_2)}}{0.48e^{-(2i\omega_1+2i\omega_2)} - 0.78e^{-(i\omega_1+i\omega_2)} - 0.25e^{-(3i\omega_1+3i\omega_2)} + 0.009e^{-(4i\omega_1+4i\omega_2)} + 1}$$

$$+\frac{-0.0003H^1_{1A}(\omega_1)e^{-(i\omega_1+7i\omega_2)} + 2.13H^1_{3A}(\omega_2)e^{-(7i\omega_1+2i\omega_2)} - 0.0006H^1_{1A}(\omega_1)e^{-(i\omega_1+3i\omega_2)}}{0.48e^{-(2i\omega_1+2i\omega_2)} - 0.78e^{-(i\omega_1+i\omega_2)} - 0.25e^{-(3i\omega_1+3i\omega_2)} + 0.009e^{-(4i\omega_1+4i\omega_2)} + 1}$$

$$+\frac{-0.019H^1_{1A}(\omega_1)H^1_{3A}(\omega_2)e^{-(i\omega_1+i\omega_2)} + 0.0003H^1_{1A}(\omega_1)e^{-(2i\omega_1+i\omega_2)}}{0.48e^{-(2i\omega_1+2i\omega_2)} - 0.78e^{-(i\omega_1+i\omega_2)} - 0.25e^{-(3i\omega_1+3i\omega_2)} + 0.009e^{-(4i\omega_1+4i\omega_2)} + 1}$$

$$+\frac{+0.0003H^1_{1A}(\omega_1)e^{-(i\omega_1+8i\omega_2)} - 0.0005H^1_{1A}(\omega_1)e^{-(2i\omega_1+8i\omega_2)} - 1.8H^1_{3A}(\omega_2)e^{-(i\omega_1+i\omega_2)}}{0.48e^{-(2i\omega_1+2i\omega_2)} - 0.78e^{-(i\omega_1+i\omega_2)} - 0.25e^{-(3i\omega_1+3i\omega_2)} + 0.009e^{-(4i\omega_1+4i\omega_2)} + 1}$$

$$+\frac{-0.17H^1_{3A}(\omega_2)e^{-(2i\omega_1+i\omega_2)} + 0.005H^1_{1A}(\omega_1)H^1_{3A}(\omega_2)(e^{-(i\omega_1+4i\omega_2)} + e^{-(4i\omega_1+i\omega_2)})}{0.48e^{-(2i\omega_1+2i\omega_2)} - 0.78e^{-(i\omega_1+i\omega_2)} - 0.25e^{-(3i\omega_1+3i\omega_2)} + 0.009e^{-(4i\omega_1+4i\omega_2)} + 1}$$

$$+\frac{-0.02H^1_{1A}(\omega_1)H^1_{3A}(\omega_2)(e^{-(3i\omega_1+i\omega_2)} + e^{-(i\omega_1+3i\omega_2)})}{0.48e^{-(2i\omega_1+2i\omega_2)} - 0.78e^{-(i\omega_1+i\omega_2)} - 0.25e^{-(3i\omega_1+3i\omega_2)} + 0.009e^{-(4i\omega_1+4i\omega_2)} + 1}$$

$$+\frac{+0.071H^1_{1A}(\omega_1)H^1_{3A}(\omega_2)(e^{-(3i\omega_1+2i\omega_2)} + e^{-(2i\omega_1+3i\omega_2)}) + 0.00061H^1_{1A}(\omega_1)e^{-(2i\omega_1+3i\omega_2)}}{0.48e^{-(2i\omega_1+2i\omega_2)} - 0.78e^{-(i\omega_1+i\omega_2)} - 0.25e^{-(3i\omega_1+3i\omega_2)} + 0.009e^{-(4i\omega_1+4i\omega_2)} + 1}$$

$$+\frac{-0.17H^1_{3A}(\omega_2)e^{-(2i\omega_1+4i\omega_2)} - 0.85H^1_{1A}(\omega_1)H^1_{3A}(\omega_2)e^{-(2i\omega_1+2i\omega_2)}}{0.48e^{-(2i\omega_1+2i\omega_2)} - 0.78e^{-(i\omega_1+i\omega_2)} - 0.25e^{-(3i\omega_1+3i\omega_2)} + 0.009e^{-(4i\omega_1+4i\omega_2)} + 1}$$

$$
\begin{aligned}
&\boldsymbol{H^2_{23A}(j\omega_1, j\omega_2)} = \\
&\frac{0.000014e^{-(7i\omega_1+4i\omega_2)} - 0.000035e^{-(3i\omega_1+8i\omega_2)} + 0.000045e^{-(5i\omega_1+8i\omega_2)}}{0.5e^{-(2i\omega_1+2i\omega_2)} - 0.78e^{-(i\omega_1+i\omega_2)} - 0.25e^{-(3i\omega_1+3i\omega_2)} + 0.009e^{-(4i\omega_1+4i\omega_2)} + 1} \\
&+\frac{+0.000027e^{-(i\omega_1+i\omega_2)} - 0.00027H^1_{2A}(\omega_1)e^{-(i\omega_1+7i\omega_2)} - 0.06H^1_{3A}(\omega_2)e^{-(7i\omega_1+2i\omega_2)}}{0.5e^{-(2i\omega_1+2i\omega_2)} - 0.78e^{-(i\omega_1+i\omega_2)} - 0.25e^{-(3i\omega_1+3i\omega_2)} + 0.009e^{-(4i\omega_1+4i\omega_2)} + 1} \\
&+\frac{+0.013H^1_{3A}(\omega_2)e^{-(5i\omega_1+3i\omega_2)} - 0.0006H^1_{2A}(\omega_1)e^{-(i\omega_1+3i\omega_2)}}{0.5e^{-(2i\omega_1+2i\omega_2)} - 0.78e^{-(i\omega_1+i\omega_2)} - 0.25e^{-(3i\omega_1+3i\omega_2)} + 0.009e^{-(4i\omega_1+4i\omega_2)} + 1} \\
&+\frac{+0.00061H^1_{2A}(\omega_1)e^{-(2i\omega_1+3i\omega_2)} + 0.0066H^1_{3A}(\omega_2)e^{-(3i\omega_1+i\omega_2)} + 0.06H^1_{3A}(\omega_2)e^{-(3i\omega_1+2i\omega_2)}}{0.5e^{-(2i\omega_1+2i\omega_2)} - 0.78e^{-(i\omega_1+i\omega_2)} - 0.25e^{-(3i\omega_1+3i\omega_2)} + 0.009e^{-(4i\omega_1+4i\omega_2)} + 1} \\
&+\frac{+0.004H^1_{3A}(\omega_2)e^{-(5i\omega_1+2i\omega_2)} + 0.0003H^1_{2A}(\omega_1)e^{-(2i\omega_1+i\omega_2)} + 0.0003H^1_{2A}(\omega_1)e^{-(i\omega_1+8i\omega_2)}}{0.5e^{-(2i\omega_1+2i\omega_2)} - 0.78e^{-(i\omega_1+i\omega_2)} - 0.25e^{-(3i\omega_1+3i\omega_2)} + 0.009e^{-(4i\omega_1+4i\omega_2)} + 1} \\
&+\frac{-0.0005H^1_{2A}(\omega_1)e^{-(2i\omega_1+8i\omega_2)} - 0.06H^1_{3A}(\omega_2)e^{-(2i\omega_1+2i\omega_2)} + 0.03H^1_{3A}(\omega_2)e^{-(8i\omega_1+i\omega_2)}}{0.5e^{-(2i\omega_1+2i\omega_2)} - 0.78e^{-(i\omega_1+i\omega_2)} - 0.25e^{-(3i\omega_1+3i\omega_2)} + 0.009e^{-(4i\omega_1+4i\omega_2)} + 1} \\
&+\frac{-0.02H^1_{2A}(\omega_1)H^1_{3A}(\omega_2)(e^{-(3i\omega_1+i\omega_2)} + e^{-(i\omega_1+3i\omega_2)})}{0.5e^{-(2i\omega_1+2i\omega_2)} - 0.78e^{-(i\omega_1+i\omega_2)} - 0.25e^{-(3i\omega_1+3i\omega_2)} + 0.009e^{-(4i\omega_1+4i\omega_2)} + 1} \\
&+\frac{+0.071H^1_{2A}(\omega_1)H^1_{3A}(\omega_2)(e^{-(3i\omega_1+2i\omega_2)} + e^{-(2i\omega_1+3i\omega_2)}) - 0.02H^1_{2A}(\omega_1)H^1_{3A}(\omega_2)e^{-(i\omega_1+i\omega_2)}}{0.5e^{-(2i\omega_1+2i\omega_2)} - 0.78e^{-(i\omega_1+i\omega_2)} - 0.25e^{-(3i\omega_1+3i\omega_2)} + 0.009e^{-(4i\omega_1+4i\omega_2)} + 1} \\
&+\frac{-0.85H^1_{2A}(\omega_1)H^1_{3A}(\omega_2)e^{-(2i\omega_1+2i\omega_2)} + 0.005H^1_{2A}(\omega_1)H^1_{3A}(\omega_2)(e^{-(i\omega_1+4i\omega_2)} + e^{-(4i\omega_1+i\omega_2)})}{0.5e^{-(2i\omega_1+2i\omega_2)} - 0.78e^{-(i\omega_1+i\omega_2)} - 0.25e^{-(3i\omega_1+3i\omega_2)} + 0.009e^{-(4i\omega_1+4i\omega_2)} + 1}
\end{aligned}
$$

$$\boldsymbol{H_{1B}^{3}(j\omega_1, j\omega_2, j\omega_3)} =$$

$$-\frac{3.52H_{1B}^{2}(\omega_1,\omega_2)e^{-(i\omega_1+i\omega_2+i\omega_3)}}{0.49e^{-(2i\omega_1+2i\omega_2+2i\omega_3)}-4.11e^{-(i\omega_1+i\omega_2+i\omega_3)}-1.52e^{-(3i\omega_1+3i\omega_2+3i\omega_3)}+0.46e^{-(4i\omega_1+4i\omega_2+4i\omega_3)}+6}$$

$$-\frac{+3.52H_{1B}^{2}(\omega_1,\omega_3)e^{-(i\omega_1+i\omega_2+i\omega_3)}}{0.49e^{-(2i\omega_1+2i\omega_2+2i\omega_3)}-4.11e^{-(i\omega_1+i\omega_2+i\omega_3)}-1.52e^{-(3i\omega_1+3i\omega_2+3i\omega_3)}+0.46e^{-(4i\omega_1+4i\omega_2+4i\omega_3)}+6}$$

$$-\frac{+3.5H_{1B}^{2}(\omega_2,\omega_3)e^{-(i\omega_1+i\omega_2+i\omega_3)}-0.17H_{1B}^{1}(\omega_2)H_{1B}^{2}(\omega_1,\omega_3)}{0.49e^{-(2i\omega_1+2i\omega_2+2i\omega_3)}-4.11e^{-(i\omega_1+i\omega_2+i\omega_3)}-1.52e^{-(3i\omega_1+3i\omega_2+3i\omega_3)}+0.46e^{-(4i\omega_1+4i\omega_2+4i\omega_3)}+6}$$

$$-\frac{-0.58H_{1B}^{1}(\omega_1)H_{1B}^{2}(\omega_2,\omega_3)(e^{-(i\omega_1+3i\omega_2+3i\omega_3)}+e^{-(3i\omega_1+i\omega_2+i\omega_3)})}{0.49e^{-(2i\omega_1+2i\omega_2+2i\omega_3)}-4.11e^{-(i\omega_1+i\omega_2+i\omega_3)}-1.52e^{-(3i\omega_1+3i\omega_2+3i\omega_3)}+0.46e^{-(4i\omega_1+4i\omega_2+4i\omega_3)}+6}$$

$$-\frac{-0.58H_{1B}^{1}(\omega_3)H_{1B}^{2}(\omega_1,\omega_2)(e^{-(3i\omega_1+3i\omega_2+i\omega_3)}+e^{-(i\omega_1+i\omega_2+3i\omega_3)})}{0.49e^{-(2i\omega_1+2i\omega_2+2i\omega_3)}-4.11e^{-(i\omega_1+i\omega_2+i\omega_3)}-1.52e^{-(3i\omega_1+3i\omega_2+3i\omega_3)}+0.46e^{-(4i\omega_1+4i\omega_2+4i\omega_3)}+6}$$

$$-\frac{-0.17H_{1B}^{1}(\omega_1)H_{1B}^{2}(\omega_2,\omega_3)e^{-(2i\omega_1+2i\omega_2+2i\omega_3)}-0.17H_{1B}^{1}(\omega_3)H_{1B}^{2}(\omega_1,\omega_2)e^{-(2i\omega_1+2i\omega_2+2i\omega_3)}}{0.49e^{-(2i\omega_1+2i\omega_2+2i\omega_3)}-4.11e^{-(i\omega_1+i\omega_2+i\omega_3)}-1.52e^{-(3i\omega_1+3i\omega_2+3i\omega_3)}+0.46e^{-(4i\omega_1+4i\omega_2+4i\omega_3)}+6}$$

$$-\frac{+0.24H_{1B}^{1}(\omega_1)H_{1B}^{2}(\omega_2,\omega_3)e^{-(4i\omega_1+4i\omega_2+4i\omega_3)}+0.24H_{1B}^{1}(\omega_2)H_{1B}^{2}(\omega_1,\omega_3)e^{-(4i\omega_1+4i\omega_2+4i\omega_3)}}{0.49e^{-(2i\omega_1+2i\omega_2+2i\omega_3)}-4.11e^{-(i\omega_1+i\omega_2+i\omega_3)}-1.52e^{-(3i\omega_1+3i\omega_2+3i\omega_3)}+0.46e^{-(4i\omega_1+4i\omega_2+4i\omega_3)}+6}$$

$$-\frac{+0.24H_{1B}^{1}(\omega_3)H_{1B}^{2}(\omega_1,\omega_2)e^{-(4i\omega_1+4i\omega_2+4i\omega_3)}}{0.49e^{-(2i\omega_1+2i\omega_2+2i\omega_3)}-4.11e^{-(i\omega_1+i\omega_2+i\omega_3)}-1.52e^{-(3i\omega_1+3i\omega_2+3i\omega_3)}+0.46e^{-(4i\omega_1+4i\omega_2+4i\omega_3)}+6}$$

$$-\frac{-0.58H_{1B}^{1}(\omega_2)H_{1B}^{2}(\omega_1,\omega_3)(e^{-(3i\omega_1+i\omega_2+3i\omega_3)}+e^{-(i\omega_1+3i\omega_2+i\omega_3)})}{0.49e^{-(2i\omega_1+2i\omega_2+2i\omega_3)}-4.11e^{-(i\omega_1+i\omega_2+i\omega_3)}-1.52e^{-(3i\omega_1+3i\omega_2+3i\omega_3)}+0.46e^{-(4i\omega_1+4i\omega_2+4i\omega_3)}+6}$$

$$-\frac{}{0.49e^{-(2i\omega_1+2i\omega_2+2i\omega_3)}-4.11e^{-(i\omega_1+i\omega_2+i\omega_3)}-1.52e^{-(3i\omega_1+3i\omega_2+3i\omega_3)}+0.46e^{-(4i\omega_1+4i\omega_2+4i\omega_3)}+6}$$

$$\boldsymbol{H^3_{2B}(j\omega_1, j\omega_2, j\omega_3)} = 0.17$$
$$\Big(\frac{0.00012e^{-(3i\omega_1+2i\omega_2+8i\omega_3)} + 0.00012e^{-(3i\omega_1+8i\omega_2+2i\omega_3)}}{0.08e^{-(2i\omega_1+2i\omega_2+2i\omega_3)} - 0.68e^{-(i\omega_1+i\omega_2+i\omega_3)} - 0.25e^{-(3i\omega_1+3i\omega_2+3i\omega_3)} + 0.077e^{-(4i\omega_1+4i\omega_2+4i\omega_3)} + 1}$$
$$+\frac{+0.00012e^{-(i\omega_1+3i\omega_2+8i\omega_3)} + 0.00012e^{-(2i\omega_1+8i\omega_2+3i\omega_3)} + 0.00012e^{-(8i\omega_1+3i\omega_2+2i\omega_3)}}{0.08e^{-(2i\omega_1+2i\omega_2+2i\omega_3)} - 0.68e^{-(i\omega_1+i\omega_2+i\omega_3)} - 0.25e^{-(3i\omega_1+3i\omega_2+3i\omega_3)} + 0.077e^{-(4i\omega_1+4i\omega_2+4i\omega_3)} + 1}$$
$$+\frac{+0.00012e^{-(8i\omega_1+2i\omega_2+3i\omega_3)} - 0.00075e^{-(i\omega_1+i\omega_2+i\omega_3)} + 0.05H^2_{2B}(\omega_1,\omega_2)e^{-(3i\omega_1+3i\omega_2+4i\omega_3)}}{0.08e^{-(2i\omega_1+2i\omega_2+2i\omega_3)} - 0.68e^{-(i\omega_1+i\omega_2+i\omega_3)} - 0.25e^{-(3i\omega_1+3i\omega_2+3i\omega_3)} + 0.077e^{-(4i\omega_1+4i\omega_2+4i\omega_3)} + 1}$$
$$+\frac{+0.05H^2_{2B}(\omega_1,\omega_3)e^{-(3i\omega_1+4i\omega_2+3i\omega_3)} + 0.05H^2_{2B}(\omega_2,\omega_3)e^{-(4i\omega_1+3i\omega_2+3i\omega_3)}}{0.08e^{-(2i\omega_1+2i\omega_2+2i\omega_3)} - 0.68e^{-(i\omega_1+i\omega_2+i\omega_3)} - 0.25e^{-(3i\omega_1+3i\omega_2+3i\omega_3)} + 0.077e^{-(4i\omega_1+4i\omega_2+4i\omega_3)} + 1}$$
$$+\frac{+0.004H^2_{2B}(\omega_1,\omega_2)e^{-(i\omega_1+i\omega_2+3i\omega_3)} + 0.004H^2_{2B}(\omega_1,\omega_3)e^{-(i\omega_1+3i\omega_2+i\omega_3)}}{0.08e^{-(2i\omega_1+2i\omega_2+2i\omega_3)} - 0.68e^{-(i\omega_1+i\omega_2+i\omega_3)} - 0.25e^{-(3i\omega_1+3i\omega_2+3i\omega_3)} + 0.077e^{-(4i\omega_1+4i\omega_2+4i\omega_3)} + 1}$$
$$+\frac{+0.004H^2_{2B}(\omega_2,\omega_3)e^{-(i\omega_1+i\omega_2+i\omega_3)} + 0.0036H^1_{2B}(\omega_1)e^{-(1.0i\omega 1+8i\omega_2+8i\omega_3)}}{0.08e^{-(2i\omega_1+2i\omega_2+2i\omega_3)} - 0.68e^{-(i\omega_1+i\omega_2+i\omega_3)} - 0.25e^{-(3i\omega_1+3i\omega_2+3i\omega_3)} + 0.077e^{-(4i\omega_1+4i\omega_2+4i\omega_3)} + 1}$$
$$+\frac{+0.0034H^1_{2B}(\omega_2)e^{-(8i\omega_1+i\omega_2+8i\omega_3)} + 0.0036H^1_{2B}(\omega_3)e^{-(8i\omega_1+8i\omega_2+i\omega_3)}}{0.08e^{-(2i\omega_1+2i\omega_2+2i\omega_3)} - 0.68e^{-(i\omega_1+i\omega_2+i\omega_3)} - 0.25e^{-(3i\omega_1+3i\omega_2+3i\omega_3)} + 0.077e^{-(4i\omega_1+4i\omega_2+4i\omega_3)} + 1}$$
$$+\frac{+0.17H^2_{2B}(\omega_1,\omega_2)e^{-(i\omega_1+i\omega_2+i\omega_3)} - 0.016H^2_{2B}(\omega_1,\omega_2)e^{-(4i\omega_1+4i\omega_2+8i\omega_3)}}{0.08e^{-(2i\omega_1+2i\omega_2+2i\omega_3)} - 0.68e^{-(i\omega_1+i\omega_2+i\omega_3)} - 0.25e^{-(3i\omega_1+3i\omega_2+3i\omega_3)} + 0.077e^{-(4i\omega_1+4i\omega_2+4i\omega_3)} + 1}$$
$$+\frac{+0.17H^2_{2B}(\omega_1,\omega_3)e^{-(i\omega_1+8i\omega_2+i\omega_3)} - 0.016H^2_{2B}(\omega_1,\omega_3)e^{-(4i\omega_1+8i\omega_2+4i\omega_3)}}{0.08e^{-(2i\omega_1+2i\omega_2+2i\omega_3)} - 0.68e^{-(i\omega_1+i\omega_2+i\omega_3)} - 0.25e^{-(3i\omega_1+3i\omega_2+3i\omega_3)} + 0.077e^{-(4i\omega_1+4i\omega_2+4i\omega_3)} + 1}$$
$$+\frac{+0.17H^2_{2B}(\omega_2,\omega_3)e^{-(8i\omega_1+i\omega_2+i\omega_3)} - 0.016H^2_{2B}(\omega_2,\omega_3)e^{-(8i\omega_1+4i\omega_2+4i\omega_3)}}{0.08e^{-(2i\omega_1+2i\omega_2+2i\omega_3)} - 0.68e^{-(i\omega_1+i\omega_2+i\omega_3)} - 0.25e^{-(3i\omega_1+3i\omega_2+3i\omega_3)} + 0.077e^{-(4i\omega_1+4i\omega_2+4i\omega_3)} + 1}$$
$$+\frac{+0.58H^1_{2B}(\omega_1)H^2_{2B}(\omega_2,\omega_3)(e^{-(i\omega_1+3i\omega_2+3i\omega_3)} + e^{-(3i\omega_1+i\omega_2+i\omega_3)})}{0.08e^{-(2i\omega_1+2i\omega_2+2i\omega_3)} - 0.68e^{-(i\omega_1+i\omega_2+i\omega_3)} - 0.25e^{-(3i\omega_1+3i\omega_2+3i\omega_3)} + 0.077e^{-(4i\omega_1+4i\omega_2+4i\omega_3)} + 1}$$
$$+\frac{+0.58H^1_{2B}(\omega_2)H^2_{2B}(\omega_1,\omega_3)(e^{-(3i\omega_1+i\omega_2+3i\omega_3)} + e^{-(i\omega_1+3i\omega_2+i\omega_3)})}{0.08e^{-(2i\omega_1+2i\omega_2+2i\omega_3)} - 0.68e^{-(i\omega_1+i\omega_2+i\omega_3)} - 0.25e^{-(3i\omega_1+3i\omega_2+3i\omega_3)} + 0.077e^{-(4i\omega_1+4i\omega_2+4i\omega_3)} + 1}$$
$$+\frac{-0.24H^1_{2B}(\omega_3)H^2_{2B}(\omega_1,\omega_2)e^{-(4i\omega_1+4i\omega_2+4i\omega_3)} + 0.17H^1_{2B}(\omega_1)H^2_{2B}(\omega_2,\omega_3)e^{-(2i\omega_1+2i\omega_2+2i\omega_3)}}{0.08e^{-(2i\omega_1+2i\omega_2+2i\omega_3)} - 0.68e^{-(i\omega_1+i\omega_2+i\omega_3)} - 0.25e^{-(3i\omega_1+3i\omega_2+3i\omega_3)} + 0.077e^{-(4i\omega_1+4i\omega_2+4i\omega_3)} + 1}$$
$$+\frac{+0.58H^1_{2B}(\omega_3)H^2_{2B}(\omega_1,\omega_2)(e^{-(3i\omega_1+3i\omega_2+i\omega_3)} + e^{-(i\omega_1+i\omega_2+3i\omega_3)})}{0.08e^{-(2i\omega_1+2i\omega_2+2i\omega_3)} - 0.68e^{-(i\omega_1+i\omega_2+i\omega_3)} - 0.25e^{-(3i\omega_1+3i\omega_2+3i\omega_3)} + 0.077e^{-(4i\omega_1+4i\omega_2+4i\omega_3)} + 1}$$
$$+\frac{+0.17H^1_{2B}(\omega_3)H^2_{2B}(\omega_1,\omega_2)e^{-(2i\omega_1+2i\omega_2+2i\omega_3)} - 0.24H^1_{2B}(\omega_1)H^2_{2B}(\omega_2,\omega_3)e^{-(4i\omega_1+4i\omega_2+4i\omega_3)}}{0.08e^{-(2i\omega_1+2i\omega_2+2i\omega_3)} - 0.68e^{-(i\omega_1+i\omega_2+i\omega_3)} - 0.25e^{-(3i\omega_1+3i\omega_2+3i\omega_3)} + 0.077e^{-(4i\omega_1+4i\omega_2+4i\omega_3)} + 1}$$
$$+\frac{-0.24H^1_{2B}(\omega_2)H^2_{2B}(\omega_1,\omega_3)e^{-(4i\omega_1+4i\omega_2+4i\omega_3)} + 0.17H^1_{2B}(\omega_2)H^2_{2B}(\omega_1,\omega_3)e^{-(2i\omega_1+2i\omega_2+2i\omega_3)}}{0.08e^{-(2i\omega_1+2i\omega_2+2i\omega_3)} - 0.68e^{-(i\omega_1+i\omega_2+i\omega_3)} - 0.25e^{-(3i\omega_1+3i\omega_2+3i\omega_3)} + 0.077e^{-(4i\omega_1+4i\omega_2+4i\omega_3)} + 1}\Big)$$

$$\boldsymbol{H_{3B}^{3}(j\omega_1, j\omega_2, j\omega_3)} = 0.17/$$

$$(1.0 - 0.68e^{-(-i\omega_1 - i\omega_2 - i\omega_3)} + 0.08e^{-(-2\omega_1 - 2\omega_2 - 2\omega_3)} + 0.077e^{-(-4\omega_1 - 6\omega_2 - 4\omega_3)}$$

$$-0.25e^{-(-3\omega_1 - 3\omega_2 - 3\omega_3)})(0.000000025e^{-(-3\omega_1 - 5\omega_2 - 2\omega_3)}$$

$$+0.000000025e^{-(-3\omega_1 - 2\omega_2 - 5\omega_3)} + 0.000000025e^{-(-5\omega_1 - 3\omega_2 - 2\omega_3)}$$

$$+0.000000025e^{-(-5\omega_1 - 2\omega_2 - 3\omega_3)} + 0.000000025e^{-(-2\omega_1 - 3\omega_2 - 5\omega_3)}$$

$$+0.000000025e^{-(-2\omega_1 - 5\omega_2 - 3\omega_3)} - 0.00000005e^{-(-6\omega_1 - 2\omega_2 - 2\omega_3)}$$

$$-0.00000005e^{-(-2\omega_1 - 6\omega_2 - 2\omega_3)} - 0.00000005^{e-(-2\omega_1 - 2\omega_2 - 6\omega_3)}$$

$$-0.00064H_{3B}^{2}(\omega_1, \omega_2)e^{-(-\omega_1 - \omega_2 - 6\omega_3)} - 0.00064H_{3B}^{2}(\omega_1, \omega_3)e^{-(-\omega_1 - 6\omega_2 - \omega_3)}$$

$$-0.00064H_{3B}^{2}(\omega_2, \omega_3)e^{-(-6\omega_1 - \omega_2 - \omega_3)} - 0.0026H_{3B}^{2}(\omega_1, \omega_2)e^{-(-\omega_1 - \omega_2 - 4\omega_3)}$$

$$-0.00089H_{3B}^{2}(\omega_1, \omega_2)e^{-(-2\omega_1 - 2\omega_2 - 4\omega_3)} + 0.0012H_{3B}^{2}(\omega_1, \omega_2)e^{-(-4\omega_1 - 4\omega_2 - 2\omega_3)}$$

$$-0.0021H_{3B}^{2}(\omega_1, \omega_2)e^{-(-4\omega_1 - 4\omega_2 - 4\omega_3)} - 0.0026H_{3B}^{2}(\omega_1, \omega_3)e^{-(-\omega_1 - 4\omega_2 - \omega_3)}$$

$$-0.00089H_{3B}^{2}(\omega_1, \omega_3)e^{-(-2\omega_1 - 4\omega_2 - 2\omega_3)} + 0.0012H_{3B}^{2}(\omega_1, \omega_3)e^{-(-4\omega_1 - 2\omega_2 - 4\omega_3)}$$

$$-0.0021H_{3B}^{2}(\omega_1, \omega_3)e^{-(-4\omega_1 - 4\omega_2 - 4\omega_3)} - 0.0026H_{3B}^{2}(\omega_2, \omega_3)e^{-(-4\omega_1 - \omega_2 - \omega_3)}$$

$$-0.00089H_{3B}^{2}(\omega_2, \omega_3)e^{-(-4\omega_1 - 2\omega_2 - 2\omega_3)} + 0.0012H_{3B}^{2}(\omega_2, \omega_3)e^{-(-2\omega_1 - 4\omega_2 - 4\omega_3)}$$

$$-0.0021H_{3B}^{2}(\omega_2, \omega_3)e^{-(-4\omega_1 - 4\omega_2 - 4\omega_3)} + 0.0028H_{3B}^{2}(\omega_1, \omega_2)e^{-(-3\omega_1 - 3\omega_2 - 4\omega_3)}$$

$$+0.0028H_{3B}^{2}(\omega_1, \omega_3)e^{-(-3\omega_1 - 4\omega_2 - 3\omega_3)} + 0.0028H_{3B}^{2}(\omega_2, \omega_3)e^{-(-4\omega_1 - 3\omega_2 - 3\omega_3)}$$

$$+0.0016H_{3B}^{1}(\omega_1)H_{3B}^{1}(\omega_2)(e^{-(-3\omega_1 - \omega_2 - 4\omega_3)} + e^{-(-\omega_1 - 3\omega_2 - 4\omega_3)})$$

$$+0.0016H_{3B}^{1}(\omega_1)H_{3B}^{1}(\omega_3)(e^{-(-3\omega_1 - 4\omega_2 - \omega_3)} + e^{-(-\omega_1 - 4\omega_2 - 3\omega_3)})$$

$$+0.0016H_{3B}^{1}(\omega_2)H_{3B}^{1}(\omega_3)(e^{-(-4\omega_1 - 3\omega_2 - \omega_3)} + e^{-(-4\omega_1 - \omega_2 - 3\omega_3)})$$

$$+0.00047H_{3B}^{1}(\omega_1)H_{3B}^{1}(\omega_2)e^{-(-2\omega_1 - 2\omega_2 - 4\omega_3)} - 0.00065H_{3B}^{1}(\omega_1)H_{3B}^{1}(\omega_2)e^{-(-4\omega_1 - 4\omega_2 - 2\omega_3)}$$

$$+0.00047H_{3B}^{1}(\omega_1)H_{3B}^{1}(\omega_3)e^{-(-2\omega_1 - 4\omega_2 - 2\omega_3)} - 0.00065H_{3B}^{1}(\omega_1)H_{3B}^{1}(\omega_3)e^{-(-4\omega_1 - 2\omega_2 - 4\omega_3)}$$

$$+0.00047H_{3B}^{1}(\omega_2)H_{3B}^{1}(\omega_3)e^{-(-4\omega_1 - 2\omega_2 - 2\omega_3)} - 0.00065H_{3B}^{1}(\omega_2)H_{3B}^{1}(\omega_3)e^{-(-2\omega_1 - 4\omega_2 - 4\omega_3)}$$

$$+0.17H_{3B}^{1}(\omega_1)H_{3B}^{2}(\omega_2, \omega_3)e^{-(-2\omega_1 - 2\omega_2 - 2\omega_3)} + 0.17H_{3B}^{1}(\omega_2)H_{3B}^{2}(\omega_1, \omega_3)e^{-(-2\omega_1 - 2\omega_2 - 2\omega_3)}$$

$$+0.17H_{3B}^{1}(\omega_3)H_{3B}^{2}(\omega_1, \omega_2)e^{-(-2\omega_1 - 2\omega_2 - 2\omega_3)} - 0.24H_{3B}^{1}(\omega_1)H_{3B}^{2}(\omega_2, \omega_3)e^{-(-4\omega_1 - 4\omega_2 - 4\omega_3)}$$

$$-0.24H_{3B}^{1}(\omega_2)H_{3B}^{2}(\omega_1, \omega_3)e^{-(-4\omega_1 - 4\omega_2 - 4\omega_3)} - 0.24H_{3B}^{1}(\omega_3)H_{3B}^{2}(\omega_1, \omega_2)e^{-(-4\omega_1 - 4\omega_2 - 4\omega_3)}$$

$$+0.58H^1_{3B}(\omega_1)H^2_{3B}(\omega_2,\omega_3)(e^{-(-\omega_1-3\omega_2-3\omega_3)}+e^{-(-3\omega_1-\omega_2-\omega_3)})$$
$$+0.58H^1_{3B}(\omega_2)H^2_{3B}(\omega_1,\omega_3)(e^{-(-3\omega_1-\omega_2-3\omega_3)}+e^{-(-\omega_1-3\omega_2-\omega_3)})$$
$$+0.58H^1_{3B}(\omega_3)H^2_{3B}(\omega_1,\omega_2)(e^{-(-3\omega_1-3\omega_2-\omega_3)}+e^{-(-\omega_1-\omega_2-3\omega_3)}))$$

$$
\begin{aligned}
\boldsymbol{H^3_{1A}(j\omega_1, j\omega_2, j\omega_3)} = -0.17(& \\
& \frac{0.69H^2_{1A}(\omega_1,\omega_2)e^{-(-4\omega_1-4\omega_2-2\omega_3)} + 7.27H^2_{1A}(\omega_1,\omega_3)e^{-(-\omega_1-\omega_2-\omega_3)}}{1.0-0.79e^{-(-\omega_1-\omega_2-\omega_3)}+0.48e^{-(-2\omega_1-2\omega_2-2\omega_3)}+0.0093e^{-(-4\omega_1-4\omega_2-4\omega_3)}-0.25e^{-(-3\omega_1-3\omega_2-3\omega_3)}} \\
& + \frac{+0.69H^2_{1A}(\omega_1,\omega_3)e^{-(-\omega_1-2\omega_2-\omega_3)} + 0.69H^2_{1A}(\omega_1,\omega_3)e^{-(-4\omega_1-2\omega_2-4\omega_3)}}{1.0-0.79e^{-(-\omega_1-\omega_2-\omega_3)}+0.48e^{-(-2\omega_1-2\omega_2-2\omega_3)}+0.0093e^{-(-4\omega_1-4\omega_2-4\omega_3)}-0.25e^{-(-3\omega_1-3\omega_2-3\omega_3)}} \\
& + \frac{+0.69H^2_{1A}(\omega_2,\omega_3)e^{-(-2\omega_1-4\omega_2-4\omega_3)} - 8.51H^2_{1A}(\omega_1,\omega_2)e^{-(-2\omega_1-2\omega_2-7\omega_3)}}{1.0-0.79e^{-(-\omega_1-\omega_2-\omega_3)}+0.48e^{-(-2\omega_1-2\omega_2-2\omega_3)}+0.0093e^{-(-4\omega_1-4\omega_2-4\omega_3)}-0.25e^{-(-3\omega_1-3\omega_2-3\omega_3)}} \\
& + \frac{-8.51H^2_{1A}(\omega_1,\omega_3)e^{-(-2\omega_1-7\omega_2-2\omega_3)} + 7.27H^2_{1A}(\omega_2,\omega_3)e^{-(-\omega_1-\omega_2-\omega_3)}}{1.0-0.79e^{-(-\omega_1-\omega_2-\omega_3)}+0.48e^{-(-2\omega_1-2\omega_2-2\omega_3)}+0.0093e^{-(-4\omega_1-4\omega_2-4\omega_3)}-0.25e^{-(-3\omega_1-3\omega_2-3\omega_3)}} \\
& + \frac{+0.69H^2_{1A}(\omega_2,\omega_3)e^{-(-2\omega_1-\omega_2-\omega_3)} - 8.51H^2_{1A}(\omega_2,\omega_3)e^{-(-7\omega_1-2\omega_2-2\omega_3)}}{1.0-0.79e^{-(-\omega_1-\omega_2-\omega_3)}+0.48e^{-(-2-\omega_1-2\omega_2-2\omega_3)}+0.0093e^{-(-4\omega_1-4\omega_2-4\omega_3)}-0.25e^{-(-3\omega_1-3\omega_2-3\omega_3)}} \\
& + \frac{-0.37H^1_{1A}(\omega_1)H^1_{1A}(\omega_2)(e^{-(-\omega_1-4\omega_2-2\omega_3)}+e^{-(-4\omega_1-\omega_2-2\omega_3)})}{1.0-0.79e^{-(-\omega_1-\omega_2-\omega_3)}+0.48e^{-(-2\omega_1-2\omega_2-2\omega_3)}+0.0093e^{-(-4\omega_1-4\omega_2-4\omega_3)}-0.25e^{-(-3\omega_1-3\omega_2-3\omega_3)}} \\
& + \frac{-0.02H^1_{1A}(\omega_1)H^2_{1A}(\omega_2,\omega_3)(e^{-(-4\omega_1-\omega_2-\omega_3)}+e^{-(-\omega_1-4\omega_2-4\omega_3)})}{1.0-0.79e^{-(-\omega_1-\omega_2-\omega_3)}+0.48e^{-(-2\omega_1-2\omega_2-2\omega_3)}+0.0093e^{-(-4\omega_1-4\omega_2-4\omega_3)}-0.25e^{-(-3\omega_1-3\omega_2-3\omega_3)}} \\
& + \frac{-0.37H^1_{1A}(\omega_1)H^1_{1A}(\omega_3)(e^{-(-\omega_1-2\omega_2-4\omega_3)}+e^{-(-4\omega_1-2\omega_2-\omega_3)}) + 0.69H^2_{1A}(\omega_1,\omega_2)e^{-(-\omega_1-\omega_2-2\omega_3)}}{} \\
& \\
& + \frac{-0.37H^1_{1A}(\omega_2)H^1_{1A}(\omega_3)(e^{-(-2\omega_1-\omega_2-4\omega_3)}+e^{-(-2\omega_1-4\omega_2-\omega_3)}) + 7.27H^2_{1A}(\omega_1,\omega_2)e^{-(-\omega_1-\omega_2-\omega_3)}}{1.0-0.79e^{-(-\omega_1-\omega_2-\omega_3)}+0.48e^{-(-2\omega_1-2\omega_2-2\omega_3)}+0.0093e^{-(-4\omega_1-4\omega_2-4\omega_3)}-0.25e^{-(-3\omega_1-3\omega_2-3\omega_3)}} \\
& + \frac{-0.02H^1_{1A}(\omega_2)H^2_{1A}(\omega_1,\omega_3)(e^{-(-\omega_1-4\omega_2-\omega_3)}+e^{-(-4\omega_1-\omega_2-4\omega_3)})}{1.0-0.79e^{-(-\omega_1-\omega_2-\omega_3)}+0.48e^{-(-2\omega_1-2\omega_2-2\omega_3)}+0.0093e^{-(-4\omega_1-4\omega_2-4\omega_3)}-0.25e^{-(-3\omega_1-3\omega_2-3\omega_3)}} \\
& + \frac{-0.02H^1_{1A}(\omega_3)H^2_{1A}(\omega_1,\omega_2)(e^{-(-\omega_1-\omega_2-4\omega_3)}+e^{-(-4\omega_1-4\omega_2-\omega_3)})}{1.0-0.79e^{-(-\omega_1-\omega_2-\omega_3)}+0.48e^{-(-2\omega_1-2\omega_2-2\omega_3)}+0.0093e^{-(-4\omega_1-4\omega_2-4\omega_3)}-0.25e^{-(-3\omega_1-3\omega_2-3\omega_3)}} \\
& + \frac{+0.075H^1_{1A}(\omega_1)H^2_{1A}(\omega_2,\omega_3)e^{-(-\omega_1-\omega_2-\omega_3)} + 0.075H^1_{1A}(\omega_2)H^2_{1A}(\omega_1,\omega_3)e^{-(-\omega_1-\omega_2-\omega_3)}}{1.0-0.79e^{-(-\omega_1-\omega_2-\omega_3)}+0.48e^{-(-2\omega_1-2\omega_2-2\omega_3)}+0.0093e^{-(-4\omega_1-4\omega_2-4\omega_3)}-0.25e^{-(-3\omega_1-3\omega_2-3\omega_3)}} \\
& + \frac{+0.075H^1_{1A}(\omega_3)H^2_{1A}(\omega_1,\omega_2)e^{-(-\omega_1-\omega_2-\omega_3)} + 3.42H^1_{1A}(\omega_1)H^2_{1A}(\omega_2,\omega_3)e^{-(-2\omega_1-2\omega_2-2\omega_3)}}{1.0-0.79e^{-(-\omega_1-\omega_2-\omega_3)}+0.48e^{-(-2\omega_1-2\omega_2-2\omega_3)}+0.0093e^{-(-4\omega_1-4\omega_2-4\omega_3)}-0.25e^{-(-3\omega_1-3\omega_2-3\omega_3)}} \\
& + \frac{+3.42H^1_{1A}(\omega_2)H^2_{1A}(\omega_1,\omega_3)e^{-(-2\omega_1-2\omega_2-2\omega_3)} + 3.42H^1_{1A}(\omega_3)H^2_{1A}(\omega_1,\omega_2)e^{-(-2\omega_1-2\omega_2-2\omega_3)}}{1.0-0.79e^{-(-\omega_1-\omega_2-\omega_3)}+0.48e^{-(-2\omega_1-2\omega_2-2\omega_3)}+0.0093e^{-(-4\omega_1-4\omega_2-4\omega_3)}-0.25e^{-(-3\omega_1-3\omega_2-3\omega_3)}} \\
& + \frac{+0.075H^1_{1A}(\omega_1)H^2_{1A}(\omega_2,\omega_3)(e^{-(-\omega_1-3\omega_2-3\omega_3)}+e^{-(-3\omega_1-\omega_2-\omega_3)})}{1.0-0.79e^{-(-\omega_1-\omega_2-\omega_3)}+0.48e^{-(-2\omega_1-2\omega_2-2\omega_3)}+0.0093e^{-(-4\omega_1-4\omega_2-4\omega_3)}-0.25e^{-(-3\omega_1-3\omega_2-3\omega_3)}} \\
& + \frac{+0.075H^1_{1A}(\omega_2)H^2_{1A}(\omega_1,\omega_3)(e^{-(-3\omega_1-\omega_2-3\omega_3)}+e^{-(-\omega_1-3\omega_2-\omega_3)})}{1.0-0.79e^{-(-\omega_1-\omega_2-\omega_3)}+0.48e^{-(-2\omega_1-2\omega_2-2\omega_3)}+0.0093e^{-(-4\omega_1-4\omega_2-4\omega_3)}-0.25e^{-(-3\omega_1-3\omega_2-3\omega_3)}} \\
& + \frac{+0.075H^1_{1A}(\omega_3)H^2_{1A}(\omega_1,\omega_2)(e^{-(-3\omega_1-3\omega_2-\omega_3)}+e^{-(-\omega_1-\omega_2-3\omega_3)})}{1.0-0.79e^{-(-\omega_1-\omega_2-\omega_3)}+0.48e^{-(-2\omega_1-2\omega_2-2\omega_3)}+0.0093e^{-(-4\omega_1-4\omega_2-4\omega_3)}-0.25e^{-(-3\omega_1-3\omega_2-3\omega_3)}} \\
& + \frac{-0.28H^1_{1A}(\omega_1)H^2_{1A}(\omega_2,\omega_3)(e^{-(-2\omega_1-3\omega_2-3\omega_3)}+e^{-(-3\omega_1-2\omega_2-2\omega_3)})}{1.0-0.79e^{-(-\omega_1-\omega_2-\omega_3)}+0.48e^{-(-2\omega_1-2\omega_2-2\omega_3)}+0.0093e^{-(-4\omega_1-4\omega_2-4\omega_3)}-0.25e^{-(-3\omega_1-3\omega_2-3\omega_3)}} \\
& + \frac{+0.28H^1_{1A}(\omega_2)H^2_{1A}(\omega_1,\omega_3)(e^{-(-3\omega_1-2\omega_2-3\omega_3)}+e^{-(-2\omega_1-3\omega_2-2\omega_3)})}{1.0-0.79e^{-(-\omega_1-\omega_2-\omega_3)}+0.48e^{-(-2\omega_1-2\omega_2-2\omega_3)}+0.0093e^{-(-4\omega_1-4\omega_2-4\omega_3)}-0.25e^{-(-3\omega_1-3\omega_2-3\omega_3)}} \\
& + \frac{-0.28H^1_{1A}(\omega_3)H^2_{1A}(\omega_1,\omega_2)(e^{-(-3\omega_1-3\omega_2-2\omega_3)}+e^{-(-2\omega_1-2\omega_2-3\omega_3)})}{1.0-0.79e^{-(-\omega_1-\omega_2-\omega_3)}+0.48e^{-(-2\omega_1-2\omega_2-2\omega_3)}+0.0093e^{-(-4\omega_1-4\omega_2-4\omega_3)}-0.25e^{-(-3\omega_1-3\omega_2-3\omega_3)}} \\
& + \frac{-0.02H^1_{1A}(\omega_1)H^1_{1A}(\omega_2)H^1_{1A}(\omega_3)(2e^{-(-3\omega_1-\omega_2-\omega_3)}+2e^{-(-\omega-3\omega_2-\omega_3)}+2e^{-(-\omega_1-\omega_2-3\omega_3)})}{1.0-0.79e^{-(-\omega_1-\omega_2-\omega_3)}+0.48e^{-(-2\omega_1-2\omega_2-2\omega_3)}+0.0093e^{-(-4\omega_1-4\omega_2-4\omega_3)}-0.25e^{-(-3\omega_1-3\omega_2-3\omega_3)}} \\
& + \frac{+0.41H^1_{1A}(\omega_1)H^1_{1A}(\omega_2)H^1_{1A}(\omega_3)(2e^{-(-3\omega_1-2\omega_2-2\omega_3)}+2e^{-(-2\omega_1-3\omega_2-2\omega_3)}+2e^{-(-2\omega_1-2\omega_2-3\omega_3)})}{1.0-0.79e^{-(-\omega_1-\omega_2-\omega_3)}+0.48e^{-(-2\omega_1-2\omega_2-2\omega_3)}+0.0093e^{-(-4\omega_1-4\omega_2-4\omega_3)}-0.25e^{-(-3\omega_1-3\omega_2-3\omega_3)}})
\end{aligned}
$$

$$
\begin{aligned}
&\boldsymbol{H^3_{2A}(j\omega_1, j\omega_2, j\omega_3)} = 0.17 \\
&\Big(\frac{0.00027e^{-(-3\omega_1-8\omega_2-8\omega_3)} + 0.00027e^{-(-8\omega_1-3\omega_2-8\omega_3)}}{1.0 - 0.79e^{-(-\omega_1-\omega_2-\omega_3)} + 0.48e^{-(-2\omega_1-2\omega_2-2\omega_3)} + 0.0093e^{-(-4\omega_1-4\omega_2-4\omega_3)} - 0.25e^{-(-3\omega_1-3\omega_2-3\omega_3)}} \\
&+\frac{+0.00027e^{-(-8\omega_1-8\omega_2-3\omega_3)} - 0.00053e^{-(-\omega_1-\omega_2-\omega_3)} - 0.00098e^{-(-8\omega_1-8\omega_2-8\omega_3)}}{1.0 - 0.79e^{-(-\omega_1-\omega_2-\omega_3)} + 0.48e^{-(-2\omega_1-2\omega_2-2\omega_3)} + 0.0093e^{-(-4\omega_1-4\omega_2-4\omega_3)} - 0.25e^{-(-3\omega_1-3\omega_2-3\omega_3)}} \\
&+\frac{+0.027H^2_{2A}(\omega_1,\omega_2)e^{-(-\omega_1-\omega_2-3\omega_3)} + 0.24H^2_{2A}(\omega_1,\omega_2)e^{-(-2\omega_1-2\omega_2-3\omega_3)}}{1.0 - 0.79e^{-(-\omega_1-\omega_2-\omega_3)} + 0.48e^{-(-2\omega_1-2\omega_2-2\omega_3)} + 0.0093e^{-(-4\omega_1-4\omega_2-4\omega_3)} - 0.25e^{-(-3\omega_1-3\omega_2-3\omega_3)}} \\
&+\frac{+0.027H^2_{2A}(\omega_1,\omega_3)e^{-(-\omega_1-3\omega_2-\omega_3)} + 0.24H^2_{2A}(\omega_1,\omega_3)e^{-(-2\omega_1-3\omega_2-2\omega_3)}}{1.0 - 0.79e^{-(-\omega_1-\omega_2-\omega_3)} + 0.48e^{-(-2\omega_1-2\omega_2-2\omega_3)} + 0.0093e^{-(-4\omega_1-4\omega_2-4\omega_3)} - 0.25e^{-(-3\omega_1-3\omega_2-3\omega_3)}} \\
&+\frac{+0.027H^2_{2A}(\omega_2,\omega_3)e^{-(-3\omega_1-\omega_2-\omega_3)} + 0.24H^2_{2A}(\omega_2,\omega_3)e^{-(3-\omega-2\omega_2-2\omega_3)}}{1.0 - 0.79e^{-(-\omega_1-\omega_2-\omega_3)} + 0.48e^{-(-2\omega_1-2\omega_2-2\omega_3)} + 0.0093e^{-(-4\omega_1-4\omega_2-4\omega_3)} - 0.25e^{-(-3\omega_1-3\omega_2-3\omega_3)}} \\
&+\frac{+0.016H^2_{2A}(\omega_1,\omega_2)e^{-(-2\omega_1-2\omega_2-5\omega_3)} + 0.016H^2_{2A}(\omega_1,\omega_3)e^{-(-2\omega_1-5\omega_2-2\omega_3)}}{1.0 - 0.79e^{-(-\omega_1-\omega_2-\omega_3)} + 0.48e^{-(-2\omega_1-2\omega_2-2\omega_3)} + 0.0093e^{-(-4\omega_1-4\omega_2-4\omega_3)} - 0.25e^{-(-3\omega_1-3\omega_2-3\omega_3)}} \\
&+\frac{+0.016H^2_{2A}(\omega_2,\omega_3)e^{-(-5\omega_1-2\omega_2-2\omega_3)} + 0.0028H^1_{2A}(\omega_1)e^{-(-\omega_1-8\omega_2-8\omega_3)}}{1.0 - 0.79e^{-(-\omega_1-\omega_2-\omega_3)} + 0.48e^{-(-2\omega_1-2\omega_2-2\omega_3)} + 0.0093e^{-(-4\omega_1-4\omega_2-4\omega_3)} - 0.25e^{-(-3\omega_1-3\omega_2-3\omega_3)}} \\
&+\frac{+0.0028H^1_{2A}(\omega_2)e^{-(-8\omega_1-\omega_2-8\omega_3)} + 0.0028H^1_{2A}(\omega_3)e^{-(-8\omega_1-8\omega_2-\omega_3)}}{1.0 - 0.79e^{-(-\omega_1-\omega_2-\omega_3)} + 0.48e^{-(-2\omega_1-2\omega_2-2\omega_3)} + 0.0093e^{-(-4\omega_1-4\omega_2-4\omega_3)} - 0.25e^{-(-3\omega_1-3\omega_2-3\omega_3)}} \\
&+\frac{+0.13H^2_{2A}(\omega_1,\omega_2)e^{-(-\omega_1-\omega_2-8\omega_3)} - +0.24H^2_{2A}(\omega_1,\omega_2)e^{-(-2\omega_1-2\omega_2-2\omega_3)}}{1.0 - 0.79e^{-(-\omega_1-\omega_2-\omega_3)} + 0.48e^{-(-2\omega_1-2\omega_2-2\omega_3)} + 0.0093e^{-(-4\omega_1-4\omega_2-4\omega_3)} - 0.25e^{-(-3\omega_1-3\omega_2-3\omega_3)}} \\
&+\frac{+0.13H^2_{2A}(\omega_1,\omega_3)e^{-(-\omega_1-8\omega_2-\omega_3)} - 0.24H^2_{2A}(\omega_1,\omega_3)e^{-(-2\omega_1-2\omega_2-2\omega_3)}}{1.0 - 0.79e^{-(-\omega_1-\omega_2-\omega_3)} + 0.48e^{-(-2\omega_1-2\omega_2-2\omega_3)} + 0.0093e^{-(-4\omega_1-4\omega_2-4\omega_3)} - 0.25e^{-(-3\omega_1-3\omega_2-3\omega_3)}} \\
&+\frac{-0.24H^2_{2A}(\omega_2,\omega_3)e^{-(-2\omega_1-2\omega_2-2\omega_3)} + 0.13H^2_{2A}(\omega_2,\omega_3)e^{-(8\omega_1-\omega_2-\omega_3)}}{1.0 - 0.79e^{-(-\omega_1-\omega_2-\omega_3)} + 0.48e^{-(-2\omega_1-2\omega_2-2\omega_3)} + 0.0093e^{-(-4\omega_1-4\omega_2-4\omega_3)} - 0.25e^{-(-3\omega_1-3\omega_2-3\omega_3)}} \\
&+\frac{-0.0052H^1_{2A}(\omega_1)(e^{-(-2\omega_1-7\omega_2-2\omega_3)} + e^{-(-2\omega_1-2\omega_2-7\omega_3)})}{1.0 - 0.79e^{-(-\omega_1-\omega_2-\omega_3)} + 0.48e^{-(-2\omega_1-2\omega_2-2\omega_3)} + 0.0093e^{-(-4\omega_1-4\omega_2-4\omega_3)} - 0.25e^{-(-3\omega_1-3\omega_2-3\omega_3)}} \\
&+\frac{-0.0052H^1_{2A}(\omega_2)(e^{-(-7\omega_1-2\omega_2-2\omega_3)} + e^{-(-2\omega_1-2\omega_2-7\omega_3)})}{1.0 - 0.79e^{-(-\omega_1-\omega_2-\omega_3)} + 0.48e^{-(-2\omega_1-2\omega_2-2\omega_3)} + 0.0093e^{-(-4\omega_1-4\omega_2-4\omega_3)} - 0.25e^{-(-3\omega_1-3\omega_2-3\omega_3)}} \\
&+\frac{-0.0052H^1_{2A}(\omega_3)(e^{-(-7\omega_1-2\omega_2-2\omega_3)} + e^{-(-2\omega_1-7\omega_2-2\omega_3)}) + 0.051H^2_{2A}(\omega_1,\omega_2)e^{-(-3\omega_1-3\omega_2-5\omega_3)}}{1.0 - 0.79e^{-(-\omega_1-\omega_2-\omega_3)} + 0.48e^{-(-2\omega_1-2\omega_2-2\omega_3)} + 0.0093e^{-(-4\omega_1-4\omega_2-4\omega_3)} - 0.25e^{-(-3\omega_1-3\omega_2-3\omega_3)}} \\
&+\frac{+0.051H^2_{2A}(\omega_1,\omega_3)e^{-(-3\omega_1-5\omega_2-3\omega_3)} + 0.051H^2_{2A}(\omega_2,\omega_3)e^{-(-5\omega_1-3\omega_2-3\omega_3)}}{1.0 - 0.79e^{-(-\omega_1-\omega_2-\omega_3)} + 0.48e^{-(-2\omega_1-2\omega_2-2\omega_3)} + 0.0093e^{-(-4\omega_1-4\omega_2-4\omega_3)} - 0.25e^{-(-3\omega_1-3\omega_2-3\omega_3)}} \\
&+\frac{+0.00089H^1_{2A}(\omega_1)e^{-(-2\omega_1-3\omega_2-3\omega_3)} + 0.00089H^1_{2A}(\omega_2)e^{-(-3\omega_1-2\omega_2-3\omega_3)}}{1.0 - 0.79e^{-(-\omega_1-\omega_2-\omega_3)} + 0.48e^{-(-2\omega_1-2\omega_2-2\omega_3)} + 0.0093e^{-(-4\omega_1-4\omega_2-4\omega_3)} - 0.25e^{-(-3\omega_1-3\omega_2-3\omega_3)}} \\
&+\frac{+0.00089H^1_{2A}(\omega_3)e^{-(-3\omega_1-3\omega_2-2\omega_3)} - 0.24H^2_{2A}(\omega_1,\omega_2)e^{-(-2\omega_1-2\omega_2-7\omega_3)}}{1.0 - 0.79e^{-(-\omega_1-\omega_2-\omega_3)} + 0.48e^{-(-2\omega_1-2\omega_2-2\omega_3)} + 0.0093e^{-(-4\omega_1-4\omega_2-4\omega_3)} - 0.25e^{-(-3\omega_1-3\omega_2-3\omega_3)}} \\
&+\frac{-0.24H^2_{2A}(\omega_1,\omega_3)e^{-(-2\omega_1-7\omega_2-2\omega_3)} - 0.24H^2_{2A}(\omega_2,\omega_3)e^{-(-7\omega_1-2\omega_2-2\omega_3)}}{1.0 - 0.79e^{-(-\omega_1-\omega_2-\omega_3)} + 0.48e^{-(-2\omega_1-2\omega_2-2\omega_3)} + 0.0093e^{-(-4\omega_1-4\omega_2-4\omega_3)} - 0.25e^{-(-3\omega_1-3\omega_2-3\omega_3)}} \\
&+\frac{-0.11H^1_{2A}(\omega_1)H^1_{2A}(\omega_2)e^{-(-2\omega_1-2\omega_2-3\omega_3)} - 0.11H^1_{2A}(\omega_1)H^1_{2A}(\omega_3)e^{-(-2\omega_1-3\omega_2-2\omega_3)}}{1.0 - 0.79e^{-(-\omega_1-\omega_2-\omega_3)} + 0.48e^{-(-2\omega_1-2\omega_2-2\omega_3)} + 0.0093e^{-(-4\omega_1-4\omega_2-4\omega_3)} - 0.25e^{-(-3\omega_1-3\omega_2-3\omega_3)}} \\
&+\frac{-0.11H^1_{2A}(\omega_2)H^1_{2A}(\omega_3)e^{-(-3\omega_1-2\omega_2-2\omega_3)} - 0.075H^1_{2A}(\omega_1)H^2_{2A}(\omega_2,\omega_3)e^{-(-\omega_1-\omega_2-\omega_3)}}{1.0 - 0.79e^{-(-\omega_1-\omega_2-\omega_3)} + 0.48e^{-(-2\omega_1-2\omega_2-2\omega_3)} + 0.0093e^{-(-4\omega_1-4\omega_2-4\omega_3)} - 0.25e^{-(-3\omega_1-3\omega_2-3\omega_3)}} \\
&+\frac{+0.02H^1_{2A}(\omega_1)H^2_{2A}(\omega_2,\omega_3)(e^{-(-4\omega_1-\omega_2-\omega_3)} + e^{-(-\omega_1-4\omega_2-4\omega_3)})}{1.0 - 0.79e^{-(-\omega_1-\omega_2-\omega_3)} + 0.48e^{-(-2\omega_1-2\omega_2-2\omega_3)} + 0.0093e^{-(-4\omega_1-4\omega_2-4\omega_3)} - 0.25e^{-(-3\omega_1-3\omega_2-3\omega_3)}} \\
&+\frac{+0.02H^1_{2A}(\omega_2)H^2_{2A}(\omega_1,\omega_3)(e^{-(-\omega_1-4\omega_2-\omega_3)} + e^{-(-4\omega_1-\omega_2-4\omega_3)})}{1.0 - 0.79e^{-(-\omega_1-\omega_2-\omega_3)} + 0.48e^{-(-2\omega_1-2\omega_2-2\omega_3)} + 0.0093e^{-(-4\omega_1-4\omega_2-4\omega_3)} - 0.25e^{-(-3\omega_1-3\omega_2-3\omega_3)}} \\
&+\frac{+0.02H^1_{2A}(\omega_3)H^2_{2A}(\omega_1,\omega_2)(e^{-(-\omega_1-\omega_2-4\omega_3)} + e^{-(-4\omega_1-4\omega--\omega_3)})}{1.0 - 0.79e^{-(-\omega_1-\omega_2-\omega_3)} + 0.48e^{-(-2\omega_1-2\omega_2-2\omega_3)} + 0.0093e^{-(-4\omega_1-4\omega_2-4\omega_3)} - 0.25e^{-(-3\omega_1-3\omega_2-3\omega_3)}} \\
&+\frac{-0.075H^1_{2A}(\omega_2)H^2_{2A}(\omega_1,\omega_3)e^{-(-\omega_1-\omega_2-\omega_3)} - 0.075H^1_{2A}(\omega_3)H^2_{2A}(\omega_1,\omega_2)e^{-(-\omega_1-\omega_2-\omega_3)}}{1.0 - 0.79e^{-(-\omega_1-\omega_2-\omega_3)} + 0.48e^{-(-2\omega_1-2\omega_2-2\omega_3)} + 0.0093e^{-(-4\omega_1-4\omega_2-4\omega_3)} - 0.25e^{-(-3\omega_1-3\omega_2-3\omega_3)}}
\end{aligned}
$$

$$
+\frac{-3.42H^1_{2A}(\omega_1)H^2_{2A}(\omega_2,\omega_3)e^{-(-2\omega_1-2\omega_2-2\omega_3)}-3.42H^1_{2A}(\omega_2)H^2_{2A}(\omega_1,\omega_3)e^{-(-2\omega_1-2\omega_2-2\omega_3)}}{1.0-0.79e^{-(-\omega_1-\omega_2-\omega_3)}+0.48e^{-(-2\omega_1-2\omega_2-2\omega_3)}+0.0093e^{-(-4\omega_1-4\omega_2-4\omega_3)}-0.25e^{-(-3\omega_1-3\omega_2-3\omega_3)}}
$$

$$
+\frac{-3.42H^1_{2A}(\omega_3)H^2_{2A}(\omega_1,\omega_2)e^{-(-2\omega_1-2\omega_2-2\omega_3)}}{1.0-0.79e^{-(-\omega_1-\omega_2-\omega_3)}+0.48e^{-(-2\omega_1-2\omega_2-2\omega_3)}+0.0093e^{-(-4\omega_1-4\omega_2-4\omega_3)}-0.25e^{-(-3\omega_1-3\omega_2-3\omega_3)}}
$$

$$
+\frac{-0.027H^1_{2A}(\omega_1)H^1_{2A}(\omega_2)(e^{-(-3\omega_1-2\omega_2-5\omega_3)}+e^{-(-2\omega--3\omega_2-5\omega_3)})}{1.0-0.79e^{-(-\omega_1-\omega_2-\omega_3)}+0.48e^{-(-2\omega_1-2\omega_2-2\omega_3)}+0.0093e^{-(-4\omega_1-4\omega_2-4\omega_3)}-0.25e^{-(-3\omega_1-3\omega_2-3\omega_3)}}
$$

$$
+\frac{-0.027H^1_{2A}(\omega_1)H^1_{2A}(\omega_3)(e^{-(-3\omega_1-5\omega_2-2\omega_3)}+e^{-(-2\omega_1-5\omega_2-3\omega_3)})}{1.0-0.79e^{-(-\omega_1-\omega_2-\omega_3)}+0.48e^{-(-2\omega_1-2\omega_2-2\omega_3)}+0.0093e^{-(-4\omega_1-4\omega_2-4\omega_3)}-0.25e^{-(-3\omega_1-3\omega_2-3\omega_3)}}
$$

$$
+\frac{-0.027H^1_{2A}(\omega_2)H^1_{2A}(\omega_3)(e^{-(-5\omega_1-3\omega_2-2\omega_3)}+e^{-(-5\omega_1-2\omega_2-3\omega_3)})}{1.0-0.79e^{-(-\omega_1-\omega_2-\omega_3)}+0.48e^{-(-2\omega_1-2\omega_2-2\omega_3)}+0.0093e^{-(-4\omega_1-4\omega_2-4\omega_3)}-0.25e^{-(-3\omega_1-3\omega_2-3\omega_3)}}
$$

$$
+\frac{-0.075H^1_{2A}(\omega_1)H^2_{2A}(\omega_2,\omega_3)(e^{-(-\omega_1-3\omega_2-3\omega_3)}+e^{-(-3\omega_1-\omega_2-\omega_3)})}{1.0-0.79e^{-(-\omega_1-\omega_2-\omega_3)}+0.48e^{-(-2\omega_1-2\omega_2-2\omega_3)}+0.0093e^{-(-4\omega_1-4\omega_2-4\omega_3)}-0.25e^{-(-3\omega_1-3\omega_2-3\omega_3)}}
$$

$$
+\frac{-0.075H^1_{2A}(\omega_2)H^2_{2A}(\omega_1,\omega_3)(e^{-(-3\omega_1-\omega_2-3\omega_3)}+e^{-(-\omega_1-3\omega_2-\omega_3)})}{1.0-0.79e^{-(-\omega_1-\omega_2-\omega_3)}+0.48e^{-(-2\omega_1-2\omega_2-2\omega_3)}+0.0093e^{-(-4\omega_1-4\omega_2-4\omega_3)}-0.25e^{-(-3\omega_1-3\omega_2-3\omega_3)}}
$$

$$
+\frac{-0.075H^1_{2A}(\omega_3)H^2_{2A}(\omega_1,\omega_2)(e^{-(-3\omega_1-3\omega_2-\omega_3)}+e^{-(-\omega_1-\omega_2-3\omega_3)})}{1.0-0.79e^{-(-\omega_1-\omega_2-\omega_3)}+0.48e^{-(-2\omega_1-2\omega_2-2\omega_3)}+0.0093e^{-(-4\omega_1-4\omega_2-4\omega_3)}-0.25e^{-(-3\omega_1-3\omega_2-3\omega_3)}}
$$

$$
+\frac{+0.28H^1_{2A}(\omega_1)H^2_{2A}(\omega_2,\omega_3)(e^{-(-2\omega_1-3\omega_2-3\omega_3)}+e^{-(-3\omega--2\omega_2-2\omega_3)})}{1.0-0.79e^{-(-\omega_1-\omega_2-\omega_3)}+0.48e^{-(-2\omega_1-2\omega_2-2\omega_3)}+0.0093e^{-(-4\omega_1-4\omega_2-4\omega_3)}-0.25e^{-(-3\omega_1-3\omega_2-3\omega_3)}}
$$

$$
+\frac{+0.28H^1_{2A}(\omega_2)H^2_{2A}(\omega_1,\omega_3)(e^{-(-3\omega_1-2\omega_2-3\omega_3)}+e^{-(-2\omega_1-3\omega_2-2\omega_3)})}{1.0-0.79e^{-(-\omega_1-\omega_2-\omega_3)}+0.48e^{-(-2\omega_1-2\omega_2-2\omega_3)}+0.0093e^{-(-4\omega_1-4\omega_2-4\omega_3)}-0.25e^{-(-3\omega_1-3\omega_2-3\omega_3)}}
$$

$$
+\frac{+0.28H^1_{2A}(\omega_3)H^2_{2A}(\omega_1,\omega_2)(e^{-(-3\omega_1-3\omega_2-2\omega_3)}+e^{-(-2\omega_1-2\omega_2-3\omega_3)})}{1.0-0.79e^{-(-\omega_1-\omega_2-\omega_3)}+0.48e^{-(-2\omega_1-2\omega_2-2\omega_3)}+0.0093e^{-(-4\omega_1-4\omega_2-4\omega_3)}-0.25e^{-(-3\omega_1-3\omega_2-3\omega_3)}}
$$

$$
+\frac{+0.02H^1_{2A}(\omega_1)H^1_{2A}(\omega_2)H^1_{2A}(\omega_3)(2e^{-(-3\omega_1-\omega_2-\omega_3)}+2e^{-(-\omega_1-3\omega_2-\omega_3)}+2e^{-(-\omega_1-\omega_2-3\omega_3)})}{1.0-0.79e^{-(-\omega_1-\omega_2-\omega_3)}+0.48e^{-(-2\omega_1-2\omega_2-2\omega_3)}+0.0093e^{-(-4\omega_1-4\omega_2-4\omega_3)}-0.25e^{-(-3\omega_1-3\omega_2-3\omega_3)}}
$$

$$
+\frac{-0.41H^1_{2A}(\omega_1)H^1_{2A}(\omega_2)H^1_{2A}(\omega_3)(2e^{-(-3\omega_1-2\omega_2-2\omega_3)}+2e^{-(-2\omega_1-3\omega_2-2\omega_3)}+2e^{-(-2\omega_1-2\omega_2-3\omega_3)})}{1.0-0.79e^{-(-\omega_1-\omega_2-\omega_3)}+0.48e^{-(-2\omega_1-2\omega_2-2\omega_3)}+0.0093e^{-(-4\omega_1-4\omega_2-4\omega_3)}-0.25e^{-(-3\omega_1-3\omega_2-3\omega_3)}})
$$